Thèse n° 10 682

Investigation of room-temperature single-photon emitters in GaN-based materials and GaN/AlN quantum dots

Présentée le 17 juin 2024

Faculté des sciences de base
Laboratoire en semiconducteurs avancés pour la photonique et l'électronique
Programme doctoral en physique

pour l'obtention du grade de Docteur ès Sciences

par

Johann Nicolaï STACHURSKI

Acceptée sur proposition du jury

Dr F. Blanc, président du jury
Prof. N. Grandjean, directeur de thèse
Prof. V. Voliotis, rapporteuse
Dr B. Gayral, rapporteur
Dr C. Galland, rapporteur

École
polytechnique
fédérale
de Lausanne

2024

Acknowledgements

It comes as no surprise that a thesis is not the work of a single person. In fact, this work has only been made possible thanks to the contributions of many, to whom I want to express my profound gratitude. First, to my supervisor Prof. Nicolas Grandjean, who, after accepting me as a master student for two years, entrusted me with another half decade of PhD. All my thanks for your considerate and thoughtful supervision throughout the years, your high sense of empathy, as well as for the passionate political discussions we have shared. I ought to express my admiration for your ability to install a positive work environment in the lab, which can be so valuable over the long run. I am also deeply grateful to prof. Gordon Callsen who taught me how to become a spectroscopist. You have been a truly inspiring and kind mentor. Ich kann dir nicht genug für Dein unerschütterliches Vertrauen und Deine Unterstützung danken.

Academic writing can be extremely tedious and painful. For his more than welcome support in writing the paper and thorough feedbacks on the thesis manuscript, I would like to thank Dr. Raphaël Butté. I am also extremely thankful to Dr. Sebastian Tamariz, to whom I owe the 5×5 mm^2 of sample that led to more than half of my thesis manuscript, and to Dr. Jean-François Carlin, who grew presciently the additional layers that helped me complete it. I would then like to express my appreciation to Prof. Valia Voliotis, Dr. Bruno Gayral, Dr. Christophe Galland and Prof. Frédéric Blanc, who took the time to review this work with a great deal of thoughtfulness.

I would also like to extend my profound gratitude to the members of the electronic and mechanical workshops, as well as to all IPHYS engineers and technicians, whose expertise has been vital to my research in many aspects. Many thanks to Florence for her considerate help with all IT issues and to Nadja and Anh for their constant benevolence.

I cannot go on with these acknowledgements without mentioning what a great time I have spent around at ~~Sat~~ the LASPE thanks to all my wonderful fellows. My warm-hearted thanks to Pierre and Hoda who joyfully put up with my exuberance for more than four years and to Anna whose cheerfulness has recently completed our room. You have been precious office mates. Thank you Yao for your superb leadership in the sea of our group indecisiveness, Danxuan for your priceless reactions to surprise and beer partnership and Samu for your great bantering friendship. Special thanks go to Thomas, a magnificent BBB partner and dearly missed english-to-english translator, to Da(da)vide for his heartfelt and comforting presence when nothing would go as planned, and to Alexandros, who I know will take a revolutionary care of the IR lab now!

The LASPE owes also much to its great team of post-docs and senior members, past and present. A big thank you to Camille for her dedication, Szymon for the tasty coffee breaks, Mayeul for his willingness to help, Etienne, François, Ian, Joachim, Jun, Pierre sr., Pirouz, Wei… and more! All my appreciation also goes to the newest generation, Guillaume, Stefanie, Valentine, with whom I have been delighted to work.

To my friends: In the deepest anxiety of missing a name and with the modest hope that you will still recognize yourselves, I would like to thank you all for the amazing times you offered me over the past few years. Whether it was around a drink, another delightful board game, or yet another demonstration hoping for some change to come, I cherish our moments. Big hug to everyone!

I would also like to express my wholehearted gratitude to my family for their comforting presence, even during times when I was not as present as I could have been. Above all, thank you Mom, Dad and my sister for your unconditional and unwavering support and for the solace of the family cocoon. I know I can count on you.

And finally to Pilar: thank you so much for being there with me over the last years, bearing with my never-ending thesis writing and my life/ecological anxieties. You made the worst moments bearable and the best moments even brighter.

Lausanne, June 2, 2024 J. S.

Abstract

Over the past decade, quantum photonics platforms aiming at harnessing the fundamental properties of single particles, such as quantum superposition and quantum entanglement, have flourished. In this context, single-photon emitters capable of operating at room temperature (RT) have garnered significant attention, as they hold a strong potential for enabling cost-efficient and scalable instruments for applications ranging from quantum cryptography to quantum sensing. Among investigated candidates, single-photon emitters (SPEs) based on the III-nitride (III-N) platform stand out as promising competitors, benefiting from a well-established semiconductor infrastructure originally developed for solid-state lighting applications.

RT single-photon emission has been demonstrated in III-N materials from quantum dots (QDs) and defect-related emitters. This thesis addresses both types of emitters, aiming to deepen our understanding of their optical properties through photoluminescence (PL) measurements performed on individual emitters and time-resolved spectroscopy performed on QD ensembles. The discussion presented here is structured into three independent chapters, each addressing complementary aspects of this thesis.

Initially, we examine the experimental challenges associated with the record of PL signal issued from point-like sources and discuss the inherent biases arising from the adopted excitation scheme. These observations are supplemented by simulations of the photon extraction efficiency and Fabry-Perot interference phenomena that emerge when investigating micrometer-thick layers.

Having established the necessary experimental foundations, we delve into the optical properties of GaN/AlN self-assembled (SA)QDs, starting with the unique influence of spectral diffusion (SD) on such polar structures and its indication of local defect concentrations. We then detail the PL response of high-energy QDs to variations in excitation power and temperature, comparing our results with phenomenological simulations of QD recombination dynamics. We further supplement the analysis by assessing the single-photon emission properties of excitonic lines between cryogenic and RT with a particular interest for the influence of biexciton PL on the single-photon purity. To complete our investigation of the QD recombination dynamics, we analyze time-resolved PL transients acquired on an ensemble of QDs with an emphasis on the exciton lifetime and multiexcitonic recombination processes.

Confronting our results with prior findings, we finally investigate the influence of growth conditions on the optical properties of GaN/AlN SAQDs.

In the final chapter, we shift our focus to the investigation of defect-related RT SPEs in GaN. We begin by highlighting the methodology developed to address these randomly distributed emitters and discuss the various protocols established to characterize their optical signature, concentration, and spatial distribution. Our results are supplemented with second-order photon autocorrelation measurements to assess the potential of such emitters for RT applications. We conclude by presenting perspective statistics to assess the spectral and spatial distribution of these SPEs along with the in-plane orientation of the emitting dipole.

Résumé

Au cours de la dernière décennie, les plateformes de photonique quantique visant à exploiter les propriétés fondamentales de particules uniques, telles que la superposition et l'intrication quantique, ont grandement évolué. Dans ce contexte, les émetteurs de photons uniques (EPU) capables de fonctionner à température ambiante suscitent un intérêt certain de par leur potentiel pour le développement d'instrumentation à bas coût et grand échelle, et pour des applications allant de la cryptographie à la détection quantique. Parmi les candidats étudiés, les émetteurs de photons uniques basés sur la plateforme nitrures d'éléments III, qui bénéficient d'une infrastructure industrielle solide initialement développée pour les diodes électroluminescentes bleues, se démarquent tout particulièrement.

L'émission de photons uniques à température ambiante a été reportée dans les nitrures d'éléments III aussi bien pour des boîtes quantiques (BQ) que pour des défauts ponctuels (DP). Cette thèse aborde les deux types d'émetteurs et a pour but d'approfondir notre compréhension de leurs propriétés optiques *via* des mesures de photoluminescence (PL) réalisées sur des émetteurs individuels, et par l'usage de la spectroscopie de PL résolue en temps. La discussion est structurée en trois chapitres indépendants, abordant chacun des aspects complémentaires.

Dans un premier temps, nous examinons les défis expérimentaux associés à l'acquisition des spectres de PL provenant de sources ponctuelles et discutons des biais inhérents au schéma d'excitation adopté. Ces observations sont complétées par des simulations de l'efficacité d'extraction de la lumière et de phénomènes d'interférence qui émergent lors de l'investigation de couches d'épaisseur micrométrique.

Après avoir établi la base expérimentale, nous nous penchons sur les propriétés optiques des BQ GaN/AlN auto-assemblées, en commençant par discuter le caractère unique de la diffusion spectrale sur de telles structures polaires et son usage en tant que révélateur de la concentration locale de défauts. Nous détaillons ensuite les variations de PL de BQ de haute énergie face à des variations de la puissance d'excitation et de la température, et comparons ces résultats avec des simulations phénoménologiques de la dynamique de recombinaison dans les BQ. Nous complétons ensuite l'analyse en évaluant les propriétés d'émission de photons uniques des lignes excitoniques de 5 K à température ambiante, en mettant l'accent sur l'influence de la luminescence du biexciton sur la pureté d'émission de photons uniques. Pour compléter l'étude de la dynamique des BQ, nous analysons des courbes de décroissance

de PL résolue en temps acquises cette fois sur un ensemble de BQ. L'accent est portée ici sur l'étude de la durée de vie des excitons et sur les processus de recombinaison multiexcitoniques. Nous concluons cette analyse en comparant nos valeurs avec des résultats antérieurs, ce qui nous permet d'identifier l'impact des conditions de croissance sur les propriétés optiques des BQ GaN/AlN auto-assemblées.

Dans la dernière partie, nous portons notre attention sur l'étude d'EPU à température ambiante liés à des DPs présents dans le GaN massif. Nous commençons par détailler la méthodologie développée pour étudier ce genre d'émetteurs, dont la distribution aléatoire complique les mesures, et discutons des différents protocoles établis pour caractériser leur signature optique, leur concentration et leur distribution spatiale. Nous complétons ces résultats par des mesures d'autocorrélation de second ordre pour évaluer le potentiel de ces émetteurs dans des applications à température ambiante. Nous concluons en présentant des résultats statistiques préliminaires visant à évaluer les distributions spectrale et spatiale de ces EPU, ainsi que l'orientation du dipôle associé dans le plan.

Contents

Introduction

The XX$^{\text{th}}$ century witnessed the advent of quantum mechanics, revolutionizing various aspects of society and paving the way for groundbreaking advances in computation, communication, and lighting, among others. Although building upon quantum principles, current applications do not fully capture the essence of ’quantum’ effects. Nowadays, we are experiencing the emergence of a new generation of quantum technologies, known as the second quantum revolution [1], which seek to directly harness the fundamental properties of individual particles, leveraging principles such as quantum state superposition and quantum entanglement.

Within this field, quantum photonics holds a place of choice, building upon the attractive properties of photons as information vectors, including their ability for high-speed, long-range transmission and their inherent low-noise properties [2]. The success of any application in this domain hinges on the use of bright single-photon sources with characteristics that ideally offer on-demand operation, high efficiency, and high purity [3].

As of today, III-arsenide quantum dots (QDs) indisputably stand out as the most mature and high-stack system for single-photon emission [4–6], but their success is hampered by their inability to operate at room temperature (RT) [7], necessitating their integration with costly and space-intensive cryogenic units, which impedes their scalability. Alternatives to these state-of-the-art QDs are thus highly desirable, particularly for less stringent applications that do not rely upon photon indistinguishability [8], including quantum metrology [9], quantum imaging [10], and, most prominently, quantum-key distribution [11].

For more than a decade, a large variety of options have been under scrutiny, with highly promising candidates including Si [12] and N vacancies [13, 14] in diamond, along with other color centers [15], defects in hexagonal boron nitride (hBN) 2D layers [16, 17], and defects in the more device-friendly [18] SiC platform [17, 19]. Among these candidates, III-nitrides (III-Ns) stand out as one of the most promising platforms for quantum photonic applications as they benefit from a well-established semiconductor infrastructure inherited from the lighting industry, resulting in excellent layer design control over epitaxial growth.

RT single-photon emission in III-N semiconductors (SCs) has been demonstrated for over a decade in GaN/AlGaN nanowire QDs [20, 21]. Since then, it has been evidenced in InGaN/-GaN nanowire QDs [22, 23] and GaN/AlN self-assembled (SA) QDs [24, 25], with III-N QDs exhibiting photoluminescence (PL) from the deep near ultraviolet (UV) to the telecom range [26–29]. More recently, RT single-photon emission has also been observed from defects embedded in bulk GaN [30–33] and AlN [34, 35], with bright emitters covering a broad spectrum ranging from the visible to the telecom range. Despite these promising results, a complete understanding of the physical properties of both types of single-photon emitters (SPEs) is still lacking, thereby hindering their further advancement toward engineering applications. This knowledge gap is particularly pronounced for defect-related SPEs, whose nature remains elusive, thus motivating further investigation.

The objective of this thesis is twofold. Firstly, to provide an in-depth understanding of the optical properties and carrier recombination dynamics at play in GaN/AlN SAQDs. This involves a combination of micro-photoluminescence (µ-PL) measurements done on individual high energy emitters and time-resolved photoluminescence (TRPL) analysis performed on a QD ensemble. Secondly, to establish a versatile platform for investigating defect based single-photon emission in GaN, with the goal of elucidating the origin and formation mechanisms of bright RT SPEs with significant potential for photonic applications. Due to the distinct nature of these two research topics, the thesis is structured around three main chapters, each focusing on a different aspect of the work conducted and largely self-contained:

- **Chapter 1: Experimental considerations** provides a detailed description of the experimental setup developed for this research, with a particular emphasis on the operational principles underlying µ-PL measurements.
- **Chapter 2: GaN/AlN quantum dots** is dedicated to the investigation of QDs. Starting with an introduction of the physical properties of III-N materials and GaN/AlN zero-dimensional structures, with a focus on their peculiarities in polar materials. Following this, this chapter outlines the sample structure and growth procedure before developing the results obtained through µ-PL and TRPL.
- **Chapter 3: Point defects acting as single-photon emitters in bulk GaN layers** introduces the theoretical framework for the investigation of point defects (PDs) and provides a comprehensive overview of the different protocols developed for the study of PD based SPEs. This chapter finally details the preliminary findings obtained from early measurements.

This thesis is concluded with a comparative perspective on the outcomes derived from QDs and PDs. The results presented in Chap. 3 have not been published yet. A portion of the results highlighted in Chap. 2 have been published in:

J. Stachurski, S. Tamariz, G. Callsen, R. Butté, N. Grandjean, "Single photon emission and recombination dynamics in self-assembled GaN/AlN quantum dots", Light: Science & Applications **11**, 114 (2022)

S. Tamariz, G. Callsen, J .Stachurski, R. Butté, N. Grandjean, "Toward bright and pure single photon emitters at 300 K based on GaN quantum dots on silicon", ACS photonics **7**, 1515 (2020)

1 Experimental considerations

Extracting the proper physical meaning from a set of measurements necessitates a comprehensive understanding of the measurement process, including potential biases and limitations. Therefore, before delving into the discussion of PL results obtained from different sets of SPEs, it is essential to elaborate on the operational principles of the μ-PL setups utilized in this study. The initial section (Sect. 1.1) offers an overview of μ-PL and introduces pertinent considerations for achieving optimal resolution. Section 1.2 elaborates further on the setup specificities regarding its automation, while details on the setup efficiency are provided in Sect. 1.3. Section 1.4 is dedicated to polarization-resolved μ-PL measurements and Sect. 1.5 focuses on the intricacies of time-resolved measurements. Finally, in Sect. 1.6, interference patterns related to Fabry-Perot cavity effects are thoroughly analyzed.

1.1 Basics of micro-photoluminescence

This PhD thesis has been structured into two projects. The first project comprised the characterization of GaN/AlN QDs using an existing μ-PL setup, designed to operate from the UV to the visible, referred to as the UV setup. The second project was dedicated to the investigation of defects in bulk GaN layers, necessitating the construction of a setup from scratch. We will refer to it as the near infrared (NIR) setup, although it has been designed with high versatility and can technically be utilized from the UV to the telecom range with minor adjustments. Both setups share a similar configuration, comprising the laser assembly, the imaging assembly, the detection assembly and the core components depicted in Fig. 1.1. The descriptions and sketches in this chapter primarily draw inspiration from the newly-built NIR setup, with the understanding that they also generally apply to the UV setup unless explicitly stated otherwise.

1.1.1 Setup description

μ-PL setups closely resemble standard macro-PL setups in their basic working principle. They involve focusing a laser beam onto the investigated sample, and collecting the PL signal while

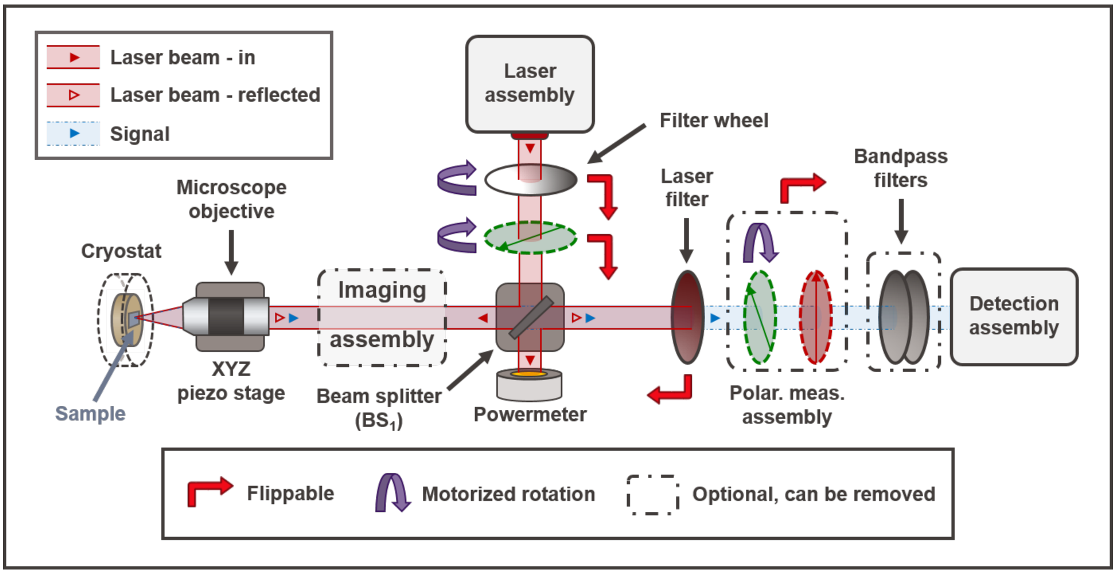

Figure 1.1: Schematic of the µ-PL setup. The general design is based on the current NIR setup, although all functional elements can be transposed to the UV setup, *mutatis mutandis*. The polarizer and half-wave plate (HWP) are depicted in red and green, respectively.

filtering out reflected and scattered laser light. The µ-PL setup specificity holds to its sub-micron resolution, achieved here with a high numerical aperture (NA) long-working distance objective, as well as to its sustained mechanical stability and sub-micron positioning accuracy. Mechanical stability must be ensured even for samples cooled down at cryogenic temperature and is only achieved through the use of an appropriate cryostat.

The UV setup is composed of a closed-cycle helium cryostat (Cryostation C2 from Montana Instruments) with a built-in three-axis piezoelectric stack from Attocube GmbH, for coarse positioning. The sample is mounted horizontally and sub-micron resolution is achieved with an M Plan APO UV ×80 Mitutoyo microscope objective (NA = 0.55). The response of the piezoelectric stack is non-linear and changes with temperature. Therefore, mapping the sample necessitates mounting the objective on a Physik Instrumente (PI) XY piezostage positioned outside the cryostat. Focusing is performed manually with a differential screw. For TRPL measurements, the objective is replaced with a conventional plano-convex lens of focal length $f = 25\,\text{mm}$.

The NIR setup is currently equipped with a continuous-flow cryostat (MicrostatHiResII from Oxford Instruments) in a vertical configuration. Coarse sample positioning is achieved by mounting the cryostat arm on two high-load linear stages. For measurements in the NIR to telecom range, a Mitutoyo M Plan APO NIR ×100 microscope objective (NA = 0.5) is employed. The objective is mounted on a PI XYZ nanopositioner used for sample mapping and depth scans. Coarse positioning of the objective is ensured through Newport crossed-roller bearing steel stages with micrometer screws.

The sample is illuminated in a backscattering configuration, whereby the excitation laser beam is directed onto the sample through the microscope objective responsible for signal collection. The beam is coupled in through a beam splitter (BS) (BS_1 in Fig. 1.1) allowing it to reach the objective parallel to the optical axis. This configuration minimizes comatic aberrations [36] that could deteriorate the laser focus, but induces a trade-off in the form of intensity losses. When using a conventional BS with a 50:50 split ratio (reflectance(R):transmittance(T)), the laser intensity is halved upon reflection and likewise after transmission through BS_1. While this is a minor concern when recording PL spectra, it can have a more substantial impact during hours-long $g^{(2)}(\tau)$ measurements, where the coincidence rate is quadratically dependent on the signal intensity. Achieving a sufficiently high laser fluence at the sample surface poses no issue, regardless of the losses along the excitation path. As such, one strategy to enhance the collection efficiency is to employ a BS with a split ratio of 10:90, ensuring that 90% of the PL signal collected through the microscope objective is transmitted. However, this solution may not be ideal for polarization-dependent measurements, as both R and T coefficients vary quantitatively between s- and p-polarized light. Here, s- and p- refer to the electric field components perpendicular and parallel to the plane of incidence, respectively. For instance, with a 10:90 UV fused silica broadband BS, the reflectance varies from 3.6 to 19.2 between p-polarized and s-polarized light. This results in a fivefold change in excitation power without any compensation scheme, impacting the reliability of the measurements. Both 50:50 and 10:90 BS are used interchangeably for experiments conducted with the UV setup.

An alternative approach involves using a dichroic mirror with a cut-on wavelength λ_{cut} close to the excitation wavelength λ_{exc}, ensuring maximum reflection of the laser ($\lambda_{\text{exc}} < \lambda_{\text{cut}}$) and optimal transmission of the luminescence signal ($\lambda_{\text{SPE}} > \lambda_{\text{cut}}$). The drawback of this solution is reduced visibility, as any peak located between λ_{exc} and λ_{cut} becomes undetectable. By default, the NIR setup is outfitted with a dichroic mirror ($\lambda_{\text{cut}} = 665\,\text{nm}$). Using an ultra broadband (0.4 to 2 µm) dielectric half mirror is an alternate way to investigate luminescence below the cut-on wavelength.

The excitation power is monitored using a motorized, continuously variable, reflective neutral density, (see filter wheel on Fig. 1.1). This filter has an optical density (OD) range from 0.04 to 4 suitable for single-shot power-dependent measurements. Automation of power control is achieved by integrating the filter wheel with a photodiode mounted on BS_1. The computation of the excitation power P_{exc} and excitation power density σ_{exc} at the sample surface can be found in Subsect. 1.2.2, while the setup automation procedure is outlined in Appendix A.1.

The laser assembly, as depicted in Fig. 1.1, comprises a combination of various lasers which can be swiftly coupled to the setup through a set of flip mirrors illustrated in Fig. 1.2. Mirrors M_1 and M_2 facilitate the rapid realignment of the laser beam along the optical axis while leaving BS_1 fixed. Both setups incorporate a 488 nm continuous-wave (CW) solid state laser (Coherent Genesis CX SLM) and a frequency-doubler (Spectra-Physics WaveTrain) for UV excitation at 244 nm. The UV setup is complemented with a CW 266 nm Nd:YAG laser from Crylas and a Teem Photonics Microchip 266 nm pulsed Nd:YAG laser, operating at a repetition

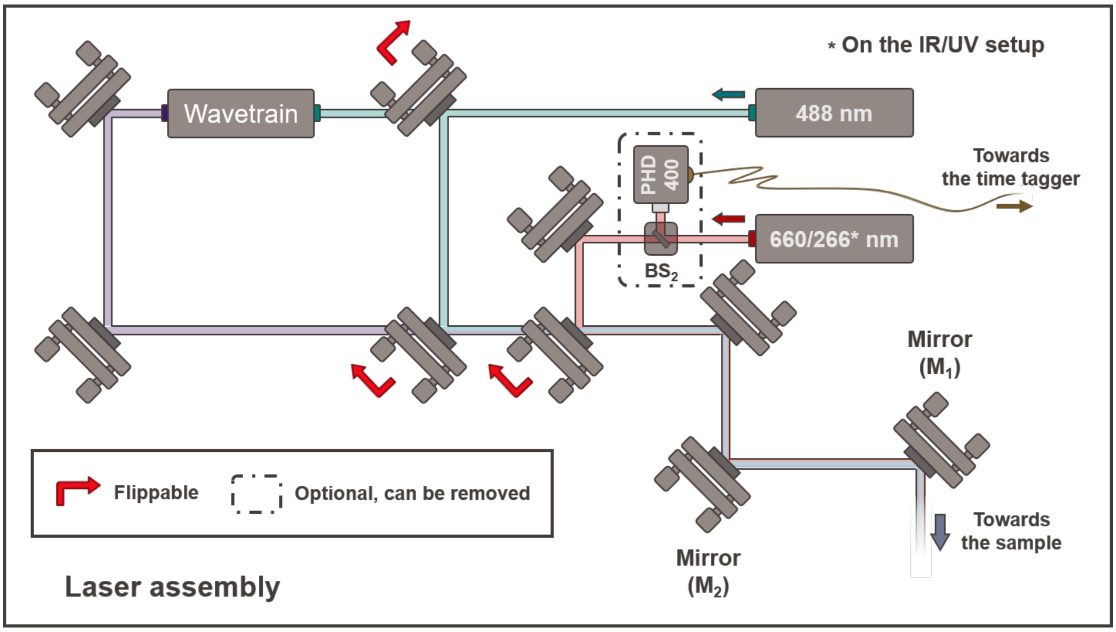

Figure 1.2: Laser assembly. The photodiode module is only present on the UV setup and is used in combination with a 266 nm pulsed laser.

rate of 8.45 kHz and a pulse duration of 440 ps. For TRPL measurements, a fraction of the pulsed laser intensity is directed through a BS (BS$_2$ in Fig. 1.2) toward a photodiode module to record the reference excitation pulse (as per Sect. 1.5 for details).

The NIR setup is equipped with a 659.6 nm CW solid state laser (Cobolt Flamenco). As of the time of writing, no pulsed laser has been installed. However, we plan to integrate a tunable picosecond laser, namely a Tsunami ultrafast Ti:sapphire oscillator operating at 80.7 MHz pumped with a continuous-wave solid-state Millenia eV (Spectra Physics). This integration, set to occur through optical fiber connections in the near future, is intended to facilitate high-resolution TRPL measurements on PDs. Additional lasers have been occasionally employed but do not form part of the default configuration. Thanks to its versatility, this setup now serves as a test platform for various devices.

Laser beams typically exhibit strong linear polarization, with the electric field oscillating in a specific direction perpendicular to the beam axis. The interaction of an SPE with the laser beam depends on its polarization angle, and monitoring the PL of a single emitter as a function of the laser polarization angle can provide insights into its excitation scheme. Similarly, investigating the polarization of the luminescence signal offers information about the nature of the radiative state(s). To conduct polarization-resolved measurements, the setups are equipped with a collection of HWP and linear polarizers (refer to the polarization measurement assembly in Fig. 1.1), which can be positioned in either the excitation or detection path. The procedure and outcomes of polarization-dependent measurements are discussed in Sect. 1.4.

The laser intensity is orders of magnitude higher than the single-defect luminescence it triggers.

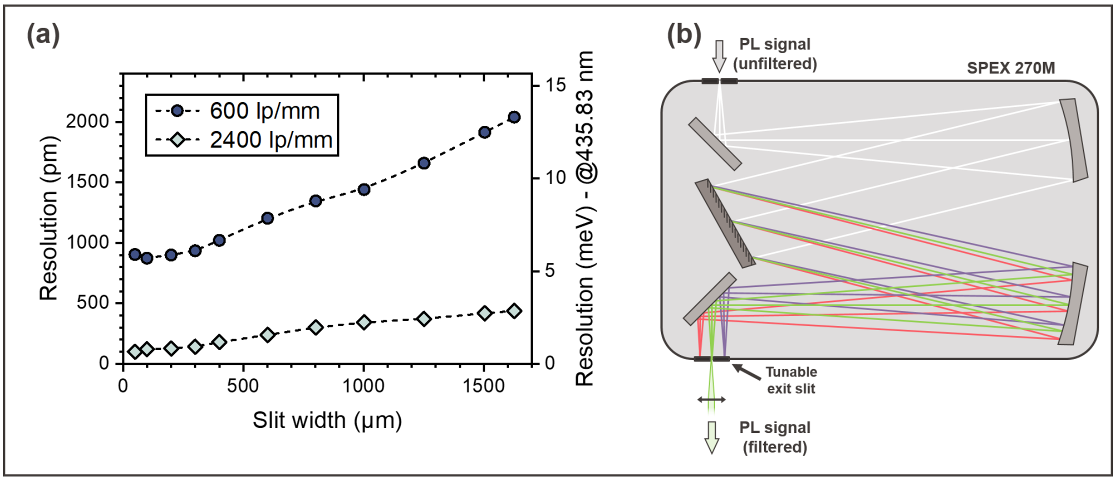

Figure 1.3: **(a)** Spectral resolution of the mercury Hg(I) line (435.83 nm), as a function of the SPEX 270M exit slit width. Two gratings are considered. Reproduced from [37] and measured by Prof. G. Callsen. **(b)** Illustrative diagram of the monochromator configuration for spectral filtering.

Hence, the reflection of the laser beam at the sample surface and interfaces can severely impede detection and needs to be filtered out. To address this, each laser is accompanied by an adapted long-pass filter characterized by a high reflectance (OD > 6) at the laser wavelength and a sharp transmission edge, to maximize the spectral range under investigation.

In the context of $g^{(2)}(\tau)$ measurements, filtering out background PL is equally crucial, and two strategies have been adopted for this purpose. The UV setup incorporates a monochromator (SPEX 270M) used to select the desired spectral window by monitoring the exit slit width (refer to the description in Fig. 1.3). It has a maximum spectral range of 2 nm for a maximum slit opening of 1.6 mm. For increased versatility, the NIR setup is equipped with a set of 10 nm dielectric bandpass filters with sharp cut-off wavelengths. These filters can be tilted and combined in pairs to select the desired spectral window.

1.1.2 Detection and analysis of the PL signal

Following filtering, the PL signal undergoes processing in one of the two detection arms illustrated in Fig. 1.4. The first arm features a spectrometer consisting of a light sensor and a monochromator in Czerny-Turner configuration, which varies according to the setup and wavelength targeted. The UV setup incorporates a spectrometer that consists of a liquid-N_2 cooled charge coupled device (CCD) (Symphony II from Horiba) attached to a Horiba FHR 640 monochromator, which features 150, 1800, and 3600 lp/mm gratings. For this study, only the first two gratings were employed. In contrast, the NIR setup incorporates three spectrometers used interchangeably. The first comprises another Symphony II CCD connected to a Triax 550 (Horiba) monochromator, optimized for the UV to visible range. Among other things, the back-illuminated silicon CCD sensor of the Symphony II is unsuitable for the NIR spectral

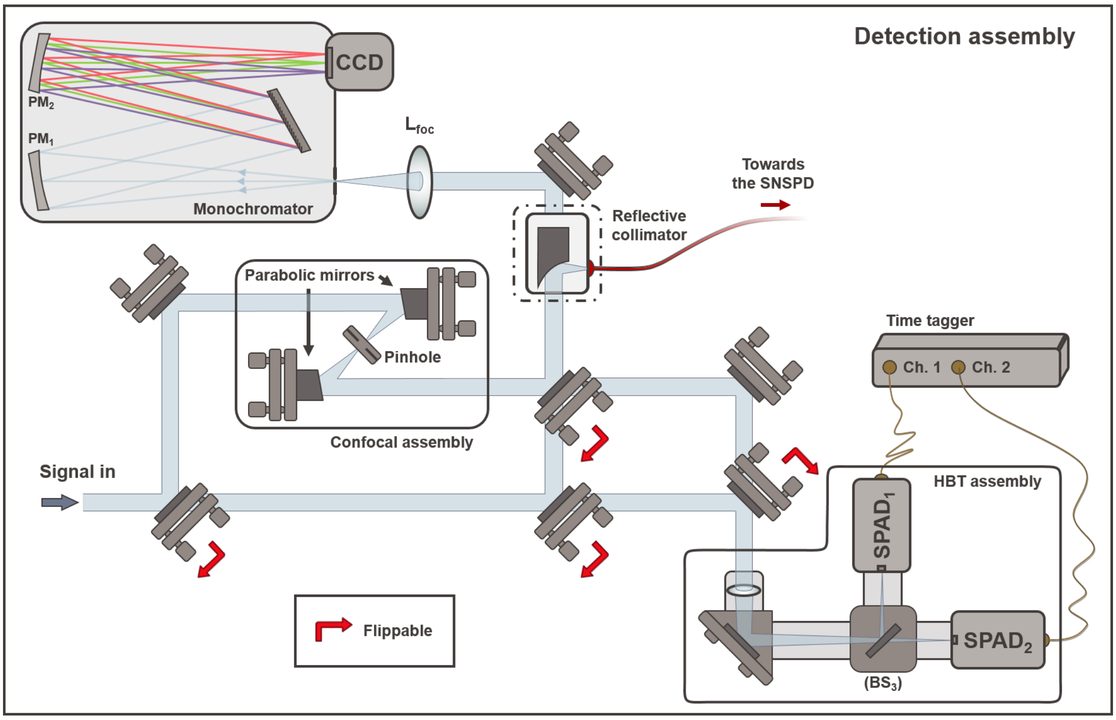

Figure 1.4: Detection assembly diagram used with the NIR setup. For the UV setup, the confocal assembly is unavailable and the HBT assembly features two photomultiplier tube (PMT) detectors in place of the single-photon avalanche diodes (SPADs). The superconducting nanowire single-photon detector (SNSPD) and its associated collimator are exclusive to the NIR setup. For the telecom range, the CCD is replaced by an InGaAs array detector connected to another dedicated monochromator.

range due to interference fringes overlaying the PL spectrum, the so-called etaloning effect, as explained in Sect. 1.6. To investigate deep-level defect luminescence, we opted for a different spectrometer, using a front-illuminated Synapse FIUV CCD (Horiba) attached to a MicroHR (Horiba) monochromator. This monochromator was originally designed for UV use and is equipped with gratings of 600 and 2400 lp/mm, with only the low-resolution grating programmed to operate above 700 nm. The current spectrometer is not optimal and warrants replacement soon with a back-illuminated deep depletion CCD featuring higher spectral resolution and specifically designed for NIR applications. Additionally, the low-resolution grating is unsuitable for measurements at cryogenic temperatures, as it is unable to resolve the narrow linewidth of SPE luminescence features. Consequently, our focus in this study was constrained to investigating defect luminescence at RT, where thermal broadening surpasses the monochromator spectral limitations. A third spectrometer is dedicated to operations in the telecom range. Traditional CCDs are unsuitable beyond the micron range, where silicon becomes transparent. Hence, an InGaAs array (iDus 1.7 µm InGaAs from Andor) is used as sensor, attached to an Andor Kymera 193i monochromator.

For the analysis, the collimated signal is focused onto the monochromator entrance slit using

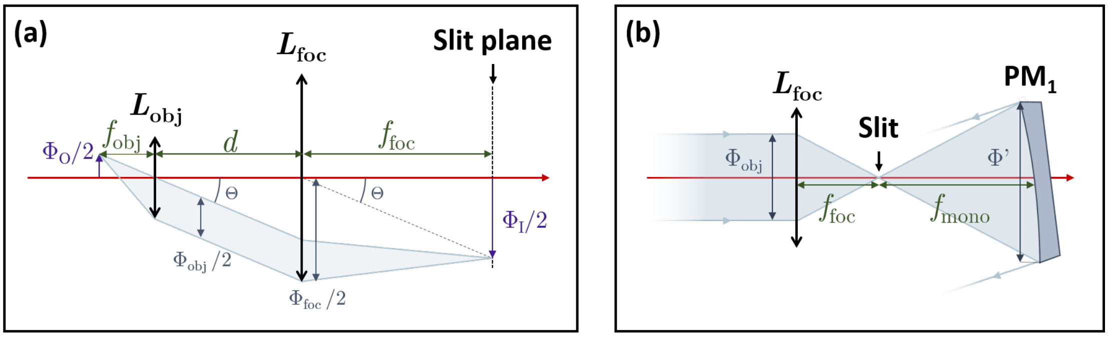

Figure 1.5: Ray tracing diagrams. **(a)** An image of the sample surface is formed in the slit plane with diameter Φ_I. **(b)** The collimated signal is focused on the monochromator entrance slit and spread over the first parabolic mirror PM_1.

the lens L_{foc} (depicted in Fig. 1.4). To achieve optimal alignment across a broad spectral range, L_{foc} should ideally be an achromatic doublet. However, these lenses are usually unavailable in the UV or with short focal lengths. The signal originating from a point object at the sample surface, offset from the optical axis, will propagate after the objective lens L_{obj} with an angle Θ depicted in Fig. 1.5(a). Therefore, the size of the object imaged on the monochromator entrance slit plane is constrained by the distance separating the objective from the focusing lens, d, and the lens diameter Φ_{foc}. The image diameter is determined by the relationship:

$$\Phi_I = \frac{\Phi_{foc} - \Phi_{obj}}{d} f_{obj}, \tag{1.1}$$

and the size of the object follows through:

$$\Phi_O = \Phi_I \frac{f_{foc}}{f_{obj}}. \tag{1.2}$$

Here, f_{obj} and f_{foc} correspond to the focal length of the objective and focusing lens, respectively, and Φ_{obj} refers to the objective rear diameter. The ratio f_{foc}/f_{obj} represents the magnification of the telescope formed by the objective and focusing lenses. In practice, the image is cut by closing the entrance slit, so that Φ_I only represents the maximum image diameter in the horizontal direction. Furthermore, luminescence is only collected from the effectively excited sample area, as detailed in Subsect. 1.1.3. The distance d must be consistently fixed to ensure that Φ_O is above the diffraction-limited spot size.

A monochromator in Czerny-Turner configuration functions in such a way that the object formed on the entrance slit is imaged on the detector chip after diffraction by the grating. The signal focused through L_{foc} undergoes collimation by a first parabolic mirror (PM_1 in Figs. 1.4 and 1.5(b)), diffraction by the grating, and subsequent refocusing by a second parabolic mirror (PM_2) on the detector plane. The two parabolic mirrors, as is common, have identical focal lengths (f_{mono}), ensuring equality in object and image size. The image of a point-like source, after passing through the lenses L_{obj}, L_{foc}, is an airy disk (see Subsect. 1.1.3) whose size is proportional to the magnification. If this spot is excessively large, it can cover multiple pixels on the detector leading to artificial broadening of spectral lines. Typically, this is not the limiting factor—the spectrometer resolution is more often constrained by its resolving power, which is proportional to the number of grooves dispersing the source signal. To optimize the resolution, we can select f_{foc} so that the signal covers the entire first parabolic mirror, with a diameter Φ'. As illustrated in Fig. 1.5(b), this involves satisfying the following relation:

$$\frac{\Phi_{\text{obj}}}{f_{\text{foc}}} = \frac{\Phi'}{f_{\text{mono}}}. \tag{1.3}$$

The spectral resolution also depends on the monochromator geometry and target wavelength, and is best estimated empirically by examining the broadening of narrow reference emission lines.

1.1.3 Resolution limit and Gaussian beam

The strength of a µ-PL setup lies in its ability to selectively address individual SPEs with a very high selectivity. This is enabled by focusing a laser spot onto a reduced sample area, with the spot size defining the resolution of the setup. Consequently, evaluating this parameter becomes essential for characterizing the setup performance. The resolution of any optical system is intrinsically limited by light diffraction, and any point-like sources are imaged as extended spots. For optics with a circular aperture, the diffraction pattern is an Airy disk mathematically described by a first-order Bessel function, characterized by a bright central disk surrounded by concentric rings [38]. When a plane-wave is directed through an objective with an entrance diameter Φ and focal length f_{obj}, the central disk radius is given by [39, 40]:

$$\mathscr{R} = 1.22\frac{\lambda f_{\text{obj}}}{\Phi}, \tag{1.4}$$

where the source has a wavelength λ. Spatial resolution is commonly assessed through the Rayleigh criterion, which posits that two point sources are considered 'just resolved' when the maximum of the diffraction pattern of one image coincides with the first minimum of the second image [40]. Consequently, the µ-PL spatial resolution is readily determined by the Airy disk radius of the focused laser spot and is best articulated as a function of the objective numerical aperture, $\text{NA} = \Phi/2f_{\text{obj}}$:

$$\mathscr{R} = 0.61\frac{\lambda}{\text{NA}}. \tag{1.5}$$

In this context, the resolution of the µ-PL setup is primarily constrained by the objective NA. However, it is crucial to note that the theoretical limit presented here assumes the focusing of a homogeneous collimated light beam, while, in practice, the laser takes the form of a Gaussian beam[I]. Ultimately, the resolution limit pertains to the extent of the laser spot focused onto the

---

[I] Semiconductor lasers typically produce beams that are elongated along one axis, deviating from an ideal Gaussian beam profile. Nevertheless, we shall assume an ideal Gaussian-like profile for simplicity in the following

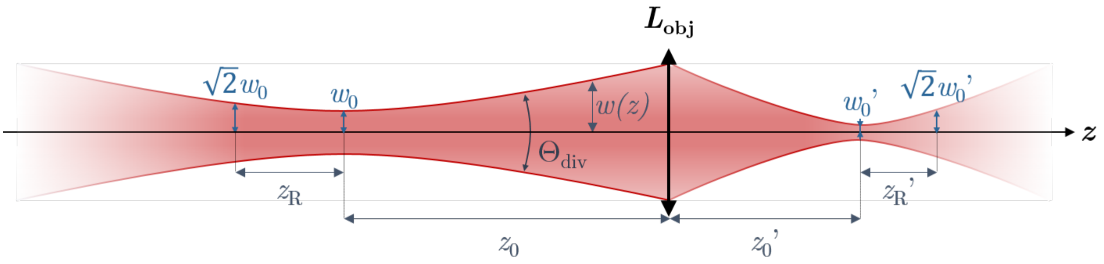

Figure 1.6: Laser Gaussian beam passing through the objective lens $\mathrm{L_{obj}}$.

sample.

For a laser beam propagating along the optical axis z, the optical intensity I can be described by the relationship [41]:

$$I(\rho, z) = A_0^2 \left(\frac{w_0}{w(z)}\right)^2 \exp\left(\frac{-2\rho^2}{w^2(z)}\right), \tag{1.6}$$

where A_0 represents the electric field amplitude, w_0 the beam waist, and ρ the radial distance. The beam width $w(z)$ is defined as the radius where the intensity has decreased by a factor $1/e^2$ of its on-axis value, and w_0 represents its minimum. The laser beam profile is illustrated in Fig. 1.6. $I(z)$ follows a Lorentzian profile with $w(z)$ given by:

$$w(z) = w_0 \sqrt{1 + \left(\frac{z - z_0}{z_{\mathrm{R}}}\right)^2}. \tag{1.7}$$

The beam waist location z_0 is typically found close to or inside the laser head. The Rayleigh range z_{R} distinguishes the near field $z < z_{\mathrm{R}}$ and far field $z > z_{\mathrm{R}}$ and is related to the waist through [42]:

$$z_{\mathrm{R}} = \frac{\pi {w_0}^2}{\lambda_{\mathrm{exc}}}, \tag{1.8}$$

in free space. The beam divergence is quantified through the angle Θ_{div}, depicted in Fig. 1.6 and is connected to the beam waist by the relation:

$$\Theta_{\mathrm{div}}/2 = \lim_{z\to\infty} \arctan\left(\frac{w(z)}{z}\right) \approx \frac{\lambda_{\mathrm{exc}}}{\pi w_0} = \sqrt{\frac{\lambda_{\mathrm{exc}}}{\pi z_{\mathrm{R}}}} \tag{1.9}$$

This angle is a measure of the laser beam quality.

To obtain the resolution limit in experimental conditions, we need to ascertain the beam waist ${w_0}'$ after it passes through the objective. This involves treating the output beam waist as the image and the input waist as the object. To achieve the diffraction limit, the condition to fulfill

---

discussion.

is essentially expressed as:

$$w_0{}' < R. \tag{1.10}$$

After the lens, the output beam waist writes [43]:

$$w_0{}' = \frac{w_0}{\sqrt{\left(1 - z_0/f_{\text{obj}}\right)^2 + \left(z_{\text{R}}/f_{\text{obj}}\right)^2}} = M w_0, \tag{1.11}$$

where M denotes the magnification. The waist position is given by:

$$z_0' = f_{\text{obj}} + M^2 (z_0 - f_{\text{obj}}) \tag{1.12}$$

and the Rayleigh range transforms to:

$$z_{\text{R}}{}' = z_{\text{R}} M^2, \tag{1.13}$$

which is readily equivalent to the depth of focus. The diffraction limit is reached when M tends to 0. For a poor beam quality ($z_{\text{R}} \lessapprox f_{\text{obj}}$) the only way to minimize the magnification consists in working in the far field, with $(z_0 - f_{\text{obj}}) \gg z_{\text{R}}$. In practice, achieving this requires an additional set of optics to collimate the laser beam. As a result, we obtain $z_0' = f_{\text{obj}}$. This is a prerequisite to ensure optimal working conditions: the PL signal needs to be collimated after collection through the microscope objective, with the emitter positioned in the objective focal plane. To ensure the highest attainable resolution, it is crucial for the laser focus to coincide with the emitter location.

High quality lasers typically distinguish themselves by a very low beam divergence, on the order of a few milliradians, with a Rayleigh range that exceeds several meters. In such cases, $z_{\text{R}}/f_{\text{obj}} \gg 1$, allowing for work in the near field with $z_0/f_{\text{obj}} \ll 1$. Under these conditions, Eqs. 1.11 and 1.12 are simplified to [41]:

$$w_0{}' = \frac{w_0}{\sqrt{1 + \left(z_{\text{R}}/f_{\text{obj}}\right)^2}} \underset{z_{\text{R}}/f_{\text{obj}} \to \infty}{\longrightarrow} 0, \tag{1.14}$$

and

$$z_0' = \frac{f_{\text{obj}}}{1 + \left(f_{\text{obj}}/z_{\text{R}}\right)^2} \approx f_{\text{obj}}. \tag{1.15}$$

Note that in practice, the condition 1.10 is easily satisfied. As an example, consider the 488 nm laser, for which $\Theta_{\text{div}} < 0.5\,\text{mrad}$ and $w_0 = 2.2\,\text{mm}$, along with the Mitutoyo NIR objective featuring $f_{\text{obj}} = 2\,\text{mm}$. Combining Eqs. 1.11 and 1.9, we derive a maximum Rayleigh range $z_{\text{R}} = 2.5\,\text{m}$ and a maximum waist $w_0{}' = 1.8\,\mu\text{m}$ - a value in close proximity to the diffraction limit of $\mathscr{R} = 0.6\,\mu\text{m}$. With a typical working distance of a few meters between the laser head and the objective, the condition expressed in Eq. 1.10 is automatically satisfied. However,

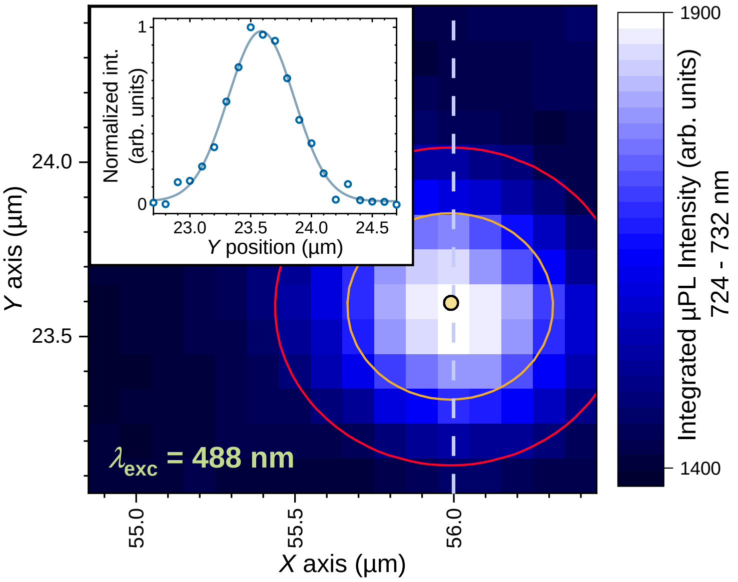

Figure 1.7: Integrated µ-PL map of an SPE. Iso-intensity lines of a 2D Gaussian fit are overlaid on the dataset, with $I = I_{\text{max}}/2$ shown in orange and $I = I_{\text{max}}/e^2$ shown in red. The position of the emitter is marked by a yellow dot. The inset displays the intensity of the emitter peak along the dashed line, fitted with a 1D Gaussian.

achieving precise correspondence between the waist position z_0' and the focal plane of the objective may pose some challenges. Applying Eq. 1.12 to our example with a working distance $z_0 = 4\,\text{m}$ results in a mismatch $z_0' - f_{\text{obj}}$ of about $0.7\,\mu\text{m}$. This discrepancy is non-negligible compared to the depth of focus $z_R{}' = 1.6\,\mu\text{m}$ and may have a slight impact on both resolution and the focusing procedure. The use of a confocal system to correct the beam divergence is anticipated in the future to enhance the setup resolution.

Additionally, we should note that a situation where the laser beam does not completely fill the objective rear aperture would result in a resolution loss. In such cases, utilizing a portion of the optics leads to an effective numerical aperture $\text{NA}_{\text{eff}} < \text{NA}$ and a larger radius in Eq. 1.5. Therefore, having a slight overfilling of the back aperture is preferable in order to optimize the resolution.

As a closing remark, we should mention that the center lobe of the Airy pattern is well-approximated by a Gaussian function, disregarding the outer rings of the diffraction pattern:

$$I(\rho) = I_{\text{max}} \exp\left(-2\frac{\rho^2}{\omega_{\text{diff}}{}^2}\right), \tag{1.16}$$

with maximum intensity I_{max}. The approximated Gaussian waist ω_{diff}, defined such that

$I(\omega_{\text{diff}}) = I_{\max}/e^2$, is related to the diffraction-limited resolution by $\mathscr{R} \approx 1.45\omega_{\text{diff}}$. The diffraction-limited waist then reads [44]:

$$\omega_{\text{diff}} = 0.42\frac{\lambda}{\text{NA}}. \tag{1.17}$$

This Gaussian approximation offers a more straightforward comparison to experimental data. As an illustration, we consider a µ-PL map, presented in Fig. 1.7, generated by raster scanning the laser spot in the vicinity of a single-defect emission line. The emitter is treated as a point-like source. Therefore, assuming a linear relationship between the laser power at a given location and the PL intensity, we can essentially reproduce an image of the laser spot. Each pixel corresponds to the PL intensity integrated between 724 and 732 nm. The 2D Gaussian fit yields $\omega_{\text{exp}} = 0.5\,\mu\text{m}$ in close agreement with the theoretical limit $\omega_{\text{diff}}(488\,\text{nm}, \text{NA} = 0.5) = 0.4\,\mu\text{m}$. This difference can be attributed to the mismatch $z_0' \neq f_{\text{obj}}$ and the non-linearity of the emitter response.

1.1.4 Confocal microscopy

The spatial and spectral resolution of the µ-PL setup can be enhanced through spatial filtering of the PL signal. Confocal microscopy offers a way to eliminate out-of-focus light by incorporating a pinhole in a conjugate plane of the sample. The confocal path has been integrated only into the NIR setup, as illustrated in Fig. 1.4, to improve the filtering of broad defect luminescence generated in the vicinity of a targeted SPE. After the microscope objective, the collimated signal is focused onto a pinhole by a parabolic mirror, ensuring alignment validity across a broad spectral range. The pinhole diameter is specified in terms of Airy units, equivalent to the size of the diffraction-limited spot $2\mathscr{R}$, times the magnification $f_{\text{conf}}/f_{\text{obj}}$, where f_{conf} denotes the focal length of the two confocal parabolic mirrors. Typically, the pinhole diameter is set around 70% of an Airy unit to optimize filtering while minimizing signal losses. It is important to note that the confocal path is intended for use with single-photon detectors (SPDs) for $g^{(2)}(\tau)$ measurements. When analyzing the PL signal with a spectrometer, the entrance slit already serves as a pinhole in the horizontal direction. Additionally, spatial filtering in the vertical direction can be achieved by considering only one or two rows of pixels on a CCD detector.

1.1.5 Köhler illumination

To facilitate the positioning of the samples under investigation, the setup includes a CMOS camera coupled with a white light source configured in Köhler illumination [45]. The ensemble forms the imaging assembly illustrated in Fig. 1.1 with detailed components shown in Fig. 1.8. The BS assembly shown on the diagram can be readily placed in and removed from the optical path and is set up in a beam offset compensating geometry. The illumination principle consists of using a deliberately defocused light source to achieve a uniformly bright illumination across the sample surface. The field diaphragm, positioned in the conjugate

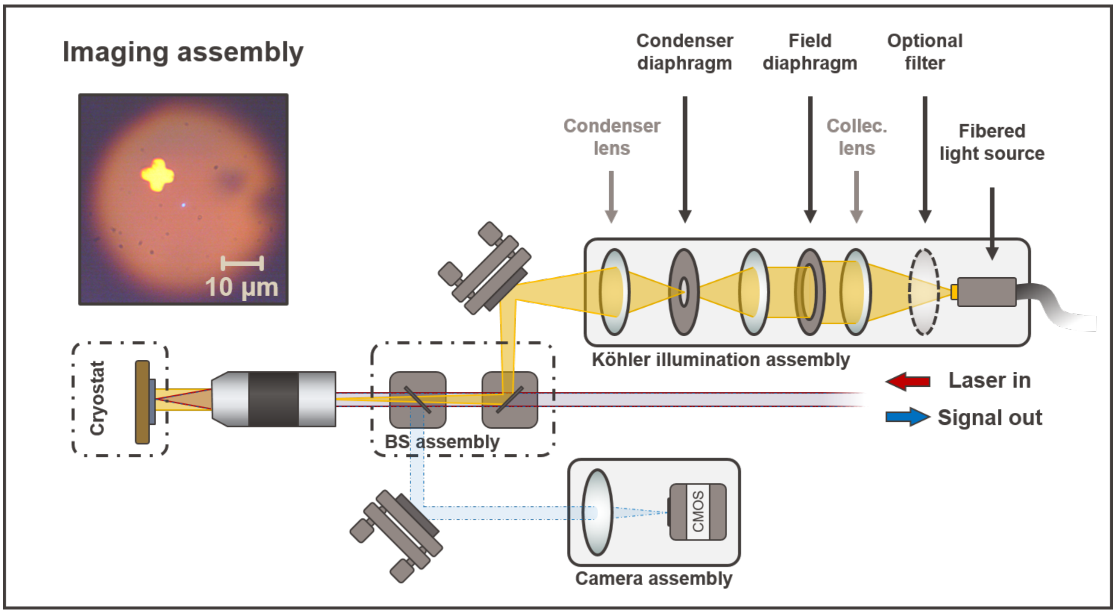

Figure 1.8: Diagram of the Köhler illumination assembly. Dashed contours highlights components that are removable. Other elements are permanently fixed to the optical table. The inset displays an image of a GaN sample with gold cross markers, where the 488 nm laser spot is also observable.

plane to both the sample and the camera sensor, enables the control of the size and shape of the illuminated area. On the other hand, closing the condenser diaphragm reduces the illumination intensity while enhancing the contrast.

A perfect alignment of the imaging assembly is not critical for the present study, since its primary purpose is to aid in the initial positioning of the microscope objective. In fact, an imperfect defocusing of the light source, as observed in the inset of Fig. 1.8 still yields images of reasonably good quality. It may, however, prove more crucial in future applications, for instance in the design of lithography masks for embedding PDs in photonic structures [46].

SUMMARY

This section highlights the meticulous design of both the UV and NIR µ-PL setups, tailored to achieve optimal spatial resolution for individual scrutiny of SPEs. The remarkable modularity showcased in Fig. 1.4 not only enhances adaptability but also empowers us to conduct PL experiments with a comprehensive array of tunable parameters. Any identified shortcomings in the NIR setup are associated with its recent implementation, with ongoing improvements expected to bring it up to the highest standards in the near future.

1.2 Experiment automation

The μ-PL setup effectiveness and adaptability hinge significantly on the level of measurement automation it provides, particularly when dealing with localized emitters of unknown positions. An illustrative example supports this point: pinpointing a localized emitter in GaN can be a time-consuming process involving hours of a laborious 'move-and-try' procedure, whereas automatically conducting raster scans of a GaN layer allows for swift insights into the presence and density of PD emitters. This section does not aim to present a comprehensive overview of the software developed to oversee experiments on the NIR setup; detailed information on this is provided in Appendix A.1. Instead, we provide here essential insights into the automation-related procedures that elucidate the acquisition of the experimental results discussed in the subsequent chapters.

1.2.1 Stability and repositioning

Given that the laser spot diameter is approximately one micron, it is imperative to ensure the stability of the alignment, even below this value, for precise and relevant measurements. While the μ-PL setups have been engineered to minimize sources of vibrations, achieving perfect stability over an extended period of time is challenging, and the alignment of the objective with respect to the sample inevitably experiences a slight drift. This drift is generally without any consequence for routine spectroscopy measurements but becomes unacceptable for prolonged $g^{(2)}(\tau)$ measurements. To address long-term instabilities during such measurements, we implemented a repositioning scheme by continuously monitoring the photon counts on each SPD. Whenever the average counts fall below a threshold value, typically 90% of the maximum counts, we initiate a repositioning of the objective. A state diagram detailing the refocusing procedure is provided in Appendix A.2, along with comprehensive details of the exact procedure. The in-plane and focus drift of the laser spot are illustrated in Fig. 1.9 for two distinct $g^{(2)}(\tau)$ measurements that lasted approximately for a day. The plots are generated by tracking the position of the piezo stage after each refocusing step. The intensity is less sensitive to focus drift than in-plane (X,Y axes) drift, hence explaining the much less frequent adjustments made to the Z axis.

There does not appear to be a consistent preferred direction for in-plane drifting, although the drift is not entirely random. Instead, there are some enduring tendencies (lasting for hours) in the drift direction, and these tendencies can vary significantly between different measurements. In contrast, the focus drift consistently changes in one direction, with the objective drifting away from the sample. The speed of this drift, however, is not constant. To date, we have been unable to pinpoint the origin of this drift, and it has not posed a hindrance to our measurements. Variations also seem to be present depending on the time of the day when measurements are conducted, indicating the sensitivity of the alignment. In Fig. 1.9, we observe how scanning can potentially be employed in the future to identify and rectify the source of the drift, rather than merely compensating for it during measurements. This involves

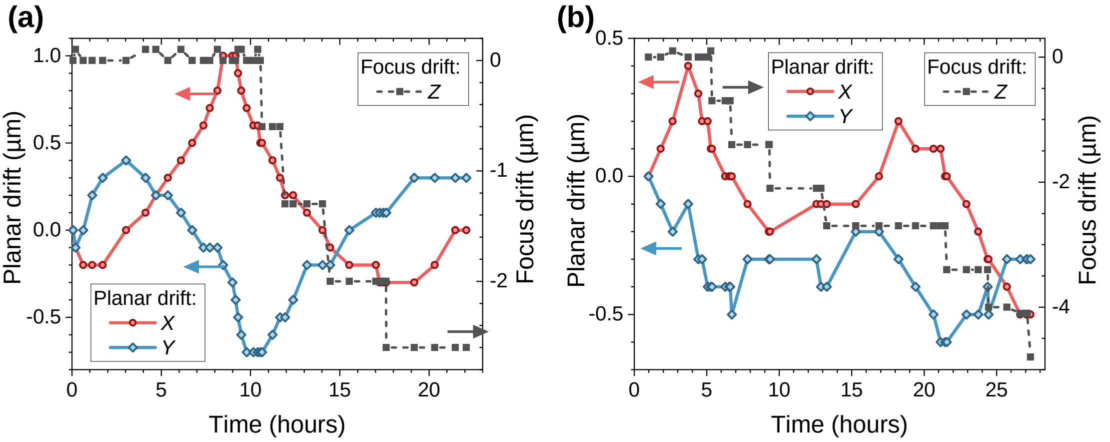

Figure 1.9: Experimental drift in the alignment between the objective and the sample during two distinct $g^{(2)}(\tau)$ acquisitions. The origin is chosen as the initial position (time = 0). Each dot corresponds to a repositioning step taken after the photon count has dropped below 90% of its maximum value. The solid and dashed lines represent in-plane and focus drift, respectively.

quantifying the speed and amplitude of the drift for different adjustments of the setup.

1.2.2 Excitation power control

Most reports in the literature mention the power (P_{exc}) at which various measurements on SPEs were conducted. However, to assign any meaningful significance to this value, it must be accompanied by the laser spot size to deduce the irradiance of the investigated emitter. From this, the excitation power density, denoted by σ_{exc}, can be extracted. The latter is a more relevant physical quantity than P_{exc}, especially if the excitation process involves directly exciting the emitter into an excited state rather than generating free carriers captured by a radiative site. This is the case in what we term 'quasi-resonant' excitation, where the laser energy is below the bandgap of the host material/barrier. This is the excitation scheme we used throughout our work.

Given that the laser spot can be well fitted by a 2D Gaussian, as discussed in Subsect. 1.1.3, the excitation power density at a distance r of the spot center can be expressed as:

$$\sigma_{\text{exc}}(r) = \sigma_0 \exp\left(\frac{-2r^2}{{\omega_{\text{diff}}}^2}\right), \tag{1.18}$$

where σ_0 denotes the power density in the center of the laser spot. The excitation power is

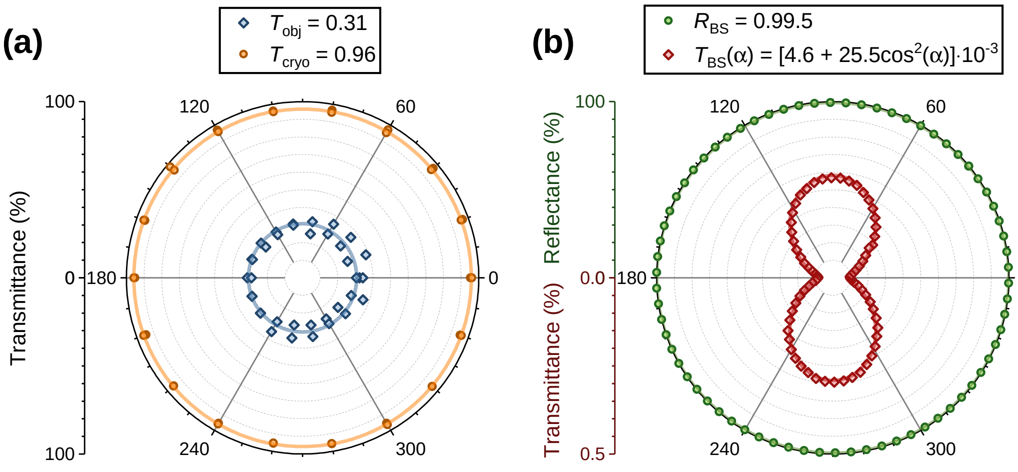

Figure 1.10: Variation of reflectance and transmittance with laser polarization at 488 nm in polar coordinates. The data are measured **(a)** for the objective and cryostat window, as well as **(b)** for the dichroic mirror BS$_1$. Solid lines indicate the mean values for T_{obj}, T_{cryo} andR_{BS}. The fitting function for T_{BS} is provided in the legend.

then expressed as:

$$\begin{aligned} P_{\text{exc}} &= \iint \sigma_{\text{exc}}(r) r \,\mathrm{d}r \,\mathrm{d}\theta = 2\pi\sigma_0 \int_0^{+\infty} e^{\frac{-2r^2}{\omega_{\text{diff}}{}^2}} \,\mathrm{d}r \\ &= \frac{2\sigma_0}{\pi\omega_{\text{diff}}{}^2}. \end{aligned} \tag{1.19}$$

If the alignment is correct, i.e. if the investigated emitter is at the center of the laser spot, we can write $\sigma_{\text{exc}} = \sigma_0$ which we assume in the following.

In practice, we do not measure the power (P_{meas}) at the sample surface, but rather after BS$_1$ (see Fig. 1.1). The relationship between P_{exc} and P_{meas} can be readily established by evaluating the transmittance of the BS (T_{BS}), that of the objective (T_{obj}), and the cryostat window (T_{cryo}), as well as the reflectance of the BS (R_{BS}). The relationship between the two powers thus reads:

$$P_{\text{exc}}(\lambda_{\text{exc}}, \alpha) = P_{\text{meas}} \left(\frac{R_{\text{BS}}}{T_{\text{BS}}} T_{\text{obj}} T_{\text{cryo}} \right) (\lambda_{\text{exc}}, \alpha), \tag{1.20}$$

where we initially consider each coefficient to depend on both wavelength and polarization, (angle α). As a matter of fact, the transmittance of the objective and cryostat window, as illustrated in Fig. 1.10 for the 488 nm laser, remains constant with polarization angle. As for BS$_1$, it depends on the BS or dichroic mirror used. When using a dichroic mirror, Fig. 1.10(b) shows that R_{BS} remains largely constant, while T_{BS} strongly depends on the laser polarization. Once reflection and transmission coefficients are defined, we can adapt the position of the filter wheel in real time to obtain the desired P_{exc} and σ_{exc} values.

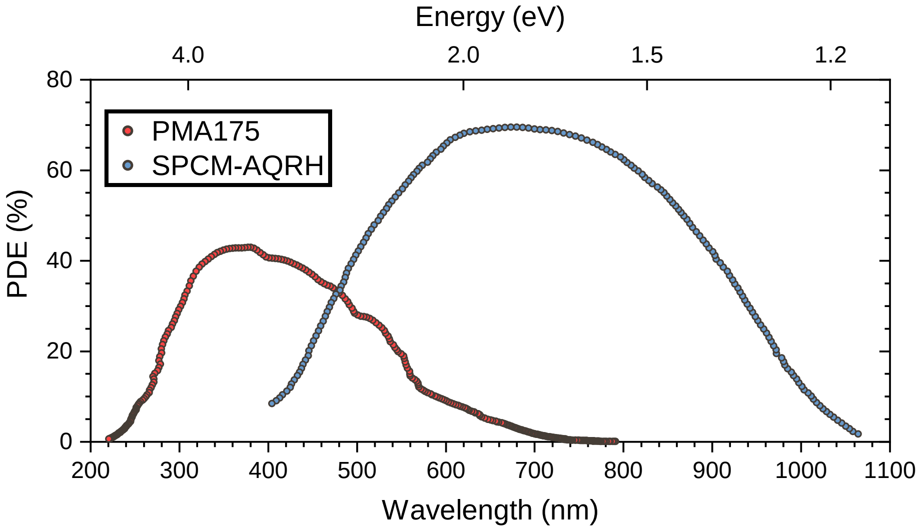

Figure 1.11: Tabulated PDE for a PicoQuant PMA175 PMT and an Excelitas SPCM_AQRH SPAD. The PDE may slightly vary between different detectors.

1.3 Setup efficiency

In order to efficiently assess the brightness of an SPE, we need to evaluate the setup efficiency

$$\eta_{\mathrm{setup}} = \eta_{\mathrm{c}} \cdot \alpha_{\mathrm{l}} \cdot \eta_{\mathrm{ph}}, \tag{1.21}$$

where the collection efficiency (η_c), the setup losses (α_l) and the photon detection efficiency (PDE) (η_{ph}) can be estimated individually. α_l depends on the optical components (mirrors, lenses, cryostat window, microscope objective and BS) used to collect the luminescence signal, and varies with the wavelength and polarization of each SPE PL line. η_{ph} depends on the type of SPDs used to collect the luminescence signal. SNSPDs are optimized to work at a relatively specific wavelength in the NIR and are polarization sensitive [47]. In contrast, PMTs and SPADs display no significant polarization sensitivity and operate on a broader spectral range. The tabulated performance of SPDs used in this work is reported in Fig. 1.11.

1.3.1 Isotropic approximation

The primary source of signal losses takes place during the light collection process by the microscope objective. These losses are a consequence of the rather high GaN refractive index n_{GaN} (~ 2.3 at 700 nm) in the wavelength range of all the studied SPEs. These stem from the fact that only photons emitted within a narrow solid angle can be gathered by the objective, because of the mismatch between n_{GaN} and n_{air}. To describe the underlying physics, the initial estimation of η_{ph} can be carried out by assuming an isotropic emitter embedded in a GaN matrix, as depicted in Fig. 1.12. A more precise model is described below in Subsect. 1.3.2.

Considering a very thin layer of GaN (typically a few µm thick), we can define the maximum collection angle i_m at which light emitted by the SPE will be collected by the objective as:

$$\sin\left(i_\mathrm{m}\right) = \frac{\sin\left(r_\mathrm{m}\right)}{n_\mathrm{GaN}} = \frac{\mathrm{NA}}{n_\mathrm{GaN}}. \tag{1.22}$$

The maximum refracted angle r_m is shown in Fig. 1.12. This translates into a light collection solid angle Ω_c given by:

$$\Omega_\mathrm{c} = \frac{1}{2}\left(1-\cos\left[\arcsin\left(\frac{\mathrm{NA}}{n_\mathrm{GaN}}\right)\right]\right). \tag{1.23}$$

n_GaN, and consequently Ω_c, vary with factors such as the wavelength of the SPE, the temperature, the GaN strain state, the doping, and the direction of light propagation. As such, values reported in the literature vary by up to 15% close to the GaN bandgap [48–50]. Each independently measured refractive index dataset is well approximated by an empirical first-order Sellmeier equation [51]:

$$n(\lambda) = \sqrt{A_0^n + \frac{\lambda^2}{\lambda^2 - A_1^n}}, \tag{1.24}$$

where, A_0^n and A_1^n are material-dependent fitting parameters. Considering two emitters at 400 and 800 nm and refractive indices reported at 300 K for ordinary rays by Lin *et al.* [49], we obtain $i_\mathrm{m}(400) = 10.4°$ and $i_\mathrm{m}(800) = 11.8°$ respectively, with $\mathrm{NA} = 0.5$. For small angles, the Fresnel coefficients [52] are almost constant and the transmission coefficient T can be approximated for any $i < i_\mathrm{m}$ by:

$$T = 1 - \frac{(n_\mathrm{GaN} - n)^2}{(n_\mathrm{GaN} + n)^2}, \tag{1.25}$$

with $n = n_\mathrm{air} \approx 1$ at the GaN/air interface. The collection efficiency thus reads:

$$\eta_\mathrm{c} = T\frac{\Omega_\mathrm{c}}{4\pi}. \tag{1.26}$$

For SPE lines peaked at $\lambda_\mathrm{SPE} = 400$ and 800 nm, Eq. 1.26 yields respectively $\eta_\mathrm{c}(400) = 6.4 \times 10^{-3}$ and $\eta_\mathrm{c}(800) = 8.9 \times 10^{-3}$. These estimates do not account for light that is reflected at the interface between GaN and the substrate. For GaN layers grown on sapphire, the reflection coefficient $R = 1 - T$ at the substrate interface under normal incidence can be estimated using tabulated values for $n_{\mathrm{Al_2O_3}}$ [53]. The reflection coefficient does not exceed 5% over the entire UV to NIR range and can be discarded in the current context. However, for GaN QDs embedded in AlN layers and grown on silicon substrate, back reflection at the AlN/Si interface can substantially affect the collection efficiency and introduce interference on the SPE signal. In this case, the AlN layer acts as a Fabry-Perot cavity [54, 55], whose effect is elaborated in more detail in Sect. 1.6. For GaN/AlN QDs the collection efficiency is rather computed using

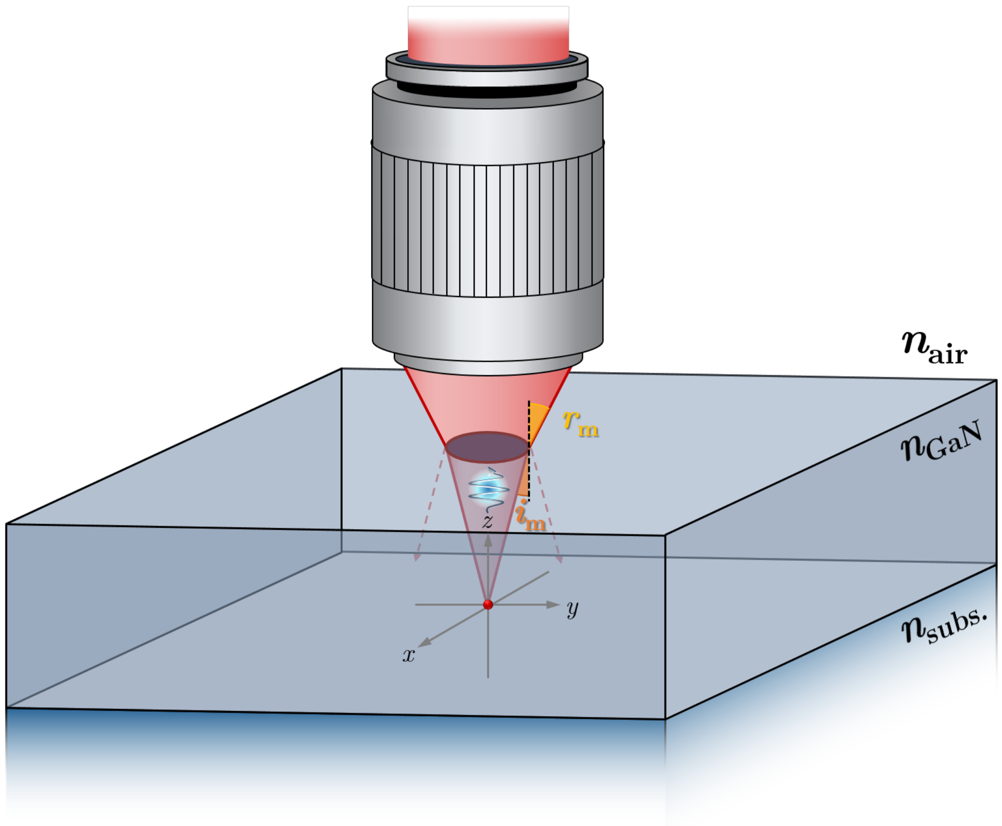

Figure 1.12: Schematic of the light collection by the microscope objective for a point-like source (red dot).

the refractive index of the surrounding medium (i.e. n_{AlN}), although this nuance does not significantly impact η_c due to the minimal mismatch between n_{GaN} and n_{AlN} [48, 56].

η_c is constrained in the above description by the NA of the objectives used. However, the collection solid angle is intrinsically limited by the critical angle θ_c under which an incident ray gets totally reflected at the GaN/air or AlN/air interface. θ_c is obtained straightforwardly by considering an NA of one, and yields $\theta_c(400) = 21.2°$ and $\theta_c(800) = 24.4°$, respectively. Hence, without the use of immersion objectives to enhance the NA or specific patterns or surface treatments of the sample, the collection efficiency cannot exceed 5%[II].

1.3.2 Dipole simulation

The isotropic approximation provides an intuitive approach to picture the main considerations at stake when we want to optimize the collection efficiency of the setup. However, it fails to

---

[II] Estimated maximum over the UV to telecom range highlight the strong intensity fluctuations the can arise from similar SPEs displaying different 3D orientations. To properly render this feature, we need to adopt a more complete description, considering at first the SPE as a linear optical dipole (1D dipole). The difference between 1D and 2D dipoles will be discussed in Sect. 1.4.

We can express the electric far field propagating along $\mathbf{e}_k$ originating from an optical dipole of moment $\mathbf{d} = \mu\mathbf{e}_\mathrm{d}$ as [57, 58]:

$$\mathbf{E}(\mathbf{r}) = \frac{D}{r}(\mathbf{e}_k \times \mathbf{e}_\mathrm{d} \times \mathbf{e}_k), \tag{1.27}$$

where D is a medium-dependent parameter and r the distance to the dipole. Adopting the reference frame depicted in Fig. 1.13 and following the approach described by Lethiec *et al.* [58], we can decompose this field in its s and p components:

$$\mathbf{E}(\theta,\varphi) = \frac{D}{r}\big(E_s(\theta,\varphi)\cdot\mathbf{e}_s + E_p(\theta,\varphi)\cdot\mathbf{e}_p\big), \tag{1.28}$$

where the unit vectors $\mathbf{e}_s$, $\mathbf{e}_p$ read, respectively:

$$\mathbf{e}_s = \begin{pmatrix} \sin(\varphi) \\ -\cos(\varphi) \\ 0 \end{pmatrix}, \quad \mathbf{e}_p = \begin{pmatrix} \cos(\theta)\cos(\varphi) \\ \cos(\theta)\sin(\varphi) \\ -\sin(\theta) \end{pmatrix}, \tag{1.29}$$

and

$$\begin{aligned} E_s(\theta,\varphi) &= \sin(\theta_\mathrm{d})\sin(\varphi-\varphi_\mathrm{d}), \\ E_p(\theta,\varphi) &= -\cos(\theta_\mathrm{d})\sin(\theta) + \sin(\varphi_\mathrm{d})\cos(\theta)\sin(\varphi_\mathrm{d}-\varphi). \end{aligned} \tag{1.30}$$

θ_d and φ_d define the orientation of the optical dipole, as illustrated in Fig. 1.13.

To express the electric field $\mathbf{E}'$ detected by the objective, we need to take into account the diffraction at the GaN/air interface incorporating the associated Fresnel coefficients, such that:

$$\mathbf{E}'(\theta,\varphi) = \frac{D}{f}\sqrt{\frac{n_\mathrm{GaN}}{\cos(\theta)}}\big(E_s t_s(\theta)\cdot\mathbf{e}_s + E_p t_p(\theta)\cdot\mathbf{e}_{p'}\big), \tag{1.31}$$

with

$$\mathbf{e}_{p'} = \begin{pmatrix} \cos(\varphi) \\ \sin(\varphi) \\ 0 \end{pmatrix}, \tag{1.32}$$

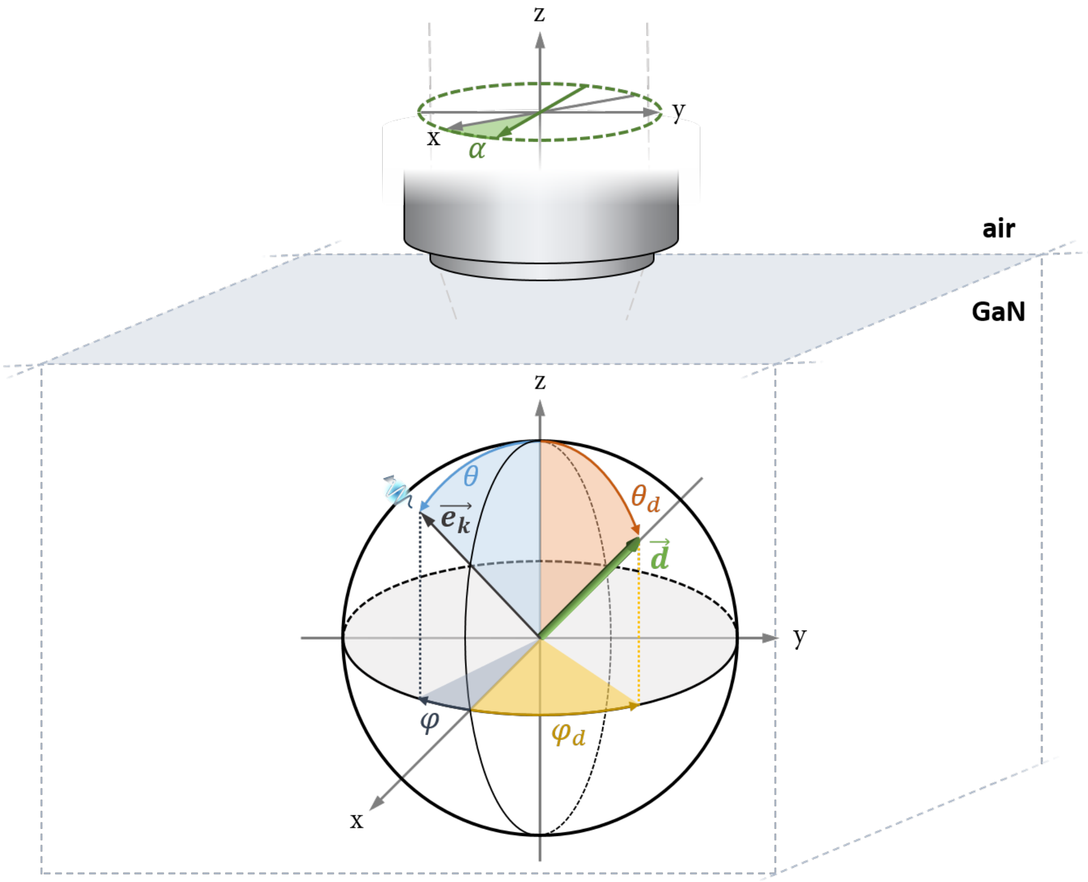

Figure 1.13: Schematic of the dipole emission and light collection scheme. A half-wave plate is set in the path when performing polarization-dependent measurements, as described in Sect. 1.4.

and

$$t_s(\theta) = \frac{2n_{\mathrm{GaN}}\cos(\theta)}{n_{\mathrm{GaN}}\cos(\theta) + \sqrt{1-(n_{\mathrm{GaN}}\sin(\theta))^2}},$$

$$t_p(\theta) = \frac{2n_{\mathrm{GaN}}\cos(\theta)}{\cos(\theta) + n_{\mathrm{GaN}}\sqrt{(1-n_{\mathrm{GaN}}\sin(\theta))^2}}. \tag{1.33}$$

In Eq. 1.31, f holds for the focal length of the objective and $n_{\mathrm{GaN}}/\cos(\theta)$ ensures the conservation of power through both the GaN/air interface and the objective [59, Ch. 3]. The contribution of the field reflection at the GaN/substrate interface is once again omitted in this description.

The calculation of η_{c} involves computing the ratio between the total intensity of the radiated

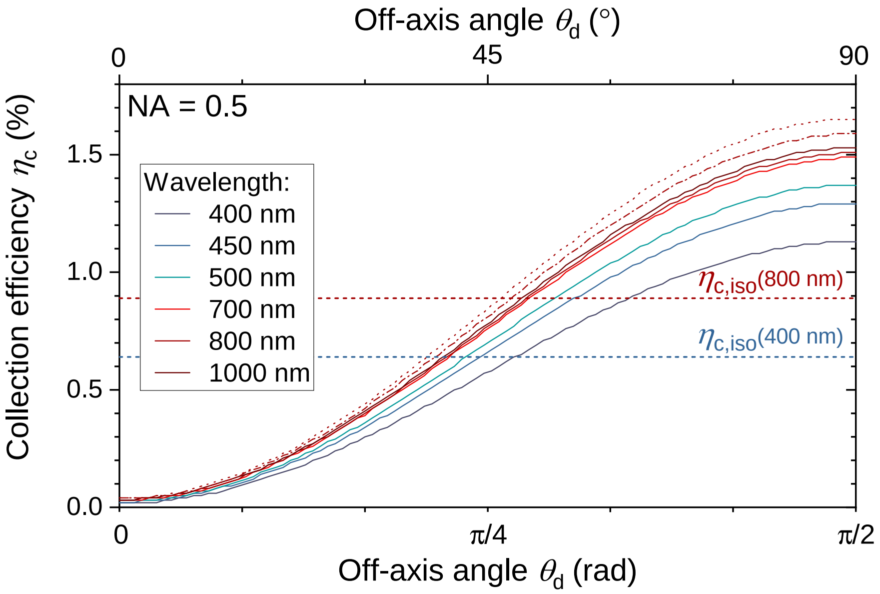

Figure 1.14: Simulated η_c for varying off-axis dipole orientations. Solid lines are simulated using n_{GaN} values reported in Lin *et al.* [49] Dotted- and dash dotted- curves are simulated at 800 nm using reports from Brunner *et al.* [48] ($n_{\mathrm{GaN}} = 2.31$) and Barker and Ilegems [50] ($n_{\mathrm{GaN}} = 2.36$), respectively. The efficiencies determined under the assumption of isotropic emission are reported as horizontal dashed lines.

field, $I_{\mathrm{tot}} = \oiiint |\mathbf{E}|^2$, and the intensity collected through the aperture, expressed as:

$$I_{\mathrm{col}} = \int_0^{2\pi} \int_0^{\rho_{\mathrm{max}}} \left|\mathbf{E}'\right|^2 \rho \, \mathrm{d}\rho \, \mathrm{d}\varphi, \tag{1.34}$$

where

$$\rho = f \sin\left(\theta'\right), \quad \rho_{\mathrm{max}} = f \mathrm{NA}, \tag{1.35}$$

and θ' is given by Snell-Descartes law:

$$\sin\left(\theta'\right) = n_{\mathrm{GaN}} \sin(\theta). \tag{1.36}$$

$\eta_c = I_{\mathrm{col}}/I_{\mathrm{tot}}$ can be evaluated numerically for any dipole orientation $\mathbf{e}_d(\theta_d, \varphi_d)$ and any set of experimental parameters (λ_{SPE}, NA). Ultimately, the in-plane component has no impact on the extraction efficiency. $\eta_c(\theta_d, \varphi_d) = \eta_c(\theta_d)$ is plotted in Fig. 1.14 for different λ_{SPE} and an NA = 0.5 matching that of the objectives used in this study. The isotropic values computed in Subsect. 1.3.1 are added as horizontal dashed lines for reference. The electric field originating from an SPE is maximized in the plane orthogonal to the dipole moment and falls to zero when $\mathbf{e}_k = \mathbf{e}_d$. Thus, dipoles oriented in-plane a exhibit a higher brightness (larger η_c) compared to those aligned along the collection axis.

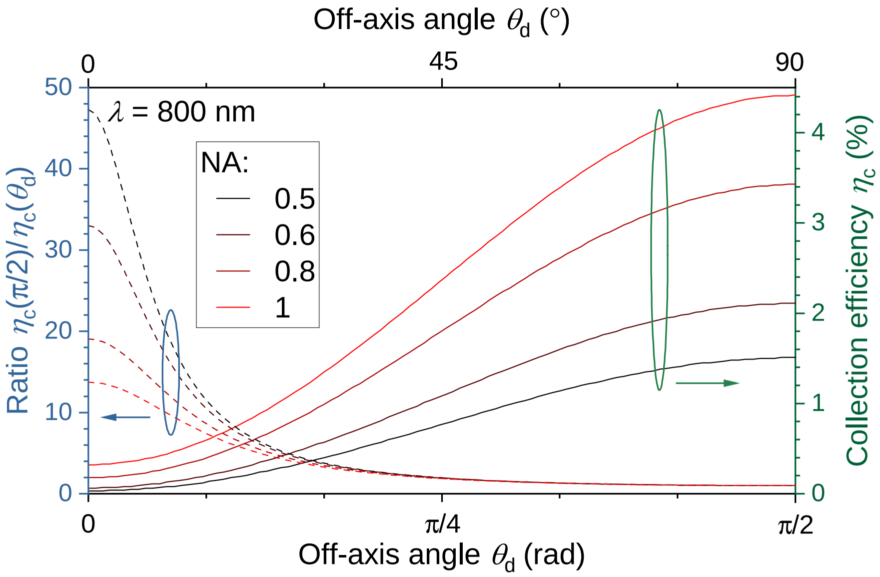

Figure 1.15: Simulated collection efficiency $\eta_c(\theta_d)$ and associated ratio $\eta_c(\pi/2)/\eta_c(\theta_d)$ for different numerical apertures.

We can quantify this contrast by evaluating the ratio $\eta_c(\pi/2)/\eta_c(\theta_d)$ between in-plane dipoles and dipoles with a random off-axis orientation, as depicted in Fig. 1.15 for different NA values. The angular selectivity of an objective increases inversely with its NA. Consequently, the contrast $\eta_c(\pi/2)/\eta_c(\theta_d)$ is maximum for small NA objectives and would theoretically tend toward ∞. For the objectives used in the study, this implies that in-plane dipoles would appear about 50 times brighter than their off-plane counterparts. This points out a selection bias inherent to the excitation/detection scheme employed here and in most µ-PL experiments: for GaN samples grown along the *c*-axis, off-plane SPEs are nearly invisible and are easily filtered out, either through manual selection of only the brightest emitters, or during automated statistical analysis if their signal-to-noise ratio (SNR) is too low. Addressing these emitters necessitates a reevaluation of the sample design. One solution could involve growing thick GaN layers to be sliced along the *m*-plane or *a*-plane and investigated with the objective axis set perpendicular to the *c*-axis. Another solution would be to grow samples along non-polar or semi-polar planes [60, 61], with the risk of altering the nature and density of PDs introduced during growth.

The reasoning described above is based on the assumption that all dipoles create identical electric fields that differ only by their dipole moment orientation. However, the intensity of an SPE also depends on its absorption rate, which is assumed to be proportional to $|\mathbf{e}_{k,\mathrm{exc}} \cdot \mathbf{d}'|^2$ [62]. Here, $\mathbf{d}'$ is the dipole moment of the absorption state excited by an electric field oriented along $\mathbf{e}_{k,\mathrm{exc}}$. Since, the excitation laser beam is focused on the sample through the objective used for collection, $\mathbf{e}_{k,\mathrm{exc}}$ is almost oriented in-plane. In this regard, the brightest SPEs are expected to display absorption states with in-plane dipole moments to maximize the dot product $\mathbf{e}_{k,\mathrm{exc}} \cdot \mathbf{d}'$. For SPEs originating from defects, the absorption and emission dipoles are typically aligned along or perpendicular to distinct crystallographic directions and are expected to be colinear [63]. As such, SPEs with absorption and emission dipoles oriented along the c-axis would simultaneously experience lower excitation and collection efficiency, making them nearly undetectable in our experiment. The physical description of defects in GaN is detailed in Sect. 3.1.

SUMMARY

In conclusion, this section underscores the pivotal role of collection efficiency as the primary determinant of the overall effectiveness of our µ-PL setups. Regardless of the equipment quality, surpassing a 1% detection efficiency for the PL signal from SPEs within GaN layers remains a challenging task without strategic enhancements to the sample structure. Our dipole simulation further accentuates the critical nature of this limitation, revealing that a notable fraction of PD SPEs may simply not be detected. It is essential to emphasize that the dipole model employed here specifically pertains to PD SPEs, as observed in GaN layers. Selection rules in GaN/AlN QDs do not conform to the same scheme, and a more sophisticated theoretical framework, accounting for the symmetry of the pyramidal QD system must be considered [64]. However, this falls beyond the scope of the present study.

1.4 Polarization-dependent measurements

1.4.1 In-plane polarization

Polarization-dependent µ-PL measurements play a crucial in the optical characterization of QDs and PDs that behave as SPEs. For QDs, such measurements are instrumental in discerning whether the emission adheres to symmetry rules and are expected to reflect the symmetry properties of their pyramidal shape. They are also critical for ensuring the proper attribution of emission lines to single- of multi-excitonic complexes. In this regard, the in-plane polarization of such excitonic complexes can be investigated through the filtering of the PL signal by placing a rotating linear polarizer in the collection path. Noting α the angle between the x-axis and the polarizer (see Fig. 1.16(a)), the intensity of a light source partially polarized along the axis $\mathbf{e}_{k'} = \cos(\varphi)\cdot\mathbf{e}_x + \sin(\varphi)\cdot\mathbf{e}_y$ is given by:

$$I(\alpha) = I_{\text{min}} + (I_{\text{max}} - I_{\text{min}})\cos^2(\alpha - \varphi), \tag{1.37}$$

where the minimum and maximum intensities I_{min} and I_{max} are fitting parameters and $I(\alpha)$ is determined by integrating the PL spectrum of an SPE . The angle φ is directly equivalent to the in-plane angle of an SPE dipole moment φ_{d}. The degree of linear polarization (DLP) is expressed as:

$$\delta_{\text{p}} = \frac{I_{\text{max}} - I_{\text{min}}}{I_{\text{max}} + I_{\text{min}}} \tag{1.38}$$

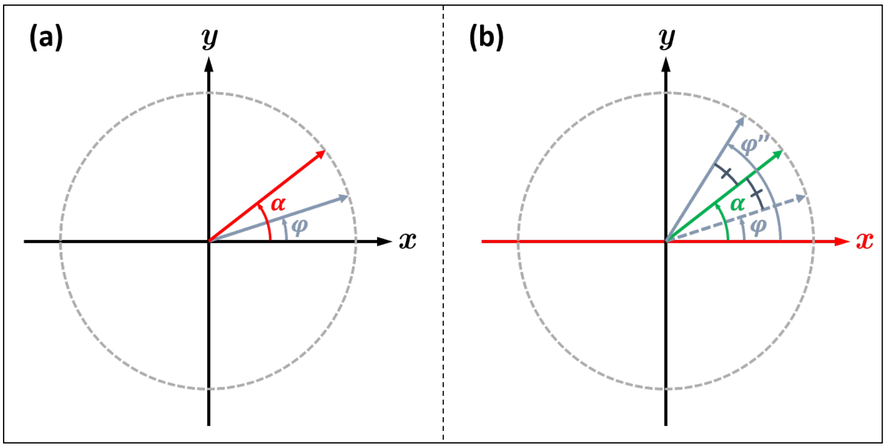

Figure 1.16: Schematic of optical components angular configuration in polarization-dependent measurements when using **(a)** a polarizer or **(b)** a half-wave plate in combination with a polarizer. The polarizer (respectively, the half-wave plate) axis is pictured in red (respectively, in green).

which quantifies the discrepancy of the signal from a fully linearly polarized light source ($\delta_\text{p} = 1$). For QDs , we mostly use DLP as a marker of the emission line purity and to characterize degenerate states with overlapping emission lines.

In practice, employing only one polarizer to conduct polarization-dependent measurements results in deviations from the expected intensity trend described by Eq. 1.37. This stems from the intricate relationship between grating efficiencies and diffraction angles, leading to a growing disparity between $s-$ and $p-$polarized light as the blaze angle increases [65]. This issue is circumvented by using a fixed polarizer aligned along $\mathbf{e}_x$ in conjunction with a rotating HWP. The HWP effectively flips the axis of polarization of the incident light along its fast axis, such that Eq. 1.37 becomes:

$$I(\alpha) = I_\text{min} + (I_\text{max} - I_\text{min})\cos^2(\varphi'') = I_\text{min} + (I_\text{max} - I_\text{min})\cos^2(2\alpha - \varphi_\text{d}). \tag{1.39}$$

Here, φ'' denotes the light polarization angle after passing through the HWP and α now represents the angle between $\mathbf{e}_x$ and the HWP fast axis, as illustrated in Fig. 1.16(b).

1.4.2 3D orientation

While the in-plane angle φ_d retains its significance when probing the luminescence of PDs, the physical interpretation of the DLP is not as readily comprehensible and will be elucidated further according to the framework developed in Subsect. 1.3.2. For PD SPEs , it is anticipated that their dipole moment aligns with specific structural features, such as Ga-N bonds, the nearest Ga-Ga axis or the nearest N-N axis for single substitutional impurities. Alternatively, it may align with the X-Y axis for complexes where X and Y represent substitutional/interstitial atoms or substitutional vacancies [33, 63]. To effectively examine the distribution of dipole orientations and gain insights into the structural properties of these defects, a 3D resolution of the SPE dipole moment orientation becomes crucial.

Among the different techniques employed to characterize the 3D orientation of PDs, defocused imaging has emerged as one of the most promising techniques [66–68]. This approach allows to determine the off-axis angle θ_d of an optical dipole by recording a slightly defocused image of its far field emission pattern. However, the success of this technique hinges on the use of highly sensitive cameras, particularly electron-multiplying charge-coupled devices (EMCCDs), capable of discerning extremely low light intensities while keeping the SNR at its maximum value [58]. Regrettably, defocused imaging is currently unfeasible with our setup due to the sensitivity required. However, it has been demonstrated by Lethiec *et al.* that employing polarization-dependent measurements within the established framework yields comparable results [58, 69]. Therefore, we will adopt this alternative approach for our investigation.

When recording the SPE PL signal with HWP and polarizer assembly, the intensity collected with the objective can readily be adapted from 1.34 into:

$$I_\mathrm{col} = \int_0^{2\pi} \int_0^{\rho_\mathrm{max}} \left|\mathrm{E}'' \cdot \mathbf{e}_x\right|^2 \rho \,\mathrm{d}\rho \,\mathrm{d}\varphi, \tag{1.40}$$

where $\mathrm{E}'' = E' \cdot \mathbf{e}_{k''}$ is the field after the HWP and $\mathbf{e}_{k''} = \cos(\varphi'') \cdot \mathbf{e}_x + \sin(\varphi'') \cdot \mathbf{e}_y$.

Up to this point, our analysis has implicitly focused on 1D dipoles, in other words, emitters exhibiting non-degenerate bright states characterized by single optical dipoles. However, other types of emitters have been observed, as exemplified by colloidal CdSe QDs [70, 71], where doubly degenerate bright states give rise to what is defined as a 2D dipole. These dipoles consist of two incoherent optical orthogonal dipoles, described with respect to their "dark-axis," which is orthogonal to the dipole plane. While the precise nature of the PDs under investigation has not been thoroughly examined to date, recent findings [33] suggest that they are primarily characterized by single optical dipoles. Consequently, we will present the computational details for 1D dipoles in the following sections, while still providing a comparative discussion with 2D dipoles.

Developing Eq. 1.40 yields a relation equivalent to the experimental fit function Eq. 1.39 where the minimum (I_min) and maximum (I_max) intensities can be expressed in terms of three coefficients A, B, and C:

$$\begin{aligned} A &= \frac{\pi}{4} D^2 \int_0^{i_\mathrm{m}} (t_s(\theta) - \cos(\theta)\, t_p(\theta))^2 \frac{\sqrt{(1 - n_\mathrm{GaN} \sin(\theta))^2} \sin(\theta)}{\cos(\theta)} \mathrm{d}\theta, \\ B &= \pi D^2 \int_0^{i_\mathrm{m}} t_p^2(\theta) \frac{\sqrt{(1 - n_\mathrm{GaN} \sin(\theta))^2} \sin^3(\theta)}{\cos(\theta)} \mathrm{d}\theta, \end{aligned} \tag{1.41}$$

and

$$C = \frac{\pi}{2} D^2 \int_0^{i_\mathrm{m}} (t_s(\theta) + \cos(\theta)\, t_p(\theta))^2 \frac{\sqrt{(1 - n_\mathrm{GaN} \sin(\theta))^2} \sin(\theta)}{\cos(\theta)} \mathrm{d}\theta,$$

with, for a 1D dipole:

$$I_\mathrm{min} = A \sin^2(\theta_\mathrm{d}) + B \cos^2(\theta_\mathrm{d}),$$
$$I_\mathrm{max} - I_\mathrm{min} = C \sin^2(\theta_\mathrm{d}). \tag{1.42}$$

From these relations, we should point out that a reduced DLP is inherent to the measurement procedure and results from the extended collection angle of the microscope objective. A larger NA value (i.e., a large θ_c) leads to a larger coefficient I_min and hence, a lower DLP. This feature can be used to determine the off-axis angle θ_d, since the relation resulting from the combination of Eqs. 1.38 and 1.42

$$\delta_\mathrm{p,1D}(\theta_\mathrm{d}) = \frac{C \sin^2(\theta_\mathrm{d})}{(2A - 2B + C) \sin^2(\theta_\mathrm{d}) + 2B}, \tag{1.43}$$

can be inverted to yield:

$$\theta_\mathrm{d1D} = \arcsin\left(\sqrt{\frac{2B}{C - (2A - 2B + C) \sin^2(\theta_\mathrm{d})}}\right). \tag{1.44}$$

The subscript "1D" is used to differentiate between equations pertaining to 1D and 2D dipoles.

1.4.3 Fitting uncertainties

While these calculations allow us theoretically to extract unequivocally the 3D orientations of PD dipoles, we need to delve into the fitting procedure to ascertain the relevance of extracted parameters. At first, let us plot the functions $\delta_\mathrm{p,1D}(\theta_\mathrm{d})$ simulated with NA = 0.5, $\lambda_\mathrm{SPE} = 800\,\mathrm{nm}$ and for n_GaN values as reported by different sources (see Fig. 1.17). The result proves to be fairly robust with a maximum standard deviation on θ_d1D of 0.65° when the DLP approaches unity. The reduced influence of fluctuations in the refractive index becomes evident when considering that n_GaN contributes solely through the term '$n_\mathrm{GaN} \sin(\theta)$' in Eq. 1.41, where $\sin(\theta) \leq \sin(i_\mathrm{m})$ approaches 0 for a low NA objective.

It follows logically that the computed off-axis angle does not vary significantly when changing the wavelength, since its impact is only experienced through variation of the GaN refractive index. This is readily observable in the simulated curves given in Fig. 1.18 for different numerical apertures and for 2D dipoles as well.

In contrast, the shape of the curve significantly depends on the objective employed. The maximum DLP, achieved for in-plane dipoles, drops below unity for increasing NA values,

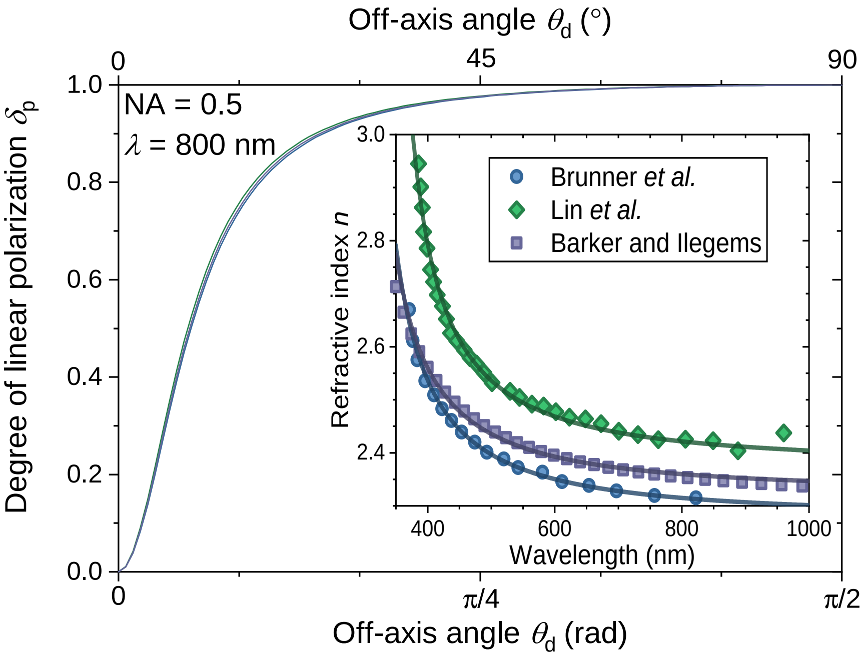

Figure 1.17: Simulated DLP for n_{GaN} extracted from different sources. Original datasets [48–50] are plotted in the inset (datapoints) along with the Sellmeier fits (Eq. 1.24) used to estimate n_{GaN} for any wavelength.

leading to a growing discrepancy between $\delta_{\mathrm{p,1D}}(\pi/2)$ and $\delta_{\mathrm{p,2D}}(\pi/2)$. As a result, it becomes theoretically feasible to assess the 1D nature of PD dipoles by measuring DLPs beyond the 2D maximum. However, this proves impossible when using an objective with NA = 0.5, as the limit $\delta_{\mathrm{p,2D}}(\pi/2) = 0.98$ falls within experimental uncertainties. Using objectives with a larger NA would also substantially enhance off-axis angle estimation as hinted by the saturating behavior of the 1D simulated curve for NA = 0.5. Indeed, when approaching unity, small uncertainties in the DLP result in uncertainties in θ_d of tens of degrees, as highlighted in Fig. 1.19. For instance, measuring a DLP of (0.98 ± 0.02) yields an off-axis angle ranging from 36.5 to 90°, rendering any inference drawn from such large error margins inconclusive.

SUMMARY

In this section, we stressed the crucial significance of polarization-dependent measurements in unraveling the origin of QD PL emission lines and elucidating the behavior of PDs acting as SPEs. We delved into the practical aspects of implementing these measurements, covering both excitation and PL signal polarization monitoring. Additionally, we provided a comprehensive investigation of how, in conjunction with dipole simulation, such measurements contribute to determining the 3D orientation of PD SPEs. Furthermore, we outlined the current experimental limitations that hinder the practical implementation of these measurements to date.

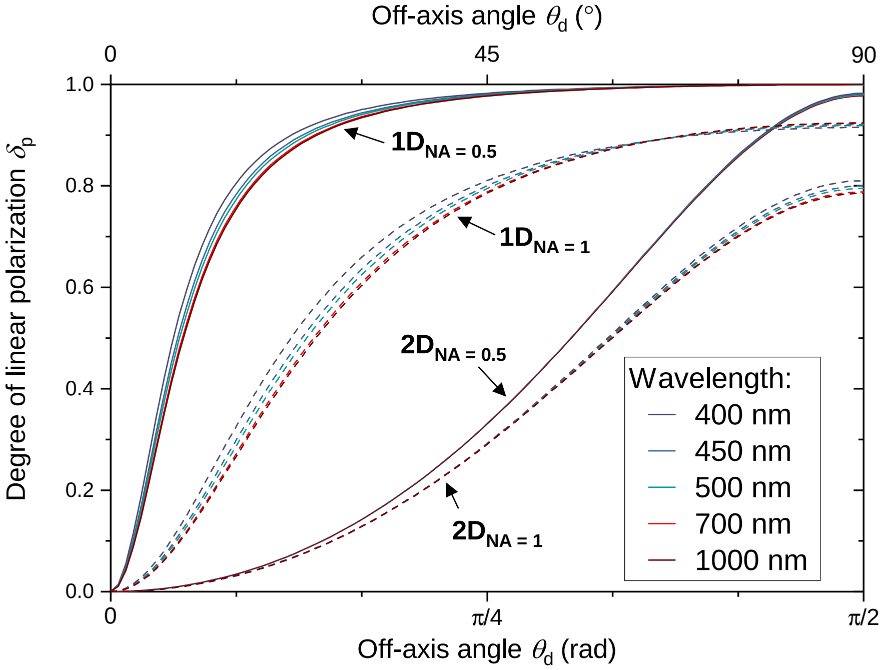

Figure 1.18: Simulated DLP for 1D (solid lines) and 2D dipoles (dashed lines), for objectives with an NA of 0.5 and 1. Each simulation is carried out at different wavelengths.

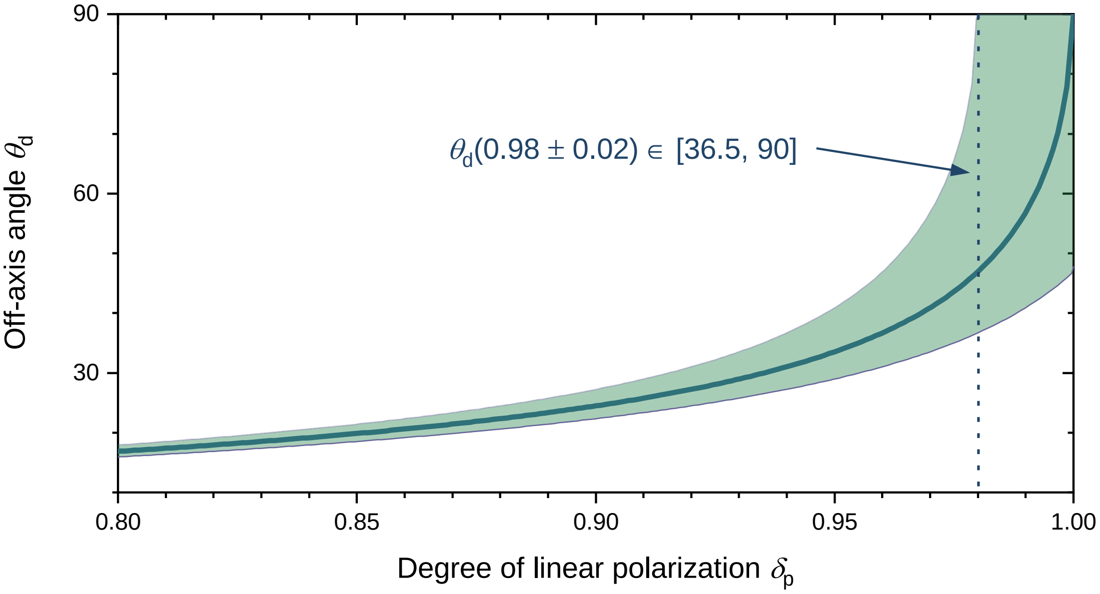

Figure 1.19: Simulated off-axis angle for 1D dipoles, for objectives with an NA value of 0.5. The shaded area corresponds to the uncertainty interval assuming an uncertainty of ±0.02 on the measured DLP.

1.5 Time-resolved spectroscopy

Time-resolved measurements are conducted using the second arm of the μ-PL setup, referred to as the Hanbury Brown and Twiss intensity interferometer (HBT) setup in Fig. 1.1. However, the term 'HBT' is specifically applicable to correlation measurements, as outlined in Subsect. 1.5.2. This detection arm comprises a time tagger/time correlator connected to two single-photon detectors, of which only one is employed for TRPL measurements (see Subsect. 1.5.1). In the UV setup, PMA 175 photomultiplier tubes from Picoquant serve as SPDs, in combination with a Picoquant Picoharp 300 time correlator. In the NIR setup, SPCM_AQRH single-photon avalanche diodes from Excelitas are employed as SPDs, and the time tagger is a quTAG from qutools. Additionally, the setup is equipped with an optical fiber reflective collimator and a fiber optic splitter to couple the PL signal into the two sensors of a superconducting nanowire single-photon detector (SNSPD) from Single Quantum, intended for future use in characterizing telecom emitters. However, none of the results presented in this study were acquired with it. In the subsequent sections, we delve into specific aspects of time-resolved measurements, providing insights into the steps required to extract relevant physical data from such measurements.

1.5.1 Time-resolved photoluminescence

At the time of writing, TRPL measurements are exclusively conducted using the UV setup. This involves employing a pulsed 266 nm laser, with a repetition rate as low as 8.45 kHz and a pulse duration of 440 ps. The TRPL measurement process is structured such that for each laser excitation pulse, a portion of the laser light is captured by a photodiode module to generate an electronic pulse, initiating the time-correlated stopwatch. Simultaneously, the luminescence signal is directed onto one of the SPDs, which halts the stopwatch. In the absence of any photon detection during the time interval between two consecutive excitations, the stopwatch resets upon the arrival of the next pulse. A TRPL transient is constructed by recording a histogram of time delays between excitation pulses and subsequent photon events. Operational limits are further detailed in Subsect. 1.5.3.

1.5.2 Hanburry Brown and Twiss interferometer—operative modes

$g^{(2)}(\tau)$ measurements are performed using an HBT interferometer. It is comprised of a 50/50 BS (BS_3), illustrated in Fig. 1.4, which divides the incident light between the two SPDs. In standard *start-and-stop* operations, the detection of a photon by the first SPD (SPD_1) triggers a stopwatch which stops when the second SPD (SPD_2) detects another photon. Delays recorded in this way are saved to a coincidence histogram which mimics to a certain extent the second order correlation function of the light source with, however, a strong limitation: any photon detected on the 2nd SPD stops the stopwatch, preventing any later incoming photon to be correlated to the "start" photon. The brighter the source, the less likely it is of recording long delays. To give a straightforward example, it is virtually impossible to measure delays on the order of seconds when using a source with a photon generation rate on the order of the GHz.

The discrepancy between actual photon statistics and the *start-and-stop* histogram can be quantified as follows: assuming an ideal coherent light source, the probability of detecting a single photon on an SPD in an arbitrary time interval τ is given as $p = \nu\tau$, where ν is the photon detection rate. Hence, after the detection of a single photon on SPD_1, the likelihood of recording a coincidence between time $t = 0$ and $t = \tau$ on SPD_2 follows the relation:

$$p(0) = p = \nu\tau. \tag{1.45}$$

If a coincidence is registered during that interval, no further coincidence can be captured in the subsequent interval ($t \in [\tau, 2\tau]$), resulting in the following relationship:

$$p(1) = p(1 - p(0)) = p(1 - p). \tag{1.46}$$

The probability $p(n)$ of recording a "stop" photon on SPD_2 in the time interval $t \in [n\tau, (n+1)\tau]$ follows immediately:

$$p(n) = p\left(1 - \sum_{k=0}^{n-1} p(k)\right). \tag{1.47}$$

The probability of recording a photon on SPD_2 in the interval $[n\tau, (n+1)\tau]$ is reduced by the probability of a photon detection at any shorter delay. For $n = 2, 3$, we thus obtain:

$$\begin{aligned} p(2) &= p(1 - p(0) - p(1)) = p\big(1 - p - p(1 - p)\big) = p(1 - p)^2, \\ p(3) &= p(1 - p - p(1 - p) - p(1 - p)^2) = p(1 - p)^3 \end{aligned} \tag{1.48}$$

from which we conjecture the following relationship:

$$p(n) = p(1 - p)^n, \tag{1.49}$$

that can be demonstrated recursively.

Additionally, $p(n)$ can be interpreted as the probability of registering a photon on SPD_2 within a brief interval τ, at a delay $t = n\tau$ after a first event registered on SPD_1. Therefore, we can express it as follows:

$$p(t) = p(n) = p(1 - \nu\tau)^n = p(0)(1 - \nu t/n)^n. \tag{1.50}$$

In the continuous limit (i.e., $\tau \to 0$ and $n \to \infty$), this relation becomes:

$$p(t) = p(0)e^{-\nu t} \tag{1.51}$$

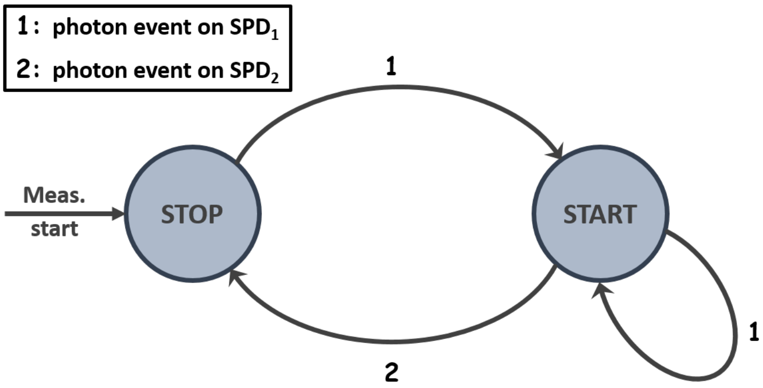

Figure 1.20: State diagram in *start-and-stop with reset* operations. The diagram has two states (START and STOP). An event on SPD$_1$ starts or resets the stopwatch while an event on SPD$_2$ stops it and adds the recorded delay to the coincidence histogram.

In other words, the probability or recording coincidences at a delay t decreases exponentially, at the photon detection rate ν. This feature can be understood as spurious bunching unrelated to the physical nature of the light source. In typical *start-and-stop* operations, when a second photon is detected on SPD$_1$ following the initial stopwatch trigger, it results in a timer reset (*start-and stop with reset*, see the state diagram in Fig. 1.20). This further reduces the probability of recording long delays, modifying Eq. 1.51 as follows:

$$p(t) = p(0)e^{-(\nu_1+\nu_2)t}, \tag{1.52}$$

where ν_1 (respectively, ν_2) is the detection rate of SPD$_1$ (respectively, SPD$_2$). The difference arises either due to fluctuations of each sensor PDE or as a result of polarization-dependent transmission and reflection coefficients of the beamsplitter. Figure 1.21 illustrates this bunching effect in an HBT experiment under a *start-and-stop with reset* operation using an attenuated 488 nm laser as a coherent light source. Coincidences are recorded here using the SPADs. The $g^{(2)}(\tau)$ histogram is directly proportional to the probability $p(t)$. Using Eq. 1.51 to fit the auto-correlation measurements, we obtain a strong match between the decay rates $\nu_{1\to2} = (174 \pm 1)\,\text{ns}$, $\nu_{2\to1} = (175 \pm 1)\,\text{ns}$ extracted from the exponential fit and the summed detection rate $\nu_1 + \nu_2 = (178 \pm 2)\,\text{kHz}$.

Due to inherent limitations of SPDs, the relationship described in Eq. 1.52 holds true only for extended delays. Following each photon event, an SPD generates an electronic pulse and undergoes a recovery period during which it cannot detect any additional photons [72]. The probability to reset the stopwatch through detection of a second photon by SPD$_1$ drops to 0 during this ’dead’ time and Eq. 1.51 applies. The duration of this recovery period varies, spanning from hundreds of picoseconds to tens of nanoseconds depending on the SPD nature [73–76]. This amounts to 23 ns for the SPADs used for recording Fig. 1.21.

To avoid the discrepancy induced by a *start-and-stop* operation, an alternative resides in

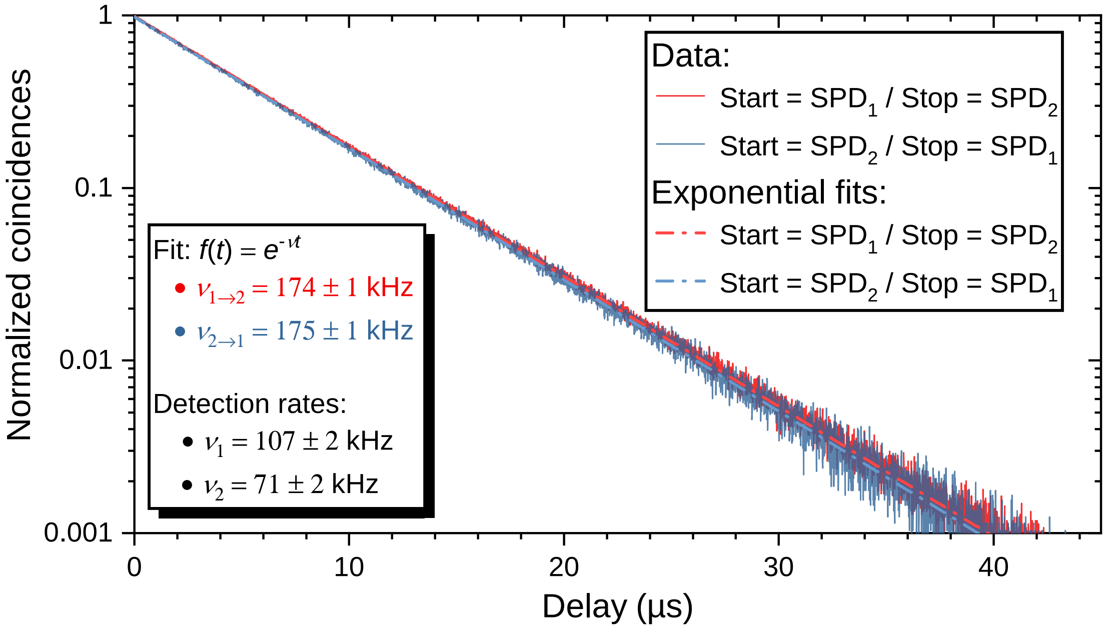

Figure 1.21: Auto-correlation measurements using a 488 nm laser as coherent light source. $g^{(2)}$ histograms are recorded using alternatively SPD_1 and SPD_2 as start/stop detectors.

recording photon events with precise time tagging for each SPD channel. The real $g^{(2)}$ histogram is then reconstructed by computing the delay between each SPD_1-related and SPD_2-related photon event. Under such *correlation* operations, the amount of data generated in real time is massive and requires a specifically designed analyzing treatment tool [77]. The difference between each operation mode is highlighted in Fig. 1.22.

1.5.3 Dead time and time resolution

DEAD TIME

Ultimately, the accuracy of the $g^{(2)}$ histogram in *correlation* operations is still limited by the SPD and associated electronics dead times, as for any time-correlated single photon counting (TCSPC) experiments [72]. Hence, the detection rate should always be constrained to ensure a negligible probability to have a photon event on a detector during its recovery period. This means ensuring that the detection rate remains orders of magnitude below the inverse of the SPD dead time, which amounts to a few tens of MHz for the SPADs. For PMA 175 PMTs, for which we recorded a pulse tail of about 10 ns, Picoquant recommends a maximum count rate of 5 MHz.

While *correlation* operation provides the most accurate results, *start-and-stop with reset* operations proves to be sufficient for characterizing features that occur within much shorter timeframes compared to spurious bunching events. When conducting auto-correlation measurements on SPEs, the antibunching dip is typically distinguishable within a time span of

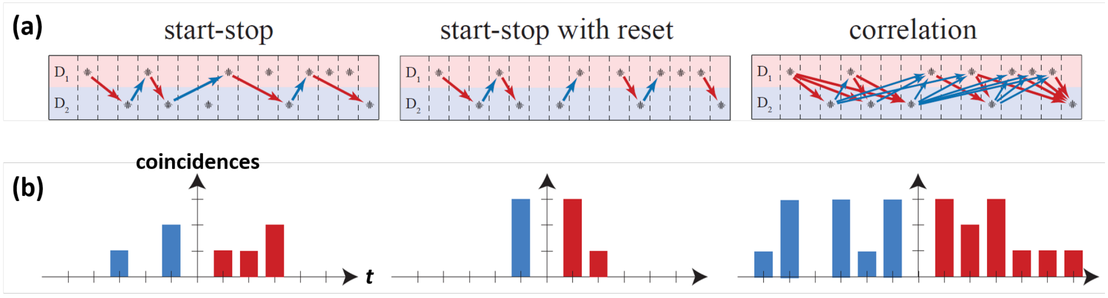

Figure 1.22: Illustration of the $g^{(2)}$ histogram calculation under *start-and-stop*, *start-and-stop with reset* and *correlation* operations. The same event stream **(a)**translates into different $g^{(2)}$ histograms **(b)** depending on the operation mode. The physics is best approached through *correlation* operations. Figure adapted from [77].

only a few tens of the characteristic emission time, i.e., the inverse of the emission rate γ. Consequently, *start-and-stop with reset* operations remain suitable as long as the detection rate remains significantly lower than the emission rate. As a result, the setup efficiency $\eta = \nu/\gamma$ needs to remain low, typically below 1%. As detailed in Sect. 1.3, this condition is inherently met in all the $g^{(2)}(\tau)$ experiments conducted in this study.

In TRPL measurements a similar limitation arises, requiring careful control of excitation power to minimize the likelihood of two-photon events per laser pulse and thereby prevent the 'pile-up' effect [78]. In 'macro-TRPL', where the laser excitation spot allows for the simultaneous excitation of multiple emitters, strict control over the excitation power is crucial. However, the constraint on the detection rate is not as stringent as commonly believed, allowing a detection rate of approximately 10 to 20% of the excitation rate without any significant signal distortion [72]. In our case, the challenge was the opposite: due to the very low repetition rate of the pulsed laser available and the low probability of detecting a photon from a single QD per pulse while maintaining a 'low-excitation' regime, we opted to perform TRPL measurements on an ensemble of QDs to achieve a sufficient detection rate, albeit at the expense of resolving the exact recombination dynamics of individual QDs.

TIME RESOLUTION

The time resolution in TCSPC techniques involves multiple factors and is quantified by the instrument response function (IRF), representing the total response time of the detection system. This can be empirically estimated using a short, well-defined light pulse and recording its auto-correlation histogram. In scenarios where the laser pulse is sufficiently short, the jitter of the laser pulse is predominantly determined by the instruments' resolution. The time resolution is then given by the full width at half-maximum (FWHM) Γ_{IRF} of the autocorrelation histogram expressed as [79]:

$$\Gamma_{\text{IRF}} = \sqrt{\Gamma_{\text{el}}^2 + \Gamma_{\text{disp}}^2 + \Gamma_{\text{det},1}^2 + \Gamma_{\text{det},2}^2}. \tag{1.53}$$

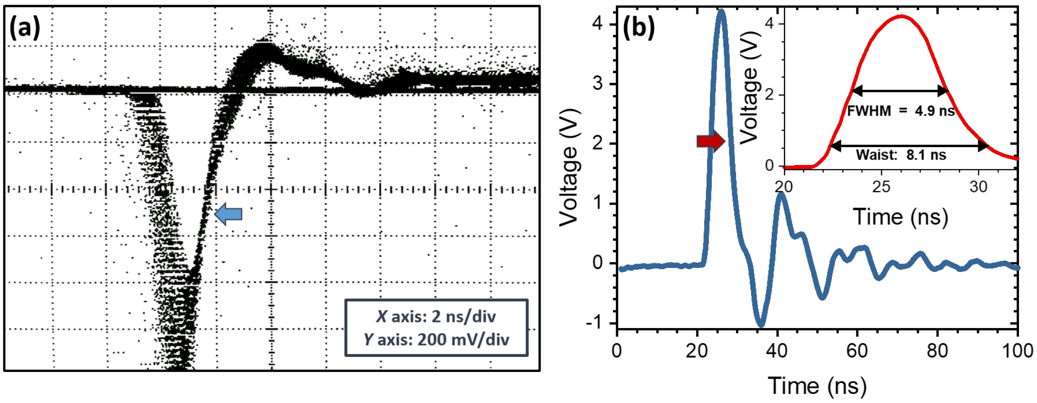

Figure 1.23: Single photon response of a **(a)** PMA 175 PMT and **(b)** SPCM_AQRH SPAD recorded with a high-speed oscilloscope (500 MHz). The selected threshold voltage is indicated by a blue arrow for the rising edge and a red arrow for the falling edge. The inset presents a zoom on the SPAD pulse.

Here, Γ_{el} represents the electronics jitter, Γ_{disp} the temporal dispersion associated to the monochromator used for spectral filtering, and $\Gamma^2_{\text{det,i}}$ $(i = 1,2)$ denotes the jitter associated with each detector, (i.e. SPD or photodiode). The dispersion introduced by the grating is estimated through the temporal separation between photons impinging on each end of the grating and is expressed by [80]:

$$\Gamma_{\text{disp}} = \frac{Lnk\lambda}{c}, \tag{1.54}$$

where L represents the size of the grating, n the groove density, k the diffraction order, and c the light velocity. Γ_{disp} is on the order of 100 ps for UV light using the SPEX 270M and becomes negligible when using bandpass filters instead of a monochromator to select the investigated spectral window. For TRPL measurements, the IRF is additionally influenced by the non-negligible duration of the laser pulse (440 ps) requiring inclusion of Γ_{pulse} in Eq. 1.53.

Both photodiodes and SPDs generate electronic pulses upon photon detection, and the time-trigger stopwatch is activated based on threshold voltage crossings. The detector jitter is thus not defined by the pulse duration, but rather by the transit time spread (TTS), associated with variations in pulse shape from one pulse to another and influenced by the threshold voltage choice. Fig. 1.23 illustrates the single photon response of a PMT and SPAD detector for further clarity.

In the PhD thesis manuscript of I. Rousseau, LASPE, EPFL, the time resolution achieved with the UV setup was assessed at different wavelengths using auto-correlation measurements on the luminescence of a GaN buffer and an InGaN quantum well (QW) grown on Si, with a decay time constant below 50 ps at RT. The reported Γ_{IRF} was ≤ 250 ps between 266 and 450 nm [37]. This time resolution sets an upper limit for the $g^{(2)}(\tau)$ measurements performed with PMTs and time-correlator electronics from Picoquant. The manufacturer guarantees a TTS below 180 ps for PMA 175 detectors and a timing jitter below 12 ps for the PicoHarp 300. Although the IRF of the HBT assembly in the NIR setup has not been empirically estimated, the datasheet for SPCM_AQRH SPADs mentions a typical timing resolution of about 350 ps, exceeding significantly the quTAG jitter ($\leq 7\,\mathrm{ps}$).

The IRF is usually well-approximated by a Gaussian function:

$$\mathrm{IRF}(t) = 2\sqrt{\frac{\ln 2}{2\pi\Gamma_{\mathrm{IRF}}^2}}\exp\left(\frac{-4\ln 2 t^2}{\Gamma_{\mathrm{IRF}}^2}\right). \tag{1.55}$$

For TRPL measurements, the experimental transients I_{exp} appear as a convolution of the IRF with the real (multi-)exponential decay (I_{phys}) that carries the physics:

$$I_{\mathrm{exp}} = \mathrm{IRF} \otimes I_{\mathrm{phys}}. \tag{1.56}$$

Without correction schemes, features that appear within the instrument time resolution cannot be resolved. Deconvolution schemes [81, 82] can further enhance the time resolution down to $\Gamma_{\mathrm{IRF}}/10$ under ideal experimental conditions [79]. Assuming, for the sake of illustration, a TRPL transient featuring a monoexponential decay (τ_{d}), the experimental curve can be approximated by [83]:

$$I_{\mathrm{exp}}(t) \propto \exp(-t/\tau_{\mathrm{d}})\left[1 + \mathrm{erf}\left(2\sqrt{\ln 2}\frac{t - \Gamma_{\mathrm{IRF}}^2/(4\ln 2\tau_{\mathrm{d}})}{\Gamma_{\mathrm{IRF}}}\right)\right]. \tag{1.57}$$

By experimentally recording the IRF prior to any TRPL measurements, we can effectively fix the fitting parameters associated with the IRF. In practice, we used a dedicated software (EasyTau 2) to accommodate multi-exponential decays while considering the exact IRF.

The same consideration applies to $g^{(2)}(\tau)$ measurements, where the histograms recorded experimentally ($G^{(2)}(\tau)$) relates to the $g^{(2)}(\tau)$ function through[III]:

$$G^{(2)}(\tau) = C \cdot \mathrm{IRF} \otimes g^{(2)}(\tau), \tag{1.58}$$

with C a normalization factor. The IRF impacts the results by smoothing sharp features and typically contributes to reducing the experimental single-photon purity ($g^{(2)}(0)$). The real $g^{(2)}(\tau)$ can also be retrieved here by applying deconvolution techniques but requires, once again, recording the IRF.

[III] The link between $g^{(2)}$ histograms and the exact $g^{(2)}(\tau)$ function is nuanced and Eq. 1.58 only applies under very low detection efficiencies [84], a condition consistently satisfied in this thesis.

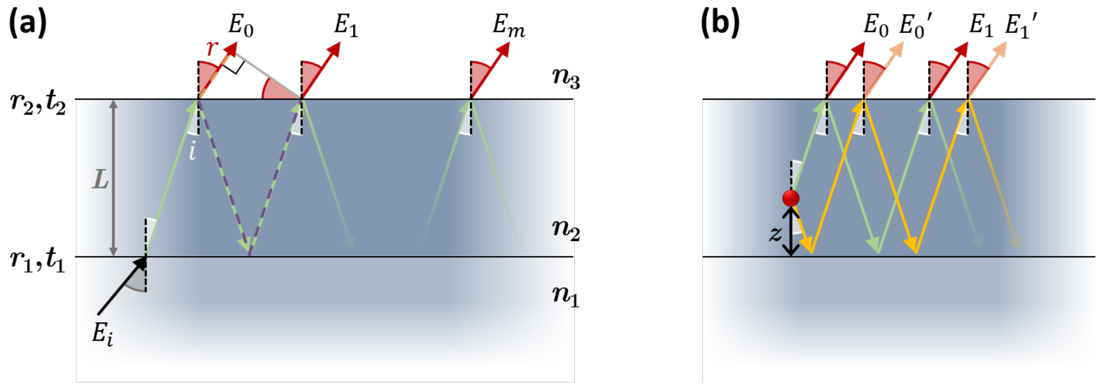

Figure 1.24: Schematic representation of a Fabry-Perot interferometer, with a source positioned **(a)** outside or **(b)** inside the cavity of refractive index n_2. The path difference δ corresponds graphically to the difference between the purple and orange dashed segments.

1.6 Fabry-Perot cavity

Fabry-Perot cavities play a ubiquitous role in semiconductor physics, particularly in the context of heterostructures. When a wave crosses an interface between two media with distinct refractive indices, a part of the wave reflects off the interface, while the rest undergoes refraction. In the context of multiple interfaces, the wave experiences numerous reflections within each intermediate layer, and the refracted wave emerges as a composite of all transmitted fractions. This gives rise to an interference pattern, a phenomenon explored in the following discussion. Our approach focuses on understanding the impact of such an interference on PL spectra and how it may affect the reliability of our results. We examine two scenarios: the first configuration, depicted in Fig. 1.24(a), involves a wave originating from medium 1 (of refractive index n_1) propagating through layer 2 (of index n_2 and finite thickness L) before exiting into medium 3, typically air ($n_3 = n_{\mathrm{air}}$). The second configuration, shown in Fig. 1.24(b), places the source inside layer 2. The field transmission coefficients are denoted as t_1 ($2 \rightarrow 1$) and t_2 ($2 \rightarrow 3$), and the reflection coefficients are denoted as r_1 ($1 \rightarrow 2$) and r_2 ($2 \rightarrow 3$).

1.6.1 Emitter positioned below the cavity

In the initial configuration, we consider a plane wave impinging on the first interface at a specified angle. The incident wave, of amplitude E_{i}, undergoes refraction at each interface, and the resulting first transmitted wave (with no reflection) amplitude E_0 is given by:

$$E_0 = t_1 t_2 E_{\mathrm{i}}. \tag{1.59}$$

Following a reflection at each interface, the transmitted field amplitude E_1 can be expressed as:

$$E_1 = r_1 r_2 E_0 e^{i\phi}, \tag{1.60}$$

where the dephasing term ϕ depends on the path difference δ (see Fig. 1.24) between the two waves:

$$\delta = \frac{2Ln_2}{\cos(i)} - 2Ln_1 \tan(i)\sin(r) = 2Ln_2\cos(i), \tag{1.61}$$

with $\sin(r) = n_{\mathrm{air}}/n_2 \sin(i)$. The phase factor is given by $\phi = \delta k_0$. where k_0 corresponds to the vacuum wavenumber of the incident wave. We assume $n_2 > n_1,\ n_3$, ensuring no additional dephasing occurs after each reflection.

After undergoing m reflections ($m \in \mathbb{N}^*$) at each interface, the transmitted field amplitude is given by:

$$E_m = (r_1 r_2)^m e^{im\phi} E_0. \tag{1.62}$$

The total transmitted field amplitude E_{t} amounts to the sum of all E_m:

$$E_{\mathrm{t}} = \sum_{m=0}^{+\infty} E_m = E_0 \sum_{m=0}^{+\infty} (r_1 r_2 e^{i\phi})^m = \frac{E_0}{1 - r_1 r_2 e^{i\phi}} = \frac{t_1 t_2 E_{\mathrm{i}}}{1 - r_1 r_2 e^{i\phi}}. \tag{1.63}$$

The power transmission coefficient T_{FP} follows:

$$\begin{aligned} T_{\mathrm{FP}} &= \left|\frac{E_{\mathrm{t}}}{E_{\mathrm{i}}}\right|^2 \left(\frac{n_3\cos(r)}{n_1\sqrt{1-(n_3/n_1)^2\sin^2(r)}}\right) \\ &= \frac{(t_1 t_2)^2}{1 + (r_1 r_2)^2 - 2r_1 r_2 \cos(\phi)} \frac{n_3 \cos(r)}{n_1\sqrt{1-(n_3/n_1)^2\sin^2(r)}}, \end{aligned} \tag{1.64}$$

where the fraction in brackets accounts for energy conservation. T_{FP} depends on the wavelength and transmission angle, r.

1.6.2 Emitter positioned inside the cavity

If the emitter is embedded within the cavity layer (second scenario), Eq. 1.64 must be adjusted to account for backward emission (yellow arrows in Fig. 1.24(b)). For each electric field E_m a second term E'_m arises from backward emission, exiting the sample with an equivalent angle r. The terms are related through:

$$E'_m = r_1 e^{i\varphi'} E_m, \tag{1.65}$$

where the dephasing term φ' depends on the vertical position z of the emitter:

$$\varphi' = 2zn_2\cos(i)k_0. \tag{1.66}$$

The transmitted field amplitude is now expressed as:

$$E_{\mathrm{t}} = \sum_{m=0}^{+\infty} E_m + E'_m = t_2 E_{\mathrm{i}} \frac{1 + r_1 e^{i\varphi'}}{1 - r_1 r_2 e^{i\phi}}. \tag{1.67}$$

and T_{FP} becomes:

$$\begin{aligned} T_{\mathrm{FP}} &= \left| \frac{E_{\mathrm{t}}}{2E_{\mathrm{i}}} \right|^2 \frac{n_3 \cos(r)}{n_2 \sqrt{1 - (n_3/n_2)^2 \sin^2(r)}} \\ &= \frac{1}{4} \frac{t_2^2 \left[1 + r_1^2 + 2r_1 \cos(\varphi')\right]}{1 + (r_1 r_2)^2 - 2r_1 r_2 \cos(\phi)} \frac{n_3 \cos(r)}{n_2 \sqrt{1 - (n_3/n_2)^2 \sin^2(r)}}. \end{aligned} \tag{1.68}$$

When considering a broad spectral source located inside the cavity, the incident light is affected by variations in the transmission coefficients, and the measured PL spectrum exhibits a modulation pattern unrelated to the source. In practice, the measured signal corresponds to light collected through the objective, and T_{FP} must be averaged over a solid angle of emission that matches the collection angle of the objective (see Sect. 1.3).

The amplitude of the interference is mainly driven by the reflection and transmission coefficients, which depend on the polarization of the electric field. For a precise description of the interference pattern, we should decompose T_{FP} into both the s- ($T_{\mathrm{t},s}$) and p- ($T_{\mathrm{t},p}$) components, such that:

$$T_{\mathrm{FP}} = \frac{|E_s|^2 T_{\mathrm{t},s} + \left|E_p\right|^2 T_{\mathrm{t},p}}{|E_s|^2 + \left|E_p\right|^2}, \tag{1.69}$$

where E_s and E_p are the components of the field generated by the point-like source. The average value of T_{FP} is computed by integrating the numerator and denominator in Eq. 1.69 individually over the collection angle.

1.6.3 A case study — GaN buffer on sapphire

To understand the impact of T_{FP} on PL detection, we can simulate its behavior in a scenario similar to that encountered in our investigation of PDs. Specifically, we consider a 4 µm-thick GaN buffer ($n_2 = n_{\mathrm{GaN}}$) grown on sapphire ($n_1 = n_{\mathrm{Al_2O_3}}$, $n_3 = n_{\mathrm{air}}$), with a point-light source embedded within the GaN layer (second scenario). This configuration is analogous to the sample labeled A4365, which is discussed in detail in Chap. 3. The refractive indices are assumed to be constant within the investigated spectral range. Figure 1.25(a) illustrates the variation in transmission for s-, p- and unpolarized light with an incidence angle $i = 12°$.

The transmittance exhibits broad oscillations, wherein the oscillation period increases proportionally with the wavelength. An increase in the buffer thickness L would lead to an increased frequency of oscillations. Despite the fact that only a small fraction of the light is reflected at

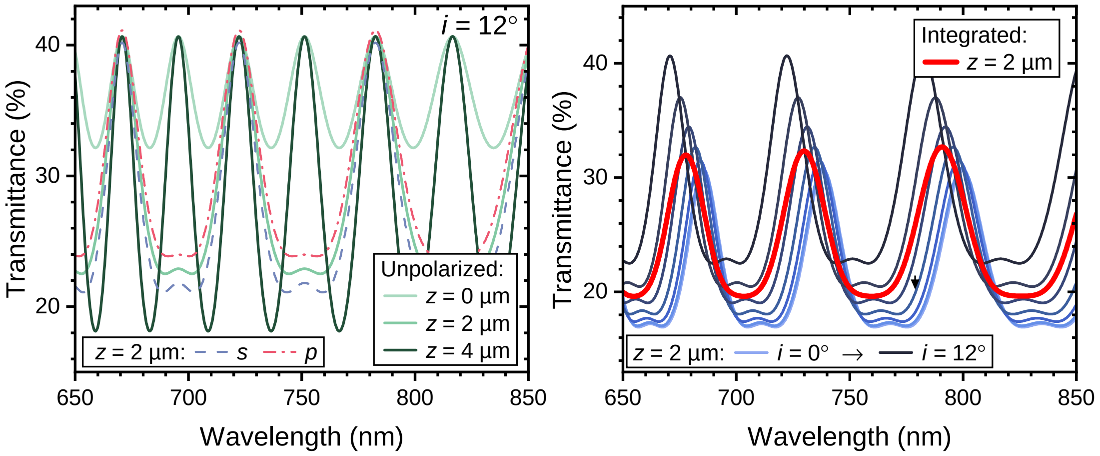

Figure 1.25: **(a)** Transmittance as a function of wavelength for different positions z of the point-like source, with an incidence angle $i = 12^\circ$. Red and blue dashed lines correspond to s- and p-polarized light, respectively. T_{FP} is illustrated by green lines for unpolarized light. **(b)** Transmittance curves of unpolarized light at different incidence angles, with the emitter positioned at $z = 2\,\mu\mathrm{m}$. The red curve illustrates the average transmittance within the objective collection solid angle.

the GaN/sapphire interface, the interference phenomenon is remarkably observable, with maxima in transmission exceeding twice the minima. The position z of the emitter within the GaN layer significantly alters the transmittance for both s- and p-polarized light. The same conclusion applies to unpolarized light, modeled here using $E_s = E_p$. This is depicted in Fig. 1.25(a), where the green lines represent the transmittance for unpolarized light at various z positions. Under normal incidence, the discrepancy between s- and p-polarized light is cancelled. The angle of incidence significantly affects the interference pattern, as shown in Fig. 1.25(b), where T_{FP} is plotted for i ranging up to the maximum collection angle i_{m}. A dephasing is observed between each curve as a consequence of the increasing path difference δ. To mimic experimental conditions, the transmittance T_{FP} must be averaged over the full collection solid angle (red line in Fig. 1.25(b)), which contributes to dampen and smoothen the oscillations.

The yellow luminescence (YL) (see Subsect. 3.1.4) observed as a background in most GaN samples is unpolarized, as can be easily verified by performing polarization-dependent measurements. As such, it should be feasible to reproduce its Fabry-Perot modulation using the approach illustrated in Fig. 1.25(b). However, the interference pattern is strongly dependent on the vertical location of the light source within the layer as evidenced again in Fig. 1.26(a) for $z = 1$ and $3\,\mu\mathrm{m}$. Coupled with the spatial inhomogeneity of the background luminescence, this prevents us from quantitatively reproducing the modulation of the YL signal. Nevertheless, we can obtain an estimate of the 'effective transmittance' by averaging the simulated T_{FP} traces for emitters located between $z = 0$ and $4\,\mu\mathrm{m}$. The average obtain over 50 simulated curves is illustrated as a green dashed line in Fig. 1.26(b).

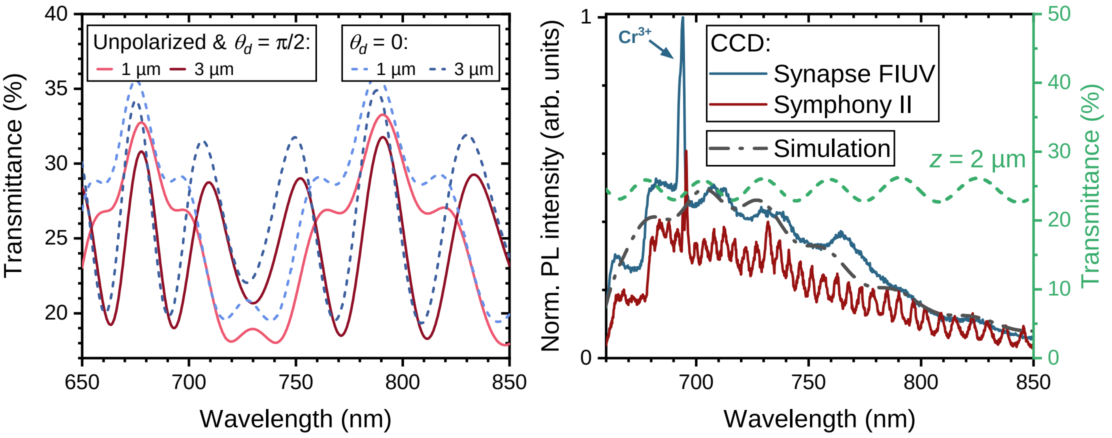

Figure 1.26: **(a)** Transmittance curves for in-plane ($\theta_\mathrm{d} = \pi/2$) and 'vertical' dipoles ($\theta_\mathrm{d} = 0$) compared to an unpolarized light source. **(b)** µ-PL spectra recorded with two different CCDs on sample A4365. The drop in intensity at short wavelength results from the use of a dichroic mirror in place of BS_2. The sharp lines around 695 nm are associated to Cr^{3+} defect luminescence [85] in the sapphire substrate. The transmittance curve for unpolarized light is reproduced in green (for $z = 2\,\mu$m).

Strikingly, the local fluctuations of the transmittance are smeared out, yielding a quasi-periodic T_FP trace which can now be directly compared with experimental measurements, such as the PL spectrum acquired from sample A4365, (see Fig. 1.26(b)). Focusing on the blue curve obtained with the front-illuminated Synapse FIUV CCD, we observe oscillations in the luminescence intensity, readily attributed to the transmittance modulation. The dash-dotted black line represents a simulated PL spectrum, generated using the transmittance curve (green line) and a Lorentzian peak multiplied by an error function to approximate both the YL and the filtering effects of the dichroic mirror, that qualitatively mimics the experimental trend.

Apart form the unpolarized background, we can also estimate the transmittance modulation for in-plane ($\theta_\mathrm{d} = \pi/2$) and 'vertical' dipoles ($\theta_\mathrm{d} = 0$), employing the framework developed in Subsect. 1.3.2. The curves simulated with $z = 1$ and $3\,\mu$m are presented in Fig. 1.26(a) in red and blue for in-plane and vertical dipoles, respectively. When $\theta_\mathrm{d} = \pi/2$, the result is equivalent to that of unpolarized light. When $\theta_\mathrm{d} = 0$, the E_s component vanishes and the transmittance curves appear slightly shifted with respect to unpolarized light. As discussed in Subsect. 1.3.2, vertical dipoles are unlikely to be detected in the current setup configuration. For in-plane dipoles, the shape of experimental PL peaks should be only weakly impacted by the Fabry-Perot cavity. Nevertheless, the modulation of the background affects the precision of DLP estimates, particularly when δ_p approaches unity, further compromising our ability to resolve the 3D orientation of dipole emitters. Transmittance fluctuations can also introduce a selection bias when visually selecting the brightest emitters.

Fabry-Perot interference, which appears on the spectra, not only results from the sample heterostructure but also emerges from the Si sensors used in conventional CCDs [86, 87]. This is illustrated in Fig. 1.26(b), with the red spectrum recorded using the back-illuminated Symphony II CCD, featuring an additional interference pattern compared to the blue curve. These features arise when the photosensitive region of the CCD sensor becomes semi-transparent in the near-infrared, allowing light to undergo multiple reflections on the Si/air and Si/electrode interfaces before absorption. This situation is equivalent to the first scenario detailed above. The oscillation period is much smaller due to the thickness of the Si layer, proving extremely detrimental for investigating sharp emission lines and preventing the use of such CCDs in the NIR.

SUMMARY

Throughout this section, we have presented a thorough exploration of Fabry-Perot cavity effects in heterostructures and their substantial impact on PL spectra. While these effects do not pose a complete obstacle to the detection of SPE PL features in our study, they can introduce nuances that affect the precision of polarization-dependent measurements if not meticulously considered. Moreover, these Fabry-Perot effects underline the limitations of Si-based CCDs in the NIR spectral range, which prompted the development of specialized devices like deep-depletion CCDs to counteract the etaloning effect. To enhance our capabilities in characterizing PD-like SPEs, the NIR setup is poised to be equipped with such a CCD in the near future.

2 GaN/AlN quantum dots

While this thesis primarily focuses on exploring the physics of zero-dimensional structures, many of their properties are directly inherited from those of bulk SCs. Therefore, we begin our examination of QDs by presenting the fundamental properties of III-N materials in Sect. 2.1, a discussion that is relevant for the subsequent chapter dedicated to PDs. Following this foundational discussion, we delve into the physics of GaN/AlN QDs by detailing extensively their optical properties in Sect. 2.2, 2.3, 2.4 and 2.5.

To provide the context, we introduce the growth technique and the structural properties of the samples examined in this chapter in Sect. 2.6, before eventually presenting the various PL experiments aimed at unraveling the optical properties of GaN/AlN SAQDs. The latter include µ-PL (Sect. 2.7 and 2.8) and second-order autocorrelation measurements (Sect. 2.9) conducted on individual high-energy QDs, followed by TRPL measurements acquired on a macroscopic QD ensemble (Sect. 2.10).

Our focus lies primarily on the phenomenological understanding of the optical properties of GaN QDs. Our approach relies almost exclusively on the use of PL characterization techniques, showcasing the wide range of results that can be obtained through this versatile tool.

2.1 III-nitrides, bulk properties

2.1.1 Structural properties and polarization characteristics

III-Ns are SC materials encompassing compounds formed between nitrogen (N) and IIIA[I] metallic atoms. Commonly encountered as binary (InN, GaN, and AlN) or ternary compounds ($Al_xGa_{1-x}N$, etc.), these materials can adopt two crystal structures [88] under 'normal' growth conditions. The first one, known as the zinc-blende phase, is commonly encountered in other compound semiconductors and in particular III-arsenide and III-phosphide SCs that are widely employed for growing SA QDs. However, III-Ns preferentially crystallize in the

---

[I] I.e., metallic atoms from the boron group of the periodic table.

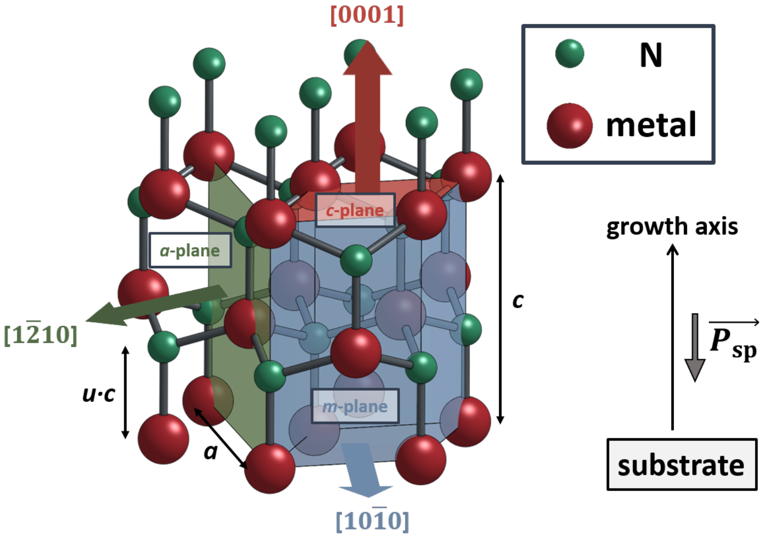

Figure 2.1: Sketch of the III-N wurtzite unit cell. Major crystal planes are highlighted by red (c-plane) green (a-plane) and blue colors (m-plane). High-symmetry directions are indicated by arrows. a and c represent the lattice constants and $u \cdot c$ denotes the interatomic bond length.

thermodynamically stable wurtzite phase [89], as observed in all samples studied, whose unit cell is illustrated in Fig. 2.1.

The wurtzite phase arises from the interleaving of two hexagonal closed-packed lattices of N and IIIA atoms, arranged in an A-B-A-B... atomic plane stacking sequence. Depending on the substrate and growth conditions, III-Ns can exhibit either metallic (metal-face) or nitrogen (N-face) polarity [90]. In most cases, including all the samples studied in this thesis, GaN epilayers possess a Ga-face polarity, with three of the four Ga atomic bonds directed toward the substrate.

The wurtzite structure is responsible for many peculiarities displayed by III-N SCs compared to their zinc-blende counterparts. Notably, the absence of inversion symmetry results in a permanent, spontaneous polarization field ($\mathbf{P}_{\mathrm{sp}}$) along the $[000\bar{1}]$ [90, 91] (refer to Fig. 2.1). Furthermore, strained III-N layers, typical in heteroepitaxy and for heterostructures like SAQDs, feature a piezoelectric ($\mathbf{P}_{\mathrm{pz}}$) polarization that is substantially greater than in zinc-blende materials under equivalent strain conditions [91]. These significant polarization fields have a profound impact on the optical properties of III-N QDs, as discussed in Subsect. 2.2.3.

2.1.2 Band structure

III-Ns are direct bandgap SCs, featuring valence band maximum (VBM) and conduction band minimum (CBM) aligned at the Γ-point of the first Brillouin zone, making them highly suited for light-emitting applications. Consequently, their optical properties are predomi-

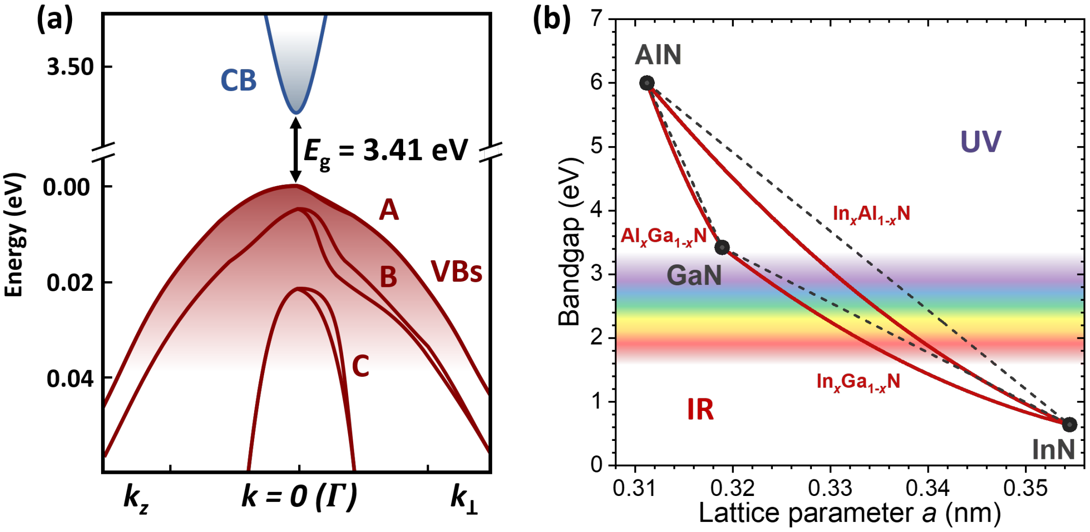

Figure 2.2: **(a)** RT GaN band structure near the Γ point, freely inspired from [88, 92]. **(b)** RT III-N bandgap as a function of in-plane lattice parameter *a*. Dashed lines are drawn by linearly interpolating between the binary compound bandgap values wile the solid red lines are obtained by considering a more realistic band bending [88]. Bandgaps and bowing parameters are taken from [88, 93–95]. The shaded area represents the visible spectrum.

nantly driven by the band structure in the vicinity of this Γ-point, illustrated in Fig. 2.2(a) for unstrained GaN.

The conduction band (CB) is primarily composed of *s*-type (Ga/Al/In) orbitals, exhibiting twofold degeneracy. In contrast, the valence band (VB) originates from nitrogen 2*p* states and is initially sixfold degenerate. However, this degeneracy is lifted by the crystal field[II] induced by the reduced symmetry of the wurtzite phase. Further inclusion of spin-orbit coupling lifts the remaining fourfold VB degeneracy, resulting in a set of three twofold degenerate VBs referred to as the A (or heavy-hole), B (or light-hole) and C (or split-off) VBs [88], with Γ_9, Γ_7 and Γ_7 symmetry, respectively, in the case of GaN [96] (see Fig. 2.2(a)). The low-symmetry wurtzite structure also introduces effective mass anisotropy, which is manifested in the distinct curvature of VBs along in-plane and out-of-plane axes.

The bandgap of III-Ns varies from the NIR (for InN) to the deep UV (for AlN), theoretically allowing fine adjustment of the desired bandgap (E_g) by tuning the metal concentrations of ternary alloys (see Fig. 2.2(b)). However, this study focuses on SPEs embedded into binary compounds. It is worth noting that strain can significantly alter the crystal field (Δ_{cr}) and spin-orbit (Δ_{so}) splittings [92, 97], thereby making the bandgap of each III-N ultimately dependent on the growth conditions. Under high tensile strain, a crossing between the A and B GaN VBs is even observed [98]. The bandgap value $E_g = 3.41$ eV [95] provided in Fig. 2.2(a) associates with unstrained GaN but is typically altered in the case of GaN QDs embedded in an AlN matrix

---

[II] Analog to the spontaneous polarization.

[99].

As the band structure results from the overlap between atomic orbitals, the bandgap is strongly temperature-sensitive. An increase in temperature enhances electron-phonon coupling and causes lattice expansion, both of which contribute to bandgap shrinkage [100]. This effect is often approximated using the empirical Varshni formula [101]:

$$E_{\mathrm{g}}(T) = E_{\mathrm{g}}(T=0) - \frac{\gamma_{\mathrm{V}} T^2}{T + \beta_{\mathrm{V}}}, \tag{2.1}$$

where γ_{V} and β_{V} are fitting parameters, although its physical relevance is questionable, particularly for wide bandgap materials [102]. Variations in the band structure consequently influence the properties of QDs, a topic thoroughly discussed in the following sections.

2.2 Physics of the exciton

The complexities of QD systems can be first apprehended by considering their fundamental role as potential traps for single electron-hole pairs (EHPs). This conceptualization comprehensively captures the fundamentals of recombination dynamics under low excitation conditions and serves as a model for emphasizing the distinctive features of III-N QD systems. Therefore, in this initial section, our focus will be on the ’single-exciton’ state, deferring the discussion of ’multi-excitonic’ states to the subsequent section.

2.2.1 Particle in a box

To gain insights into the physics of QDs, we begin with a simplified scenario——the particle in a box model. Within this framework, we envisage a particle confined in a rectangular prism-shaped box defined by a potential barrier. Specifically, we consider a potential field that is zero within the box dimensions and infinite elsewhere:

$$\begin{aligned} &V(x,y,z) = 0 \ \forall\ x,y \in [0, L_{\mathrm{QD}}] \wedge \forall\ z \in [0, h_{\mathrm{QD}}], \\ &V(x,y,z) \to +\infty \ \text{ elsewhere,} \end{aligned} \tag{2.2}$$

with L_{QD} and h_{QD} the QD width and height, respectively. Solving the time-independent Schrödinger equation in the effective mass approximation [103] leads to eigenfunctions and eigenenergies, which describe the quantum states of the confined particle. The resulting wavefunctions are denoted as [104]:

$$\Psi_{l',m',n'}(x,y,z) = \frac{2\sqrt{2}}{L_{\mathrm{QD}}\sqrt{h_{\mathrm{QD}}}} \sin\left(\frac{l'\pi x}{L_{\mathrm{QD}}}\right) \sin\left(\frac{m'\pi y}{L_{\mathrm{QD}}}\right) \sin\left(\frac{n'\pi z}{h_{\mathrm{QD}}}\right), \tag{2.3}$$

and the associated confinement energies are given by:

$$E(l,m,n) = \frac{\hbar^2\pi^2(l'^2+m'^2)}{2m^*{}_\perp L_{\mathrm{QD}}^2} + \frac{\hbar^2\pi^2 n'^2}{2m^*{}_\parallel h_{\mathrm{QD}}^2} \tag{2.4}$$

where $m^*{}_\perp$ and $m^*{}_\parallel$ distinguish between effective masses (m^*) parallel and perpendicular to the c-axis [105]. l', m' and n' denote the quantum numbers of the system. In the formalism introduced here, the eigenfunctions are separable, allowing them to be expressed as a combination of two envelope wavefunctions, respectively in-plane ($\phi_{l',m'}(x,y)$) and along the c-axis ($\chi_{n'}(z)$):

$$\Psi_{l',m',n'}(x,y,z) = \phi_{l',m'}(x,y)\chi_{n'}(z), \tag{2.5}$$

with $\phi_{l',m'}(x,y) = 2/L_{\mathrm{QD}}\sin\left(l'\pi x/L_{\mathrm{QD}}\right)\sin\left(m'\pi y/L_{\mathrm{QD}}\right)$ and $\chi_{n'}(z) = \sqrt{2/h_{\mathrm{QD}}}\sin\left(n'\pi z/h_{\mathrm{QD}}\right)$. This separability property persists as a first-order approximation even when considering the exact QDs symmetry and will be consistently assumed to hold throughout the chapter.

Applying this framework to electrons and holes in a QD, we obtain confinement energies (h_k and e_k) associated with specific wavefunctions ($\Psi_{e,k}$ and $\Psi_{h,k}$). The quantum states are labeled by an index k, denoting the k^{th} state of either carrier. Throughout this thesis, subscripts e and h are consistently employed to denote electron and hole characteristics. While theoretically, the eigenenergies (Eq. 2.4) lead to degenerate excited states, the in-plane anisotropy of SAQDs effectively lifts this degeneracy.

The first radiative state of a QD involves an EHP with both particles in their first energy state, forming what is known as an exciton state, i.e., an EHP in Coulomb interaction. The ground state energy of this exciton (E_{X}) is given by:

$$E_{\mathrm{X}} = E_{\mathrm{g}} + e_1 + h_1 + J_{eh}, \tag{2.6}$$

where J_{eh} (< 0) accounts for the electron-hole Coulomb interaction [106]. For the subsequent discussion, it is essential to distinguish the term 'exciton ground state' introduced here, which denotes the lowest energy state of an exciton within the QD, from the concept of the 'QD ground state', representing an empty QD with no electrons or holes.

The exciton energy is strongly influenced by the QD geometry, particularly through the confinement energies e_1 and h_1, which diverge as L_{QD} and h_{QD} approach zero, (refer to Eq. 2.4). The rise in E_{X} with decreasing QD size is visually depicted in Fig. 2.3(a). In practical terms, GaN/AlN SAQDs typically adopt a truncated hexagonal pyramid shape inherited from the wurtzite crystal symmetry [107, 108] (Fig. 2.2.1(b)), often highly flattened, with an aspect ratio (AR), given by $h_{\mathrm{QD}}/L_{\mathrm{QD}}$, ranging between 1:4 and 1:10 [109–112]. Consequently, vertical confinement dominates the QD properties, to the extent that the QD can be treated as a QW to derive energy levels [113]. This dominance is also reflected in the QD density of states, where all the first excited states ($k = 2,3,4...$) result from in-plane confinement,

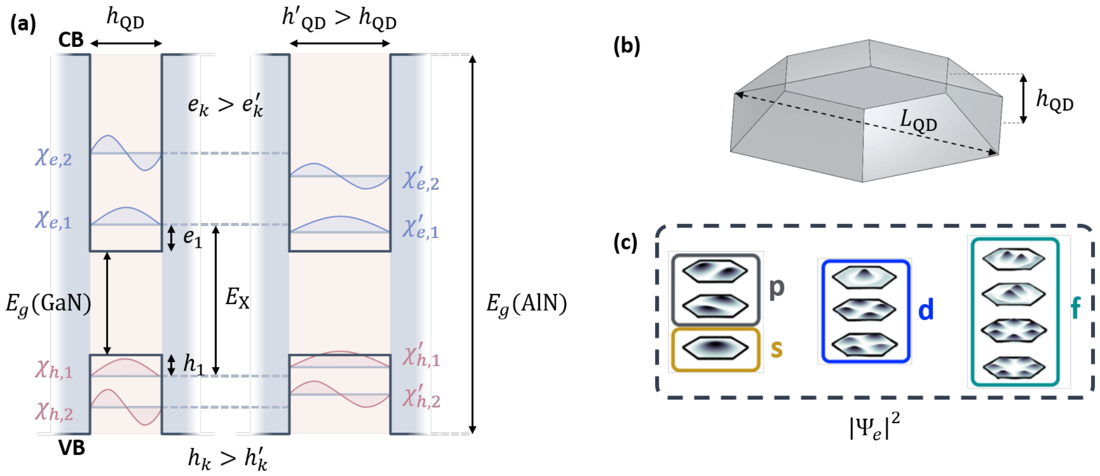

Figure 2.3: **(a)** Illustration of electron and hole confinement for QDs of different size. The infinite barrier potential is replaced here by the AlN matrix, representative of a 'real' QD configuration, with neglect of Coulomb interaction. The AR is assumed to be conserved. In this sketch, we neglect the effect of the 'built-in field' detailed later in Subsec. 2.2.3. **(b)** Schematic of a GaN/AlN SAQD with a truncated hexagonal pyramid shape. **(c)** Depiction of the electron densities computed using an 8 band $k \cdot p$ theoretical framework, organized by shells. Adapted from [117].

with k stemming from a linear combination of l' and m' values. Envelope wavefunctions $\chi_{e,2}$ and $\chi_{h,2}$ shown in Fig. 2.3(a) are not associated with the first exciton excited state, and $E_{e,h}(2,1,1) \sim E_{e,h}(1,2,1) \ll E_{e,h}(1,1,2)$[III]. It is noteworthy that QDs exhibit an 'atom-like' shell structure [114], with discrete electronic energy levels displaying notable similarities with atomic orbitals. Using the same nomenclature, QD electron and hole wavefunctions are sorted into $s-$, $p-$, $d-$, $f-$,... shell states based on their symmetry. The first electron wavefunctions are illustrated in Fig. 2.3(c) along with their corresponding shell index. Due to their generally larger effective mass [115], holes exhibit a greater density of states. This density is further increased by considering hole states associated with the A, B, or C VBs [116].

2.2.2 Fine structure splitting

As mentioned in Subsect. 2.1.2, the GaN CB exhibits an s-type configuration with zero orbital angular momentum ($l = 0$), while the VBs result from the combination of atomic p orbitals ($l = 1$). Consequently, electrons in the CB have two possible spin configurations, $s = \pm 1/2$, while holes originating from the A (or heavy-hole-like) VB have spin configurations of $j = \pm 3/2$ [118][IV]. In this context, the ground exciton state, formed by an electron at the CBM and a hole at the VBM, typically constrained to the A VB in a QD, is four-fold degenerate. Its four states

---

[III] In presence of in-plane anisotropy, the degeneracy between $E_{e,h}(2,1,1)$ and $E_{e,h}(1,2,1)$ is lifted.

[IV] Owing to spin-orbit coupling, l and s are no longer good quantum numbers and are replaced by j.

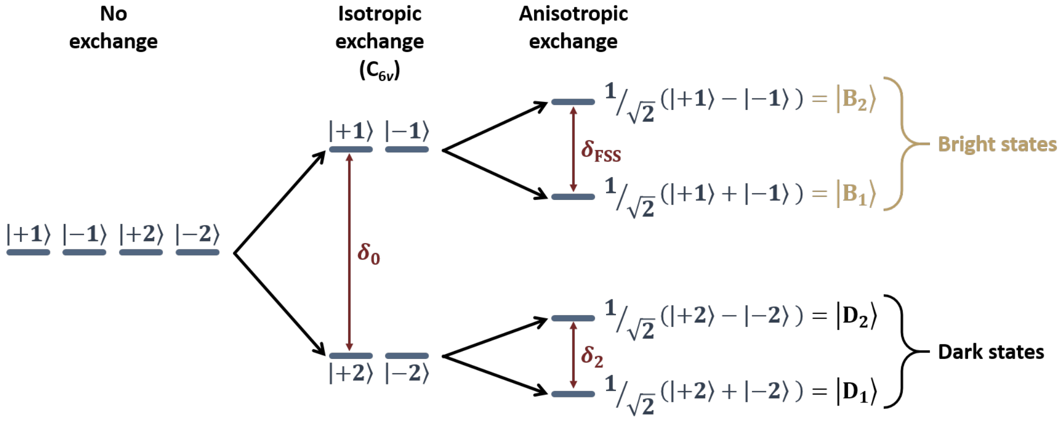

Figure 2.4: Influence of isotropic and anisotropic factors on the degeneracy of the exciton ground state. The result for C_{6v} symmetry is extracted from [119]. This illustration is in contrast with the scenario observed in arsenide QDs with C_{4v} symmetry, where the degeneracy of the dark states is already eliminated by isotropic exchange [120].

are denoted by $|\pm1\rangle$ and $|\pm2\rangle$, where ±1 and ±2 denote the total angular momentum (TAM) (m) of the exciton.

So far, our discussion has solely considered Coulomb interaction and confinement of EHPs to assess the energy of excitons. However, taking into account the fermionic nature of electrons and holes (with half-integer spin) and adhering to Pauli's exclusion principle introduces an additional energy term referred to as the exchange interaction [119]. This interaction lifts the degeneracy of the fourfold exciton states, resulting in two bright states ($|\pm1\rangle$) and two dark states ($|\pm2\rangle$) [120], separated in energy by δ_0 (Fig. 2.4). The terms 'bright' and 'dark' refer to the fact that bright excitons can recombine radiatively, emitting photons with spin $|\pm1\rangle$, while the radiative recombination of dark states $|\pm2\rangle$ is forbidden by spin conservation.

In 'real-world' GaN/AlN SAQDs, the ideal hexagonal shape with C_{6v} symmetry is hardly observed. The elongation of the QD along different directions introduces anisotropy effects that fully lift the degeneracy, resulting in additional splittings δ_1 and δ_2 between bright and dark states. Dark states, being optically inactive, render δ_2 usually inaccessible in PL measurements. On the other hand, the bright state splitting, is readily observable in PL spectra. It is known as the fine structure splitting (FSS), denoted by $\delta_1 = \delta_{FSS}$, and typically amounts to a few meV for high-energy GaN QDs ($E_g > 4\,\text{eV}$) [121, 122]. Interestingly, the FSS exhibits a strong dependence on the QD size, decreasing as the QDs become larger. This trend contrasts with the commonly observed behavior in arsenide QDs [123, 124] and directly results from the quantum confined Stark effect (QCSE) discussed next.

2.2.3 Quantum confined Stark effect

The description provided so far overlooks a crucial aspect of the studied QDs inherent to III-N heterostructures grown along the wurtzite c-axis, which stems from the significant polarization field characteristic of these polar materials. The polarization, primarily aligned with the growth axis, leads to surface charge densities at each GaN/AlN interface [125]:

$$\sigma_{\mathrm{GaN/AlN}} = \left(\mathbf{P}_{\mathrm{sp}}^{\mathrm{GaN}} + \mathbf{P}_{\mathrm{pz}}^{\mathrm{GaN}} - \mathbf{P}_{\mathrm{sp}}^{\mathrm{AlN}} - \mathbf{P}_{\mathrm{pz}}^{\mathrm{AlN}}\right) \cdot \mathbf{n}_{\mathrm{GaN/AlN}}, \tag{2.7}$$

where $\mathbf{n}_{\mathrm{GaN/AlN}}$ is the unit vector normal to each interface and pointing outwards from the GaN. It is important to note that the AlN strain may differ at both interfaces, although both the buffer AlN [126, 127] and AlN spacer [128] are usually quasi-relaxed, with only a slight tensile strain remaining ($P_{\mathrm{pz}}^{\mathrm{AlN}} \sim 0$).

The surface charges lead to a significant built-in field within the QDs, which can be estimated in a 1D approximation along the c-axis [129]:

$$\mathbf{F}_{\mathrm{bi}} = \frac{\sigma_{\mathrm{GaN/AlN}}}{\epsilon_{\mathrm{QD}}} \cdot \hat{\mathbf{e}}_{\mathbf{z}}, \tag{2.8}$$

with $\mathbf{F}_{\mathrm{bi}}$ pointing toward the substrate for QDs grown with metallic polarity. Here, ϵ_{QD} denotes the GaN permittivity inside the QDs. While $\mathbf{F}_{\mathrm{bi}}$ is not uniform in practice [108, 125], the approximation holds well for flat QDs and is sufficient for first-order quantitative predictions. Experimentally, this built-in field has been estimated at 7-9 $\mathrm{MV \cdot cm^{-1}}$ [99, 113, 130]. Additionally, the GaN/AlN lattice mismatch combined to the QD geometry yields an in-plane $\mathbf{P}_{\mathrm{pz}}^{\mathrm{GaN}}$ component contributing to the lateral confinement of EHPs inside the QDs [108, 125].

These effects have profound implications for QD physics, as the built-in field generates band bending along the c-axis (see Fig. 2.5(a)), progressively reducing the exciton energy as the QD size increases. Equation 2.6 can be adapted to account for this bending [106]:

$$E_{\mathrm{X}} = E_{\mathrm{g}} + e_1 + h_1 + J_{eh} - eF_{\mathrm{bi}} h_{\mathrm{QD}}, \tag{2.9}$$

with e representing the elementary charge. The so-called Stark shift ($e\mathbf{F}_{\mathrm{bi}} h_{\mathrm{QD}}$) exhibits a linear dependence on the QD height, which can be evidenced by the observable redshift of the exciton PL line with increasing h_{QD}. The linear correlation is well established in experiments [99], where the AR tends to remain constant for QDs of different size originating from the same growth [131]. For large QDs with h_{QD} larger than the exciton Bohr radius[V], confinement effects are significantly reduced, making the Stark shift the primary mechanism for driving exciton energy.

[V] In the context of bulk SC, excitons are often approximated using a hydrogen-like model [132]. This model introduces an effective Bohr radius (a_{B}), which is related to the hydrogen Bohr radius ($a_0 \simeq 53\,\mathrm{pm}$) through the expression $a_{\mathrm{B}} = a_0 m_e \epsilon_r / \mu^*$. Here, ϵ_r denotes the relative permittivity of the medium (in this case, GaN), m_e is the electron's mass, and $\mu^* = m_e^* m_h^* / (m_e^* + m_h^*)$ represents the reduced mass. In bulk GaN, a_{B} is on the order of a few nm [133, 134].

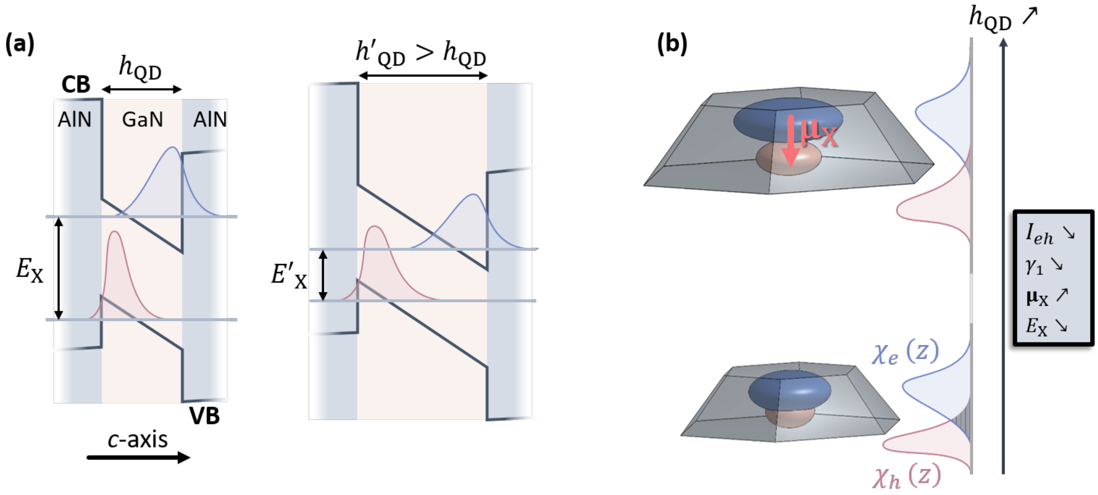

Figure 2.5: **(a)** Illustration of the band bending under the influence of QCSE for QDs of different size. **(a)** 3D representation of the electron-hole wavefunction separation due to QCSE.

The redshift in the PL features is accompanied by an increase of the radiative lifetime of EHPs which, together, constitute the quantum confined Stark effect (QCSE). This increased lifetime can be understood by observing that $\mathbf{F}_{\text{bi}}$ pushes electrons toward the apex of the QD pyramids while holes are confined at their bottom [108] (Fig. 2.2.3(b)). In other words, the built-in electric field leads to a separation of the electron and hole wavefunctions which increases with the QD height, as illustrated in Fig. 2.5.

The exciton radiative recombination rate is given by [135]:

$$\gamma_1 = \frac{n_{\text{GaN}} E_X^3 \mathscr{D}_X{}^2}{3\pi\epsilon_0 \hbar^4 c_0^3}, \tag{2.10}$$

where ϵ_0 and c_0 are the vacuum permittivity and the speed of light, respectively and $\mathscr{D}_X$ quantifies the overlap of electron and hole wavefunctions. Under weak lateral confinement, Eq. 2.10 can be simplified as:

$$\gamma_1 \propto E_X^3 |I_{eh}|^2, \tag{2.11}$$

which aligns well with experimental findings [130]. Here,

$$I_{eh}(z) = \int \chi_e(z)\chi_h(z)dz, \tag{2.12}$$

represents the overlap integral of the electron and hole vertical envelope wavefunctions. The influence of electron-hole separation on the exciton radiative lifetime $\tau_X^{\text{rad}} = 1/\gamma_1$ can be intuitively understood through Eq. 2.11. Notably, I_{eh} exhibits orders of magnitude variations when the height of the QD changes from a few to a few tens of nm leading to exciton lifetime variations from sub-ns to µs. This feature is analyzed in depth in Sect. 2.10.

$\mathscr{D}_\mathrm{X}$ is known as the exciton transition dipole moment, reflecting the probability of the exciton-to-ground-state transition, or exciton recombination. This term is connected to the oscillator strength (f_osc) commonly employed through $f_\mathrm{osc} \propto E_\mathrm{X}{\mathscr{D}_\mathrm{X}}^2$ [136]. It is essential not to confuse $\mathscr{D}_\mathrm{X}$ with the exciton dipole moment, defined as [137]:

$$\boldsymbol{\mu}_\mathrm{X} = \langle \Psi_h | \hat{\mathbf{z}} | \Psi_h \rangle - \langle \Psi_e | \hat{\mathbf{z}} | \Psi_e \rangle\,, \tag{2.13}$$

where $\hat{\mathbf{z}}$ represents the position operator along the c-axis. $\boldsymbol{\mu}_\mathrm{X}$ is linked to the classical notion of electronic dipole and quantifies the spatial separation of positive (hole) and negative (electron) charges. Its impact on QD optical properties is further explored in Sect. 2.7.

2.2.4 Photon statistics: the two-level model

Under low excitation power, the pump rate (π) of EHPs into the QDs decreases below the recombination rate of the exciton state, assumed to be equivalent to the radiative recombination rate ($\gamma_1 = 1/\tau_\mathrm{X}^\mathrm{rad}$). Non-radiative recombinations are implicitly neglected here, an assumption justified throughout the chapter. When $\pi \ll \gamma_1$, the probability of featuring multiple EHPs in the QD is effectively suppressed. In such a scenario, the system can be treated as a two-level system (TLS), comprising a ground $|1\rangle$ and an excited state $|0\rangle$ with populations $n_{0,1} \in [0,1]$. The notation emphasizes the number of EHPs (N_EHP) present in the QD, which characterizes the QD ground ($N_\mathrm{EHP} = 0$) and exciton state ($N_\mathrm{EHP} = 1$). This notation proves convenient when addressing multi-excitonic states ($N_\mathrm{EHP} > 1$) in Sect. 2.4. It should not be confused with the notations adopted in Subsect. 2.2.2, where the exciton states are defined by their TAM (m). Note that treating the QD as a TLS implicitly discards the subtleties related to its fine structure, a strong assumption that will be investigated further in this chapter.

A primary goal of QD physics is to utilize them as SPEs, where the generation of photons is ensured through the radiative recombination of the exciton state. To confirm the SPE-like nature of individual QDs, we must investigate their photon statistics, specifically the second-order photon intensity autocorrelation ($g^{(2)}(\tau)$) function. For a TLS, this is defined as [138]:

$$g^{(2)}_\mathrm{TLS}(t+\tau, t) = \frac{\langle a^\dagger(t) a^\dagger(t+\tau) a(t+\tau) a(t)\rangle}{\langle a^\dagger(t+\tau) a(t+\tau)\rangle \langle a^\dagger(t) a(t)\rangle} = \frac{\langle a^\dagger(t) a^\dagger(t+\tau) a(t+\tau) a(t)\rangle}{\langle I(t+\tau)\rangle \langle I(t)\rangle}, \tag{2.14}$$

where $a^\dagger$ and a represent the creation and annihilation operators, respectively. The photon intensity $I(t)$ is related to the exciton population through $I(t) = \gamma_1 \cdot n_1(t)$. $g^{(2)}_\mathrm{TLS}(t+\tau, t)$ represents the probability of photon emission at time $t+\tau$ considering a first photon emission occurred at time t. Under CW excitation, adopted for $g^{(2)}(\tau)$ measurements throughout the thesis, $\langle I(t)\rangle = \mathrm{cst} = I^\mathrm{ss} = \gamma_1 n_1^\mathrm{ss}$. The superscript 'ss' refers to the steady-state regime. Setting the origin at $t = 0$, Eq. 2.14 transforms into:

$$g^{(2)}_\mathrm{TLS}(\tau) = \frac{\gamma_1 n_1(\tau) I^\mathrm{ss}}{{I^\mathrm{ss}}^2} = \frac{n_1(\tau)}{n_1^\mathrm{ss}}, \tag{2.15}$$

where $n_1(\tau)$ is elucidated by considering the rate equation that defines the TLS dynamic:

$$\frac{\mathrm{d}n_1}{\mathrm{d}t} = -\gamma_1 n_1 + \pi n_0, \tag{2.16}$$

with $n_0 + n_1 = 1$. Solving the first-order differential equation with $n_1(t) = 0^{\mathrm{VI}}$ yields:

$$g^{(2)}_{\mathrm{TLS}}(\tau) = 1 - e^{-(\pi+\gamma_1)\tau}. \tag{2.17}$$

Experimentally, the $g^{(2)}(\tau)$ function is recorded, as detailed in Sect. 1.5, by measuring photons impinging at times t_1 and t_2 on two detectors, SPD_1 and SPD_2, respectively, with $\tau = t_2 - t_1$ the delay between two photon events. Owing to the symmetry of the setup, negative delays are also recorded, and Eq. 2.17 rewrites as:

$$g^{(2)}_{\mathrm{TLS}}(\tau) = 1 - e^{-(\pi+\gamma_1)|\tau|}. \tag{2.18}$$

An ideal SPE features a null probability to emit two photons simultaneously, as evidenced in Eq. 2.18 by $g^{(2)}_{\mathrm{TLS}}(0) = 0$. The single photon purity of a quantum emitter is thus benchmarked by evaluating its $g^{(2)}(0)$ value. For uncorrelated background emission, $g^{(2)}(0)$ is linked to the SNR (ρ_{SNR}) by [139]:

$$g^{(2)}(0) = 1 - \rho^2_{\mathrm{SNR}}, \tag{2.19}$$

where ρ_{SNR} is determined by the intensity of the analyzed signal divided by the total intensity. In the presence of a significant SNR Eq. 2.18 takes the form:

$$g^{(2)}_{\mathrm{noisy}}(\tau) = \rho^2_{\mathrm{SNR}}\left[g^{(2)}_{\mathrm{TLS}}(\tau) - 1\right] + 1 = 1 - \rho^2_{\mathrm{SNR}} e^{-(\pi+\gamma_1)\tau}. \tag{2.20}$$

This development can be generalized to the $g^{(2)}(\tau)$ function obtained in any framework.

2.3 Biexcitons

While our discussion was initially focused on exciton states, it is crucial to acknowledge that the occupancy of a QD is not limited to a single EHP. From the standpoint of the single-particle perspective, a QD can potentially accommodate numerous electrons and holes, correlating with the number of confined levels available for each carrier. In the next two sections, we delve into the physics governing such multi-excitonic states with a primary emphasis on the biexciton state, composed of two EHPs. This state holds particular significance in quantum applications, such as the generation of single photons and entangled photon pairs [140, 141], and exhibits intricate features with the exciton.

[VI] There is no EHP in the QD following exciton recombination.

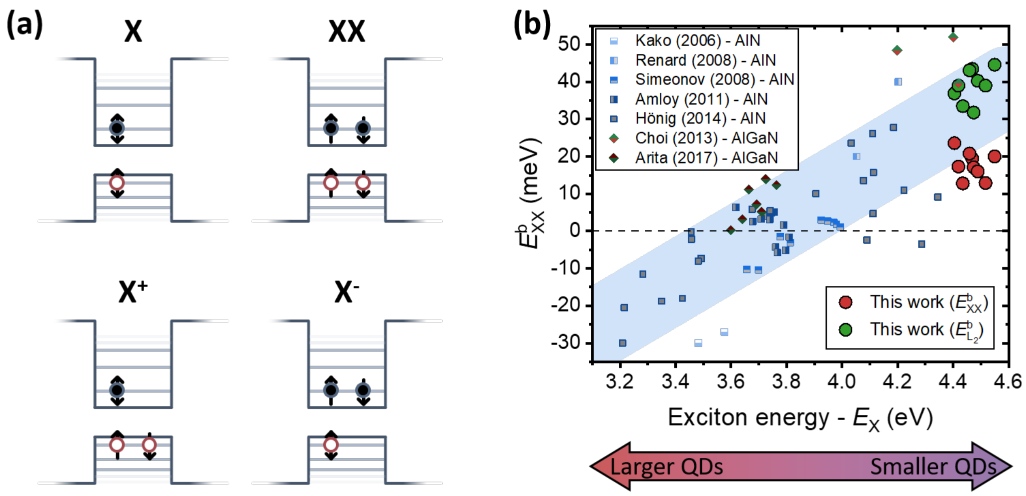

Figure 2.6: **(a)** Schematic filling of the QD levels from one to two EHPs. Adding electrons or holes would start populating higher excited states. Doubly-ended arrows are used when either spin orientation is possible **(b)** Evolution of the biexciton binding energy as a function of exciton energy, for GaN/Al(Ga)N QDs. Alongside datapoints obtained from this study, experimental outcomes are aggregated from various sources [122, 142–148]. The shaded blue area is a guide to the eye. The distinction between E^b_{XX} and $E^b_{L_2}$ is discussed in Sect. 2.8.

2.3.1 Biexciton binding energy

During the QD filling process that leads to the formation of multi-excitonic states, each electron or hole state[VII] can accommodate two particles with antiparallel spin to minimize the overall energy, as depicted in Fig. 2.6(a) for charged excitons[VIII] and biexcitons. For a more accurate portrayal of these multi-excitonic states, interactions between particles, akin to those in excitons, must be considered. Setting aside the exchange interaction, the energy of the ground biexciton (composed of two EHPs) can be expressed as:

$$E_{XX} = 2E_g + 2e_1 + 2h_1 + J'_{eh} + J'_{hh} + J'_{ee}, \tag{2.21}$$

where the last terms account for the Coulomb interaction between each type of charges. Notably, E_{XX} is not simply twice the exciton energy. The energy difference between two virtual exciton states and the biexciton state, denoted as the biexciton binding energy (E^b_{XX}):

$$E^b_{XX} = 2E_X - E_{XX}, \tag{2.22}$$

represents the gain in energy resulting from the combination of the two separate excitons. It is essential to acknowledge that under 3D confinement E^b_{XX} may not necessarily be positive, and the occurrence of an 'antibinding' biexciton ($E^b_{XX} < 0$) is possible, owing to the confinement

---

[VII] Let us recall that each p-, d-, etc., shell comprises multiple electron or hole states.

[VIII] A charged exciton is formed by the combination of an EHP with an additional electron (X^-) or hole (X^+).

of EHP in QDs. In GaN/AlN QDs, $E^{\mathrm{b}}_{\mathrm{XX}}$ varies within the range of tens of meV, displaying an antibinding to binding transition experimentally observed around an exciton energy of approximately 3.7 eV, as depicted in Fig. 2.6(b). This feature arises due to the QCSE: decreasing the height of a QD strongly enhances the positive Coulomb interaction between charges of opposite sign by increasing the overlap of electron-hole wavefunctions. In absence of an in-plane built-in field, the lateral confinement of carriers is much less impacted by variations in the QD diameter. Consequently, the binding energy increases inversely with the size of the QD. The concept of binding energy can be extended to higher multi-excitonic states ($N_{\mathrm{EHP}} > 2$), although these are scarcely observed in CW PL experiments and will not receive a specific attention in the following.

We should emphasize that Eq. 2.21 does not incorporate the QCSE discussed in Subsect. 2.2.3 for the exciton state (Eq. 2.9). In practice, this consideration extends to higher multiexcitonic states, necessitating an adjustment of Eq. 2.21 for GaN/AlN QDs to accommodate the impact of band bending. This influence is implicit in Eq. 2.22. It is noteworthy that the presence of multiple EHPs within the QD can result in the screening of the built-in field [113, 149, 150], causing the binding energy to manifest as a complex interplay of multiple factors.

2.3.2 Biexciton cascade

The ability to manipulate the biexciton binding energy through the QCSE stands out as a critical characteristic of GaN/AlN QDs. This parameter is theoretically adjustable by carefully controlling the growth conditions to achieve QDs with the desired size. In order to understand the caveats behind the applications of the biexciton for quantum applications, it is essential to delve into the specificities of its recombination dynamics.

As previously mentioned, the commonly accepted model pictures the ground state of the biexciton as two EHPs, where electrons (and holes) with opposite spins fully occupy their respective ground states (see Fig. 2.6(a)). Due to these closed shells, this ground state is fully degenerate [120], exhibiting zero TAM ($m = 0$). As a result, it can only undergo radiative recombination by transitioning into a state with $m \pm 1$, specifically, the exciton bright states. The biexciton and subsequent exciton recombinations collectively constitute the radiative biexciton cascade illustrated in Fig. 2.7(a). In the absence of FSS (QD with C_{6v} symmetry), the photons emitted through the biexciton cascade are circularly polarized, with biexciton and exciton recombinations producing photons of opposite spin [123, 151]:

$$|\mathrm{XX}\rangle \xrightarrow{\sigma_{\pm}} |\pm 1\rangle \xrightarrow{\sigma_{\mp}} |\mathrm{GS}\rangle\,. \tag{2.23}$$

Here, $|\mathrm{GS}\rangle$ stands for the QD ground state (empty QD). Introducing an FSS through QD asymmetry alters the biexciton cascade, resulting in pairs of linearly polarized photons (π_x, π_y):

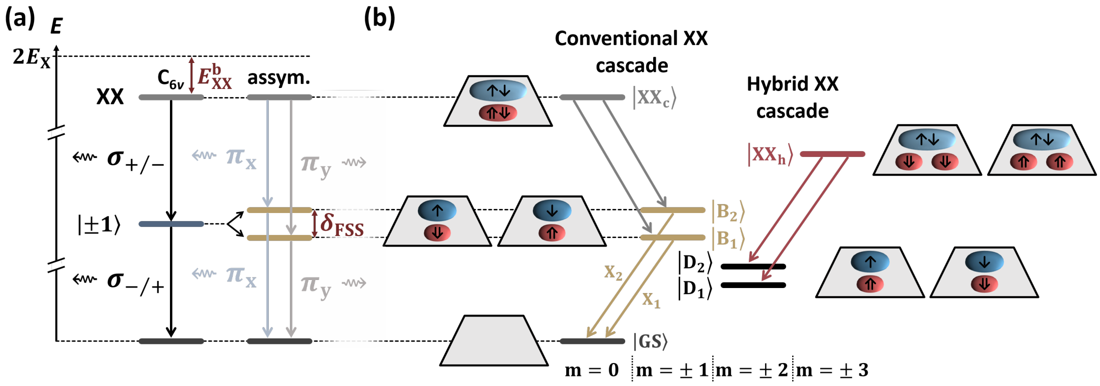

Figure 2.7: **(a)** Influence of the fine structure splitting (FSS) on the biexciton cascade. The diagram is inspired by [123]. **(b)** Schematic differentiation between the conventional and hybrid biexciton cascades. The electron (blue) and hole (red) wavefunctions are depicted for each state, and their spins are represented by ↑,↓ and ⇑,⇓, respectively. Excitonic transitions are denoted as X_1 and X_2, following the notation used for describing photoluminescence spectra. $|XX_c\rangle$ and $|XX_h\rangle$ represent the conventional and hybrid biexciton states, respectively.

$$\begin{aligned} &|XX\rangle \xrightarrow{\pi_x} |B_2\rangle \xrightarrow{\pi_x} |GS\rangle\,, \\ &|XX\rangle \xrightarrow{\pi_y} |B_1\rangle \xrightarrow{\pi_y} |GS\rangle\,, \end{aligned} \tag{2.24}$$

where the polarization axes x and y are parallel and perpendicular to the QD anisotropy axis, respectively [120]. It is noteworthy that this description does not account for an intermediate polarization state, resulting in an abrupt transition between circularly and linearly polarized light when anisotropy effects are introduced. A transition is observed in practice when an FSS smaller than the exciton linewidth causes the spectral overlap of PL originating from each bright exciton state, effectively reducing the degree of linear polarization (DLP) of each line.

While the biexciton cascade is envisioned as a fundamental component for generating entangled photon pairs [140, 152], the FSS generally proves detrimental for quantum applications. This is intuitive as the splitting between bright states compromises photon indistinguishability by generating spectrally distinct emission lines [153]. Achieving the generation of energy and polarization entangled photon pairs necessitates simultaneously nullifying the biexciton binding energy and exciton FSS [141, 154], a task that, at the time of writing, remains unfulfilled, despite promising photon statistics features reported for QDs with binding energies below the exciton linewidth [155]. It is worth noting that alternative schemes have been proposed to generate entangled photon pairs from QDs exhibiting a non-zero FSS, such as 'time reordering' [156, 157], although these schemes still rely on the cancellation of the biexciton binding energy [152].

In contrast to earlier considerations, applications relying on SPEs, such as quantum key distribution (QKD) in the BB84 protocol [158], demand sources with high single-photon purity. Leveraging exciton recombination for photon generation becomes more advantageous when the QD possesses a larger biexciton binding energy, thus minimizing the chances of spurious detection of photons originating from the biexciton recombination channel [3]. This requirement becomes even more critical at RT, where the broadening of emission lines further amplifies the exciton/biexciton overlap [143]. QDs with substantial $E_{\mathrm{XX}}^{\mathrm{b}}$ values are typically found at both ends of the E_{X} spectral range (Fig. 2.6(b)). However, low-energy QDs are characterized by low recombination rates (see Subsect. 2.2.3), which limits their attractiveness. In this work, individual high-energy/small-size QDs were investigated, typically exhibiting positive binding energies in the tens of meV range.

Surprisingly, early theoretical computations performed within the conventional biexciton framework described earlier struggled to anticipate positive binding energies of this magnitude [64, 143]. In these calculations, repulsive Coulomb interactions between identical charges consistently overshadowed the electron-hole Coulomb attraction, leading to predictions of strongly antibinding (for large QDs) or nearly non-binding (for small QDs) biexciton states. Given this discrepancy, Hönig *et al.* [148] introduced an alternative model for characterizing the biexciton ground state, known as the hybrid biexciton.

In this novel conceptual framework, the authors suggested that weak lateral confinement conditions, characteristic of flat QDs with low AR, could promote the spatial separation of hole wavefunctions. This separation is favored by the large effective mass of heavy-holes, resulting in their reduced effective Bohr radius. The pyramidal shape of GaN/AlN SAQDs could additionally contribute to favoring this spatial separation, as holes are pushed toward the pyramid base, with a large diameter of tens of nm. According to this model, electron wavefunctions remain overlapped, with electrons confined at the QD apex (see Fig. 2.7)(b)). Theoretical simulations conducted within this hybrid biexciton model, considering an AR ranging between 1:5 and 1:10, yielded results consistent with experimental observations, notably reproducing the $E_{\mathrm{XX}}^{\mathrm{b}}$ zero-crossing evidenced in Fig. 2.6(b). The transition from the conventional to the hybrid ground biexciton state is ultimately dictated by lateral confinement and, consequently, by the AR.

Owing to their holes with parallel spins, hybrid biexciton exhibit a TAM of $m = \pm 3$ translating into a distinct biexciton cascade, as depicted by red arrows in Fig. 2.7(b). The radiative recombination of hybrid biexcitons ($|\mathrm{XX_h}\rangle$) proceeds as follows:

$$\begin{aligned} &|\mathrm{XX_h}\rangle \xrightarrow{\pi_x} |\mathrm{D_2}\rangle\,, \\ &|\mathrm{XX_h}\rangle \xrightarrow{\pi_y} |\mathrm{D_1}\rangle\,, \end{aligned} \tag{2.25}$$

notably transitioning toward either of the exciton dark states, thereby impeding the subsequent exciton radiative recombination depicted in the conventional biexciton cascade.

At this point of the discussion, it is appropriate to propose a preliminary visualization of how the discussed physics manifests into PL spectra. To this end, a PL spectrum acquired

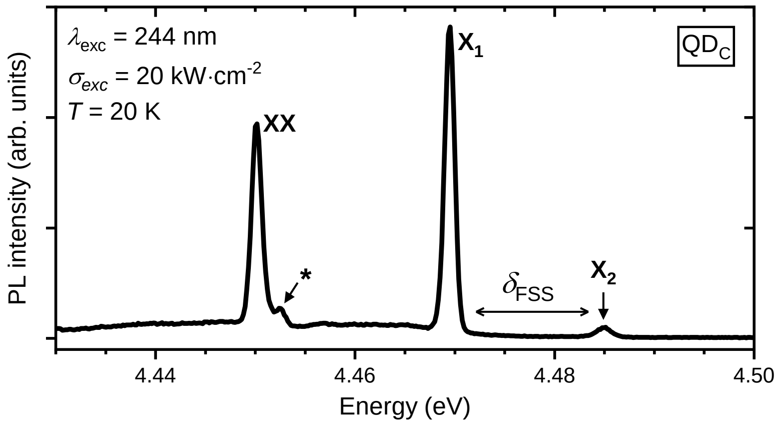

Figure 2.8: PL spectrum of on individual QD labeled QD_C. The QD numbering is aligned on the notations we used in [24] and does not adhere to a chronological sequence. X_1 and X_2 denote the recombination peaks associated with transitions from the $|B_1\rangle$ and $|B_2\rangle$ states, respectively. XX corresponds to biexciton recombination, as does the feature marked by an asterisk (*). A more detailed analysis of the spectral lines is provided in Sect. 2.8.

from a single QD is depicted in Fig. 2.8, clearly showing two exciton lines (X_1 and X_2) and a single bright biexciton (XX) line. We should mention that the high-energy tail of the XX peak, indicated by an asterisk, associates with the missing biexciton line, although a clear explanation of these PL features is deferred to Sect. 2.8.

It is crucial to note that, at this stage, the QD recombination scheme is essentially incomplete, as inter-exciton and biexciton transitions are optically forbidden. For a comprehensive understanding of the QD dynamics, the exciton-phonon interaction must be considered, as discussed in Sect. 2.5.

2.4 Multiexcitonic recombination dynamics

2.4.1 Theoretical framework

However, to intuitively understand the recombination dynamics of multiexcitons, we can initially disregard phonon-related processes and treat each i^{th} exciton as a single state characterized solely by its number of EHPs ($N_{\text{EHP}} = i$ for state $|i\rangle$). Under CW excitation, each state connects to its 'nearest neighbor' $|i \pm 1\rangle$ through a decay rate γ_i and a pump rate π dictated by the excitation power density (see Fig. 2.9(a) for illustration).

Consequently, the QD dynamics is described by the following system:

$$\begin{cases} \frac{\mathrm{d}n_i}{\mathrm{d}t} = \pi n_{i-1} - (\pi + \gamma_i) n_i + \gamma_{i+1} n_{i+1} \ \forall \ i \geq 1, \\ \frac{\mathrm{d}n_0}{\mathrm{d}t} = -\pi n_0 + \gamma_1 n_1, \\ \sum_{i=0}^{+\infty} n_i = 1, \end{cases} \tag{2.26}$$

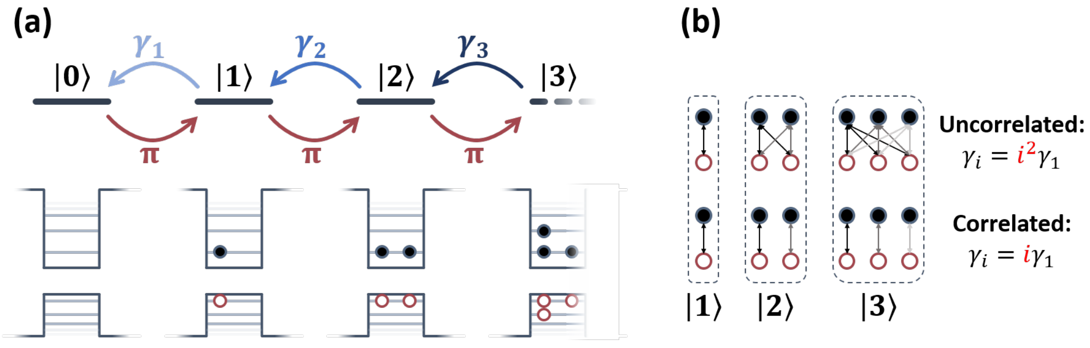

Figure 2.9: **(a)**Illustration of the multiexcitonic recombination dynamics under CW excitation. **(b)** Schematic of the decay rate scaling in uncorrelated and correlated systems, respectively. Arrows represent allowed recombination channels.

where n_i represents the occupancy of $|i\rangle$. Under CW excitation (steady-state 'ss' regime with $\mathrm{d}n_i/\mathrm{d}t = 0 \ \forall\ i \ \in \mathbb{N}$), there exists an analytical solution[IX], which reads:

$$n_i^{\mathrm{ss}} = c\prod_{k=0}^{i}\frac{\pi}{\gamma_k}, \tag{2.27}$$

with the normalization factor $c^{-1} = \sum_{i=0}^{+\infty}\left(\prod_{k=0}^{i}\pi/\gamma_k\right)$. Eq. 2.27 features an infinite number of variables, which makes it unsuitable for empirical studies. To compare our model with experimental data, we need to make assumptions about how the coefficients γ_i scale. In an uncorrelated system (e.g., electrons and holes in the bulk), γ_i is simply driven by the number of charges, which would translate here into:

$$\gamma_i = i^2\gamma_1, \tag{2.28}$$

as depicted in Fig. 2.9(b). In a QD, however, the electron and hole wavefunctions cannot be treated separately, and selection rules apply such that we can genuinely anticipate [159]:

$$\gamma_i = i\gamma_1. \tag{2.29}$$

This assumption does not account for the variations in electron-hole wavefunction overlap, which can drastically affect the decay rates. For instance, γ_2/γ_1 ratios ranging between 1 and 2 have been predicted in various QD systems [160], while experimentally, biexciton decay rates close to the exciton lifetime have been reported for CdSe QDs [161]. Although Eq. 2.29 is often over-simplistic, it has proven acceptable in the description of multiexcitonic recombination dynamics in various systems, as for state-of-the-art InAs/GaAs SAQDs [159], which motivates

---

[IX] Outline of the inductive proof: if Eq. 2.27 holds $\forall\ k \leq i$, then $n_{i+1} = c/\gamma_{i+1}\cdot[\pi/\gamma_i\cdot(\gamma_i+\pi)-\pi]\prod_{k=0}^{i-1}\pi/\gamma_k = c\prod_{k=0}^{i+1}\pi/\gamma_k$ and Eq. also holds for $k = n+1$.

its use as a starting point.

2.4.2 Caveats of the linear scaling assumption

Following Eq. 2.29, Eq. 2.27 yields a Poisson distribution:

$$n_i^{\mathrm{ss}} = \frac{\overline{\mu}^i e^{-\overline{\mu}}}{i!}, \tag{2.30}$$

in which $\overline{\mu} = \pi/\gamma_1$ represents the average number of EHPs and is denoted as the mean occupation number. Equation 2.29 assumes purely radiative excitonic recombination ($\gamma_i = \gamma_i^{\mathrm{rad}}$), allowing the steady-state PL intensity (I_i^{ss}) for a given state $|i\rangle$ to be expressed as:

$$I_i^{\mathrm{ss}} = \gamma_i n_i^{\mathrm{ss}} = \gamma_1 \frac{\overline{\mu}^i e^{-\overline{\mu}}}{(i-1)!}. \tag{2.31}$$

Given that the pump rate π is proportional to the excitation power, Eq. 2.31 can be rewritten for fitting purposes as:

$$I_i^{\mathrm{ss}}(P_{\mathrm{exc}}) = I_i^0 \left(\frac{P_{\mathrm{exc}}}{P_0} \right)^{\tilde{n}_i} \exp\left(-\frac{P_{\mathrm{exc}}}{P_0} \right), \tag{2.32}$$

where P_0 and $\tilde{n}_i$ are fitting parameters, with the scaling factor $\tilde{n}_i = i$ in the ideal case. In theory:

$$I_i^0 = \frac{I_1^0}{(i-1)!}, \tag{2.33}$$

where the parameter $I_1^0 = \eta_{\mathrm{setup}} \gamma_1$ accounts for the setup efficiency (η_{setup}, refer to Sec. 1.3). However, practically, I_i^0 parameters are often decoupled to remove constraints on the fitting procedure.

Notably, Eq. 2.31 predicts scaling factors of $\tilde{n}_{\mathrm{X}} = 1$ and $\tilde{n}_{\mathrm{XX}} = 2$ for exciton and biexciton lines, respectively (refer to Fig. 2.10(a)). This scaling pattern has been consistently observed in various studies, encompassing nanowire GaN/Al(Ga)N QDs [144, 147], GaN/AlN SAQDs [142, 145, 146], and QDs induced by interface fluctuations [122]. These observations, spanning energies E_{X} between 3 and 4.5 eV, suggest a potential 'universal feature,' corroborating the validity of this model. Nonetheless, there are several caveats in its application that we address in the following.

One notable observation pertains to the scaling of multiexcitonic decay rates. Although we assumed $\gamma_i = i\gamma_1$ in deriving Eq. 2.32, it is worth noting that a simple proportionality rule ($\gamma_i = \alpha \cdot i\gamma_1$) is sufficient to retrieve the same relation, with the proportionality factor α concealed within the fitting parameter P_0. Therefore, empirically determining the correct scaling factor does not automatically prove the validity of Eq. 2.29. The model also anticipates a triexciton line distinctly visible at $P_{\mathrm{exc}} = P_0$, with $I_1(P_0) = I_2(P_0) = 0.5 I_3(P_0)$. However, as of our current

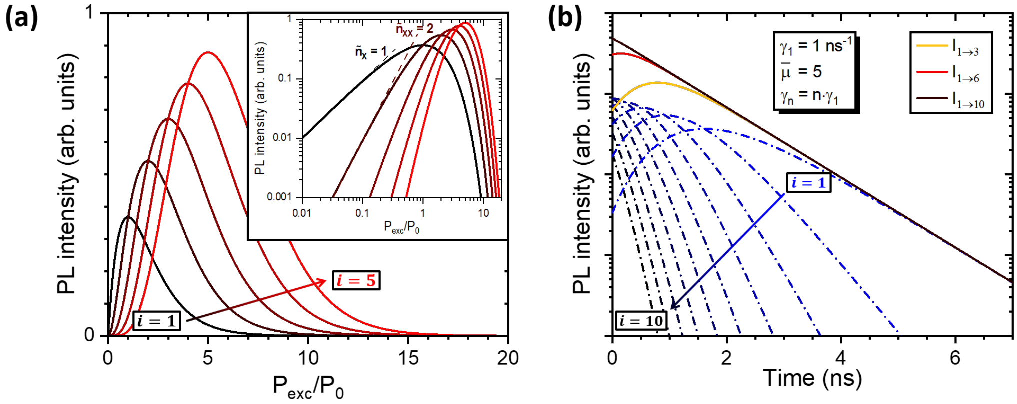

Figure 2.10: **(a)** Simulated power-dependent PL of different QD multiexcitonic states (from $i = 1$ to 5) under CW excitation. The inset depicts the same results on a logarithmic scale, highlighting how the initial slopes align with the scaling factor associated with each excitonic state. **(b)** Visualization of the TRPL transient predicted by Eq. 2.37 for a mean occupation number $\overline{\mu} = 5$. Dash-dotted lines represent the individual transients of the initial ten multiexcitonic states, while solid lines illustrate the transient resulting from the combination of 3, 5, and 10 excitonic lines, respectively. The predicted monoexponential decay is effectively replicated by combining 10 lines.

knowledge, such behavior has never been reported for GaN/AlN QDs. Additionally, reports of scaling behaviors deviating from the aforementioned prediction have been documented [148, 162, 163], further challenging the asserted ’universality.’ Explanations for this inconsistency are further explored in the context of the hybrid biexciton framework in Sect. 2.5.3.

Another limitation arises when applying this linear scaling assumption to pulsed excitation. Under such experimental conditions, a rapid, high-energy pulse initially generates a substantial number of EHPs within the QD, subsequently undergoing recombination in a system permanently out of equilibrium. The initial generation of EHPs is typically assumed to follow a Poisson distribution [159, 164, 165]. This outcome can be retrieved within the framework of Eq. 2.26, assuming a pump rate significantly larger than multiexcitonic decay rates ($\pi \gg \gamma_i$) and a gate profile for the pulse. For the duration of the pulse, we can write:

$$\begin{cases} \frac{\mathrm{d}n_i}{\mathrm{d}t} = \pi n_{i-1} - \pi n_i \ \forall \ i \geq 1, \\ \frac{\mathrm{d}n_0}{\mathrm{d}t} = -\pi n_0, \\ \sum_{i=0}^{+\infty} n_i = 1. \end{cases} \tag{2.34}$$

Assuming solutions of the form $n_i(t) = A_i t^i e^{-\pi t}$ yields $A_i = A_0 \pi / i$, with $A_0 = 1$, leading to the recovery of a Poisson distribution:

$$n_i = \frac{\overline{\mu}^i e^{-\overline{\mu}}}{i!}, \tag{2.35}$$

where $\overline{\mu}(\tau) = \pi\tau$ is a function of the pump rate and the pulse duration τ. In this context, the hypothesis of an initial Poisson distribution holds for a pulse duration shorter than the decay rates of the excited states significantly populated at time $t = \tau$. After the pulse, the system can only transition toward lower excited states, following:

$$\begin{cases} \frac{\mathrm{d}n_i}{\mathrm{d}t} = -\gamma_i n_i + \gamma_{i+1} n_{i+1} \ \forall \ i \geq 1, \\ \frac{\mathrm{d}n_0}{\mathrm{d}t} = -\gamma_1 n_1, \\ \sum_{i=0}^{+\infty} n_i = 1. \end{cases} \tag{2.36}$$

Under the linear scaling assumption (Eq. 2.29), the solution to Eq. 2.36 is expressed [159, 162] as:

$$n_i(t) = \exp\left(-\overline{\mu} e^{-\gamma_1 t}\right)\left(\overline{\mu} e^{-\gamma_1 t}\right)^i / i!, \tag{2.37}$$

where we recognise a Poisson distribution with a moving average $\overline{\mu}^*(t) = \overline{\mu} e^{-\gamma_1 t}$. In TRPL performed on an ensemble of QDs, the luminescence resulting from individual excitonic states cannot be resolved, and transients are treated as an overlap between all emission lines. This results in a PL intensity $I_{\mathrm{TRPL}}(t)$ given by[X]:

$$I_{\mathrm{TRPL}}(t) = \sum_{i=1}^{+\infty} \gamma_i n_i(t) = \gamma_1 e^{-\overline{\mu}^*} \sum_{i=1}^{+\infty} \frac{i\, \overline{\mu}^{*\,i}}{i!} = \gamma_1 \overline{\mu}^* e^{-\gamma_1 t}. \tag{2.38}$$

Therefore, the linear assumption predicts a monoexponential trend (see Fig.2.10(b)) strongly contradicting experimental observations at high excitation power, which clearly exhibit supra-linear scaling of the radiative recombination rates, as discussed in detail in Sect. 2.10. Supra-linear scaling is not entirely unexpected and may be explained within the framework of purely radiative recombinations. For example, Shulenberger *et al.* [166] observed a γ_2/γ_1 ratio in CdSe nanocrystals (NCs) of approximately 4, justified by bright- and dark-states spin mixing, as further discussed in Subsect. 2.5.3. They subsequently recorded a γ_3/γ_2 ratio of approximately 1, attributed to pure '*s*-like'[XI] recombination of the triexciton state, highlighting the complexity of radiative recombination processes, strongly dependent on electron-hole wavefunction overlap and selection rules.

As a final note, we should mention that exhaustive studies on NC QDs [167] have emphasized the significance of non-radiative Auger recombination processes in the luminescence quenching of multiexcitonic states in such systems. The term 'Auger' refers to the Auger-Meitner (AM) effect [168, 169], wherein the excess energy resulting from an EHP recombination can be transferred to another carrier without photon emission [167]. In this context, the recombination rates γ_i encompass both a radiative γ_i^{rad} and a non-radiative AM-related γ_i^{AM} compo-

---

[X] Result obtained by noticing that: $\sum_{i=1}^{+\infty} i\, \overline{\mu}^{*\,i}/i! = \overline{\mu}^* \sum_{i=0}^{+\infty} \frac{\mathrm{d}\left(\overline{\mu}^{*\,i}\right)}{\mathrm{d}\overline{\mu}^*}/i! = \overline{\mu}^* \frac{\mathrm{d}\left(\sum_{i=0}^{+\infty} \overline{\mu}^{*\,i}/i!\right)}{\mathrm{d}\overline{\mu}^*} = \overline{\mu}^* \frac{\mathrm{d}\left(e^{\overline{\mu}^*}\right)}{\mathrm{d}\overline{\mu}^*} = \overline{\mu}^* e^{\overline{\mu}^*}$.

[XI] The triexciton consists of three EHPs, with two EHPs in the '*s*-type' ground state and one in the first excited '*p*-type' shell. If radiative recombination involving *p*-type charges is negligible, the process is described as purely *s*-like, and vice versa.

nent[XII]. γ_i^{AM} features a quadratic ($\propto N_{\mathrm{EHP}}{}^2$ [164]) to cubic or 'statistical' scaling ($\propto N_{\mathrm{EHP}}{}^3$ or $\propto N_{\mathrm{EHP}}{}^2(N_{\mathrm{EHP}}-1)$ [171, 172]) depending on the QD size.

It is essential to note that typical CdSe or PbSe NC QDs differ in many ways from the SAQDs studied in this work. Notable peculiarities of GaN/AlN SAQDs include the absence of surface states, the presence of a strong built-in field, a distinct QD geometry and wider (GaN and AlN) bandgaps. Additionally, it is worth noting that AM processes have not been extensively studied in GaN QDs so far. Nonetheless, we should remain mindful of the existence of such non-radiative recombination channels when analyzing experimental results.

2.4.3 Second-order exciton autocorrelation function

Closed-form approximation:

Despite the mentioned limitations, the linear assumption (Eq. 2.29) remains appealing due to its simplicity and reasonable predictions under low excitation power, where the impact of diverging high-order multiexcitonic recombination rates is minimized. In the context of $g^{(2)}(\tau)$ measurements, avoiding an overparameterized model is crucial for extracting relevant features from experimental data. Hence, we initially adhered to this framework, choosing to discuss our results considering its inherent limitations.

The $g^{(2)}(\tau)$ function computed in Subsect. 2.2.4 is inadequate to reproduce all experimentally observed features, particularly when increasing the excitation power beyond a mean occupation number of $\overline{\mu} = 1$. Consequently, the exciton $g^{(2)}(\tau)$ function ($g_{\mathrm{X}}^{(2)}(\tau)$) is refined in the multiexcitonic model [173, 174], by solving the system in Eq. 2.26 under the condition $n_0(0) = 1$. Despite the substantial simplification assumed, obtaining an analytic solution for the $g^{(2)}(\tau)$ function remains challenging. Therefore, we resorted to the closed-form approximation derived by C. Kindel [162] through numerical analysis:

$$g_{\mathrm{X}}^{(2)}(\tau) = \left(1 - e^{-\gamma_1|\tau|}\right)\exp\left[\overline{\mu}e^{-\gamma_1|\tau|}\right]. \tag{2.39}$$

In the low-excitation regime ($\overline{\mu} < 1$), Eq. 2.39 closely reproduces the antibunching feature characteristic of a TLS system (see Eq. 2.18). The discrepancy arises when $\overline{\mu} > 1$ (see Fig. 2.11), i.e., when higher multiexcitonic states start to be populated. Under such conditions, Eq. 2.39 features a maximum $e^{\overline{\mu}-1}/\overline{\mu}$ at $|\tau| = \ln\left(\frac{\overline{\mu}}{\overline{\mu}-1}\right)/\gamma_1$.

This can be intuitively understood by recalling that $g_{\mathrm{X}}^{(2)}(\tau)$is essentially driven by the occupancy probability of the exciton state: $g_{\mathrm{X}}^{(2)}(\tau) = n_1(\tau)/n_1(\pm\infty)$. When the QD is on average populated by multiple EHPs (i.e., when $\overline{\mu} \geq 2$), it becomes more likely for the QD to experience a fast repopulation with a subsequent exciton recombination ($|\mathrm{GS}\rangle \rightarrow |\mathrm{X}\rangle \rightarrow |\mathrm{GS}\rangle$) than to undergo multiple successive EHP recombinations (e.g., ($|\mathrm{XX}\rangle \rightarrow |\mathrm{X}\rangle \rightarrow |\mathrm{GS}\rangle$). The higher probability

---

[XII] The 'AM' superscript is employed here to acknowledge L. Meitner's contribution to the discovery of this effect [170]. Henceforth, the acronym 'AM' will be used instead of the more frequent term 'Auger'.

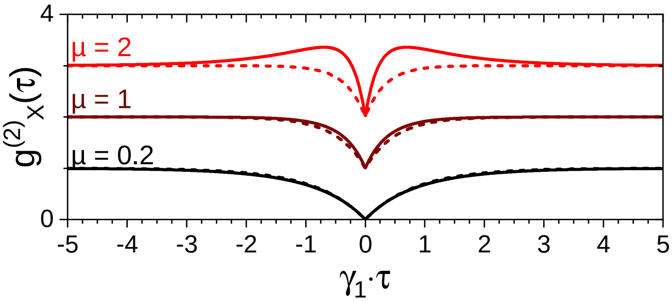

Figure 2.11: Simulated exciton $g^{(2)}(\tau)$ functions for $\overline{\mu} = 0.2$, 1 and 2, stacked with an arbitrary offset. $g^{(2)}_{\mathrm{TLS}}(\tau)$is plotted for reference (dashed lines) with the same mean occupation values.

of recording a second exciton recombination shortly after a first event manifests itself as a bunching in the $g^{(2)}_{\mathrm{X}}(\tau)$function, whose amplitude increases with the mean occupation number.

The three-level approximation:

Despite the appealing simplicity of the above framework, the statistic described though Eq. 2.39 is expected to markedly deviate from empirical observations in QD systems where the linear scaling of multiexcitonic recombination rates ($\gamma_i = i\gamma_1$) is not upheld. In scenarios where $\gamma_2 \gg \gamma_1$, higher-order multiexcitonic states have minimal impact on exciton statistics under low excitation power, effectively reducing the QD to a three-level system comprising the ground, the exciton and the biexciton states.

Within this framework, the system of rate equations governing the QD dynamics is expressed as:

$$\mathrm{d}_t\mathbf{n} = \mathrm{d}_t \begin{pmatrix} n_0 \\ n_1 \\ n_2 \end{pmatrix} = \begin{pmatrix} -\pi & \gamma_1 & 0 \\ \pi & -(\pi+\gamma_1) & \gamma_2 \\ 0 & \gamma_1 & -\gamma_2 \end{pmatrix} \cdot \mathbf{n} = \boldsymbol{M} \cdot \mathbf{n}, \tag{2.40}$$

This system is solved analytically by determining the eigenvalues λ of the matrix $\boldsymbol{M}$, (i.e, by posing $\det\{\boldsymbol{M} - \lambda\mathbb{1}\} = 0$). Subsequently, the occupancy probabilities are derived as:

$$n_i(t) = a_{i1} e^{-\gamma_1^{\mathrm{d}} t} + a_{i2} e^{-\gamma_2^{\mathrm{d}} t} + a_{i3}, \tag{2.41}$$

where $\gamma^{\mathrm{d}}_{1,2} = \lambda_{1,2}$ represent the characteristic decay rates of the system and $a_{i,j}$ are normalization parameters. Solving:

$$\det\{\lambda\mathbb{1} - \boldsymbol{M}\} = \lambda^3 + \lambda^2(2\pi + \gamma_1 + \gamma_2) + \lambda(\pi^2 + \pi\gamma_2 + \gamma_1\gamma_2) = 0, \tag{2.42}$$

yields:

$$\gamma_{1,2}^{\mathrm{d}} = \frac{A' \pm B'}{2}, \tag{2.43}$$

with:

$$\begin{aligned} A' &= 2\pi + \gamma_1 + \gamma_2, \\ B' &= \sqrt{(\gamma_1 - \gamma_2)^2 + 4\pi\gamma_1}. \end{aligned} \tag{2.44}$$

As detailed in Subsect. 2.2.4, the exciton $g^{(2)}(\tau)$ function is obtained through:

$$g_{\mathrm{X}}^{(2)}(\tau) = \frac{n_1(|\tau|)}{n_1(+\infty)} = \frac{n_1(|\tau|)}{a_{13}}, \tag{2.45}$$

using the initial conditions:

$$\begin{cases} n_1(0) = 0 = a_{11} + a_{12} + a_{13}, \\ \mathrm{d}_t n_1(0) = \pi n_0(0) - \gamma_1 n_1(0) = \pi = -\gamma_1^{\mathrm{d}} a_{11} - \gamma_2^{\mathrm{d}} a_{12}, \end{cases} \tag{2.46}$$

where a_{13} is additionally determined by solving Eq. 2.40 in the steady state ($\mathrm{d}_t \mathbf{n} = 0$), yielding:

$$a_{13} = \left(\gamma_1/\pi + 1 + \pi/\gamma_2\right)^{-1}. \tag{2.47}$$

As a result, the exciton $g^{(2)}(\tau)$ function is given by:

$$g_{\mathrm{X}}^{(2)}(\tau) = 1 + C_1 e^{-\gamma_1^{\mathrm{d}}|\tau|} + C_2 e^{-\gamma_2^{\mathrm{d}}|\tau|}, \tag{2.48}$$

where:

$$\begin{aligned} C_1 &= \frac{(\gamma_1 + \pi + \pi^2/\gamma_2) - \gamma_2^{\mathrm{d}}}{B'}, \\ C_2 &= \frac{\gamma_1^{\mathrm{d}} - (\gamma_1 + \pi + \pi^2/\gamma_2)}{B'}. \end{aligned} \tag{2.49}$$

In contrast to Eq. 2.39, Eq. 2.48 introduces an additional fitting parameter (γ_2) which may become crucial when the behavior of the system diverges from the linear approximation (Eq. 2.29). Both models are applied to experimental data and discussed in Sect. 2.9. It is worth noting that while the three-level system outlined here shares mathematical similarities with the framework used to characterize PD dynamics (see Sect. 3.1.5), their underlying physics diverges significantly. Thus, it is crucial to recognize that a strong correlation between the chosen $g^{(2)}(\tau)$ model and the experimental dataset does not automatically validate the model itself.

2.5 Exciton-phonon interactions

So far, QDs have been analyzed within a framework that isolates them from their surroundings, attributing their dynamics solely to radiative transitions. However, this simplistic representation falls short when aiming at elucidating the entire intricacy of PL processes. To comprehensively address the optical properties of QDs, it is imperative to consider the coupling of confined carriers to phonons. We will not delve into an exhaustive description of this coupling here. Instead, we aim to present an intuitive overview of three specific aspects of this interaction: phonon relaxation (in Subsect, 2.5.1), thermal broadening (in Subsect, 2.5.2), and spin-flip processes (in Subsect. 2.5.3).

2.5.1 Phonon relaxation

Phonons appear at first crucial for determining the conditions under which the assumption of considering excitonic states solely in their ground configuration remains valid. Although radiative processes resulting from the recombination of excited multiexcitonic states have been systematically excluded from the theoretical framework, the use of a non-resonant laser implies the initial generation of EHPs in a high-energy configuration. With $E_{\text{exc}} > E_{\text{X}}$ a relaxation process must exist to facilitate the transition of hot carriers to their respective ground states. While PL from intraband transitions has been reported in GaN/AlN QDs [175], the dominant relaxation process is attributed to relaxation through phonon emission, which we discuss in the following.

It is worth noting that Stranski-Krastanov (SK)-like SAQDs, such as those under study here, form on top of a residual layer known as the wetting layer (WL). This GaN WL layer acts as a thin QW with high confinement energy and features a band structure typical of 2D materials, (more details are provided in Sect. 2.16). The energy diagram proposed earlier can be adapted to offer a more realistic depiction of the QD potential, as shown in Figs. 2.12(a) and 2.12(b). Under 'non-resonant' excitation (Fig. 2.12(b)), excited EHPs are either generated in the matrix material (AlN) or more commonly in the WL. The relaxation process is thus divided into two steps: an initial capture time (τ_{cap}[XIII]) followed by intradot relaxation denoted by a time constant τ_{rel}. Radiative recombination in the WL (see Subsect. 2.6.2) competes with the capture process, and a more efficient pumping scheme, generating less background luminescence, is achieved by pumping the QD below the WL. In this 'quasi-resonant' scheme, EHPs are generated directly inside the QD in an excited configuration[XIV], and the relaxation is governed by τ_{rel}. This quasi-resonant scheme was adopted for all measurements discussed in this chapter.

τ_{rel} captures the relaxation of excited carriers toward their ground state through multiple

---

[XIII] The capture time τ_{cap} varies depending on the excitation process. When the excitation occurs in the matrix material, an initial capture in the WL (τ''_{cap}) is expected, followed by a subsequent capture in the QD (τ'_{cap}).

[XIV] The capture time is then limited by the laser fluence and QD absorption efficiency at the excitation wavelength and $\tau_{\text{cap}} = \tau_{\text{exc}}$.

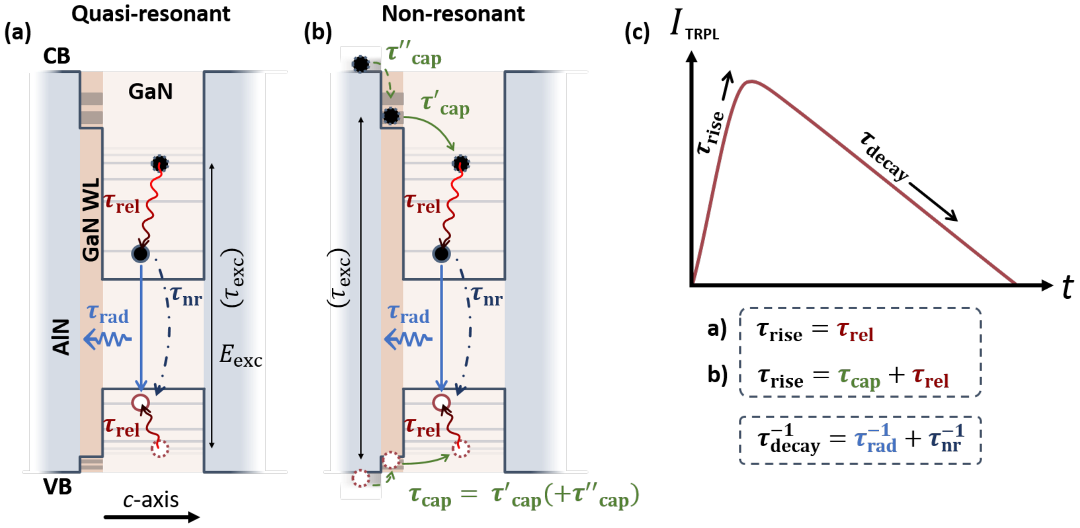

Figure 2.12: Illustration of the pumping relaxation and recombination mechanisms under **(a)** quasi-resonant excitation and **(b)** non-resonant excitation. **(c)** Schematic of the associated TRPL transients when probing the exciton radiative recombination.

phonon emissions. The energy of these emitted phonons matches the electronic level splittings, ensuring adherence to the principle of energy conservation. For QDs, which feature a reduced number of available electronic energy states resulting from 0D quantization, phonon-induced relaxation was initially predicted to take nanoseconds in the early 90s [176, 177], resulting in a 'bottleneck effect' preventing EHPs from efficiently relaxing to their ground state. This prediction explained the poor PL efficiency of such systems at that time, primarily due to the large splitting between the first electron and hole excited states, requiring multiphonon processes to be overcome [178]. However, experimental observations in InGaAs/GaAs QDs contradicted this prediction, showing relaxation times of tens of picoseconds [179, 180] even at low excitation powers. While early proposed AM-assisted relaxation processes could not explain it [181, 182], a more convincing explanation was later proposed by Li *et al.* [183], suggesting that anharmonic LO-phonon coupling to acoustic phonons would preserve an efficient exciton relaxation process, even with a detuning of tens of meV between LO-phonon energies and the electronic states splitting. This approach was later refined in the polaron picture[XV] [184, 185], with results supporting an efficient relaxation process allowed through various anharmonic couplings of the LO-phonon [186, 187].

While subsequent findings have generally supported the notion of an efficient phonon-assisted relaxation process, most of research works have been centered around cutting-edge III-arsenide QDs, with limited theoretical predictions available for GaN/AlN QDs. III-N QDs exhibit larger electron and hole effective masses compared to their III-As counterparts[115, 188], resulting in a greater energy splitting between electronic states that could potentially

---

[XV] The polaron is a quasiparticle arising from the strong coupling between an electron and a cloud of virtual polar phonons (also dubbed lattice polarization).

impede the relaxation process. Conversely, the substantial dipole moment generated by spatially separated EHPs enhances the exciton-phonon interaction [189], which, in turn, should facilitate a rapid relaxation process. It is worth noting that the concept of a 'bottleneck' arises when competing processes hinder the complete relaxation of EHPs. However, GaN/AlN QDs exhibit longer lifetimes compared to III-As QDs, a finding further explored in Sect. 2.10. In this context, 'long' relaxation processes appear less likely when compared to radiative recombination ones and we can reasonably assume that QD PL features effectively stem from the radiative recombination of EHPs in their ground state.

In this scenario, TRPL transients, as discussed in Sect. 2.10, can be understood in the context of the mechanism outlined in Fig. 2.12(c). Following a laser pulse of negligible duration ($\tau_{\text{exc}} \to 0$), EHPs generated in the QD undergo a rapid relaxation process, experimentally quantified by a fast PL rise time (τ_{rise}), followed by radiative recombination. In practice, experimental transients are convoluted with the IRF (see Sect. 1.5), making the interpretation of fast features more challenging.

2.5.2 Thermal broadening

In addition to providing an efficient route for the relaxation of hot EHPs, phonons are the main source of homogeneous PL broadening at high temperature, through carrier-phonon scattering processes. The broadening has a universal character, with the model applied here originating from a theoretical study led on excitons in GaAs/AlGaAs QWs [190] later applied with success to a large variety of systems such as bulk GaN [191], InGaN QDs [192] or even perovskite 2D layers [193]. The original model accounted for scattering by impurities, a likely process for mobile carriers. It can be discarded when considering 3D confined excitons to only retain the following terms [194]:

$$\Gamma(T) = \Gamma_0 + \gamma_{\text{ac}} T + \Gamma_{\text{LO}} N_{\text{LO}}(T) = \Gamma_0 + \Gamma_{\text{th}}(T). \tag{2.50}$$

Here, γ_{ac} and Γ_{LO} are broadening parameters which account for the exciton coupling strength with acoustic and LO phonons, and Γ_{th} refers to thermal broadening. The 0 K broadening Γ_0 accounts for the intrinsic linewidth[XVI] of the investigated state. However, spectral diffusion (SD) effects in polar QDs significantly broaden PL lines above their intrinsic limit and Γ_0 can be effectively replaced by Γ_{SD}, whose origin is extensively discussed in Sect. 2.7.

N_{LO} represents the LO-phonon occupation number, which follows a Bose-Einstein statistics, according to the bosonic nature of phonons[XVII]:

$$N_{\text{LO}}(T) = \frac{1}{\exp\left(E_{\text{LO}}/k_{\text{B}} T\right) - 1}. \tag{2.51}$$

[XVI] According to the time-energy uncertainty principle, the finite lifetime of an excited state relates to an uncertainty in energy, $\Delta E \sim \hbar \Delta t$, amounting to a few µeV.

[XVII] It should be noted that $\gamma_{\text{ac}} T$ in Eq. 2.50 is obtained as a first order expansion of the exponential term associated to the occupation number of acoustic phonons, akin to N_{LO}

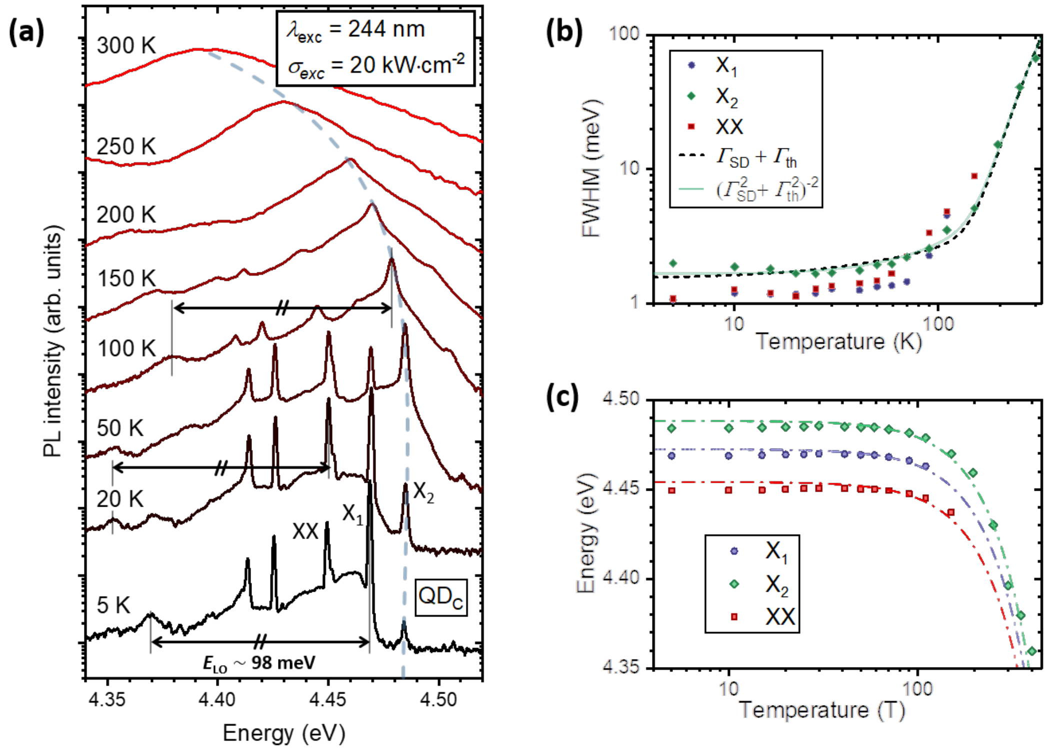

Figure 2.13: **(a)** Temperature-dependent PL spectra of an individual QD. The LO-phonon replicas of the $X_{1,2}$ lines are emphasized by black arrows. The dashed line is a guide to the eye following the position of the X_2 line. The **(b)** FWHM and the **(c)** energy shifts of the labelled lines, $X_{1,2}$ and XX, are also displayed. The QD numbering is aligned on the notations we used in [196] and does not adhere to a chronological sequence. In (b), the black and green lines represent fits of the X_2 FWHM using Eq. 2.50 and Eq. 2.52, respectively. In (c), the datasets are fitted with shared parameters based on the empirical Varshni law (Eq. 2.1).

Owing to the large LO-phonon energy[XVIII], thermal broadening is dominated by acoustic phonon coupling at cryogenic temperature. However, once $\gamma_{\mathrm{ac}} T \ll \Gamma_{\mathrm{LO}} N_{\mathrm{LO}}(T)$, LO-phonon broadening takes over as the temperature increases and dominates at RT. The validity of Eq. 2.50 is tested for illustration on an exciton line, whose temperature dependence is illustrated in Fig. 2.13(a). X_1 (X_2, respectively) corresponds to the luminescence of the low-energy bright state $|B_1\rangle$ (the high-energy bright state $|B_2\rangle$, respectively) and the line labelled XX stems from a biexciton state. The identification of additional emission lines is left for Sect. 2.8. However, we can already notice the presence of one LO-phonon replica for each identified peak, with an energy separation $E_{\mathrm{LO}} \sim 98\,\mathrm{meV}$. This splitting is notably larger than in bulk GaN and coincides with previous observations made by Callsen *et al.* [189] who proposed an averaging mechanism between AlN and GaN LO-phonon energies to explain this result.

[XVIII] The LO-phonon energies are almost constant between cryogenic and RT, with $A_{1(\mathrm{LO})} = 91.3\,\mathrm{meV}$ and $E_{1(\mathrm{LO})} = 92.2\,\mathrm{meV}$ at 6 K [195].

While the lattice temperature increases, the broadening of QD emission lines switches from an inhomogeneous (through SD) to a homogeneous character, due to the dominance of thermal broadening. In this intermediate regime, line broadening is best approximated by a Voigt profile [197]. Equation 2.50 can be adapted to account for the different origin of the two broadening processes, which yields:

$$\Gamma(T) = \sqrt{\Gamma_{\mathrm{SD}}{}^2 + \Gamma_{\mathrm{th}}{}^2(T)}, \tag{2.52}$$

where Γ_{SD} is considered temperature independent in first approximation. The fit discrepancy between Eq. 2.50 and Eq. 2.52 remains however minor, as illustrated in Fig. 2.13(b) for the X_2 FWHM. The slight narrowing of PL lines observed between 5 and 30 K, along with the small blueshift visible in Fig. 2.13(c) in the same temperature range, is well explained through the framework of SD discussed in Sect. 2.7 and most probably originates from a depletion of defects surrounding the single QD of interest. Given the fluctuations of SD-related broadening and its predominance at low temperature, the parameter $\gamma_{\mathrm{ac}} = (11 \pm 3)\,\mu\mathrm{eV} \cdot \mathrm{K}^{-1}$ is barely precise, although it compares well with values reported in bulk GaN, (13 to $16\,\mu\mathrm{eV} \cdot \mathrm{K}^{-1}$ in [191]). By contrast, the fitted value $\Gamma_{\mathrm{LO}} = (3.6 \pm 0.3)\,\mathrm{eV}$ is between seven to ten times larger than in bulk GaN [191], in line with previous observations made for both GaN [189] and InAs QDs [198].

As a final note, we should mention that, as the temperature increases, the line broadening[XIX] progressively diverges from a 'pure dephasing' phenomenon [199], with the increasing overlap of phonon sidebands (PSBs) associated with either absorption or emission of acoustic phonons during an EHP radiative recombination event. This additional broadening is typically asymmetric, with the intensity of the low-energy sideband (high-energy sideband, respectively) proportional to $N_{\mathrm{ac}}(E,T)+1$ ($N_{\mathrm{ac}}(E,T)$, respectively) [200], where N_{ac} represents the occupation number of the involved acoustic phonon modes. As for LO phonons, this occupation number follows a Bose-Einstein statistic. We should incidentally mention that LO-phonon replicas are part of a similar phenomenon although such features are spectrally decoupled from the exciton line due to the large LO-phonon energy.

2.5.3 Phonon-assisted spin-flips

Until now, we have elucidated how rapid phonon emission and scattering processes underpin the multiexcitonic model presented in Sect. 2.4 and the thermal broadening illustrated in Fig. 2.13. However, there is one more process that requires discussion, specifically concerning transitions between exciton or biexciton states with different TAM. These transitions can be described as phonon-mediated processes involving the emission or absorption of phonons with energies matching the (bi-)exciton level discrepancy. Noticeably, a significant distinction arises with regard to the process detailed in Subsect. 2.5.1, insofar as these transitions lead to

---

[XIX] The broadening discussed thus far applies to the zero-phonon line (ZPL), i.e., the dominant PL feature originating from EHP recombination in absence of phonon absorption or emission. This concept is further detailed in Chap. 3 in the context of defect PL.

a net variation in TAM, unlike relaxation processes that are constrained by spin-preserving phonon-mediated transitions [201]. Theoretically, such spin relaxation has been estimated as an inefficient process, lasting orders of magnitude longer than spin-preserving transitions [202, 203]. Experimentally, this inefficiency has been ascribed to a low-temperature quenching of the dark-to-bright transition in materials like InAs [204, 205] or CdSe QDs [206], where spin-flip is predicted to occur on the order of tens of nanoseconds, a timescale much slower than the radiative recombination of bright states. However, other studies led on similar systems have reported spin-flip rates ranging from 10 (CdSe QDs [207]) to $30\,\mathrm{ns}^{-1}$ (InAs QDs [208]), indicating a substantial variability in the QD dynamics among different emitters.

One potential explanation for this inconsistency lies in the variable QD anisotropy. Theoretical calculations, for example, suggest that introducing a mere 20 % in-plane QD elongation could elevate spin-relaxation rates from $\sim 1\,\mathrm{s}^{-1}$ to $\sim 10\,\mathrm{ns}^{-1}$ [209]. As for wurtzite GaN/AlN QDs, the literature is notably lacking, albeit we can anticipate a rapid process due to the strong electron-phonon coupling in such polar systems compared to other materials. While most theoretical calculations rely on acoustic-phonon-mediated spin-flips, the substantial splitting between exciton states in high-energy GaN QDs may additionally require the consideration of LO-phonon-mediated transitions. Although theoretical computations are beyond the scope of this work, many aspects can still be comprehended within a phenomenological framework, as elaborated in the following.

Taking the considerations outlined above into account, we can now complete the diagram proposed in Fig. 2.7(b) by incorporating spin-flips, as depicted in Fig. 2.14(a). Here, we consider phonon-assisted transitions between dark and bright states, as well as between conventional ($|\mathrm{XX_c}\rangle$) and hybrid biexcitons ($|\mathrm{XX_h}\rangle$). For the sake of simplicity, $|\mathrm{D}_1\rangle$ and $|\mathrm{D}_2\rangle$ are treated as a combined state ($|\mathrm{D}_{1-2}\rangle$), given the typically sub-meV dark state splitting [148]. For the sake of completeness, we additionally include higher multiexcitonic states ($|i\rangle$, with $i > 2$), assuming that transitions both from and toward the conventional and hybrid biexcitons are allowed. These higher order states merely act as reservoirs under high pumping conditions but exert little influence on the discussed physics.

Phonon-assisted spin-flip rates are accounted for through $\gamma^i_{\nwarrow}$ and $\gamma^i_{\searrow}$ where $i = \mathrm{B}_1, \mathrm{B}_2$ or XX and [207, 210]:

$$\begin{cases} \gamma^i_{\nwarrow}(T) = \gamma^i_{\mathrm{SF}} N^i_{\mathrm{ph}}(T), \\ \gamma^i_{\searrow}(T) = \gamma^i_{\mathrm{SF}}(1 + N^i_{\mathrm{ph}}(T)), \\ N^i_{\mathrm{ph}}(T) = \frac{1}{e^{\delta_i / k_{\mathrm{B}} T} - 1}. \end{cases} \tag{2.53}$$

Here, δ_i represents the energy separation between $|\mathrm{B}_1\rangle$ and $|\mathrm{D}_{1-2}\rangle$ ($\delta_{\mathrm{B}_1} = \delta_0 - \delta_{\mathrm{FSS}}/2$), between $|\mathrm{B}_2\rangle$ and $|\mathrm{D}_{1-2}\rangle$ ($\delta_{\mathrm{B}_2} = \delta_0 + \delta_{\mathrm{FSS}}/2$), and between biexciton states (δ_{XX}). γ^i_{SF} accounts for the spin-flip rates and is by default considered equal for all phonon-mediated transitions ($\gamma^{\mathrm{B}_1}_{\mathrm{SF}} = \gamma^{\mathrm{B}_2}_{\mathrm{SF}} = \gamma^{\mathrm{XX}}_{\mathrm{SF}}$). The different radiative decay rates are illustrated in Fig. 2.14(a) and we assume at first $\gamma_1 = \gamma^{\mathrm{B}_1}_1 = \gamma^{\mathrm{B}_2}_1 = 1/2\gamma^{\mathrm{c}}_2 = 1/2\gamma^{\mathrm{h}}_2$.

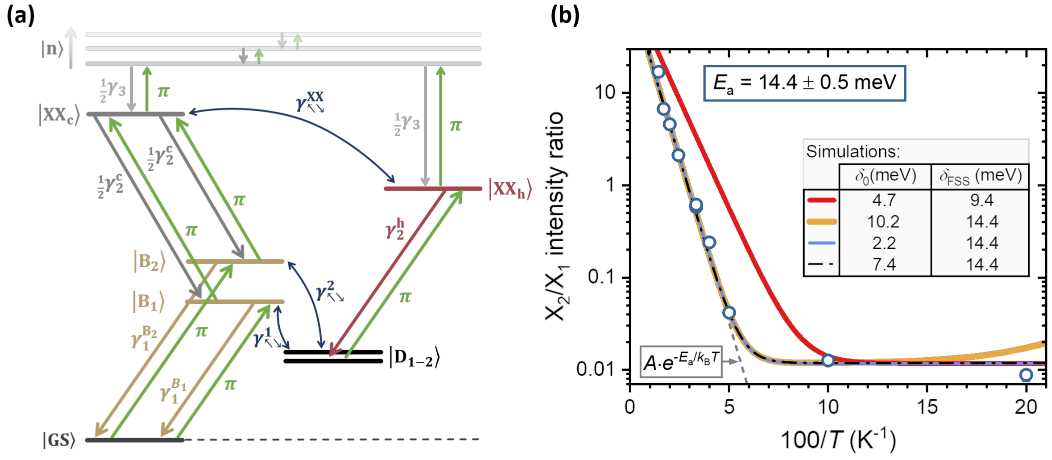

Figure 2.14: **(a)**. Illustration of the multiexcitonic model, taking into account phonon-mediated spin-flips. The dark states are considered degenerate for simplicity. **(b)** Evolution of the PL intensity ratio between $\mathrm{QD_C}$ $\mathrm{X_2}$ and $\mathrm{X_1}$ exciton lines as a function of temperature. The grey dashed line corresponds to an Arrhenius fit with an activation energy $E_\mathrm{a} = (14.4 \pm 0.5)$ meV. Solid and dash-dotted lines correspond to simulations using the model depicted in **(a)** and fitting parameters provided in the inset table. The solid blue and dashed black lines completely overlap.

Although the implication of this model are thoroughly discussed throughout this work, a key feature related to the pronounced FSS observed for high-energy GaN QDs can already be highlighted here, considering $\mathrm{QD_C}$ for the sake of illustration. At low temperature, large values of δ_FSS impede the population of the high-energy bright state through phonon-mediated spin-flips, resulting in a weak $\mathrm{X_2}$ PL signal. With increasing temperature, the phonon population (N^i_ph) also rises, progressively increasing the occupancy probability of $|\mathrm{B_2}\rangle$. Experimental confirmation comes from monitoring the evolution of the intensity ratio between the two exciton lines, $\mathrm{X_2}/\mathrm{X_1}$, as illustrated in Fig. 2.14(b). The ratio starts to increase above a temperature threshold (here ~ 20 K), following an exponential trend. Fitting the data with an Arrhenius fit (grey dashed line) yields an activation energy of (14.4 ± 0.5) meV, relatively close to the FSS, $\delta_\mathrm{FSS} = 15.3\,\mathrm{meV}$, extracted from the PL spectra shown in Fig. 2.13(a).

A more robust confirmation comes from solving the rate equations associated with the multiexcitonic model (see Appendix B.1), which can accurately reproduce the results with proper parameter tuning. Notably, simulated exciton intensity ratios are minimally affected by the pump rate (π), multiexcitonic radiative decay rates (γ_i, $i > 1$), or biexciton spin-flip rates ($\gamma^\mathrm{XX}_{\nwarrow\searrow}$), leaving only δ_0, δ_FSS, δ_2, $\gamma_1^{\mathrm{B_1}}$, $\gamma_1^{\mathrm{B_2}}$, and γ_SF as effective tuning parameters. Interestingly, the exponential trend is primarily driven by δ_FSS, regardless of the chosen value for δ_0, and yields similar results whether considering or neglecting direct transitions between $|\mathrm{B_1}\rangle$ and $|\mathrm{B_2}\rangle$. Graphically, this is evidenced by the overlap between simulated trends obtained using $\delta_0 = 10.2\,\mathrm{meV}$ (yellow line), $\delta_0 = 2.2\,\mathrm{meV}$ (blue line) and $\delta_0 = 7.4\,\mathrm{meV}$ (black line). However, the model predicts an initial decrease in the X_2/X_1 ratio with temperature when setting $\delta_{B_1} > 0$ (yellow line), which is not observed experimentally. This is intuitively understood as a faster activation of the low-energy bright state (increasing X_1), leading to a mathematical reduction of the X_2/X_1 ratio. This discrepancy suggests the presence of a low-energy bright state located close (black line) or below the exciton dark state (blue line), implying that $\delta_{B_1} \leq 0$.

It is also noteworthy that the exponential increase in the exciton intensity ratio is almost exclusively influenced by the disparity between the bright and dark state recombination rates, a phenomenon easily explained through the multiexcitonic model. At high temperatures, fast phonon-mediated transitions dominate the dynamics, resulting in an averaging effect between the occupancy probabilities of $|B_1\rangle$ and $|B_2\rangle$ ($n_{B_1} \sim n_{B_2}$). As a consequence, the exciton intensity ratio converges to:

$$\frac{I_{X_2}}{I_{X_1}} = \frac{\gamma_1^{B_2} n_{B_2}}{\gamma_1^{B_1} n_{B_1}} \xrightarrow[k_B T \gg \delta_{FSS}]{} \frac{\gamma_1^{B_2}}{\gamma_1^{B_1}} \tag{2.54}$$

In our specific case (QD_C), this results in a striking difference in the radiative recombination rates between the two bright states, with $\gamma_1^{B_2} \sim 130\gamma_1^{B_1}$ exceeding by far the discrepancy observed in, for example, InAs QDs ($\gamma_1^{B_2}/\gamma_1^{B_1} \sim 10$ in Ref. [208]). For the fitting, we selected $\gamma_1^{B_1} = 0.4\,\mathrm{ns}^{-1}$, in adequation with TRPL results presented in Sect. 2.9, although the absolute decay rate has little influence on the simulated ratio. While simulated results should be approached with caution at this point, it is crucial to emphasize that once the decay rates are fixed, the baseline [XX] can be regulated by the amplitude of the 0 K spin-flip rate. A larger γ_{SF} value leads to a more efficient depletion of the high-energy bright state at low temperatures, thereby further decreasing the exciton intensity ratio. In Fig. 2.14(b), the baseline is well reproduced, with all other parameters kept fixed as mentioned above, using $\gamma_{SF} = 2.2\,\mathrm{ps}^{-1}$. However, this final parametrization is not robust and is highly sensitive to the variations of other parameters, such as the exciton decay rates, the pump rate, the inclusion of bright-to-bright phonon-mediated transitions, and the dynamics of higher excited states. Nevertheless, it suggests the existence of a pronounced phonon-mediated spin relaxation channel for the exciton bright states, with γ_{SF} significantly surpassing the radiative decay rates. With these observations in mind, we can now elucidate the discrepancies between experimental observations and theoretical predictions based on the model developed in Sect. 2.4.

Placing ourselves in the strong electron-phonon coupling regime ($\gamma_{SF} \gg \gamma_1$), it is now possible to reevaluate the predictions on the power dependence of the exciton and biexciton lines as initially estimated through Eq. 2.32. We restrict the study to a low-temperature range (6.5 to 50 K) in which the high-energy exciton bright state and the conventional biexciton states are weakly populated. To satisfy this condition, we fixed $\delta_{XX} = 35\,\mathrm{meV}$ based on results by Hönig *et al.* [148], and $\delta_{B_2} = 14.4\,\mathrm{meV} \gg k_B \cdot 50\,\mathrm{K}$. Consequently, we focus here on the PL originating from $|B_1\rangle$ and $|XX_h\rangle$. Two situations are considered, with the low-energy bright state either on par with ($\delta_{B_1} = 0\,\mathrm{meV}$) or above the dark states ($\delta_{B_1} = 5\,\mathrm{meV}$). Both scenarios are illustrated in

---

[XX] The 'baseline' is defined here as the almost constant X_2/X_1 ratio for $k_B T \ll \delta_{FSS}$.

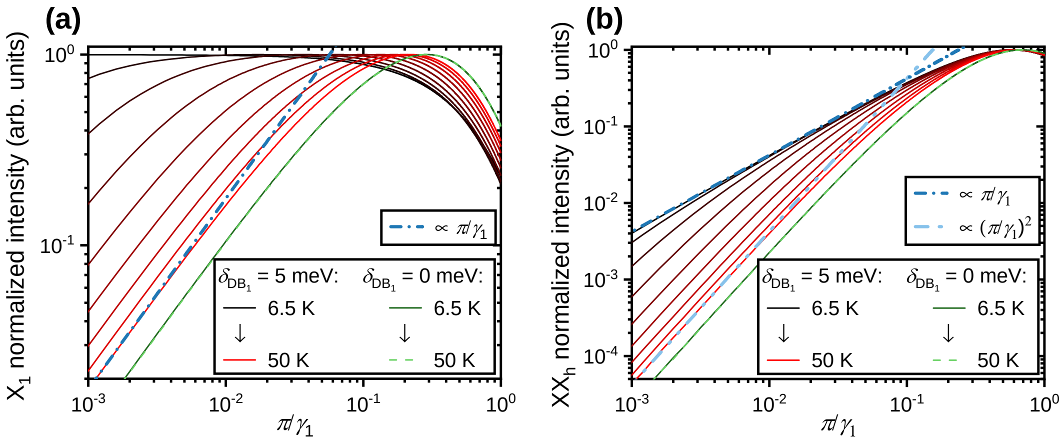

Figure 2.15: Simulation of the PL intensity of the **(a)** X_1 and **(b)** XX_h lines as a function of pump rate. Simulations are performed in the high electron-phonon coupling regime ($\Gamma_{SD} \gg \gamma_1$). Here, we fixed $\gamma_1^{B_1} = \gamma_1^{B_2} = \gamma_1$ for simplicity, although the high-energy bright state has a negligible influence on the dynamics at low temperature. The results are normalized for clarity, but we should note that the X_1 absolute PL intensity decreases exponentially with temperature. Dash-dotted lines are used to emphasize the linear (dark blue line) or quadratic dependence (light blue line) of the simulated curves.

Fig. 2.15.

The first conclusion that arises is that for a negligible δ_{B_1}, i.e., when the low-energy bright state is fully activated at low temperature, we retrieve the result predicted by Eq. 2.32. This is illustrated here by overlapping the solid and dashed green lines corresponding to simulations performed with $T = 6.5\,\mathrm{K}$ and $50\,\mathrm{K}$, which fully reproduce the linear (exciton) or quadratic (biexciton) intensity scaling predicted before. By contrast, the simulations are strongly temperature-dependent when considering $\delta_{B_1} > 0$, with an X_1 line scaling factor $\tilde{n}_{B_1}$ increasing from 0 to 1 as the temperature increases. At low temperature, recombination processes from the low-energy bright state are strongly impeded, so that the exciton starts to act as the 'effective ground state'. Consequently, the biexciton scaling factor tends to 1 as it effectively becomes the first radiative state of the multiexcitonic cascade. The normal behavior ($\tilde{n}_{XX_h} = 2$) is fully retrieved at 50 K in parallel with the thermally-activated population of the low-energy bright state.

These simulations show that, by taking into account the phonon-mediated spin relaxation and the temperature activation of the bright state, we can readily reproduce the sub-linear and sub-quadratic trends reported for exciton and biexciton lines, respectively, in previous studies [148, 162, 163]. We should additionally mention that the description qualitatively holds upon inverting the stability of conventional and hybrid biexciton states ($\delta_{XX} < 0$), with both biexciton lines actually featuring the same temperature-dependent trends. Finally, it is noteworthy that, while the simulated curves are normalized in Fig. 2.15, the low-energy bright state PL intensity drops by 3 to 5 orders of magnitude between 50 and 6.5 K in the scenario where $\delta_{B_1} = 55\,\text{meV}$. Experimentally, such exciton lines should be extremely faint at low temperature, and thus be readily discarded in μ-PL investigations led on single QDs where bright emitters are considerably easier to investigate. This could explain why many reports exist on exciton lines scaling linearly with power, with $\delta_{B_1} \sim 0$.

Summary

At this stage of the chapter, we have reviewed most of the physics needed to apprehend the complexity of GaN/AlN QDs and their optical properties. We started by establishing the theoretical framework required to describe the physics of zero-dimensional systems. Subsequently, we addressed the peculiarities of such QDs, inherited from the wurtzite structure of III-N materials. Understanding these features is crucial to discern the disparities between GaN systems and benchmark III-As QDs, frequently referenced throughout our theoretical discussion.

After introducing the fundamental physics of QDs through the exciton framework, we developed a model to encompass multiexcitonic states. We extensively discussed the predictions and caveats of this model, laying the groundwork for interpreting empirical studies. The initial experimental findings were introduced in the context of exploring the impact of phonon-related processes and served as a support to illustrate the influence of spin relaxation on the temperature-dependent recombination dynamics of GaN/AlN QDs.

The phenomenological model, completed in this section, provides a robust foundation for comparison with experimental observations and has proven effective in explaining temperature and power-dependent features. However, it is essential to acknowledge that certain unexplained features have been set aside thus far and will receive more detailed attention in subsequent sections of this chapter. However, before delving into those aspects, we will introduce the growth and processing methods employed in this work to generate and isolate individual QDs emitters, as outlined in Sect. 2.6. SD is another phenomenon requiring special consideration and will be addressed in Sect. 2.7, prior to the core spectroscopic investigations.

2.6 Growth and processing

This thesis does not center on the growth procedure of the examined QDs, as the growth optimization has been extensively covered in the PhD thesis of S. Tamariz (LASPE, EPFL 2019 [211]). Nonetheless, it is essential to provide a summary of the growth procedure and explain how a high-quality sample was achieved. The QD optical properties directly correlate with the growth conditions, which are crucial for understanding the differences between our study and various literature reports. While the growth procedure is extensively detailed in [212, 213], we provide here a digest on the topic of SAQD growth by molecular beam epitaxy (MBE) (Subsect. 2.6.1) before highlighting the growth and processing conditions applied to the sample utilized in this study (Subsect. 2.6.2).

2.6.1 Growth strategy of self-assembled quantum dots

During epitaxy, both 2D and 3D growth modes are commonly observed. The (3D) Volmer-Weber (VW) growth mode occurs when adatoms are more strongly bound together than with the substrate, resulting in the formation of 3D islands. This mode is common for metallic growth on insulator [214]. In contrast, the Frank-van der Merwe (FM) or layer-by-layer growth mode involves adatoms attaching more favorably to the substrate than to each other, resulting in a 2D thin film growth. When adatom mobility increases, and the substrate is slightly misoriented from a low-index plane, forming monoatomic steps at its surface, it transitions into a step-flow mode. In this mode, adatoms diffuse at the surface and incorporate at step edges, typically resulting in smooth, high-quality surfaces. The growth recipe developed by S. Tamariz during his PhD thesis utilizes this mode for growing AlN layers, on top of which GaN QDs are grown.

When the lattice-mismatch between the substrate and adsorbate layers is large, the strain induced by this mismatch can favor the transition from a 2D FM growth to 3D island formation after the grown layer reaches a critical thickness to release the strain. This transitional growth mode is referred to as the SK mode, one of the most common techniques employed to form QDs. The randomly distributed 3D islands are commonly referred to in the literature as SA QDs [114]. The thin 2D layer on which they stand is known as the WL and has implications for the optical properties of these QDs, as detailed below.

In this work, we report on SAQDs grown on AlN. While controlling the AlN strain field could theoretically influence the localization of 3D GaN island formation [215], the QD formation process remains essentially random. Various strategies have been tested to create adequate samples for the investigation of single QDs. With a laser spot size of approximately one micron in μ-PL (see Subsect. 1.1.3), the target QD density is around $\sim 10^8\,\mathrm{cm}^{-2}$ to safely address QDs individually. In contrast to the prototypical InAs/GaAs SAQDs, where the large lattice-mismatch (7.2 %) between InAs and GaAs allows for efficient tuning of their density [216], the 2.5% low lattice-mismatch between GaN and AlN makes achieving the SK growth mode more challenging. The density of GaN/AlN QDs is quite robust and lies around $10^{10}\ \mathrm{cm}^{-2}$ [127, 217–219]. This feature appears in heteroepitaxy, where the mismatch between AlN and the substrate (sapphire, Si(111) or SiC) leads to the formation of edge dislocations, altering the strain field [220] and acting as preferential nucleation sites for SAQDs [221].

As a result, S. Tamariz initially developed an MBE growth recipe, employing ammonia as a precursor (NH_3-MBE), to tailor the density of SAQDs grown on AlN single-crystal [213]. This approach, with a low density of edge dislocations, achieved densities below $10^{10}\ \mathrm{cm}^{-2}$ at very low growth rates. However, it led to a broad UV luminescence band, attributed to PDs in AlN [222], originating from the single-crystal template and significantly impeding the isolation of specific QD PL lines. Additionally, the low growth rate may promote the introduction of PDs near the SAQDs, potentially affecting their optical performance [211].

2.6.2 GaN/AlN SAQDs on Si(111)

Ultimately, the most promising strategy consisted in growing a thin AlN layer on a Si(111) substrate to efficiently suppress AlN defect luminescence. High substrate quality for epitaxial growth was achieved through annealing the substrate at 1200 °C to remove the native oxide. The AlN nucleation layer was formed at 800 °C, followed by a 100 nm thick AlN layer grown at 1100 °C. SK growth was performed based on a method developed by B. Damilano *et al.* [26] for NH_3-MBE. After depositing an equivalent of 6 monolayers (MLs) of GaN at 820 °C in the FM-growth mode, the NH_3 flux was interrupted to induce a 2D-to-3D transition. GaN evaporation and ripening[XXI] occurred simultaneously, accompanied by a reduction in the WL thickness. A capping AlN layer of 20 nm was then grown, followed by a second plane of GaN QDs. This top plane was exclusively grown for atomic force microscopy (AFM) imaging and subsequently evaporated on half of the sample used for μ-PL studies. An AFM image of the top QD plane is provided in Fig. 2.16(a) and reveal the broad QD size distribution, with QDs featuring a large base of a few tens of nanometers and a height ranging from 1 to 3 nm.

The QD density achieved with this modified SK growth recipe was on the order of 10^{10} cm^{-2}, owing to the growth on a foreign substrate, and does not allow for PL measurements on individual QDs. To enable single-dot spectroscopy an additional processing step was implemented to isolate SPEs. A portion of the sample without surface QD layer was further patterned into mesas ranging from 0.05×0.05 μm^2 up to 2×2 μm^2 using electron beam lithography (EBL) and subsequent etching down to the AlN buffer layer. In practice, only the smallest mesas, comparable in size to the laser spot, proved effective in isolating single QDs. Remarkably enough, the etching process unintentionally left some areas untouched, leading to the formation of additional mesas similar in size to the smallest intentionally created ones. These unintended mesas can be observed in all secondary electron (SE) images of the processed surface presented in Fig. 2.16(b) and were also investigated through μ-PL. Gold crosses, added to aid in repositioning the laser spot onto promising QDs, are also observable in the large-scale SE image. An optical microscope image of the surface is provided in Fig. 2.16(c), featuring numbers engraved by EBL for accurate repositioning. The mesas are identified in the plane through a chessboard numbering scheme. A schematic representation of the patterned sample is given in Fig. 2.16(d). A portion of the sample was left unetched for TRPL measurements.

Thanks to the evaporation and ripening process, the WL thickness was effectively reduced, leading to a nearly complete spectral dissociation between the QD ensemble and the WL PL, a necessity to achieve high single-photon purity. This feature is evidenced through cathodoluminescence (CL) measurements, as depicted in Fig. 2.17. The luminescence peak at 5.3 eV is associated with a WL thickness of ∼ 1.5 ML [223]. Further confirmation of this peak attribution can be obtained through temperature-dependent measurements, as conducted by S. Tamariz in his thesis [211], on a QD sample with a WL peaking at 4.4 eV investigated by PL. The WL PL quenches around 200 K due to increased non-radiative recombination of free carriers, while the QDs remain bright at RT, thanks to 3D carrier confinement.

[XXI] Aggregation of small GaN islands to form larger QDs.

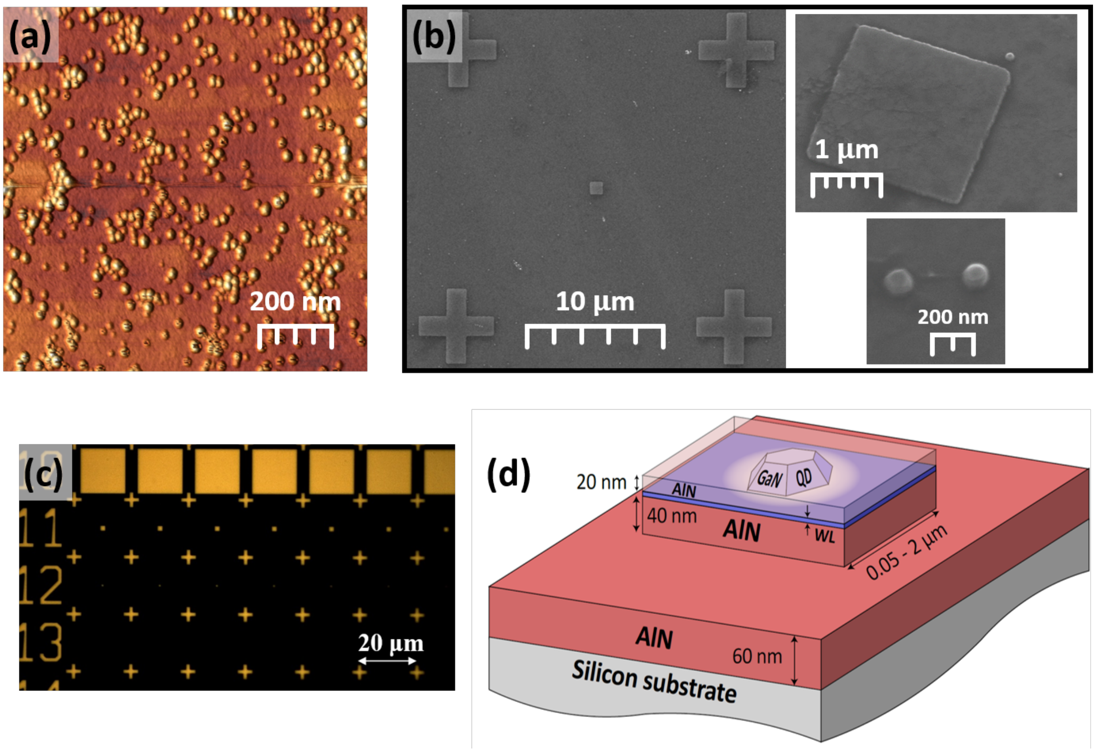

Figure 2.16: Imaging of the sample L1244. **(a)** 1 × 1 µm^2 height-mode AFM image of the top SAQD plane. displaying a broad distribution of dot sizes. **(b)** Plan and birds eye view SE images of the patterned surface after etching. Unintendedly formed mesas are well observed in small-scale SE images. **(c)** Optical microscope image of the patterned sample. All images were acquired by S. Tamariz. **(d)** Schematic of the mesa structure. This figure is not to scale.

As shown in Fig. 2.17(b) a 266 nm laser appears generally well-suited for quasi-resonant µ-PL measurements, as its energy falls below the low-energy tail of the broad WL luminescence spectrum. In contrast, the WL would still be partially excited by employing a 244 nm laser. At RT this hindrance is expected to decrease due to rapid non-radiative recombination of EHPs generated in the WL.

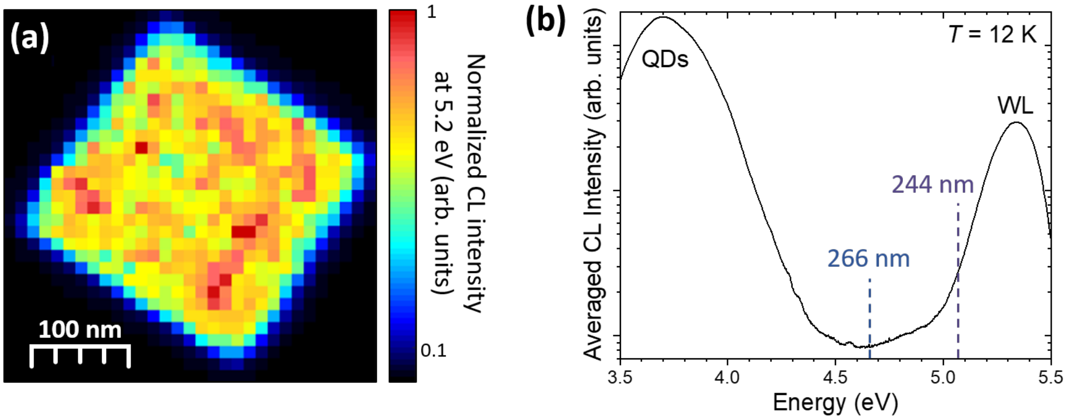

Figure 2.17: **(a)** CL intensity map of a single mesa at an energy of 5.2 eV. An average of the CL over the whole mesa is illustrated in **(b)** and features the broad QD luminescence along with the high-energy WL luminescence. Results acquired by S. Tamariz at 12 K using an acceleration voltage of 6 kV. Dashed lines are used to illustrate the excitation energy of the two UV lasers used in this work.

2.7 Spectral diffusion in GaN/AlN quantum dots

The linewidth of an SPE emission line is a critical parameter for quantum applications, where a narrow linewidth is essential for achieving temporal coherence. At RT, linewidth broadening is primarily driven by the exciton-phonon coupling, occurring on a picosecond timescale, which imposes limitations on the applications of SPEs. This broadening diminishes as the temperature approaches 0 K (see Subsect. 2.5.2), theoretically allowing for a line broadening close to the natural linewidth. However, at low temperatures, another broadening effect known as spectral diffusion (SD) becomes prominent, significantly limiting the achievable spectral resolution. SD refers to random temporal variations in the emission wavelength of a quantum emitter, typically stemming from charge fluctuations of defects located in its immediate vicinity. In the following sections, we will delve into the manifestations of SD in μ-PL and $g^{(2)}(\tau)$ measurements performed on GaN/AlN QDs, presenting a simple formalism to quantify its effects. It is crucial to note that SD is intricately linked to the physics of defects causing spectral jittering, and the description provided here can readily be applied to the SD effects experienced by PD SPEs.

2.7.1 Phenomenological description

SD significantly impacts III-N QDs due to the QCSE, causing a substantial separation of electron and hole wavefunctions, hence resulting in a large permanent dipole moment for any excitonic complex [224, 225], (see Subsect. 2.2.3). The energy shift induced by an external electric field $\mathbf{F}_{\mathrm{ext}}$ can be described by [226]:

$$\Delta E(t) = \boldsymbol{\mu}_{\mathrm{X}} \cdot \mathbf{F}_{\mathrm{ext}}(t). \tag{2.55}$$

For a given excitonic complex, we assume here a constant permanent dipole moment (as defined by Eq. 2.13), considering its variation induced by $\mathbf{F}_{\mathrm{ext}}$ as negligible ($\mathbf{F}_{\mathrm{bi}} \gg \mathbf{F}_{\mathrm{ext}}$) [225]. Eq. 2.55 is generalized to any multiexcitonic state through:

$$\Delta E_i(t) = (\boldsymbol{\mu}_i - \boldsymbol{\mu}_{i-1}) \cdot \mathbf{F}_{\mathrm{ext}}(t) = \Delta\boldsymbol{\mu}_i \cdot \mathbf{F}_{\mathrm{ext}}(t), \tag{2.56}$$

to account for the shift of both the initial state (with dipole moment $\boldsymbol{\mu}_i$) and final state (with dipole moment $\boldsymbol{\mu}_{i-1}$) in the PL line shift ΔE_i. Owing to the QCSE, dipole moments are aligned along the c-axis, so only the vertical component of $\mathbf{F}_{\mathrm{ext}}$, denoted F^z_{ext}, contributes to the line shift.

$\mathbf{F}_{\mathrm{ext}}$ is generated by the ensemble of N defect states lying in the vicinity of the emitter. Assuming they stem from a common origin (same type of impurity or PD), they should feature the same occupancy probability p_{oc}. A defect X_k contributes by an amount F_k to the resultant F^z_{ext} when effectively charged, such that the mean external field $\overline{F^z_{\mathrm{ext}}}$ and the associated root mean square (RMS) σ_{ext} are expressed by [162]:

$$\begin{aligned} \overline{F^z_{\mathrm{ext}}} &= \mathrm{Exp}\left(\sum_k^N X_k\right) = p_{\mathrm{oc}} \sum_k^N F_k = p_{\mathrm{oc}} F_{\mathrm{max}}, \\ \sigma^2_{\mathrm{ext}} &= \mathrm{Var}\left(\sum_k^N X_k\right) = p_{\mathrm{oc}}(1-p_{\mathrm{oc}}) \sum_k^N F_k^2 = p_{\mathrm{oc}}(1-p_{\mathrm{oc}})(2\sigma_{\mathrm{max}})^2, \end{aligned} \tag{2.57}$$

where F_{max} represents the virtual field generated assuming a full occupancy of the N defects and σ_{max} sets an upper limit on the RMS. Both parameters are uniquely defined for each QD. The average line shift generated by $\overline{F^z_{\mathrm{ext}}}$ immediately follows:

$$\overline{\Delta E_i} = p_{\mathrm{oc}} \Delta\mu_i F_{\mathrm{max}}, \tag{2.58}$$

and the SD-limited emission linewidth ($\Gamma_{\mathrm{SD},i}$) reads:

$$\Gamma_{\mathrm{SD},i} = 4\sqrt{2\ln 2}\sqrt{p_{\mathrm{oc}}(1-p_{\mathrm{oc}})}\Delta\mu_i \sigma_{\mathrm{max}}, \tag{2.59}$$

where the linewidth is defined as the peak FWHM. At this stage, no value has been estimated for F_{max}. However, the formalism already accounts for the inhomogeneous (Gaussian) broadening of QD emission lines observed at cryogenic temperatures [197]. Additionally, it is worth noting that, as per Eq. 2.59, the linear relation between the emission linewidth broadening and the dipole moment differences $\Delta\mu_i$. This relationship can be utilized to help sorting out emission lines originating from the same QD. According to the calculations performed by Hönig *et al.*

[225], the following inequalities apply:

$$\Gamma_{\mathrm{SD},X} > \Gamma_{\mathrm{SD},X^{\pm}} > \Gamma_{\mathrm{SD},XX} > \Gamma_{\mathrm{SD},XX^{\pm}}, \tag{2.60}$$

where $\Gamma_{\mathrm{SD},X}$, $\Gamma_{\mathrm{SD},X^{\pm}}$, $\Gamma_{\mathrm{SD},XX}$ and $\Gamma_{\mathrm{SD},XX^{\pm}}$ correspond to the exciton, charged exciton, biexciton and charged biexciton linewidths, respectively. As a rule of thumb, the SD-limited linewidth increases inversely with the number or carriers. A corollary of this relation is used in Subsect. 2.7.3.

2.7.2 Power dependence of the defect occupancy

The validity of Eqs. 2.58 and 2.59 cannot be tested as it stands, necessitating a more detailed understanding of the dynamics governing defect occupancy. SD has previously been observed in a large variety of systems [199, 227–230], and is well documented for GaN/AlN SAQDs [137, 225, 231, 232] though its specific origin in this context remains elusive. Generally, SD can arise from diverse sources, including extended and point defects, surface states, etc. [233]. In our case, impurities, notably silicon (Si) diffusing from the Si(111) substrate into the AlN buffer layer [234, 235] and n-type O or C impurities [236, 237], are the most probable contaminants present in our sample [238]. Additionally, hydrogen-related PDs may also be encountered [239, 240]. To gain some insight, we adopt an approach inspired by A. Berthelot [241], by modeling defects as two-level traps with trapping ($\tau_{\downarrow}$) and release times ($\tau_{\uparrow}$). The release time ($\tau_{\uparrow}$) primarily involves a temperature-dependent, phonon-assisted process [242], while, at low temperatures, $\tau_{\downarrow}$ is expected to be influenced by the pumping laser. Various power-law relationships can be considered, such as $1/\tau_{\downarrow} \propto \sqrt{P_{\mathrm{exc}}}$ [243], depending on the excitation energy. The impact of SD can be significantly reduced by employing a quasi-resonant (below bandgap) excitation scheme [244]. In such a scenario, a more plausible linear dependence between the release rate and excitation power ($1/\tau_{\downarrow} \propto P_{\mathrm{exc}}$) emerges [137], as also corroborated in Chap. 3 under low-excitation conditions. The two-level trap is described by the following rate equation:

$$\frac{\mathrm{d}p_{\mathrm{oc}}}{\mathrm{d}t} = \frac{(1 - p_{\mathrm{oc}})}{\tau_{\downarrow}} - \frac{p_{\mathrm{oc}}}{\tau_{\uparrow}}, \tag{2.61}$$

yielding the following relation in the steady state (CW excitation):

$$p_{\mathrm{oc}} = \frac{1}{1 + \tau_{\downarrow}/\tau_{\uparrow}} = \frac{1}{1 + R_{\downarrow\uparrow}}, \tag{2.62}$$

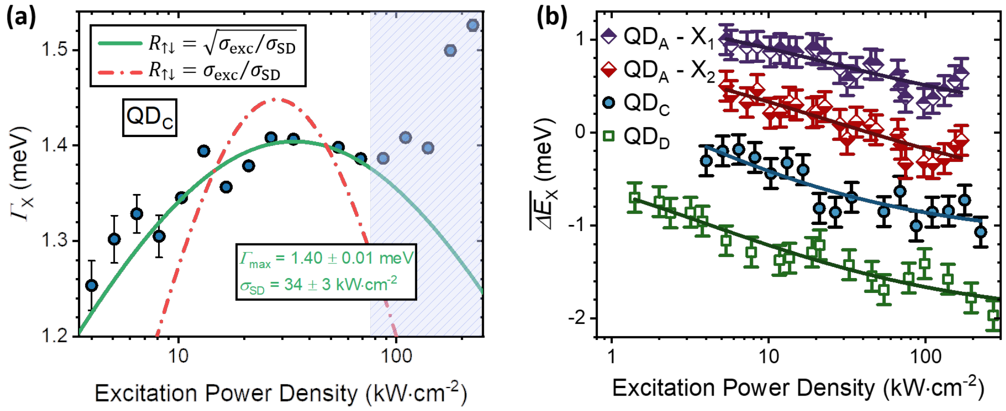

Figure 2.18: **(a)** Exciton linewidth plotted against excitation power density. The solid green line represents the 'square root' fit, and the fitting parameters are displayed in the figure. The hatched area is excluded from the fitting range. **(b)** Power-dependent energy shift observed for various exciton lines, presented with an arbitrary offset. Data obtained at 5 K with excitation wavelengths of $\lambda_{\mathrm{exc}} = 244\,\mathrm{nm}$ (QD$_{\mathrm{A,C}}$) and $\lambda_{\mathrm{exc}} = 266\,\mathrm{nm}$ (QD$_{\mathrm{D}}$).

with $R_{\downarrow\uparrow} = \tau_\downarrow/\tau_\uparrow$. Substituting this equation in Eqs. 2.58 and 2.59, we can write:

$$\overline{\Delta E_i} = \frac{\overline{\Delta E_{\mathrm{max},i}}}{1+R_{\downarrow\uparrow}},$$

$$\Gamma_{\mathrm{SD},i} = \Gamma_{\mathrm{max},i}\sqrt{1-\left(\frac{2}{1+R_{\downarrow\uparrow}}-1\right)^2}, \tag{2.63}$$

where the constants $\overline{\Delta E_{\mathrm{max},i}} = \Delta\mu_i \cdot F_{\mathrm{max}}$ and $\Gamma_{\mathrm{max},i} = 4\sqrt{2\ln 2}\cdot\Delta\mu_i\cdot\sigma_{\mathrm{max}}$ represent the maximum SD-related energy shift and linewidth broadening experienced by an excitonic line. For linear or square root power laws, the ratio $R_{\downarrow\uparrow}$ reads $R_{\downarrow\uparrow} = P_{\mathrm{exc}}/P_{\mathrm{SD}}$ and $\sqrt{P_{\mathrm{exc}}/P_{\mathrm{SD}}}$, respectively, where P_{SD} denotes the excitation power at which $\tau_\downarrow = \tau_\uparrow$. The SD-induced broadening reaches its maximum when $P_{\mathrm{exc}} = P_{\mathrm{SD}}$, corresponding to $p_{oc} = 1/2$, and theoretically decreases to 0 at very high or very low excitation power (when defects are all filled or all empty).

Now the validity of Eq. 2.63 can be tested by extracting the linewidth from a series a μ-PL spectra acquired at different excitation powers, as depicted in Fig. 2.18(a) for the exciton line of an emitter labelled QD$_{\mathrm{C}}$, representative of the features we have typically observed. The labeling choice aligns with the results we published in Ref. [196], and the QDs are not numbered based on their chronological appearance in this thesis. Notably, only defects located a few nm away from a QD will significantly influence its state [162], implying that all defects contributing to SD experience the same excitation power density. For future comparisons with other studies, we can substitute $R\downarrow\uparrow = P_{\mathrm{exc}}/P_{\mathrm{SD}}$ with $\sigma_{\mathrm{exc}}/\sigma_{\mathrm{SD}}$ and plot the data against the excitation power density (σ_{exc}, see Subsect. 1.2.2).

In Fig. 2.18(a), both linear and square root power laws are examined, and the fitting results are depicted by dashed-red and solid-green lines, respectively. In contrast to the earlier conjecture, the 'linear' fit proves to be inconsistent with experimental results across all datasets and ranges considered. The 'square root' fit accurately reproduces the broadening observed at low power but predicts spectral narrowing at high excitation power density, a feature almost never observed across the various QDs investigated. On the contrary, the linewidth usually broadens above a certain limit, as emphasized in Fig. 2.18(a) by the hatched area. This sudden broadening cannot be explained by sample heating, given the weak laser absorption in AlN at the excitation wavelength ($\lambda_{\text{exc}} = 244\,\text{nm}$) and the reduced thickness of the GaN layer, nor by the presence of a second type of defect with a larger σ_{SD} parameter. The inflection point observed around $100\,\text{kW}\cdot\text{cm}^{-2}$ in Fig. 2.18(a) is not reproduced when adapting Eq. 2.63 to account for two types of defects, regardless of the adopted power laws.

In contrast, Eq. 2.63 with $R_{\downarrow\uparrow} = P_{\text{exc}}/P_{\text{SD}}$ aligns well with the energy shift experienced by excitonic lines ($\overline{\Delta E_i} = \overline{\Delta E_{\text{X}}}$), as highlighted in Fig. 2.18(b) for different QDs. For clarity, each dataset is shifted by an arbitrary offset that does not impact the physics. The maximum shift induced when all defects are filled, $\overline{\Delta E_{\text{max}}}$, is consistently negative, although its sign depends on the overall positioning of the defects around the QDs. This constant redshift of the exciton lines with increasing excitation power suggests a common spatial origin for the defects inducing SD. We can likely dismiss the contribution of surface states at the AlN/air interface that is located too far from the QDs to significantly contribute to the external electric field $\mathbf{F}_{\text{ext}}$ near the QDs. A preferential incorporation of defects above or below the GaN QD layer, depending on the growth conditions, would probably best account for the fixed sign of F^{z}_{ext}, with the formation of structural defects favored by the lattice-mismatch between GaN and AlN. A more systematic study of the SD origin is left for future work.

Finally, it is noteworthy that the energy shifts illustrated in Fig. 2.18(b) exhibit faint irregular oscillations not accounted for by the present model. We attribute these oscillations to SD occurring on a second to tens of seconds timescale, as reported in the literature [245, 246] and evidenced in Subsect. 2.7.3. The resulting spectral jittering is clearly observable in 2.18(b) since each power-dependent dataset is acquired sequentially from left to right (low power to high power). Since the frequency of spectral jumps is directly related to the excitation power [246], we can reasonably assume that the broadening observed at high power in Fig. 2.18(a) results from the impact of long timescale SD broadening of the exciton PL line at high power, which does not contribute as significantly at lower power for a few seconds integration time.

2.7.3 Long-timescale spectral diffusion

The spectral fluctuations induced by long-timescale charge fluctuations are easily discernible in µ-PL measurements when tracking the positions of excitonic lines over time. A representative time series for QD$_{\text{C}}$ is presented in Fig. 2.19(a), with the characteristic PL spectrum provided in the inset, featuring labeled exciton (X) and biexciton (XX) peaks. The additional

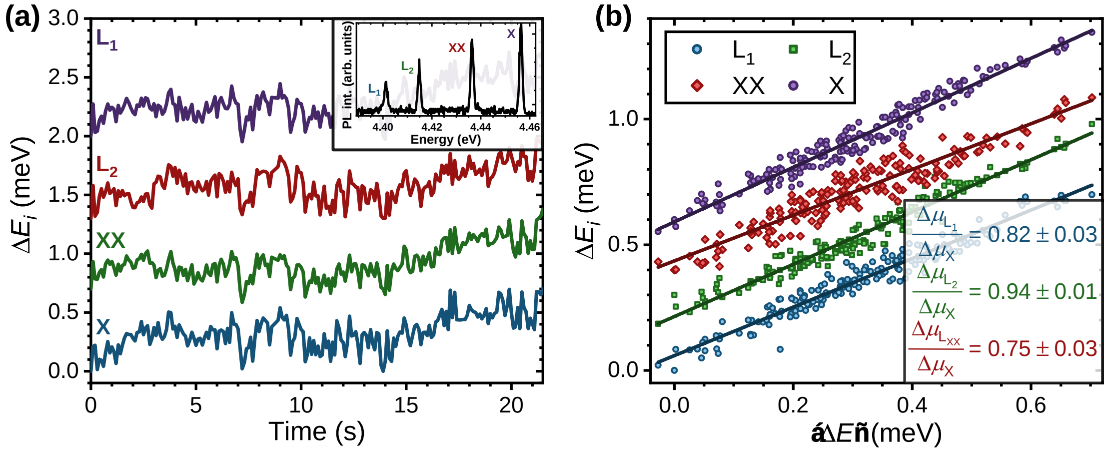

Figure 2.19: **(a)** Time jitter in the PL of excitonic lines extracted from $\mathrm{QD_C}$. The inset shows a PL spectrum recorded for this QD. **(b)** Relative energy shift of individual lines as a function of the average energy shift for all lines. Both graphs feature datasets shifted by an arbitrary offset for clarity, which has no impact on the underlying physics. The results were obtained at 5 K with $\lambda_{\mathrm{exc}} = 244\,\mathrm{nm}$ and $\sigma_{\mathrm{exc}} = 36\,\mathrm{kW\cdot cm^{-2}}$.

low-energy peaks $\mathrm{L_1}$ and $\mathrm{L_2}$ are not specifically assigned to a particular excitonic complex at this stage, and a discussion on their origin is deferred to Sect. 2.8. The relative energy shift ΔE_i is arbitrarily measured with respect to the first data point ($\Delta E_i(t) = E_i(t) - E_i(0)$), and each curve is offset arbitrarily for clarity.

By evaluating the average energy shift for each PL spectrum through:

$$\langle \Delta E \rangle (t) = \sum_{i=1}^{4} \Delta E_i(t)/4, \tag{2.64}$$

we can compare the relative motion of each line with respect to the others by plotting their respective energy shifts against $\langle \Delta E \rangle$, as depicted in Fig. 2.19(b). The correlation between each line, is evident graphically from the collective variations highlighted in Fig. 2.19(a) but can be rigorously quantified by evaluating the Pearson correlation coefficient (Cor) between each pair of lines [247]:

$$\mathrm{Cor}(\Delta E_i, \Delta E_j) = \frac{\mathrm{Cov}(\Delta E_i, \Delta E_j)}{\sigma_{\Delta E_i}, \sigma_{\Delta E_j}}, \tag{2.65}$$

where $\sigma_{\Delta E_{i,j}}$ represents the standard deviation of each line's relative shift $\Delta E_{i,j}$. Coefficient values are reported in Table 2.1, with a minimum Cor between $\mathrm{L_2}$ and XX lines of 0.77, still suggesting a strong correlation of the jitter experienced by all emission lines and corroborating their common spatial origin.

Figure 2.19(b) also provides information about the nature of each QD (multi-)excitonic state,

Cor	**L$_1$**	**L$_2$**	**XX**	**X**
L$_1$	1	0.83	0.91	0.92
L$_2$	0.83	1	0.77	0.84
XX	0.91	0.77	1	0.90
X	0.92	0.84	0.90	1

Table 2.1: Pearson correlation coefficients between multiexcitonic lines of QD$_\mathrm{C}$.

given that Eq. 2.58 yields:

$$\frac{\Delta E_i}{\Delta E_j} = \frac{\Delta \mu_i}{\Delta \mu_j}, \tag{2.66}$$

with the ratio $\Delta E_i/\Delta E_j$ being equal to the ratio of the slope of the linear regressions provided in Fig. 2.19(b). It is thus possible to evaluate the dipole moment of different excitonic states, using, for instance, the exciton line as a reference. The ratios $\Delta E_i/\Delta E_\mathrm{X}$, with $i = \mathrm{L}_1, \mathrm{L}_2, \mathrm{XX}$ are reported in the figure legend.

A corollary to Eq. 2.60 can be expressed as follow:

$$\Delta\mu_\mathrm{X} > \Delta\mu_{\mathrm{X}^\pm} > \Delta\mu_\mathrm{XX} > \Delta\mu_{\mathrm{XX}^\pm}. \tag{2.67}$$

In our measurements, the biexcitonic line is associated with the minimum dipole moment, with a ratio of $\Delta\mu_\mathrm{XX}/\Delta\mu_\mathrm{X} = 0.75 \pm 0.03$, in strong agreement with the coefficient of 0.74 ± 0.04 reported by Hönig *et al.* [225]. This further corroborates the proposed identification of excitonic and biexcitonic states. It is noteworthy that the trend observed in our data, $\Delta\mu_\mathrm{X} > \Delta\mu_{\mathrm{L}_1} > \Delta\mu_{\mathrm{L}_2} > \Delta\mu_\mathrm{XX}$ suggests that L$_{1,2}$ do not originate from higher multiexcitonic states (less than two EHPs). This observation is further explored in Sect. 2.8.

2.7.4 Spectral diffusion and defect concentration

The phenomenological description provided in Subsect. 2.7.1 establishes a direct correlation between low-temperature spectral broadening and the presence of defects near emitters. The linewidth of excitonic states is found to increase proportionally to their permanent dipole moment. Smaller QDs, characterized by a reduced vertical electron-hole wavefunction separation, exhibit a lower sensitivity to their environment, resulting in narrower emission lines compared to larger QDs. This observation is obvious when examining the linewidth of single exciton lines at different energies, as depicted in Fig. 2.20(a), where E_X increases with confinement. The trend aligns with previous findings made at lower energy values by Kindel *et al.* [231]. Notably, this contrasts with the linewidth statistics recorded at RT (Fig. 2.20(b)), revealing that thermal broadening follows a normal distribution weakly dependent on the QD size. A slight decrease in linewidth is still observed as the energy increases. The permanent dipole moment also leads to an asymmetric linewidth distribution, a phenomenon explored by C. Kindel in his thesis [162], which can be empirically approximated by a Fréchet

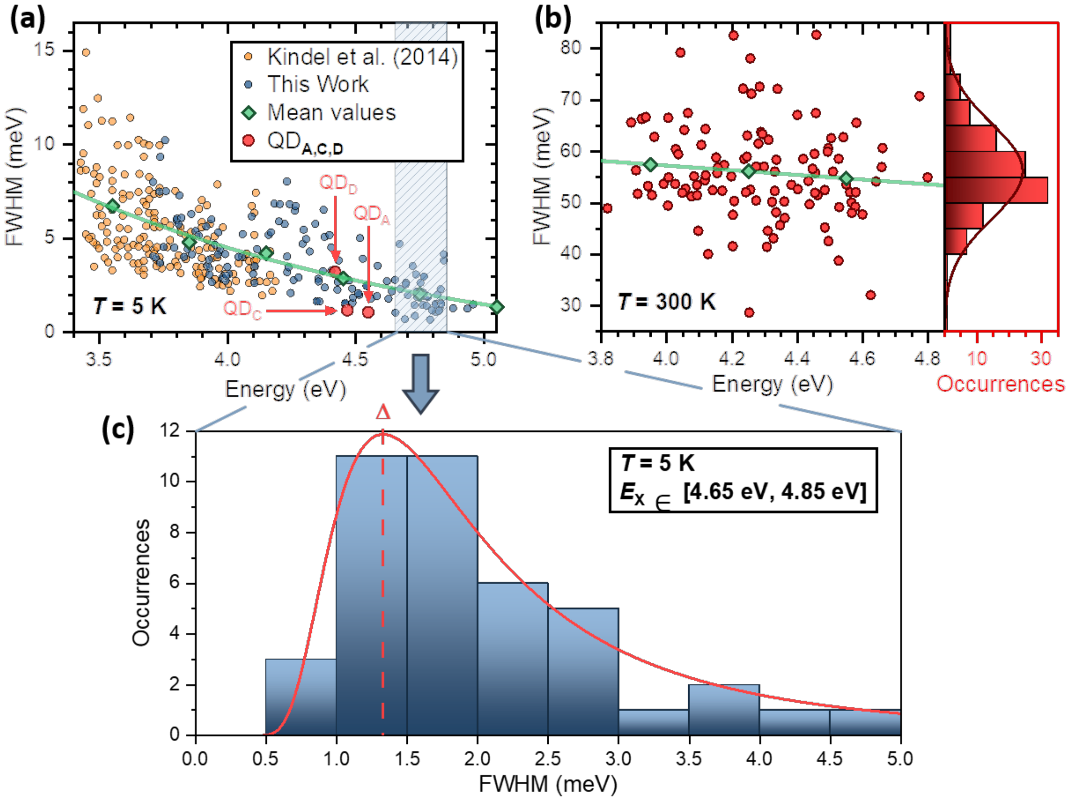

Figure 2.20: Linewidth statistics at **(a)** 5 K and **(b)** 300 K. Blue and red datapoints where manually extracted at low excitation power over processed areas of the sample L1244. Orange dots correspond to QDs grown by metalorganic vapor-phase epitaxy (MOVPE) on SiC [231]. Green points represent mean values computed over 0.3 eV intervals and solid green lines are provided as guides to the eye. Linewidths determined for QDs emitting in the range of 4.65 to 4.85 eV (hatched area) are reported in a histogram **(c)**. The distribution is fitted with the Fréchet probability distribution function (PDF) (Eq. 2.68) times a normalization factor. $\Delta_{SD} = (1.3 \pm 0.3)$ meV was determined as an average over multiple binning parameters.

distribution closely linked to defect concentration. Intuitively, an increased number of defects should, on average, create a larger electric field ($\mathbf{F}_{\text{ext}}$) in the vicinity of a QD, resulting in larger energy fluctuations.

The Fréchet-like PDF of the exciton linewidth for a given exciton energy is approximated by [162]:

$$f_{Fr}(\Gamma_{SD}) = \frac{\alpha}{s}\left(\frac{\Gamma_{SD}}{s}\right)^{-1-\alpha} \exp\left[-\left(\frac{\Gamma_{SD}}{s}\right)^{-\alpha}\right]. \tag{2.68}$$

Here, the scaling parameter s and the shape parameter α are considered as free parameters. The Fréchet PDF features a maximum denoted as Δ_{SD} which relates to the defect concentration (denoted as $\tilde{c}$) through [162]:

$$\tilde{c}(E_X) = \frac{3}{4\pi}\left[\frac{1}{2\sqrt{2\ln 2}}\frac{1}{\sqrt{p_{\mathrm{oc}}(1-p_{\mathrm{oc}})}}\right]^{3/2}\left(\frac{\Delta_{\mathrm{SD}}(E_X)}{\kappa e}\right)^{3/2}, \tag{2.69}$$

where e is the elementary charge, and κ is a coefficient computed through Monte-Carlo simulations that varies with the exciton energy E_X. Since Eq. 2.69 is energy-dependent, we should theoretically apply Eq. 2.68 on a dataset acquired over a restricted spectral range. To estimate the defect concentration based on a statistically significant dataset, we selected excitons lines between 4.65 and 4.85 eV, as indicated in Fig. 2.20(a) by a hatched rectangle. The associated histogram is reproduced in Fig. 2.20(c). Although the dataset may be insufficient for an accurate reproduction of the Fréchet PDF, it is substantial enough for a precise estimate of Δ_{SD}. We computed a minimum defect density of $10^{18}\,\mathrm{cm}^{-3}$, which aligns well with the $\sim 2\times 10^{19}\,\mathrm{cm}^{-3}$ defect density reported by C. Kindel [162]. In comparison, Holmes *et al.* [137] estimated for their part a minimum defect density around $10^{17}\,\mathrm{cm}^{-3}$ for site-controlled GaN/AlGaN nanowire QDs, consistent with their reported sub-meV linewidths.

2.7.5 Spectral diffusion in second-order correlation measurements

In Subsect. 2.7.3, we demonstrated the occurrence of SD on different timescales. While the characteristic time of spectral jittering occurring in a matter of seconds is readily observable with a conventional setup, pico- to nanosecond features cannot be resolved with a CCD, which typically has integration times above the millisecond and readout noise that strongly impacts the SNR when recording low photon counts. However, such features are accessible in correlation measurements, and we will explore how $g^{(2)}(\tau)$ functions transform when considering short-timescale SD. In the following, we present a model developed by Sallen *et al.* [248], which we limit to the case of autocorrelation for the sake of conciseness, by considering the same spectral window (see Fig. 2.21(a)) for both SPD of the HBT, in accordance with our experimental setup.

Let us first consider a TLS experiencing SD, as schematized in Fig. 2.21(b), with negligible natural broadening so that the system can be considered either entirely 'inside' or 'outside' the HBT detection range. At a time τ, the system is in one of four states: two ground states $|0,\mathrm{in}\rangle$, $|0,\mathrm{out}\rangle$, and two excited states $|1,\mathrm{in}\rangle$, $|1,\mathrm{out}\rangle$, with respective populations $n_{0,\mathrm{in}}$, $n_{0,\mathrm{out}}$, $n_{1,\mathrm{in}}$, and $n_{1,\mathrm{out}}$. All transition rates are reported in Fig. 2.21(b). Denoting $N_i = n_{i,\mathrm{in}} + n_{i,\mathrm{out}}$ with $i \in 0,1$ and $N_{\mathrm{s}} = n_{0,\mathrm{s}} + n_{1,\mathrm{s}}$ with $\mathrm{s} \in \mathrm{in},\mathrm{out}$, the following rate equations hold:

$$\frac{\mathrm{d}N_1}{\mathrm{d}t} = \pi N_0 - \gamma_1 N_1, \tag{2.70}$$

$$\frac{\mathrm{d}N_{\mathrm{in}}}{\mathrm{d}t} = \gamma_{\mathrm{in}} N_{\mathrm{out}} - \gamma_{\mathrm{out}} N_{\mathrm{in}}. \tag{2.71}$$

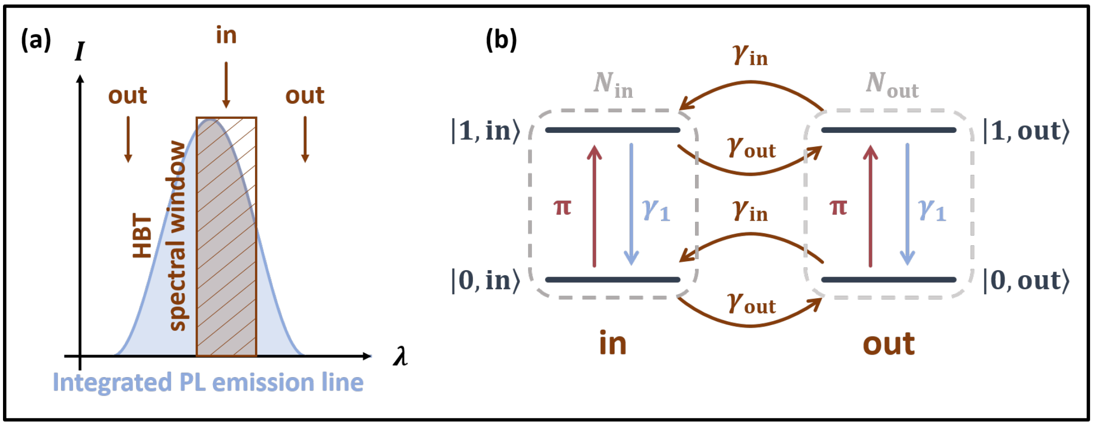

Figure 2.21: Illustration of **(a)** the spectral selectivity of $g^{(2)}(\tau)$ measurements and **(b)** the associated modeling of SD in a TLS. γ_{in} anf γ_{out} represent the rate at which the emission PL emission transitions in and out of the spectral HBT spectral window.

Knowing that $N_0 + N_1 = 1$, $N_{\text{in}} + N_{\text{out}} = 1$, the solutions read:

$$N_1(\tau) = \frac{\pi}{\gamma_1 + \pi} + A\exp^{-(\gamma_1+\pi)\tau}, \tag{2.72}$$

and

$$N_{\text{in}}(\tau) = \frac{\gamma_{\text{in}}}{\gamma_{\text{in}} + \gamma_{\text{out}}} + B\exp^{-(\gamma_{\text{in}}+\gamma_{\text{out}})\tau}, \tag{2.73}$$

where A and B depend on the initial conditions. From the axiom of conditional probability[XXII], we obtain:

$$n_{1,\text{in}} = N_1 N_{\text{in}}. \tag{2.74}$$

The second-order autocorrelation function of the probed state, namely $|1,\text{in}\rangle$, is then readily derived by combining Eqs. 2.72, 2.73 and 2.74, with the starting condition $n_{0,\text{in}}(0) = 1$:

$$g^{(2)}_{\text{TLS(SD)}}(\tau) = \frac{n_{1,\text{in}(|\tau|)}}{n_{1,\text{in}(+\infty)}} = \frac{N_1(|\tau|)}{N_1(+\infty)}\frac{N_{\text{in}}(|\tau|)}{N_{\text{in}}(+\infty)} = g^{(2)}_{\text{TLS}}(\tau)g^{(2)}_{\text{SD}}(\tau). \tag{2.75}$$

$g^{(2)}_{\text{TLS}}(\tau)$corresponds to the two-level second-order autocorrelation function derived in Subsect. 2.2.4, while $g^{(2)}_{\text{SD}}(\tau)$is given by:

$$g^{(2)}_{\text{SD}}(\tau) = 1 + \left(\frac{\gamma_{\text{SD}}}{\gamma_{\text{in}}} - 1\right)e^{-\gamma_{\text{SD}}|\tau|}, \tag{2.76}$$

with $\gamma_{\text{SD}} = \gamma_{\text{in}} + \gamma_{\text{out}}$.

[XXII] Given two events E_1 and E_2, the probability that both occur simultaneously follows the relation $P(E_1 \cap E_2) = P(E_1|E_2)/P(E_2)$.

This solution can be generalized to any model with an arbitrary number of states, provided that each of them splits into 'in' and 'out' states when taking SD into account. The notion of 'in' and 'out' only refers to the electronic environment, ensuring that the probed state (e.g., an exciton bright state or a radiative defect state) is located inside or outside the HBT spectral window. It still applies if other radiative states of the system are effectively emitting outside of this spectral window.

The expression derived in Eq. 2.76 thus applies on a large scale to any system experiencing SD independently of its specific nature, resulting in a bunching phenomenon that superimposes onto the intrinsic features of the system. However, this effect is not necessarily substantial and depends on the experimental conditions and the temporal scale of SD. The SD-related bunching is driven by γ_{SD}, a characteristic SD rate that reflects the timescale at which charge fluctuations occur. SD does not depend on the chosen HBT spectral window [244, 248]. Instead, γ_{in} and γ_{out} depend on whether a spectral jump is likely to drive the system in or out of the measurement window and scale with the portion of the PL peak encompassed within this spectral window. This is graphically illustrated in Fig. 2.21(a), with γ_{in} equal to γ_{SD} times the ratio between the brown and brown+blue areas. Thus, the amplitude of the SD bunching is directly related to the extent of the HBT spectral window and effectively disappears when the measurement window is chosen larger than the PL peak. This feature can be apprehended intuitively: the bunching feature reflects the high likelihood of measuring a second photon event in the HBT window after measuring a first detection, given the emitter's environment had no time to change. When γ_{SD} is much larger than the recombination rate γ_1, SD becomes imperceptible. As such, long timescale SD features described in Subsect. 2.7.3 are not expected to impact the $g^{(2)}(\tau)$ measurements.

In contrast, the SD primarily responsible for the PL line broadening detailed in Subsect. 2.7.2 occurs on a timescale smaller than the integration time required to obtain an exploitable SNR, and as such, $\tau_{\mathrm{SD}} = \gamma_{\mathrm{SD}}{}^{-1}$ has been initially estimated below a few tens of ms for GaN/AlN SAQDs [231]. In more recent studies, the formalism reproduced here has been applied to interface fluctuations GaN/AlGaN QDs [232] and InGaN/GaN SAQDs [244], yielding at $T \leq 10\,\mathrm{K}$ SD times of $\sim 10\,\mathrm{ns}$ to hundreds of ns, respectively. We can reasonably assume that our system features similar SD timescales, although our HBT setup functioning in the *start-and-stop* mode (see Subsect. 1.5.2) in the UV significantly hinders the detection of spectral features that require recording $g^{(2)}(\tau)$ traces over hundreds of ns.

We should additionally note that the above formalism it not limited to the description of SD related to the charge fluctuations of external defects. State fluctuations internal to the QD can likewise result in a reduced probability of recording photon events stemming from the same excitonic states long after the detection of a first event, as has already been evidenced for oscillations between neutral ($|\mathrm{X}\rangle$) and charged ($|\mathrm{X}^{\pm}\rangle$) exciton states [249, 250].

As a final comment, we should mention that γ_{SD} is expected to drastically increase with temperature, although the exact relationship is tied to the origin of defect-related traps, be they shallow defects driven by an increased density of free carriers or deep defects experiencing photoexcitation and phonon or Auger-Meitner relaxation. Simultaneously, as T increases, the line broadening is increasingly dominated by a phonon-mediated dephasing process bound to occur at a ps timescale [251–253], well faster than the time-resolution of the HBT setup. As such, the emission line can no longer be treated as a delta function, rendering the above formalism incompatible with experimental observations. Intuitively, we can anticipate that thermal broadening (Γ_{th}) progressively reduces the SD bunching amplitude to an extent where it completely disappears, as the SD-related broadening becomes negligible ($\Gamma_{\mathrm{sd}} \ll \Gamma_{\mathrm{th}}$).

2.7.6 Summary

At this juncture, we have presented a phenomenological understanding of spectral jittering impacting emission lines, elucidating how this phenomenon, known as spectral diffusion (SD), markedly broadens excitonic lines in GaN/AlN QD structures at cryogenic temperatures. The broadening effect arises due to the significant permanent excitonic dipole moment. SD manifests itself on various timescales, ranging from a few nanoseconds to tens of seconds, indicative of the diverse mechanisms and types of defects involved in this phenomenon. While SD poses challenges for quantum applications, its effects can be harnessed for the precise identification of excitonic PL features. It is crucial to emphasize that long timescale SD is not a hindrance for quantum applications [254], unlike ultrafast SD features. This underscores the necessity of distinguishing between the two. While our intention was not to provide an unequivocal identification of the defects responsible for SD in GaN/AlN SAQDs, this section offers a comprehensive description of the limitations encountered when studying the PL properties of quantum emitters strongly coupled to their environment. Similar features have been reported for GaN defects behaving as SPEs [255], heralding analogous challenges for our work on PDs (Chap. 3).

2.8 Photoluminescence of individual quantum dots

While several PL spectra have already been partly commented in Sect. 2.5 and 2.7, the discussion has been until now centered on the behavior of well-identified exciton and biexciton lines. However, the high-energy QDs investigated in this work usually display a more complex optical signature that we try to unravel in this section.

2.8.1 Optical signature

Excluding PL peaks related to phonon replicas (as briefly discussed in Subsect. 2.5.2), all QD PL lines are typically attributed either to different multiexcitonic complexes (exciton, biexciton, triexciton, etc.) or to different energy levels within the same multiexcitonic state, (i.e., different energy levels for a given N_{EHP}) [256]. Setting aside non-radiative processes, the relative intensity of each line arises from a complex interplay between the oscillator strength

(f_{osc}) of each envisaged optical transition and the occupancy probability of the associated initial state. As a result, the PL spectrum strongly depends on the excitation power and temperature, as emphasized in Sect. 2.4 and 2.5, but can also vary from one QD to another, following size and anisotropy variations. While theoretical studies predict the existence of a multiplicity of radiative states in GaN/AlN QDs [64, 108, 116], experimental evidence remains sparse, with the majority of publications reporting the presence of lines readily attributed to the ground exciton and biexciton states.

Throughout this work on high-energy QDs, we have nevertheless repeatedly observed an optical signature consisting of 4 main emission lines at 5 K under reasonably low excitation power density. Representative PL spectra of individual QDs are reported in Fig. 2.22(a), with high-energy bright exciton (X_1) and biexciton (XX) lines, as previously investigated. As detailed in Subsect. 2.8.2, the two additional lines share many similarities with the biexciton line and we should already discard the possibility that they originate from an exciton state. For consistency with our previous publications [24, 196], they are labelled $L_{1,2}$ throughout this chapter.

The spacing between PL lines is not uniform. Instead, the energy separation between X_1 and additional lines appears to fluctuate around an average value, which seems, at first, relatively consistent regardless of the QD size within the narrow (~ 100 meV) spectral window investigated (see Fig. 2.22(b)). The average energy spacing amounts, for the different lines, to $E_{X_1} - E_{XX} = (18 \pm 4)$ meV, $E_{X_1} - E_{L_2} = (39 \pm 5)$ meV and $E_{X_1} - E_{L_1} = (53 \pm 5)$ meV over the dataset recorded.

This apparent uniformity contradicts previous remarks (see Sect. 2.3.1), as the binding energy of multiexcitonic states, equivalent as a first approximation[XXIII] to the energy differences plotted in Fig. 2.22(b), is expected to increase as the QD height reduces. However, changes in height should follow a discrete trend, with variations of a single ML altering the exciton energy by hundreds of meV [145]. Therefore, small energy variations are most certainly related to variations in the QD diameter. In this scenario, increased confinement is expected to strengthen the electron-electron and hole-hole repulsive interactions, leading to a reduction in the binding energy with an increase of the exciton energy, similarly to the case of InAs/GaAs QDs [257].

Bearing these two competitive processes in mind, we can tentatively reinterpret our dataset by assuming that QDs featuring closely related binding energies and exciton energies have the same height, while larger discrepancies are observed for QDs of different height. Graphically, datapoints associated with the same QD height are located on the same dashed lines in Fig. 2.22(c). These correspond to linear guidelines with a shared slope of $-100\,\mathrm{meV}\cdot\mathrm{eV}^{-1}$ and are evenly spaced by 11 meV. Note that these parameters are not supported by any physical simulation and are only found to reproduce accurately empirical observations.

[XXIII] When the FSS is large in comparison to the energy difference between exciton and multiexciton lines, the notion of binding energy defined through Eq. 2.22 becomes ambiguous. Here, we disregard the influence of FSS, as it does not affect the reasoning. A comprehensive reevaluation of the binding energy is proposed in Subsect. 2.8.2.

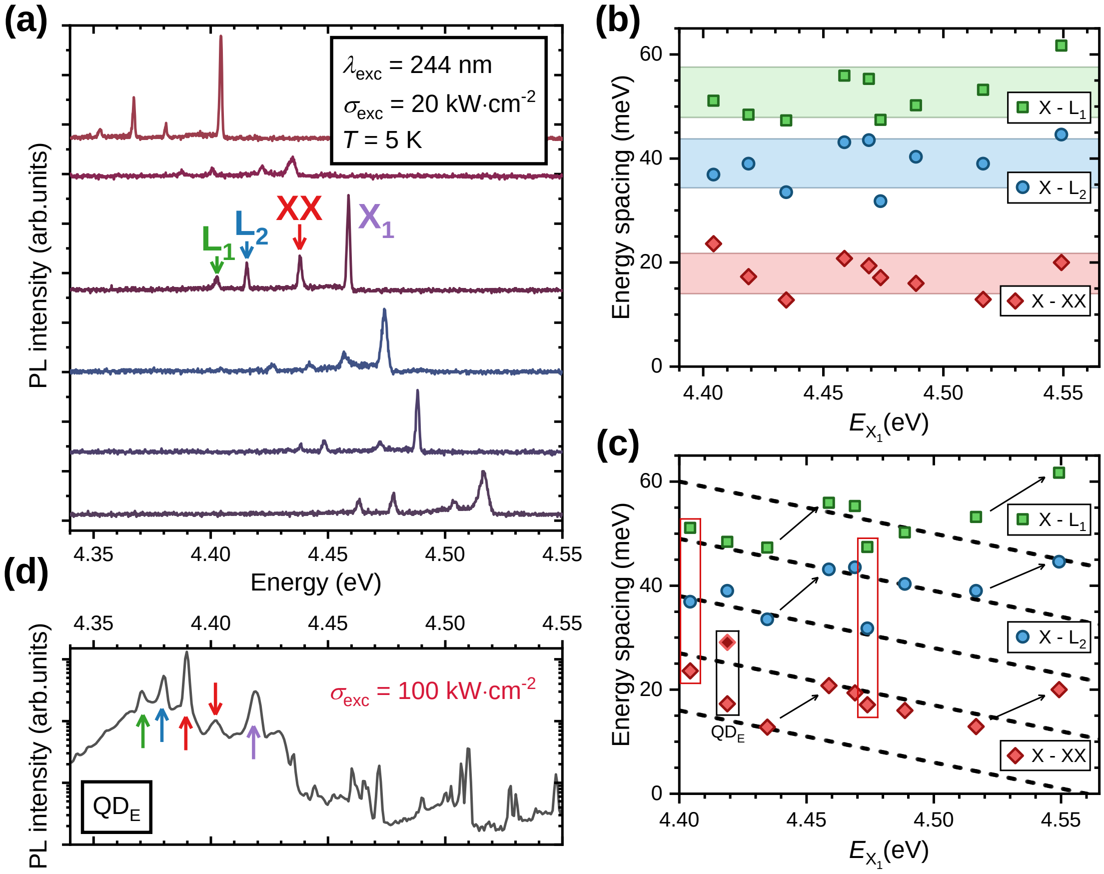

Figure 2.22: **(a)** Representative PL spectra acquired on individual QDs at 5 K. **(b)** Energy spacing between each emission line and the exciton line, as a function of exciton energy. The colored areas denote the mean spacing (using the standard deviation) of the L1 (green), L2 (blue), and XX (red) lines, respectively. **(c)** Reproduction of the energy spacing between pairs of PL lines as a function of exciton energy. Here, we added dashed lines as a guide to the eye with a common slope of $-100\,\mathrm{meV\cdot eV^{-1}}$ and a line spacing of 11 meV. The datapoints highlighted by rectangles are discussed in the text. Black arrows are used to emphasize 'vertical shifts' in the binding energy observed between different sets of QDs. **(d)** PL spectrum of an individual QD ($\mathrm{QD_E}$) acquired at high excitation power density and plotted on a logarithmic scale. The position of the 5 main emission lines is highlighted with arrows. The two alternatives for the XX line (red arrows) are discussed in the text.

We can observe that XX as well as $L_{1,2}$ binding energies seem to align well with this conjecture, with a few exceptions. However, energy shifts attributed to height variations are not fully consistent over the whole dataset. In particular, we can pinpoint two outliers (highlighted by red rectangles in Fig. 2.22(c)) for which the XX binding energy does not align with that of L_1 and L_2. Typically, a 'vertical shift' in binding energy should impact all the lines of a QD simultaneously, but this phenomenon is not observed for these two outliers. At this stage, we can only envisage misattribution of certain PL lines to explain these artifacts. In fact, upon a strong increase in excitation power, multiple other lines can be observed (see Fig. 2.22(d)), hinting at the complexity of a complete QD optical signature. The emitter labelled QD_E illustrates well this potential incorrect assignement, with more than 4 lines clearly visible in the emission spectrum. By attributing one of the two peaks pointed out by red arrows in Fig. 2.22(d) to the XX, we either confirm the conjecture discussed above or generate another outlier (see black rectangle in Fig. 2.22(c)).

Given the above discussion, we can now envisage that, while most of the QDs feature 4 clearly distinguishable PL lines, those transitions may not systematically originate from the same optically active complex. As such, large variations in the binding energy of multiexcitonic complexes originating from QDs with similar exciton energy may be related to a change in the optically 'dominant' state rather than to a height variation. In the following section, we will try to refine our understanding through power- and polarization-dependent measurements.

2.8.2 A case study (QD_C)

Power-dependent photoluminescence

As evidenced in Sect. 2.4, the behavior of PL lines under varying excitation power is closely linked to the radiative multiexcitonic states from which they originate. Examining the PL power series, illustrated in Fig. 2.23(a) for QD_C aids in identifying these optical transitions. The integrated intensity of each line can be evaluated through peak fitting, employing Gaussian, Lorentzian, or Voigt profiles depending on the temperature conditions (refer to Subsect.2.5.2). We should mention here that all error bars are derived from peak fitting. However, this method tends to overlook the contribution of the PSB, particularly affecting the fitting precision for closely spaced lines and becoming less precise with rising temperature. Therefore, the error bars should be interpreted as lower limits on the achievable precision rather than absolute values. Nevertheless, peak fitting remains more reliable than coarse spectral integration due to its enhanced selectivity and can even be applied to weak PL lines if they are distinct from other spectral features. For example, it facilitated the extraction of the X_2 line intensity at 5 K, despite its low intensity (see Fig. 2.23(a)).

The integration results for QD_C are presented in Fig. 2.23(b) and are representative of most investigated QDs. The two exciton lines exhibit a scaling factor close to unity, consistent with the framework outlined in Sect. 2.4. Indeed, a scaling factor $\tilde{n}_{X_2} = 1$ is also anticipated when considering phonon-assisted spin-flips, despite the considerable activation energy of

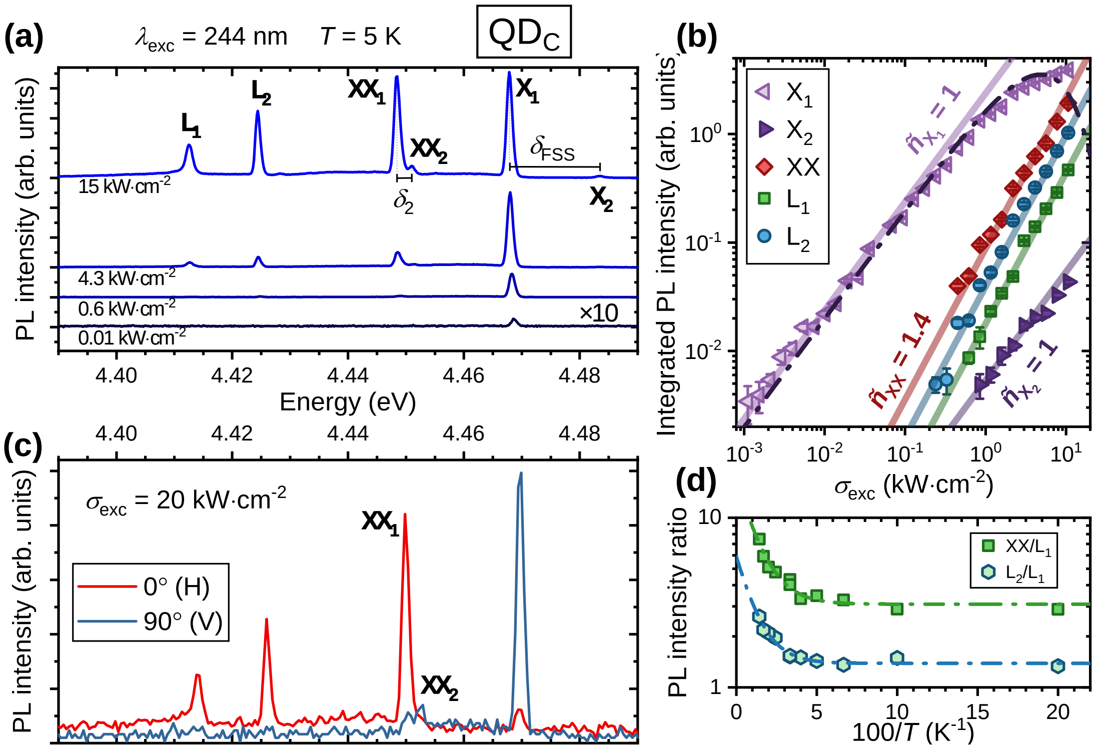

Figure 2.23: **(a)** Power-dependent PL spectra of QD_C, captured at 5 K with $\lambda_{exc} = 244$ nm. $XX_{1,2}$ lines are attributed to hybrid biexciton recombination. **(b)** Variation in the integrated intensity of QD_C PL lines with excitation power density. The X_1 dataset is fitted with Eq. 2.32 (dash-dotted line). **(c)** PL acquired from QD_C for vertical and horizontal polarization. The spectrum is averaged over three CCD pixels to accentuate the presence of the vertically polarized XX_2 line. **(d)** Intensity ratio between pairs of PL lines plotted against inverse temperature. An activation energy of ~ 8 meV is deduced from an Arrhenius fit applied to both intensity ratios (dash-dotted lines).

the high-energy bright state. This can be understood by the efficient relaxation pathway provided by the low-energy bright state toward the ground state, preventing the X_2 line from displaying the sub-linear trend discussed in Subsect. 2.5.3 and illustrated in Fig. 2.15. This outcome further suggests that the low-energy bright state is already activated at 5 K, indicating a close-to-zero or negative dark-to-B_1 (δ_{B_1}) energy splitting for this QD.

In contrast, XX, L_1 and L_2 exhibit a similar behavior, characterized by a superlinear scaling factor $\tilde{n}_{XX} \sim \tilde{n}_{L_1} \sim \tilde{n}_{L_2} \sim 1.4$. This reinforces the hypothesis that these lines do not originate from an exciton state but likely have a common multiexcitonic origin. The subquadratic trend remains puzzling and will be explored in detail in a dedicated subsection (refer to Subsect. 2.8.5). However, it is important to emphasize that the experimental results generally deviate from the predictions based on the assumption of linear scaling of multiexcitonic recombination rates ($\gamma_i = i\gamma_1$). This discrepancy is illustrated in Fig. 2.23(b) by the dash-dotted line obtained from fitting the X_1 dataset using Eq. 2.32. The model anticipates a significant decrease in exciton line intensity under high excitation, when the QD is on average populated by multiple EHPs. Such a drop was never observed in practice throughout this study.

Polarization-dependent photoluminescence

To enrich our understanding of the QD optical signature, we expanded our investigations with polarization-dependent measurements. Alongside the time-dependent correlation among emissions lines discussed in Subsect. 2.7.3, this first serves to confirm that all the observed PL features originate from the same QD. Typically, the PL lines from a single QD are aligned either parallel or perpendicular to one another, exhibiting a strong DLP. For $\mathrm{QD_C}$, PL spectra corresponding to the two principal polarization directions[XXIV] are presented in Fig. 2.23(c), where the vertical axis is arbitrarily defined along the polarization direction of $\mathrm{X_1}$. While it may seem logical to attribute the emission lines XX and $L_{1,2}$ to conventional and hybrid biexciton recombination, it is noteworthy that those three lines feature identical horizontal polarization across all investigated QDs. Given that both conventional and hybrid scenarios predict two orthogonally polarized recombination channels for the biexciton cascade, this initial attribution does not hold. However, we should emphasize that XX usually exhibits an additional cross-polarized shoulder, clearly discernible in Figs. 2.23(a) and 2.23(c). Following the analysis proposed by Hönig *et al.* [148], we assign this pair of lines to radiative transitions from the hybrid biexciton state to either of the two exciton dark states, (refer to Subsect. 2.3.2 for details). Based on this assignment, we label these two lines $\mathrm{XX_1}$(H) and $\mathrm{XX_2}$(V), respectively. Within this framework, the energy difference between $\mathrm{XX_1}$ and $\mathrm{XX_2}$ corresponds to the dark-state splitting, which appears, as expected, to be significantly smaller than the FSS (δ_{FSS} in Fig. 2.23(a)), amounting to $\delta_2 = 2.5\,\mathrm{meV}$ for $\mathrm{QD_C}$. In the hybrid biexciton scenario, the binding energy can be directly inferred from the QD PL spectrum, when disregarding the dark state splitting, using the relation (refer to Fig. 2.24 for a graphical illustration):

$$E^{\mathrm{b}}_{\mathrm{XX_h}} = \mathrm{X_1} - \mathrm{XX} + \delta_{\mathrm{FSS}}/2. \tag{2.77}$$

Here, labels $\mathrm{X_1}$ and XX refer to the energy of the respective PL lines, with XX taken as an average over $\mathrm{XX_1}$ and $\mathrm{XX_2}$. When applied to $\mathrm{QD_C}$, Eq. 2.77 yields $E^{\mathrm{b}}_{\mathrm{XX_h}} = 27\,\mathrm{meV}$. It is worth noting that in the literature, the binding energy is usually reported as the energy difference $\mathrm{X_1} - \mathrm{XX}$, without considering the FSS influence, (refer, for instance, to the data reported in Fig. 2.6).

Since $\mathrm{L_1}$, $\mathrm{L_2}$ and $\mathrm{X_2}$ are horizontally polarized[XXV], we can still consider associating one of these lines to the $|\mathrm{XX_c}\rangle \rightarrow |\mathrm{B_1}\rangle$ transition. In this scenario, the binding energy cannot be directly extracted from the PL spectrum. Instead, it can be estimated, again disregarding the dark state splitting, through:

$$E^{\mathrm{b}}_{\mathrm{L}_i} = \mathrm{X_1} - \mathrm{L}_i - \delta_0 = \mathrm{X_1} - \mathrm{L}_i - \delta_{\mathrm{FSS}}/2 - \delta_{\mathrm{B_1}}, \tag{2.78}$$

[XXIV] These directions are expected to align with the anisotropy axes of the confinement potential [120].

[XXV] The horizontal polarization of $\mathrm{X_2}$ is evidenced in Subsect. 2.8.4.

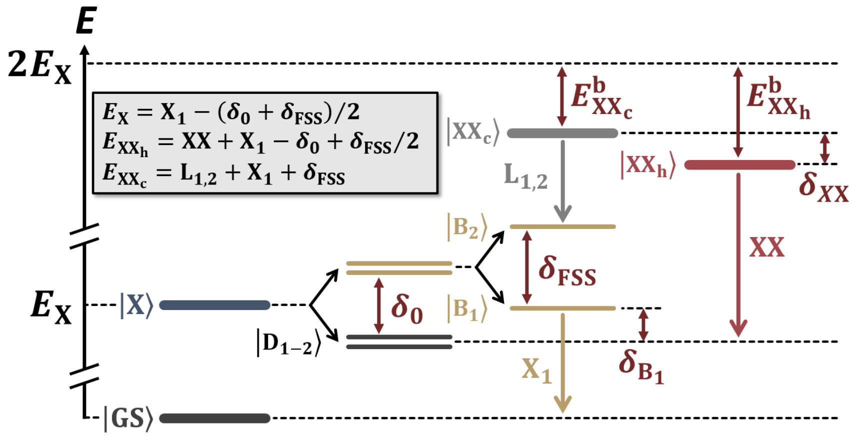

Figure 2.24: Illustration of the QD PL channels in the conventional and hybrid biexciton scenarios, assuming either L_1 or L_2 originates from $|XX_c\rangle$. XX is averaged over the XX_1 and XX_2 lines. δ_{XX} represents the energy difference between the hybrid and the conventional biexciton. The horizontal axis has no physical meaning and the energy levels are arranged to ease the visual presentation.

with $i = 1$ or 2. Drawing from our earlier discussion, we estimated $\delta_{B_1} \leq 0$ allowing us to establish a lower limit on the binding energy. Although δ_{B_1} can take negative values, its magnitude cannot physically exceed half of the FSS ($\delta_{B_1} \geq -\delta_{FSS}/2$), thereby providing an upper limit. We thus obtain the following inequality:

$$X_1 - L_i \geq E^b_{L_i} \geq X_1 - L_i - \delta_{FSS}/2. \tag{2.79}$$

Applying Eq. 2.79 to QD_C, we obtain $43\,\text{meV} \geq E^b_{L_1} \geq 36\,\text{meV}$ and $55\,\text{meV} \geq E^b_{L_2} \geq 48\,\text{meV}$, respectively.

Temperature-dependent photoluminescence

If valid, this finding would imply that, irrespective of the value of δ_{B_1} and the specific PL line under consideration, the conventional biexciton configuration may exhibit greater stability compared to the hybrid biexciton configuration by about 10 to 30 meV. This outcome is highly unexpected, given that no theoretical investigation has thus far predicted such significant positive binding energies for the $|XX_c\rangle$ state (see Subsect. 2.3.2), and we can cast serious doubts on the validity of our conjecture. To further address this issue, we can explore the temperature dependence of XX and $L_{1,2}$.

In a manner similar to the approach outlined in Subsect. 2.5.3, we plot the intensity ratios between XX and L_1 on the one hand, and L_2 and L_1 on the other hand, for QD_C in Fig. 2.23(d) as a function of inverse temperature. While the thermal activation of XX is less pronounced than the activation of X_2 evidenced in Fig. 2.14, we can still observe its gradual increase in intensity relative to L_1. This observation suggests, akin to the behavior exhibited by the bright exciton states, a rise in the population of the hybrid biexciton state with increasing temperature, indicative of a possible phonon-assisted process. However, unlike the exciton, the dominance of the XX line is already evident at 5 K in this example, with an intensity ratio XX/L_1 of approximately 3. The thermal activation is also less pronounced with an activation energy derived from an Arrhenius fit of approximately 8 meV. Although imprecise with an uncertainty of several meV, this activation energy is insufficient to explain the significant energy disparity between $E^{\mathrm{b}}_{\mathrm{L}_1}$ and $E^{\mathrm{b}}_{\mathrm{XX}_\mathrm{h}}$ under the assumption that $|XX_\mathrm{c}\rangle$ gives rise to L_1. Moreover, the temperature-independent intensity ratio between XX and L_2 contradicts the proposal that L_2 could stem from the radiative recombination of a stable conventional biexciton. Therefore, it seems highly improbable that either L_1 or L_2 effectively originates from $|XX_\mathrm{c}\rangle$.

2.8.3 Charged excitons

Considering the inadequacy of the conventional biexciton model in accounting for the presence of the low-energy $\mathrm{L}_{1,2}$ lines, an alternative hypothesis arises in which these additional features may originate from charged (multi-)excitonic states. Initially, we dismissed this idea due to the limitations of the quasi-resonant scheme adopted, which primarily generates EHPs within the QD, hindering the capture of individual carriers. However, we can envisage an alternative mechanism proposed by Hönig *et al.*, where charged states occur through the tunneling of individual carriers toward, e.g., structural defects in the vicinity of the QD [148]. Occasional Auger-Meitner recombination could also explain the formation of such charged states.

From the insights gained in the analysis of long-timescale SD discussed in Subsect. 2.7.3, it appears clearly that charged biexciton states ($\mathrm{XX}^{\pm}$) are unlikely candidates for explaining the presence of $\mathrm{L}_{1,2}$. This conclusion stems from the observation of large dipole moment variations $\Delta\mu_{\mathrm{L}_{1,2}}$ for these lines, which are notably smaller than the biexciton dipole moment variation, thereby contradicting the theoretical expectation that $\Delta\mu_{\mathrm{XX}} > \Delta\mu_{\mathrm{XX}^{\pm}}$. This further suggests a greater compatibility of these lines with charged exciton states ($\mathrm{X}^{\pm}$) with, in theory, $\Delta\mu_{\mathrm{XX}} < \Delta\mu_{\mathrm{X}^{\pm}}$.

Specifically, the positively charged exciton (X^{+}) emerges as the most viable candidate due to its theoretically predicted large positive binding energy and linear polarization aligned with XX_1 and X_1 [148], in agreement with our experimental observations. Nevertheless, key disparities exist between our findings and those detailed in Ref. [148], which warrant some clarification: (i) While Hönig *et al.* noted the occurrence of X^{+} alongside an antibinding X^{-} line (i.e., a line blueshifted compared to the exciton lines), we either found it absent or too weak to be reliably detected in our PL measurements. Conversely, proposing a binding X^{-} state to account for the presence of two low-energy lines ($\mathrm{L}_{1,2}$) seems inconsistent with theoretical predictions, as the proximity of electrons at the apex of the QDs is expected to result in a dominant repulsive Coulomb interaction. (ii) While the intensity of $\mathrm{L}_{1,2}$ varies across emitters, their occurrence is nearly systematic for the high-energy bright QDs investigated here, contrasting with the scarce appearance of such charged states reported in Ref. [148]. A distinct carrier escape mechanism may be necessary to elucidate the features highlighted in this context, although this aspect extends beyond the scope of the current study.

As a concluding note, it is worth emphasizing that the charged exciton scenario seems compatible with the biexciton-like power dependence observed for $L_{1,2}$ lines, evidenced in Fig. 2.23(b), given that these states would be populated via the biexciton state following a single carrier escape. While a linear scaling is often anticipated [249, 258], various scaling behaviors have been documented in different studies [259, 260], with each behavior closely tied to the excitation scheme employed and the specificity of each system. Notably, a biexciton-like scaling behavior has already been documented for charged excitons in InGaN QD systems [261]. At this stage, while L_1 (or L_2) is more likely due to a positively charged exciton (X^+ or positive trion), there remain some areas of uncertainty, particularly regarding the origin of a second line (L_2 or L_1). Further elucidation of these complexities is awaiting future investigation.

2.8.4 Complementary analysis (QD_A)

Although the preceding discussion largely represents our present comprehension of the optical characteristics of the high-energy QDs under investigation, it is essential to emphasize the non-uniqueness of the features observed on QD_C. To further illustrate this point, we present additional PL findings obtained from another emitter labeled QD_A, on which we additionally performed temperature-dependent $g^{(2)}(\tau)$ measurements presented in the forthcoming Subsect. 2.9.2.

While we previously presented polarization-dependent measurements conducted at 5 K in Subsect. 2.8.2, a clearer overview is attained by working at slightly higher temperatures, to enable the observation of temperature-activated features. Specifically, measurements carried out on QD_A at 35 K (Fig. 2.25(a)) highlight the horizontal polarization of the high-energy bright state, otherwise hardly detectable at 5 K. All lines exhibit a clear linear polarization, with a DLP consistently exceeding 0.9 (as illustrated in the inset for XX_1 and X_1). The deviations from unity are primarily attributed to polarizer imperfection, setup limitations (as discussed in Subsect. 1.4) and line spectral overlap.

We can incidentally mention that XX_1 and XX_2 appear here energetically inverted compared to QD_C, which, lacking *ab initio* simulations, we consider a plausible characteristic. Additionally, since we have not conducted any calculations of the oscillator strengths, we can only discuss the relative intensities of each line from a phenomenological standpoint. In this regard, it seems crucial to replicate the striking temperature-induced activation of the high-energy bright state, previously evidenced for QD_C in Subsect. 2.5.3. To achieve this, we extracted the integrated intensities of X_1 and X_2 up to 80 K from the temperature-dependent PL data shown in Fig. 2.25(b). Note that above this temperature, the X_1 intensity can no longer by reliably extracted due to the dominance of X_2 PL. The resulting X_2/X_1 intensity ratio is presented in Fig. 2.25(c).

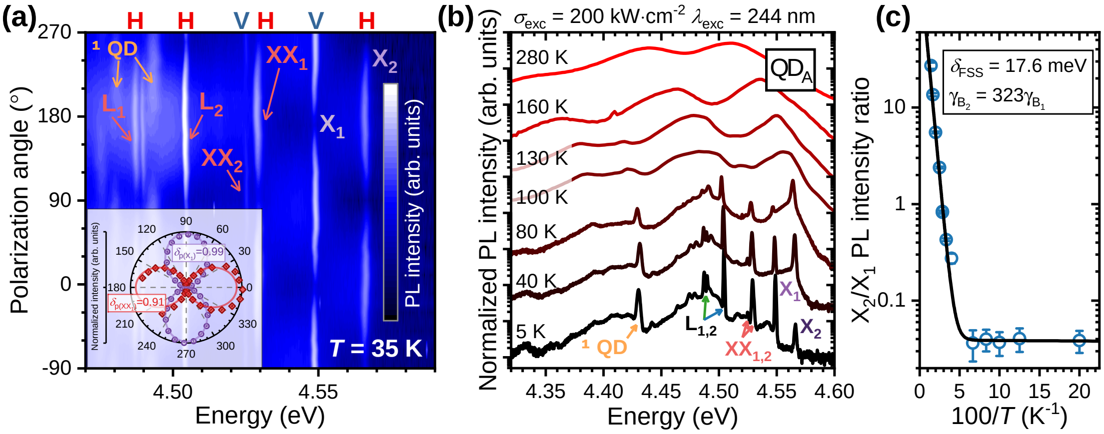

Figure 2.25: **(a)** Polarization-dependent PL of QD_A. The inset illustrates the integrated intensity variations for the XX_1 and X_1 lines as a function of polarization angle. The orientation of all labelled lines is indicated above the graph. The color scale is logarithmic in order to enhance the visibility of faint features. **(b)** Evolution of the PL of QD_A as a function of temperature. Above 80 K, the spectra were recorded using a low-resolution grating (150 lp/mm). **(c)** Intensity ratio X_2/X_1 as a function of inverse temperature from 5 K to 80 K. The black line is simulated using the parameters in the legend and within the framework developed in Subsect. 2.5.3.

As for QD_C, the X_2/X_1 ratio for QD_A is again accurately reproduced by an Arrhenius fit, using the FSS extracted from photoluminescence spectra ($\delta_{FSS} = 17.6\,\text{meV}$) as the activation energy, thereby confirming the thermal activation process discussed in Subsect. 2.5.3. Employing our multi-excitonic model, we successfully replicated the experimental trend (black line in Fig. 2.25(c)) assuming a recombination rate ratio $\gamma_1^{B_2}/\gamma_1^{B_1} = 323$ and a picosecond-scale spin-flip rate (γ_{SF}) at 0 K. While the substantial $\gamma_1^{B_2}/\gamma_1^{B_1}$ ratio surpasses previous findings by orders of magnitude (see, e.g., Ref. [148]), its increase from QD_C to QD_A aligns well with the elevated FSS, which scales with increasing exciton energy. It is worth mentioning that the FSS does not exhibit a linear evolution with exciton energy and is anticipated to sharply rise above 4 meV [121], which is significantly impacting the recombination dynamics of bright exciton states.

2.8.5 The biexciton scaling behavior (QD_E)

While the power-dependent behavior of XX and $L_{1,2}$ typically shows a clear superlinear trend ($\tilde{n}_{L_{1,2},XX} > 1$, as depicted in Fig. 2.23(c)), the scenario proposed in Subsect. 2.5.3 to explain non-linear and non-quadratic scaling behaviors falls short in capturing experimental findings. In our multiexcitonic model, $\tilde{n}_{XX} \to 2$ as $\tilde{n}_X \to 1$, yet experimentally, biexciton lines consistently exhibit a subquadratic scaling factor even for QDs featuring a linear exciton scaling factor. As evidenced in Subsect. 2.8.2, another inconsistency of our model lies in the predicted rapid decrease of the exciton PL intensity at high pumping power, a phenomenon never observed empirically. Instead, the X_1 intensity tends to saturate, as observed again with QD_E in Fig. 2.26.

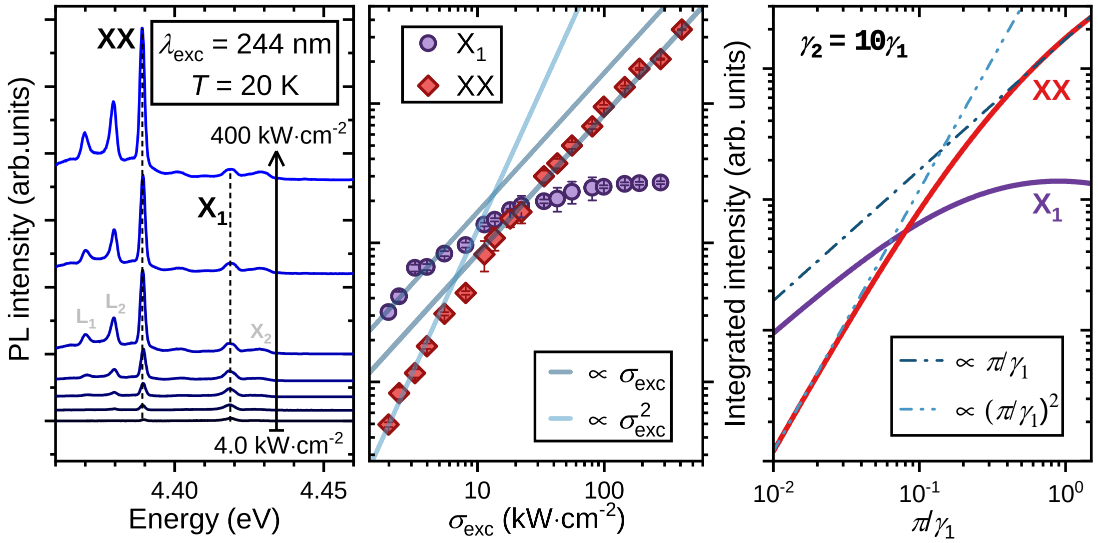

Figure 2.26: **(a)** Power-dependent PL spectra of QD$_E$, recorded at 20 K with λ_{exc} = 244 nm. **(b)** Variation in the integrated intensity of exciton and biexciton lines against excitation power density. Linear and quadratic fits are represented by solid dark and light blue lines, respectively, illustrating the asymptotic behavior of each PL line. **(c)** Simulated exciton and biexciton intensities assuming $\gamma_2 = 10\gamma_1$. This parameterization is not intended to precisely replicate the experimental trends depicted in (b) but rather serves to illustrate the dual scaling behavior described in the main text.

These apparent discrepancies can be reconciled by relaxing the linear constraint on multiexcitonic recombination rates ($\gamma_i \neq i\gamma_1$), assuming instead $\gamma_2 \gg \gamma_1$. In this scenario, the biexciton intensity exhibits distinct scaling behaviors at low and high excitation power. When $\pi \ll \gamma_1$, the QD is mostly empty, and the exciton (the biexciton) scales linearly (quadratically), as illustrated by simulated curves in Fig. 2.26(c). When $\gamma_1 < \pi < \gamma_2$, the exciton intensity saturates, with n_1^{ss} approaching unity. In this regime, the biexciton intensity transitions to a linear scaling behavior, clearly observable in Fig. 2.26(c), which persists until the pump rate approaches γ_2. The larger the difference between γ_1 and γ_2, the more pronounced this dual behavior. To better understand this outcome, let us consider a scenario where the exciton recombination rate tends to 0. In this limit, transitions toward the ground state are mostly impeded, and the biexciton effectively becomes the first excited state of the QD, exhibiting exciton-like behavior with $\tilde{n}_{XX} = 1$.

For QD$_E$, the exciton saturation is particularly pronounced, allowing us to discern the dual behavior of the biexciton, as depicted in Fig. 2.26(b). However, in most cases, the biexciton line is barely resolved in PL spectra at low excitation power density, thus hindering the observation of quadratic scaling. This may, for instance, elucidate the trend previously recorded for QD$_C$ (see Fig. 2.23(b)).

The significant difference between exciton and biexciton recombination rates also explains why higher-order multiexcitonic states are typically not observed under CW excitation, as the excitation power required to efficiently populate such level usually exceeds our experimental capabilities. In this regard, we defer the discussion on higher-order multiexcitonic recombination to experiments performed under pulsed excitation (see Sect. 2.10).

As a closing remark, let us note that while we assumed purely radiative (multi-)excitonic recombinations to reproduce PL results, considering the contribution of non-radiative–e.g. AM–recombination processes does not affect the simulated trends. In fact, non-radiative recombination only affects the absolute intensity of each PL line and would merely lead to a vertical shift of simulated curves if taken into account, with:

$$I_i = \gamma_{\mathrm{i}}^{\mathrm{rad}} n_i \leq \gamma_i n_i = n_i(\gamma_{\mathrm{i}}^{\mathrm{rad}} + \gamma_i^{\mathrm{nrad}}), \tag{2.80}$$

where non radiative recombination rates are denoted by γ_i^{nrad}.

2.8.6 Summary

In conclusion of this section, we have evidenced the peculiar optical signature of high-energy QDs investigated in this thesis and proposed a physically consistent description of the power-, temperature-, polarization- and energy-dependent behavior of the main PL lines. While notable grey areas remain, in particular regarding the attribution of low energy PL lines L_1 and L_2, we proposed here an exhaustive set of scenarios which should serve as groundwork for any future investigation.

2.9 Second-order autocorrelation measurement

While the µ-PL outcomes presented thus far offer substantial clarity regarding the identity of individual emission lines, the definitive assessment of the origin of single-QD features is achieved through second-order correlation measurements conducted on individual PL lines. Given the constraints of our UV µ-PL setup, which does not permit simultaneous investigation of multiple spectral windows, our focus in this thesis has been on autocorrelation measurements exclusively performed on exciton lines. At 5 K, the exciton PL is primarily characterized by the X_1 line, whose analysis is detailed in Subsect. 2.9.1. With increasing temperature, the prominence shifts to X_2, whose characteristics are examined in Subsect. 2.9.2 and 2.9.3.

2.9.1 Single photon emission at cryogenic temperature

The $g^{(2)}(\tau)$ traces depicted in Fig. 2.27(a) were acquired for various excitation power densities at 5 K. They exhibit clear antibunching at zero delay time, accompanied by signatures of bunching stemming from multi-exciton state occupancy under high excitation conditions. The single-photon purity ($g^{(2)}(0)$) was determined through fitting with Eq. 2.39 (indicated by red lines) revealing values as low as $g^{(2)}(0) = 0.05$ under low excitation power density. Here, the fitting procedure does not account for the IRF, whose impact diminishes considerably when recording 'large' antibunching dips. Consequently, the slight increase in $g^{(2)}(0)$ with excitation power density is mainly attributed to the time resolution of our setup.

The $g^{(2)}(\tau)$ data underwent fitting with a shared exciton recombination rate, yielding a decay time of ${\gamma_1}^{-1} = (16 \pm 4)\,\text{ns}$. This value notably surpasses by approximately one to two orders of magnitude the decay times previously reported for GaN QDs emitting above the bulk GaN bandgap [113, 130, 262, 263]. While initially ascribed [196] to the interplay of exciton dark states acting as a long-lived reservoir [207, 249], findings detailed in Subsect. 2.8.4 cast doubt on this hypothesis, suggesting the presence of a low-energy bright state already fully activated at 5 K. A prolonged decay time may instead be consistent with the considerable difference between high- and low-energy bright state recombination rates elucidated in 2.5.3 and 2.8.4, though the PL intensity ratio analysis provided in these sections does not yield an absolute γ_1 value.

Additionally, fitting $g^{(2)}(\tau)$ traces with Eq. 2.39 allows for the estimation of the mean occupation number ($\overline{\mu}$) of QD$_\text{A}$ at each excitation power density, with values reported in the inset of Fig. 2.28(a). $\overline{\mu}$ demonstrates a sublinear behavior, possibly attributable to pump rate saturation [264]. As detailed in Subsect. 2.5.3, the generation of EHPs under quasi-resonant excitation follows a two-step process: initial capture of an EHP (with time τ_exc), followed by intradot relaxation (with time τ_rel). While the capture rate is assumed to scale linearly with power density ($\tau_\text{exc}^{-1} = \alpha_\text{abs}\sigma_\text{exc}$, where the absorption coefficient α_abs is accounting for the pumping efficiency), subsequent phonon-assisted relaxation (τ_rel) is independent of σ_exc, such that:

$$\pi^{-1} = (\alpha_\text{abs}\sigma_\text{exc})^{-1} + \tau_\text{rel}. \tag{2.81}$$

Injecting Eq. 2.81 in $\overline{\mu} = \pi/\gamma_1$, we obtain:

$$\overline{\mu} = \frac{\overline{\mu}_\text{sat}}{1 + \sigma_\text{sat}/\sigma_\text{exc}}, \tag{2.82}$$

with $\overline{\mu}_\text{sat} = (\tau_\text{rel}\gamma_1)^{-1}$ and $\sigma_\text{sat} = (\alpha_\text{abs}\tau_\text{rel})^{-1}$. It is noteworthy that Eq. 2.82 theoretically grants access to the intradot relaxation time and yields $\tau_\text{rel} = 5.5\,\text{ns}$ for QD$_\text{A}$. However, the simplistic nature of the fitting procedure, ignoring factors like enhanced relaxation through AM processes or potential recombination of excited states, casts some uncertainty on these results. Moreover, $\overline{\mu}$ values were derived under the assumption of $\gamma_i = i\gamma_1$, a conjecture repeatedly challenged throughout the preceding sections.

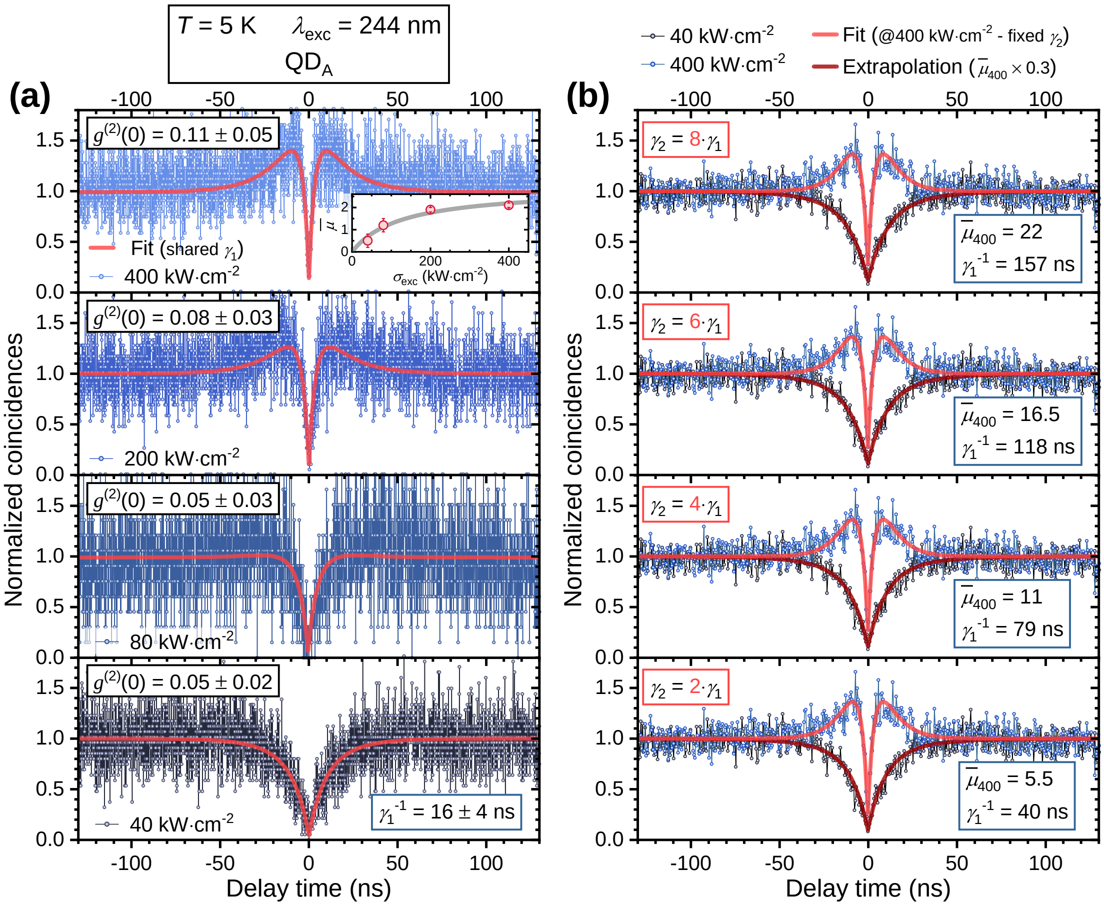

Figure 2.27: **(a)** $g^{(2)}(\tau)$ traces of QD$_A$ recorded at 5 K for excitation power densities ranging from 40 to 400 kW · cm^{-2}, along with convoluted fits shown in red. The channel resolution is 200 ps/channel at 80 kW · cm^{-2} due to a reduced number of coincidences recorded, and 100 ps/channel otherwise. The fitted curves are generated using Eq. 2.39 with a shared recombination rate $\gamma_1 = (16 \pm 4)$ ns across all datasets. The mean occupation numbers ($\bar{\mu}$) extracted from the fits are reported in the inset, yielding $\bar{\mu}_{sat} = 2.9$ when fitting with Eq. 2.82. **(b)** Similar $g^{(2)}(\tau)$ traces recorded at 40 and 400 kW · cm^{-2}, displayed with a resolution of 500 ps/channel for enhanced clarity. The high-power trace is fitted with Eq. 2.48 for varying γ_2/γ_1 ratios (light red curves). The low-power trace is consistently reproduced (dark red curves) by setting $\bar{\mu}$ at 0.3 of its high-power value ($\bar{\mu}_{400}$) while keeping all other fitting parameters fixed.

To evaluate further the validity of our model, we employed an alternative fitting approach using the $g^{(2)}(\tau)$ function (Eq. 2.48) obtained within the three-level framework outlined in Subsect. 2.4.3. This model introduces an additional degree of freedom (γ_2), offering flexibility to fit the data for different values of the γ_2/γ_1 ratio. As depicted in Fig. 2.27(b), we fitted the $g^{(2)}(\tau)$ trace obtained at $400\,\mathrm{kW\cdot cm^{-2}}$ using Eq. 2.48 for $\gamma_2/\gamma_1 = 2,\ 4,\ 6,$ and 8 (light red lines). Remarkably, the experimental dataset is consistently replicated for various ratio values, yielding exciton decay times ranging between 40 and 157 ns, with minimal differences observed between the fitted curves. It is worth noting that $\overline{\mu} = \pi/\gamma_1$ values obtained through this framework (reported for each fit in Fig. 2.27(b)) no longer relate to the mean number of EHPs captured in the QD. In each scenario, the $g^{(2)}(\tau)$ trace recorded at $40\,\mathrm{kW\cdot cm^{-2}}$ is then accurately reproduced (dark red lines) by scaling $\overline{\mu}$ by 0.3[XXVI], demonstrating robust fitting accuracy regardless of the initial assumption.

In the absence of a comprehensive understanding of the scaling behavior of multiexcitonic recombination rates (γ_i), the accuracy of the fit demonstrated in Fig. 2.27(a) does not independently validate Eq. 2.39, and caution must be exercised when interpreting both the mean occupation numbers and exciton decay times determined through this fitting. However, $g^{(2)}(0)$ values remain negligibly affected by the fitting assumptions and are considered reliable. It is worth noting that while neither fitting approach enables the extraction of a quantitative value for π (or equivalently, $\overline{\mu}$), both approaches reveal a sublinear scaling of the pump rate with excitation power density, giving extra credibility to the saturation mechanism described above.

2.9.2 Evolution with temperature

While single-photon emission phenomena have been extensively documented across various systems in the literature, the distinctive feature of GaN/AlN QDs lies in their remarkable preservation of SPE-like behavior up to RT. This remarkable characteristic arises from the strong confinement experienced by trapped EHPs, preventing their thermally-induced escape at elevated temperatures. This feature is prominently illustrated in Fig. 2.28(a), where we replicated the $g^{(2)}(\tau)$ trace acquired at 5 K with an excitation power density of $\sigma_{\mathrm{exc}} = 400\,\mathrm{kW\cdot cm^{-2}}$ for the X_1 line, alongside traces recorded at 150 and 300 K for X_2.

Although values for γ_1 and $\overline{\mu}$ are provided in the legend for the sake of completeness, their reliability is strongly questionable in light of the preceding discussion (see Subsect. 2.9.1). Nervetheless, the narrowing of the antibunching dip when transitioning from the X_1 to the X_2 line aligns with the observed disparity between $\gamma_1^{B_1}$ and $\gamma_1^{B_2}$ discussed earlier. The further reduction of the X_2 antibunching dip between 150 K and RT could potentially be attributed to the influence of thermally-activated non-radiative recombination processes or an increase in the pump rate due to thermally-enhanced intradot relaxation, which may alleviate the saturation behavior discussed in Subsect. 2.9.1.

[XXVI] In practice, the fitting function utilizes the pump rate π as a variable, and $\overline{\mu}$ is derived from the ratio π/γ_1.

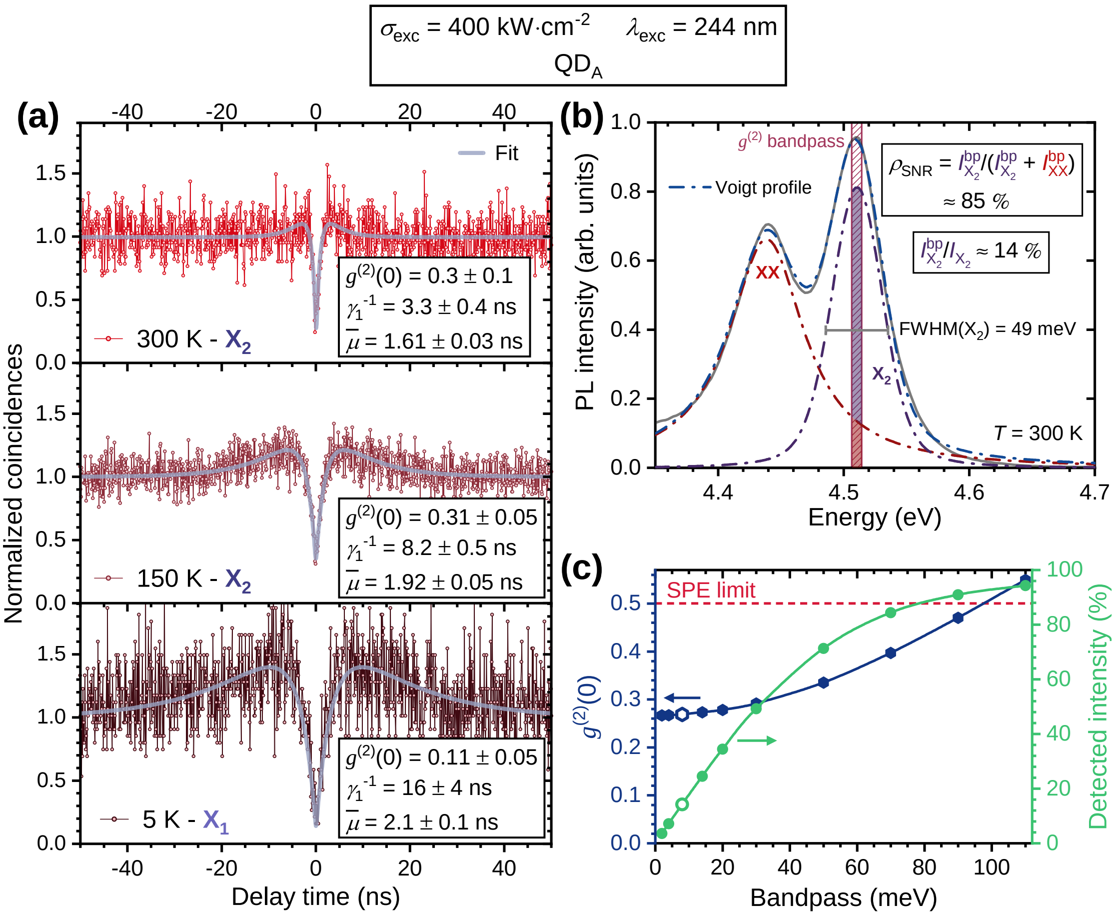

Figure 2.28: **(a)** $g^{(2)}(\tau)$ traces recorded at 400 kW·cm^{-2} on QD$_\mathrm{A}$, as a function of temperature. At 5 K (150 and 300 K, respectively) the HBT spectral window is centered on X$_1$ (X$_2$, respectively). The data are fitted (blues lines) using Eq. 2.39. **(b)** RT PL spectrum recorded on QD$_\mathrm{A}$. The QD signal is approximated by two Voigt profiles, with the biexciton and exciton contributions illustrated by red and purple dashed lines. The hatched rectangle represents the HBT detection window with the filled areas corresponding to the X$_2$ ($I^{\mathrm{bp}}_{\mathrm{X}_2}$) and XX contributions ($I^{\mathrm{bp}}_{\mathrm{XX}}$). I_{X_2} denotes the total intensity of the X$_2$ line. **(c)** Predicted single-photon purity and collected fraction of the exciton PL plotted against the extent of the HBT detection window (bandpass). Empty hexagons correspond to experimental conditions (8 meV bandpass). The solid lines serve as a guide to the eye and all data points are estimated based on the fitting depicted in (b).

It is worth mentioning that variations in capture time should also arise from temperature-dependent changes in the absorption coefficient (α_{abs}). Photoluminescence excitation (PLE) measurements [117, 265] have shown that QD absorption is increased when the laser is resonant with a QD excited state. The redshift experienced by any QD state with increasing temperature should consequently affect α_{abs} in a hardly-predictable manner, making it virtually impossible to maintain a constant pump rate at different temperatures.

Despite the apparent preservation of single-photon purity illustrated in Fig. 2.28(a), we still observe a rise in the $g^{(2)}(0)$ value measured at elevated temperatures. This increase is attributed to the presence of parasitic background emission from the biexciton line, as all PL features are thermally broadened. To confirm this attribution, we examined the RT PL of QD_A, illustrated in Fig. 2.28(b). The overlap between exciton (X_2) and biexciton (XX) PL is evidenced by approximating each line with a Voigt profile. While the XX is predominently Lorentzian, X_2 exhibits a strong Gaussian-like shape, suggesting the presence of another unresolved PL component. Ignoring this feature, we can estimate the SNR for our $g^{(2)}(\tau)$ measurements by assuming all parasitic emission stems from XX:

$$\rho_{\text{SNR}} = \frac{I^{\text{bp}}_{\text{X}_2}}{I^{\text{bp}}_{\text{X}_2} + I^{\text{bp}}_{\text{XX}}}. \tag{2.83}$$

Here, $I^{\text{bp}}_{\text{X}_2}$ and $I^{\text{bp}}_{\text{XX}}$ represent the exciton and biexciton PL intensities integrated over the HBT detection window. By applying:

$$g^{(2)}_{\text{X}}(0) = 1 - \rho^2_{\text{SNR}}, \tag{2.84}$$

with the SNR ($\rho_{\text{SNR}} = 0.85$) estimated from the PL spectrum (Fig. 2.28(b)), we obtain $g^{(2)}(0) = 0.27$, in close agreement with the $g^{(2)}(0) = 0.3$ value extracted from the corresponding RT $g^{(2)}(\tau)$ trace (Fig. 2.28(a)). This agreement confirms that the reduction of single-photon purity is primarily driven by the exciton-biexciton overlap.

It is important to mention that while we refer here to the low-energy line observed in Fig. 2.28(b) as a biexciton, the energy splitting between both lines is more consistent if we instead attribute this low-energy feature to L_2. The label 'XX' originates from the chronology of our work (see Ref. [24, 196]) and refers more generally to the 'biexciton-like' behavior of this line, given the challenge in properly resolving closely related features such as $\text{L}_{1,2}$ and XX at RT.

Although our UV HBT setup imposes a maximum detection window of 8 meV, there is theoretically room to enhance the collection efficiency of exciton PL by utilizing a larger detection window, while minimizing any compromise to single-photon purity. This potential is demonstrated in Fig. 2.28(c), where we inferred the prospective changes in $g^{(2)}(0)$ values and collection efficiency with varying HBT bandpass. These extrapolations rely on parameters derived from peak fitting, as depicted in Fig. 2.28(b), and indicate that single-photon emission ($g^{(2)}(0) \leq 0.5$) can be maintained for QD_A while capturing up to 90% of the exciton PL. More interestingly, $g^{(2)}(0)$ should remain remarkably stable up to a 50% collection efficiency of the exciton PL, yielding $g^{(2)}(0) = 0.29$ for a bandpass of 30 meV. Utilizing such a bandpass would facilitate measurements at lower excitation power densities, further reducing the contribution of the biexciton line. Hence, there is substantial potential for improving our results.

2.9.3 Single photon emission at room temperature

The remarkable high RT single-photon purity observed with $\mathrm{QD_A}$ is not an isolated occurrence. Similar characteristics were noted across all analyzed exciton traces (see Fig. 2.29(b)), with a record low $g^{(2)}(0) = (0.17 \pm 0.08)$ measured at 300 K for the emitter designated as $\mathrm{QD_B}$. Figure 2.29(b) displays the $g^{(2)}(\tau)$ traces recorded on this QD at various excitation power densities. PL spectra captured on $\mathrm{QD_B}$ at RT reveal a trend akin to that observed on $\mathrm{QD_A}$ (cf. Fig. 2.29(c)), albeit with an additional line clearly discernible under high excitation. While initially attributed to the $\mathrm{X_1}$ line (see Ref. [211]), our previous discussion, along with the XX-like behavior it exhibits in Fig. 2.29(d), suggests instead a 'biexcitonic' origin. Hence, it is referred to as XX^* here, although its minimal impact on the SNR allows us to disregard its influence in the subsequent analysis. Incidentally, it is worth noting that employing the 266 nm laser for excitation enabled us to achieve a higher pump rate on $\mathrm{QD_B}$ than on $\mathrm{QD_A}$, as evidenced here by the pronounced bunching observed in Fig. 2.29(b). The decision to switch between 266 nm and 244 nm lasers was primarily driven by technical contingencies.

Despite the overlapping signals of exciton and biexciton lines, we are still able to estimate the integrated intensity of each feature using the peak fitting method demonstrated in Fig. 2.29(d). It is worth reiterating that experimental uncertainties are likely underestimated with fitting errors providing us only with a lower bound. The data are well approximated by Eq. 2.32 suggesting a smaller discrepancy between $\gamma_1^{\mathrm{B_2}}$ and γ_2 compared to the previously reported difference between $\gamma_1^{\mathrm{B_1}}$ and γ_2 at low temperatures. However, the model yields sublinear ($\tilde{n}_{\mathrm{X_2}} = 0.77$) and subquadratic ($\tilde{n}_{\mathrm{X_2}} = 0.1.29$) scaling factors for the exciton and biexciton lines, respectively, despite X_2 being thermally activated at RT with $k_{\mathrm{B}}T(300\,\mathrm{K}) = 25.7\,\mathrm{meV} > \delta_{\mathrm{FSS}}$. These observed behaviors cannot be fully explained within our current multiexcitonic framework (refer to Subsect. 2.5.3), necessitating further analysis which we defer to future investigations.

Owing to the large exciton-biexciton overlap, the single-photon purity exhibits a strong dependence on power, with a vanishing antibunching dip under high excitation not solely attributable to the time resolution of the HBT setup. In fact, $g^{(2)}(\tau)$ traces depicted in Fig. 2.29(b) are fitted with Eq. 2.39 considering the IRF to minimize overestimations. The resulting $g^{(2)}(0)$ values are presented in Fig. 2.29(e).

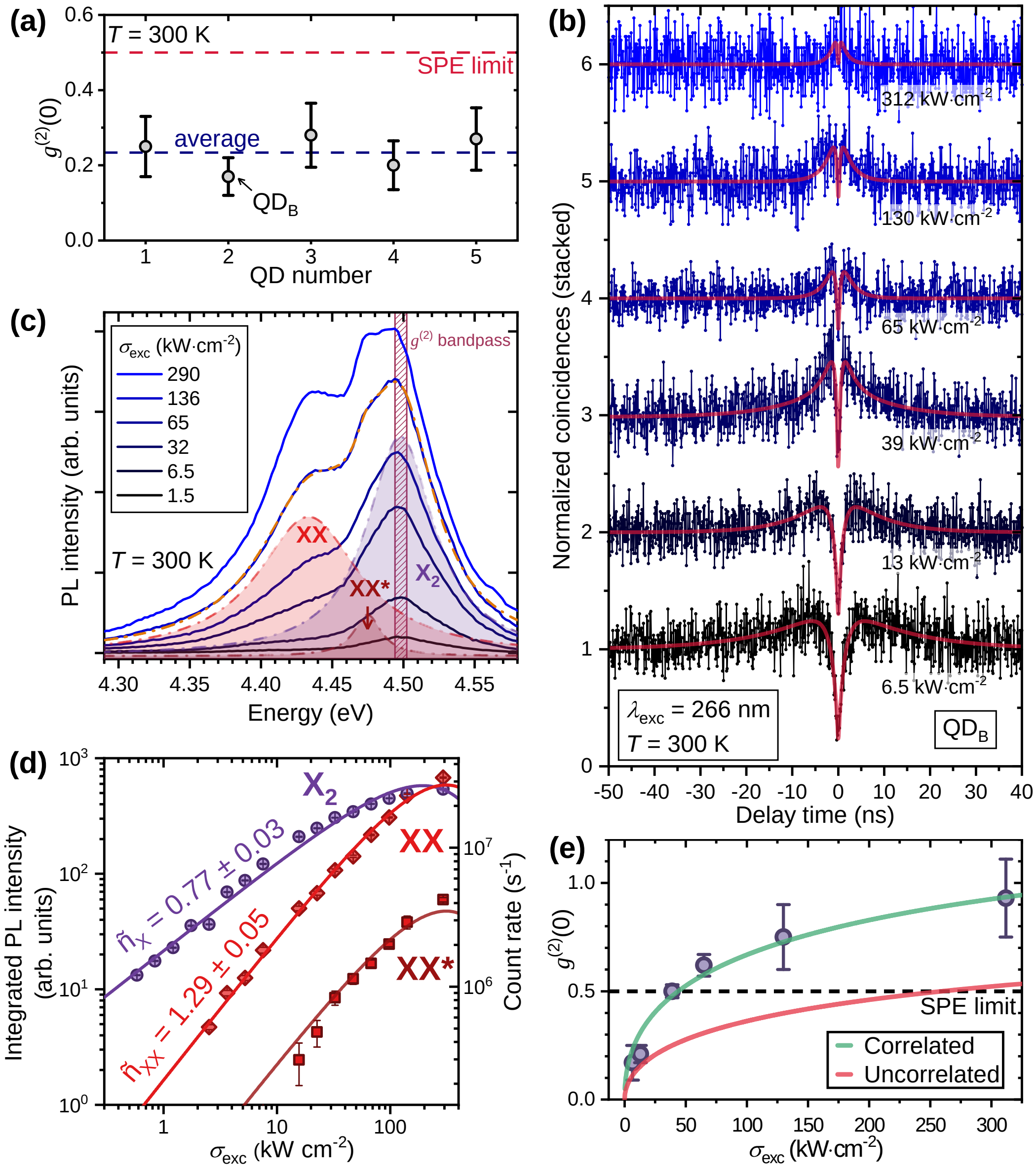

Figure 2.29: **(a)** minimum $g^{(2)}(0)$ value recorded for different QDs. **(b)** $g^{(2)}(\tau)$ traces recorded at RT on $\mathrm{QD_B}$ as a function of excitation power density. **(c)** RT PL spectra recorded on $\mathrm{QD_B}$ at various excitation power densities. The QD signal is approximated by three Voigt profiles, for XX, XX^* and $\mathrm{X_2}$ lines, respectively. The hatched rectangle represents the HBT detection window. **(d)** Variation in the integrated intensity of XX, XX^* and $\mathrm{X_2}$ against excitation power density. XX and $\mathrm{X_2}$ are fitted using Eq. 2.32 (after replacing P_exc/P_0 by $\sigma_\mathrm{exc}/\sigma_0$) with a global σ_0 parameter. XX^* is subsequently fitted using the parameters extracted from fitting XX. **(e)** $g^{(2)}(0)$ values extracted from (b) along with estimated values assuming correlated (green) and uncorrelated background (red lines). The fitting procedure is detailed in the main text.

At high excitation power densities, the degradation of single-photon purity cannot be explained by the simplistic approach employed for $\mathrm{QD_A}$ in Subsec. 2.9.2. This becomes evident when attempting to replicate the trend of $g^{(2)}(0)$ while treating the PL signal from the biexciton as uncorrelated background. In this framework, combining Eq. 2.84 with Eq. 2.83 allows for the estimation of $g^{(2)}(0)$ with:

$$g^{(2)}_{\mathrm{X,exp}}(0) = 1 - \frac{1}{\left(1 + I^{\mathrm{bp}}_{\mathrm{XX}}/I^{\mathrm{bp}}_{\mathrm{X_2}}\right)^2}, \tag{2.85}$$

where $g^{(2)}_{\mathrm{exp}}(0)$ represents the zero-delay value of the $g^{(2)}(\tau)$ function recorded experimentally. Considering the constant linewidth of (multi-)excitonic lines at RT the XX/X intensity ratio can be reformulated using Eq. 2.32 as:

$$I^{\mathrm{bp}}_{\mathrm{XX}}/I^{\mathrm{bp}}_{\mathrm{X_2}} = \rho_{\mathrm{bp}}\sigma_{\mathrm{exc}}{}^{\tilde{n}_{\mathrm{XX}}-\tilde{n}_{\mathrm{X_2}}}. \tag{2.86}$$

Here, the constant parameter ρ_{bp} represents the biexciton/exciton intensity ratio within the HBT bandpass. Its value ($\rho_{\mathrm{bp}} = 0.023$) is determined using the scaling factors derived from Fig. 2.29(d) and the experimental intensity ratio obtained from the PL spectrum recorded at 136 $\mathrm{kW\cdot cm^{-2}}$ (see Fig. 2.29(d)).

The predicted scaling of $g^{(2)}(0)$ within this uncorrelated model (illustrated by the solid red line in Fig. 2.29(e)) substantially underestimates the decline in single-photon purity. To better apprehend this result it is crucial to recognize that Eq. 2.84 is only valid when there is no connection between the spurious light source and the emitter under investigation. This assumption does not hold for the biexciton, as its PL is intricately linked to that of the exciton.

To elaborate on this assertion, we should first highlight that when exciton and biexciton PL are superimposed in the detection window, the recorded $g^{(2)}(\tau)$ trace comprises four terms, corresponding to exciton and biexciton second order auto- and cross-correlation functions, denoted as $g^{(2)}_{i\to j}(\tau)$, where i and j represent the 'start' and 'stop' photons, respectively (refer to Subsect. 1.5.2 for details). $g^{(2)}_{\mathrm{exp}}(\tau)$ is then expressed as:

$$g^{(2)}_{\mathrm{exp}}(\tau) = C' \sum_{i,j\in\{\mathrm{X_2},\mathrm{XX}\}} I^{\mathrm{bp}}_{\mathrm{i}} I^{\mathrm{bp}}_{j} g^{(2)}_{i\to j}(\tau), \tag{2.87}$$

where the normalization parameter (C') is given by:

$$1/C' = \sum_{i,j\in\{\mathrm{X_2},\mathrm{XX}\}} I^{\mathrm{bp}}_{\mathrm{i}} I^{\mathrm{bp}}_{j} g^{(2)}_{i\to j}(+\infty) = \left(I^{\mathrm{bp}}_{\mathrm{X_2}} + I^{\mathrm{bp}}_{\mathrm{XX}}\right)^2. \tag{2.88}$$

Among the four potential recombination channels[XXVII], only the biexciton-to-exciton second-order cross-correlation function ($g^{(2)}_{\mathrm{XX}\to\mathrm{X_2}}(\tau)$) does not vanish at zero-delay ($\tau = 0$). As a result,

---

[XXVII] A coincidence is recorded after measuring one photon on each SPD either generated by exciton or biexciton recombination. As such four processes must be considered: $\mathrm{X_2} \to \mathrm{X_2}$, $\mathrm{X_2} \to \mathrm{XX}$, $\mathrm{XX} \to \mathrm{X_2}$ or $\mathrm{XX} \to \mathrm{XX}$.

we obtain:

$$\begin{aligned} g^{(2)}_{\mathrm{exp}}(0) &= \frac{I^{\mathrm{bp}}_{\mathrm{X}_2} I^{\mathrm{bp}}_{\mathrm{XX}}}{\left(I^{\mathrm{bp}}_{\mathrm{X}_2} + I^{\mathrm{bp}}_{\mathrm{XX}}\right)^2} g^{(2)}_{\mathrm{XX}\to\mathrm{X}_2}(0), \\ &= \frac{1}{\rho_{\mathrm{bp}} {\sigma_{\mathrm{exc}}}^{\tilde{n}_{\mathrm{XX}} - \tilde{n}_{\mathrm{X}_2}} + 2 + {\sigma_{\mathrm{exc}}}^{\tilde{n}_{\mathrm{X}_2} - \tilde{n}_{\mathrm{XX}}} / \rho_{\mathrm{bp}}} g^{(2)}_{\mathrm{XX}\to\mathrm{X}_2}(0), \\ &= A^{\mathrm{bp}} g^{(2)}_{\mathrm{XX}\to\mathrm{X}_2}(0). \end{aligned} \tag{2.89}$$

In addition to the different prefactors obtained in the uncorrelated (as per Eq. 2.85) and correlated cases (A^{bp} in Eq. 2.89), the primary distinction arises from the inclusion of the cross-correlation term ($g^{(2)}_{\mathrm{XX}\to\mathrm{X}_2}(0)$). $g^{(2)}_{\mathrm{XX}\to\mathrm{X}_2}(\tau)$ typically exhibits bunching at zero-delay, due to the enhanced probability of observing exciton recombination immediately following biexciton recombination, with $n_1(0) = 1$. As such, the degradation of single-photon purity is further compounded by spurious biexciton PL than in the uncorrelated background scenario, underscoring the necessity for a substantial exciton-biexciton splitting to achieve high single-photon purity at RT.

The value of $g^{(2)}_{\mathrm{XX}\to\mathrm{X}_2}(0)$ is strongly relying on the pump rate, making it challenging to accurately estimate the trend of $g^{(2)}(0)$ through Eq. 2.85. For instance, within the multiexcitonic model, $g^{(2)}_{\mathrm{XX}\to\mathrm{X}_2}(0)$ is given by [162]:

$$g^{(2)}_{\mathrm{XX}\to\mathrm{X}_2}(0) = e^{\overline{\mu}} / \overline{\mu}, \tag{2.90}$$

while the expression derived within the three-level model (see Subsect. 2.4.3) reads:

$$g^{(2)}_{\mathrm{XX}\to\mathrm{X}_2}(0) = \gamma_1^{\mathrm{B}_2} / \pi + 1 + \pi / \gamma_2. \tag{2.91}$$

The detailed computation is given in Appendix B.2. Considering the intricate nature of $g^{(2)}_{\mathrm{XX}\to\mathrm{X}_2}(0)$, which relies on multiple unknown parameters, we can simplify our analysis by substituting this term with a constant parameter. An estimation of its value can be determined through the fitting of the experimental $g^{(2)}(0)$ dataset with Eq. 2.89. The resulting curve is depicted in Fig. 2.29(e) (green line) and remarkably aligns with the empirical trend, yielding $g^{(2)}_{\mathrm{XX}\to\mathrm{X}_2}(0) \sim 5.3$.

It is noteworthy that this value is not implausible, with lower limits obtained from Eq. 2.90 and Eq. 2.91 (assuming $\gamma_2 = 2\gamma_1^{\mathrm{B}_1}$) equal to 2.7 and 1.4, respectively. Additionally, this suggests again a saturation of the pump rate preventing the cross-correlation term from diverging as $\pi \to +\infty$. In conclusion, this finding confirms the biexcitonic origin of the XX line, specifically indicating a heightened likelihood of detecting a photon event from X_2 immediately following the observation of photoluminescence from XX.

2.9.4 Summary

In this section, we have demonstrated the remarkable conservation of single-photon purity exhibited by the exciton lines of GaN/AlN QDs. Analyzing the evolution of $g^{(2)}(0)$ values at RT, we have further highlighted that the primary hindrance to the enhancement of single-photon emission at high temperature stems from the spurious PL of the biexciton line, aggravated by the intricate relationship between exciton and biexciton states. Additionally, we employed $g^{(2)}(\tau)$ measurements to explore aspects of the QD recombination dynamics, particularly observing the saturation behavior of the excitation pump rate. Our investigation revealed significant limitations in the insights we could derive from fitting $g^{(2)}(\tau)$ traces, underscoring the constraints of the various models employed. Achieving a more comprehensive understanding of the QD dynamics necessitates supplementary experiments, which are addressed in the subsequent section through TRPL measurements.

2.10 Time-resolved photoluminescence on quantum dot ensembles

Although we demonstrated robust single-photon emission at RT for GaN/AlN SAQDs, several puzzling results require a greater attention, starting with exciton decay times of tens of ns measured at 5 K on a QD (QD_A) emitting at approximately 4.5 eV that deviates from previous experimental findings [113, 130, 262, 266]. To obtain a broader and more definitive understanding of the exciton dynamics within this system, we conducted TRPL measurements on a collection of SAQDs, investigating an unprocessed area of the sample L1244. PL transients were recorded over a temperature range from 5 to 300 K and excitation power densities spanning from 2 to 1.2×10^3 $\text{mW} \cdot \text{cm}^{-2}$, resulting in a maximum energy density per pulse of $0.15\,\text{mJ} \cdot \text{cm}^{-2}$. Even though, in the low-density regime, the PL spectra of the QD ensemble consistently peaked at approximately 3.5 eV for all the temperatures (refer to Fig. 2.30(a)), the PL intensity remained sufficiently high to capture PL transients from QDs emitting between 3.2 and 4.5 eV.

TRPL data collected at 5 and 300 K are presented in Figs. 2.30(b) and 2.30(c), respectively, for a large set of QD emission energies. Each transient is recorded within a spectral window of finite width, defined by the exit slit of the filtering monochromator, which varies from 4 meV for low-energy QDs to 8 meV for high-energy QDs. Similar to CW measurements, the contribution from the WL is disregarded in the analysis proposed here due to the quasi-resonant pumping method employed.

A notable decrease in the decay rate at higher energies is observed in the TRPL signals, reflecting a diminished QCSE concurrent with the reduction in QD size, as discussed in detail in Subsect. 2.2.3. Additionally, at the elevated excitation power densities used here, all TRPL decay curves exhibit a multiexponential decay profile, indicating the contribution of multiexcitonic states. This decay profile constitutes a clear rebuttal to the linear scaling of multiexcitonic recombination, a topic further investigated in Subsect. 2.10.3. However, given the complexity of multiexcitonic recombination processes, we initially focused on exciton recombination

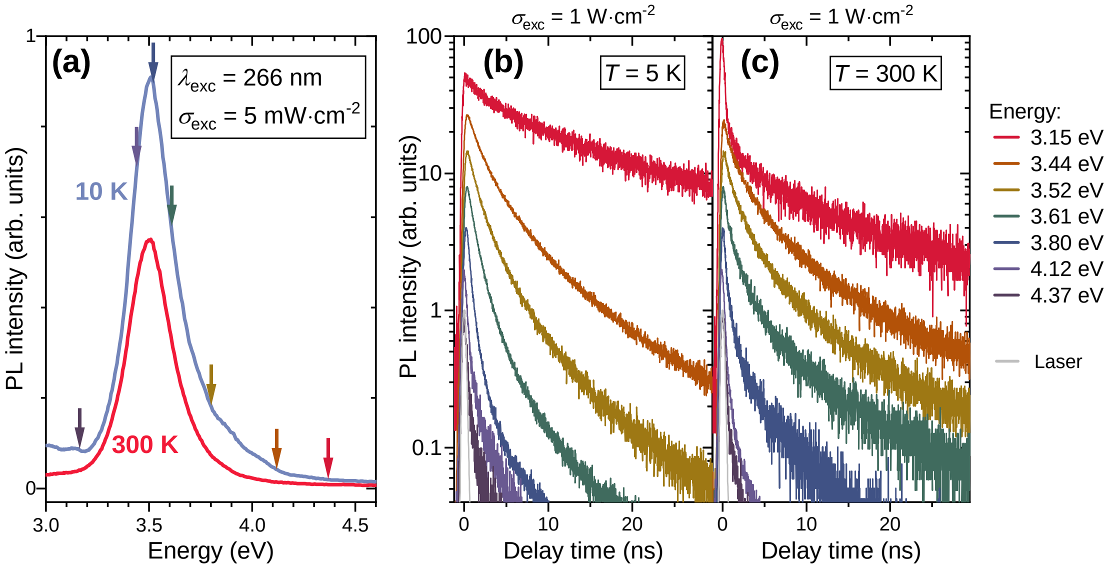

Figure 2.30: **(a)** Temperature dependence of the PL from the QD ensemble. The arrows indicate the energies at which TRPL transients depicted in (b) and (c) were recorded. The excitation power density is deliberately kept low to predominantly capture PL arising from exciton recombination. TRPL transients measured at **(b)** 5 K and **(c)** 300 K. Additionally, the laser transient is depicted by a grey line.

dynamics by investigating the tail of TRPL transients in the following subsection.

2.10.1 Exciton recombination

For each transient portrayed in Figure 2.30, we observe a long-lived monoexponential decay, which we attribute in the following to exciton recombinations across the QD ensemble. Figures 2.31(a) and 2.31(b) illustrate the evolution of 5 K TRPL transients as the excitation power density increases for QDs emitting at 3.80 and 4.25 eV, respectively. Under low excitation, the monoexponential decay persists over a dynamic range exceeding two orders of magnitude, without any indication of the existence of an even longer decay component, as recently observed by Hrytsaienko *et al.* [113]. The long-lived decay associated to each dataset is measured as $\tau_L = 6.5$ ns and $\tau_L = 2.8$ ns at 3.80 and 4.25 eV, respectively (refer to the yellow dash-dotted lines in Figs. 2.31(a) and 2.31(b)). Notably, this prolonged decay is consistently maintained at higher excitation levels with no variation in lifetime, consistent with expectations for the radiative recombination of excitons for a given QD size.

To further corroborate this interpretation regarding single exciton decay, we complemented low-temperature TRPL measurements with a series of temperature-dependent experiments focusing on QDs emitting around 3.80 eV (see Fig. 2.31(c)). The resulting transients consistently exhibit tails that can be effectively approximated by a single decay time $\langle \tau_L \rangle = 7.2$ ns average over all transients, with a slight deviation from the previously reported value attributed to

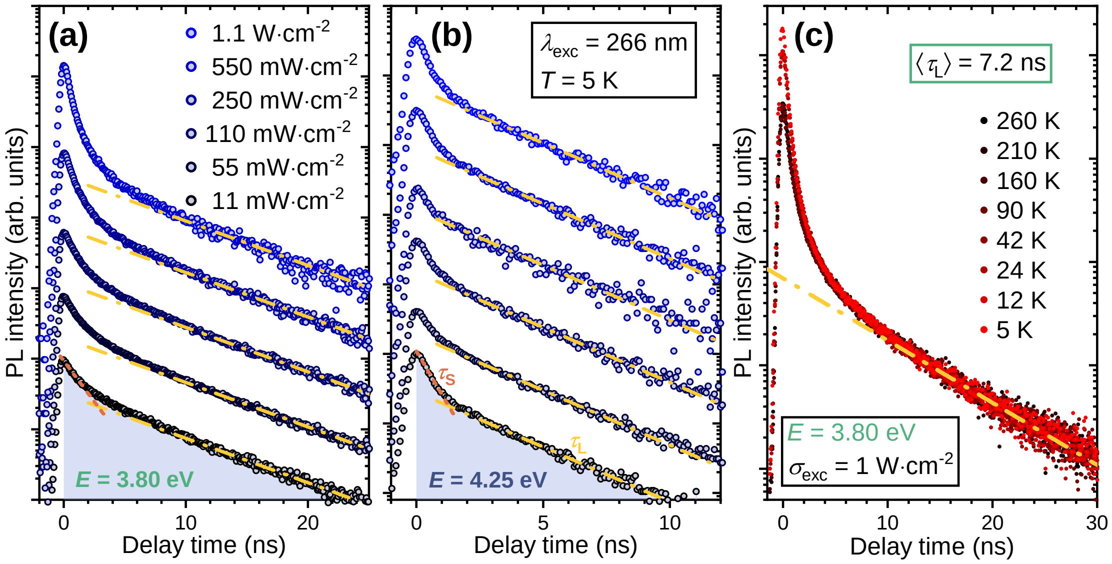

Figure 2.31: TRPL decay curves captured at 5 K as a function of excitation power density for QDs emitting at **(a)** 3.80 eV and **(b)** 4.25 eV. For each set of transients, the tail is approached by a monoexponential function (yellow dash-dotted lines) with constant decay $\tau_L = 6.5$ ns and $\tau_L = 2.8$ ns, respectively. The fast component of the biexponential decay observed at 11 mW · cm^{-2} is additionally highlighted by an orange dashed line. The resolution is reduced down to 80 ps/channel to enhance the qualitative assessment of decay time preservation. The shaded regions illustrate the integrated TRPL intensity ($I^{\text{tot}}_{\text{TRPL}}$) at 11 mW · cm^{-2}. **(c)** PL decays captured between 5 and 260 K at 1 W · cm^{-2} for QDs emitting around 3.80 eV . Transients are stacked so as to superimpose the long-lived tail. The resolution is reduced down to 80 ps/channel. The tails are approached by a concatenated monoexponential fit (yellow dash-dotted lines) with decay $\langle\tau_L\rangle = 7.2$ ns.

experimental uncertainties. This trend is anticipated for 0D nanostructures, for which the radiative lifetime is determined by the geometry of the emitter, and has been previously observed with GaN/AlN SAQDs grown on *c*-plane sapphire [267]. This constant decay behavior is also consistent with a system devoid of non-radiative recombinations. In this context, the decline in intensity observed at high temperature in Fig. 2.30(a) may be associated with selective bleaching of QDs located near non-radiative recombination centers, with such deactivated emitters no longer contributing to the global TRPL decays. A comprehensive study of this PL decrease is beyond the scope of this work.

With compelling evidence that long-lived PL arises from radiative exciton recombination, our focus shifts to examining the onset of TRPL decay curves. For each transient, we start by assessing the contribution of the long-lived monoexponential decay to the entire TRPL profile. To achieve this, we determine the intensity of the long-lived components ($I^{\text{L}}_{\text{TRPL}}$) using the monoexponential fit ($I^{\text{L}}_{\text{TRPL}} = A_{\text{L}} e^{-t/\tau_{\text{L}}}$, with A_{L} a fitting parameter) and then normalize it to the integrated intensity ($I^{\text{tot}}_{\text{TRPL}}$) evaluated across the entire transient (for $t > 0$, as shown in Figs. 2.31(a) and 2.31(b) for illustration). The resulting intensity ratio, denoted as $r_{\mathrm{L/S}}$, is reproduced in Fig. 2.32(a) for QDs emitting around 3.52, 3.80 and 4.25 eV.

The $r_{\mathrm{L/S}}$ metric represents the 'PL weight' of exciton recombination, which logically decreases with increasing excitation power density as the QDs become increasingly populated ($\overline{\mu}$ increases), leading to an enhanced contribution of multiexcitonic states. Surprisingly, however, the rapid components of the TRPL decays do not entirely vanish at low excitation power, exhibiting a persistent biexponential behavior which can be approximated by:

$$I(t) = A_{\mathrm{L}} e^{-t/\tau_{\mathrm{L}}} + A_{\mathrm{S}} e^{-t/\tau_{\mathrm{S}}}. \tag{2.92}$$

The enduring short-lived exponential decay (characterized by parameters A_{S} and τ_{S}) is depicted in Figs. 2.31(a) and 2.31(b) by orange dashed lines. The asymptotic saturation of the intensity ratio ($r_{\mathrm{L/S}}$) is clearly discernible in the semi-logarithmic plots provided in Fig. 2.32(a) with the low-excitation limit ($r^0_{\mathrm{L/S}}$) expressed as:

$$r^0_{\mathrm{L/S}} = \frac{\tau_{\mathrm{L}} A_{\mathrm{L}}}{\tau_{\mathrm{L}} A_{\mathrm{L}} + \tau_{\mathrm{S}} A_{\mathrm{S}}} = \frac{1}{1 + \frac{\tau_{\mathrm{S}} A_{\mathrm{S}}}{\tau_{\mathrm{L}} A_{\mathrm{L}}}}. \tag{2.93}$$

This asymptotic behavior was observed consistently across all the studied emission energies and temperatures. In fact, the long-lived component seems to weaken at higher temperature ($r^0_{\mathrm{L/S}}$ decreases) with saturation occurring more rapidly, as highlighted in Fig. 2.32(a) for $E = 3.80\,\mathrm{eV}$ by the solid (5 K) and dashed (300 K) green lines. While the reduced PL of high- and low-energy QDs prevents us from performing TRPL measurements at low excitation power densities for QDs at each end of the PL spectrum, we can still confirm the temperature-dependent decline of the long-lived TRPL component (A_{L}) when recording transients at sufficiently high excitation power. As an example, Fig. 2.32(b) illustrates a RT transient recorded at $\sigma_{\mathrm{exc}} = 0.35\,\mathrm{W \cdot cm^{-2}}$ and $E = 4.25\,\mathrm{eV}$, yielding $r_{\mathrm{L/S}} = 0.25$, a value substantially below the ratio recorded under similar conditions at 5 K ($r_{\mathrm{L/S}} \sim 0.8$).

At this stage, we should endeavor to propose a theoretical explanation that can bridge the short-lived and long-lived components of the PL decays. Referring to the multiexcitonic model depicted in Fig. 2.14(a), two potential hypotheses naturally emerge to explain this biexponential trend.

In a first scenario, this behavior may be ascribed to the interplay between dark and bright states. Within this picture, bright excitons may either undergo radiative recombination (at a rate ${\tau_{\mathrm{S}}}^{-1}$) or experience a spin-flip process toward a dark state. The persistence of the long-lived decay could thus be associated with the reloading from the dark state, characterized by the time constant τ_{L} [249]. However, the thermal activation of the bright state reloading, as detailed in Subsect. 2.5.3, is expected to progressively shorten the long-lived decay until the biexponential decay vanishes, as τ_{L} approaches τ_{S}. This temperature-dependent behavior, observed with CdSe QDs [207, 249], is contradicted here by the thermal stability of the long-lived decay evidenced in Fig. 2.31(c). The anticipated discrepancy between high- and low-energy bright

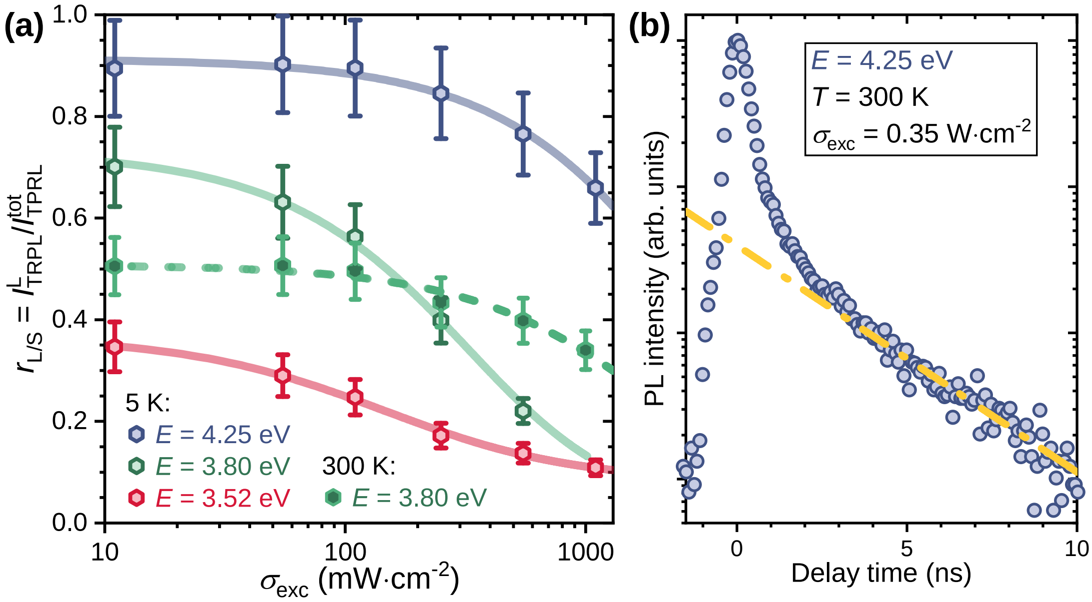

Figure 2.32: **(a)** Evolution of the $I^{\mathrm{L}}_{\mathrm{TRPL}}/I^{\mathrm{tot}}_{\mathrm{TRPL}}$ ratio against excitation power density for different emission energies. At 3.80 eV, the intensity ratio is plotted at 5 and 300 K. Solid and dashed lines are provided as a guide to the eye. The substantial error bars reflect the challenge in consistently deriving $I^{\mathrm{tot}}_{\mathrm{TRPL}}$, leading to a considerable absolute uncertainty. However, the relative uncertainty between each data point is comparatively smaller. **(b)** RT PL decay curve of QDs emitting around 4.25 eV recorded at $0.35\,\mathrm{W\cdot cm^{-2}}$. The tail is fitted with a monoexponential yielding $\tau_{\mathrm{L}} = 2.8\,\mathrm{ns}$ (yellow dash-dotted line) and $r_{\mathrm{L/S}}(0.35\,\mathrm{W\cdot cm^{-2}}) = 0.25$.

states highlighted in Sect. 2.8 also opposes the concept of a unique exciton recombination rate $\tau_{\mathrm{S}}{}^{-1}$ valid across the whole QDs and suggests an alternative explanation for the observed biexponential decay.

In a second scenario, we can instead attribute this dual trend to the recombination process of low-energy ($|\mathrm{B}_1\rangle$) and high-energy ($|\mathrm{B}_2\rangle$) bright excitons. At low temperatures, the PL is expected to be dominated by the $|\mathrm{B}_1\rangle$ recombination due to the suppressed thermal repopulation of $|\mathrm{B}_2\rangle$. Assuming rapid phonon-assisted transitions between bright $|B_1\rangle$ and dark states $|\mathrm{D}_{1-2}\rangle$, we can ascribe the long-lived decay solely to radiative recombination, with $\tau_{\mathrm{L}} = \gamma_1^{\mathrm{B}_1\,-1}$, thus explaining its insensitivity to temperature.

Despite the dominant PL of low-energy bright states at low temperatures, radiative recombination from $|\mathrm{B}_2\rangle$ is not fully cancelled and we can thus interpret the short-lived decay as the lifetime of the high-energy bright state. In this context, τ_{S} should be seen as a combination between radiative recombination and phonon-mediated transitions toward the dark states, with $\tau_{\mathrm{S}}{}^{-1} \sim \gamma_1^{\mathrm{B}_2} + \gamma_{\searrow}^2$. This second scenario seems more compatible with experimental findings. First, the increase in $r^0_{\mathrm{L/S}}$ with emission energy highlighted in Fig. 2.32(a) aligns well with an enhanced FSS for small QDs, which further hinders the repopulation of $|\mathrm{B}_2\rangle$ at low temperatures. Additionally, the reduction of the $r^0_{\mathrm{L/S}}$ intensity ratio at RT is compatible with a thermally-activated population of the high-energy bright state, confirming its increased contribution at RT.

While these observations support our working hypothesis, we must interpret them with caution since we lack TRPL results on individual QD lines to identify the precise source of each decay. Although not thoroughly analyzed, recent findings have reported biexponential decays measured on individual GaN/AlN SAQDs PL lines [25], casting doubts on our own interpretation. Additionally, the complete thermalization of exciton states, along with the enhancement of phonon-mediated transitions between dark and bright exciton states, should theoretically cancel the biexponential trend at high temperature, resulting in a unique decay time driven by the fastest recombination process[XXVIII]. This is clearly not observed at RT, contradicting earlier conclusions regarding the enhanced 0 K spin-flip rate (γ_{SF}) for high-energy QDs, (see Sect. 2.5 and 2.8). It is worth emphasizing that QDs investigated through TRPL differ in energy from those probed around 4.5 eV through μ-PL, making direct comparisons challenging. Left aside these apparent inconsistencies, reconciling TRPL data with $g^{(2)}(\tau)$ measurements presents another daunting endeavor. The thermal independence of long-lived TRPL decay times contrasts sharply with the temperature-dependent decay rates determined through second-order autocorrelation measurements (see Fig. 2.27). Given the incompleteness of the $g^{(2)}(\tau)$ fitting procedure evidenced in Subsect. 2.9.1, we leave this as an open question for future investigation.

2.10.2 Impact of energy fluctuations on time-resolved transients

While we have explored various scenarios regarding the physics of individual QDs to explain the observed biexponential decays, we have yet to consider the influence of the finite width of the detection window on the recorded transients. To assess this impact, we aim to replicate the transients expected when averaging TRPL decays over a large set of QDs. First, we can examine the evolution of the long-lived decay for different emission energies, depicted in Fig. 2.33(a), which incidentally confirms the temperature-insensitivity of the long-lived decay (τ_{L}) for any emission energy. The decay time decreases with increasing energy, consistent with the weakening of the QCSE along with a diminution of the QD size, (cf. Subsect. 2.2.3), supporting the excitonic origin of the long-lived decay. The trend is well-approximated by an empirical exponential fit (black dash-dotted line):

$$\tau_{\mathrm{L}}(E) = \tau_{\mathrm{L}}^{0} e^{-E/E_{\mathrm{L}}} + \tau_{\mathrm{L}}^{\infty}, \tag{2.94}$$

where τ_{L}^{0}, E_{L} and $\tau_{\mathrm{L}}^{\infty}$ are fitting parameters. The contribution of $\tau_{\mathrm{L}}^{\infty} \sim 2.5\,\mathrm{ns}$ is negligible below 4 eV and is consequently discarded in the following discussion.

Next, considering TRPL measurements on an ensemble of QDs with emission energies fluctu-

---

[XXVIII] The transition rates $\gamma_{\searrow}^{1,2}$ and $\gamma_{\nwarrow}^{1,2}$ are thermally activated and theoretically approach infinity. Consequently, at elevated temperatures, the transitions between exciton states are nearly instantaneous, leading to all recombination processes contributing to the overall depletion of this 'averaged' exciton state.

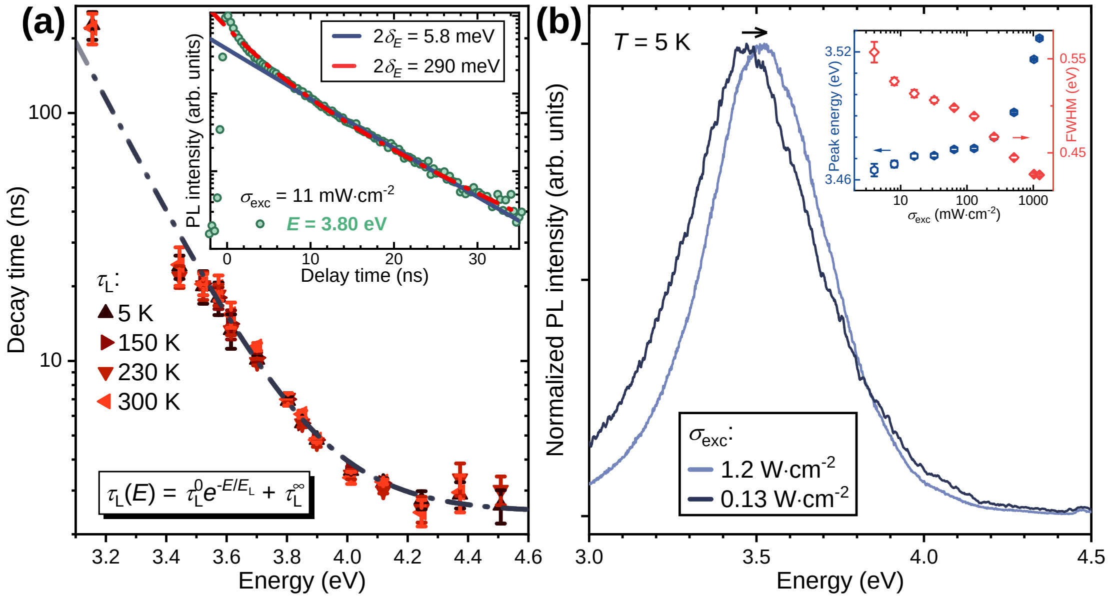

Figure 2.33: **(a)** Evolution of the long-lived decay (τ_L) as a function of emission energy, from 5 K to RT. The dash-dotted line is an exponential approximation of the trend (see legend). The inset illustrates the fitting of the TRPL transient recorded at 3.80 eV and 5 K using Eq. 2.96. The solid blue line is obtained using the exact width of the detection window ($2\delta_E = 5.8$ meV), while the red dash-dotted line represents the best agreement with the dataset. **(b)** Low-temperature PL spectra of the QD ensemble recorded at 0.13 and 1.2 W $\cdot$ cm^{-2}. The inset illustrates the blueshift and the narrowing of the PL peak with increasing excitation power density.

ating around a central value E, we can evaluate the impact of this finite detection window (of width $2\delta_E$) on the TRPL transients. For a single emitter, the TRPL intensity is proportional to the occupancy probability of the investigated state (denoted as n_L in this context) and can be expressed as:

$$I_{\text{TRPL}}(E,t) = n_L(E,t)/\tau_L(E) = e^{-t/\tau_L(E)}/\tau_L(E), \tag{2.95}$$

assuming no multiexcitonic recombinations and τ_L given by Eq. 2.94. The ensemble TRPL intensity ($\langle I_{\text{TRPL}}(E,t)\rangle$) is obtained by integrating Eq. 2.95 over the detection window, considering for the sake of simplicity a homogeneous distribution of QDs within the investigated spectral range ($f(E) = 1/(2\delta_E)$). We expect this distribution to provide an upper estimate of the impact of energy fluctuations. Following this, $\langle I_{\text{TRPL}}(E,t)\rangle$ is given by:

$$\begin{aligned}
\langle I_{\text{TRPL}}(E,t)\rangle &= \int_{E-\delta_E}^{E+\delta_E} f(E')n_L(E',t)/\tau_L(E')\mathrm{d}E' \\
&= \frac{1}{2\delta_E\tau_L^0}\int_{E-\delta_E}^{E+\delta_E} e^{E'/E_L}\exp\left(-\left(t/\tau_L^0\right)e^{E'/E_L}\right)\mathrm{d}E', \\
&= -\frac{E_L}{2\delta_E t}\left[\exp\left(-\left(t/\tau_L^0\right)e^{E'/E_L}\right)\right]_{E-\delta_E}^{E+\delta_E}.
\end{aligned} \tag{2.96}$$

Under the assumption of a homogeneous QD distribution, Eq. 2.96 yields an analytical expression which serves as a fitting function. The inset of Fig. 2.33(a) illustrates the fitting of the tail of a TRPL transient recorded at 5 K around $E = 3.80$ eV using Eq. 2.96 with a detection window of $2\delta_E = 5.8$ meV (solid blue line) matching experimental conditions. The deviation from a monoexponential fit is minimal, and consequently, the obtained decay time $\tau_{\mathrm{L}}(E) = \tau_{\mathrm{L}}^{0} e^{-E/E_{\mathrm{L}}}$ aligns closely with the previous outcome. This validates the underlying assumption made in Subsect. 2.10.1 that the biexponential trend does not result from the finite detection window but rather reflects the inherent physics of QDs at specific emission energies.

To emphasize this conclusion, we can nevertheless attempt to replicate the TRPL transient using Eq. 2.96 with δ_E as a variable. The inset of Fig. 2.33(a) presents the closest match to the dataset, depicted by a red dash-dotted line, which, however, does not align well with experimental observations. With an estimated spectral width of $2\delta_E = 290$ meV, the simulated trend exhibits only a slight deviation from the monoexponential curve, resembling more a stretched exponential shape, distinct from the observed biexponential trend.

The resilience of the TRPL signals to increasing energy fluctuations can help in understanding the consistent decay times τ_{L} observed as the temperature rises. Indeed, thermal expansion influences both the GaN and AlN matrix materials, reducing their bandgap. Consequently, this lowers the emission energy of QDs, and should simultaneously affect their recombination dynamics. Quantifying the influence of thermal expansion on the QD emission energies can help to elucidate its impact on the long-lived decay τ_{L}. Monitoring the energy shift from the ensemble PL data in Fig. 2.30(a) reveals a modest redshift of less than 10 meV, contrasting with the approximately 60 meV redshift previously reported for a GaN/AlN QD ensemble peaking around 4.4 eV [267]. However, due to the sensitivity of ensemble PL to thermal variations in the absorption efficiency (α_{abs}) of QDs, a more reliable approach involves tracking the shifts experienced by individual QDs to draw conclusions about the QD ensemble. For example, for $\mathrm{QD_C}$, we observed a thermal shift of the $\mathrm{X_2}$ line of about 90 meV, consistent with previous findings [20] and closely aligning with the Varshni shift experienced in bulk AlN [88], underscoring the influence of matrix material strain on the optical properties of SAQDs. As depicted in Fig. 2.33(a), a shift of approximately 90 meV should have a slight but measurable impact on the lifetime of a given set of QDs. However, in practice, this effect is counterbalanced by employing a fixed detection window, causing the TRPL decays recorded within a fixed energy range to originate from different sets of QDs at 5 K and RT. The combined effects of these two counterbalancing factors, along with the relatively small influence of thermal expansion, sufficiently explain the thermal insensitivity of the long-lived decay.

Introducing another and more critical aspect of energy fluctuation, we ought to quantify the energy shift resulting from changes in the multiexcitonic states contributing to the QD ensemble PL as we vary the excitation power density. Indeed, each EHP added to a QD results in a reconfiguration of the Coulomb interaction and screening of the built-in field (see Subsect. 2.3.1), resulting in a complex evolution of the emission energy. To investigate the multiexcitonic recombination process across the ensemble of QDs while maintaining the detection window fixed, it is crucial to ensure that the lifetime fluctuations associated to this energy shift remain negligible compared to variations in the recombination rate of different multiexcitonic states. This is achieved by monitoring the spectral shift of QD PL as a function of excitation power density.

Unlike temperature-dependent measurements, the absorption efficiency of QDs is minimally affected by laser fluence. Hence, we can evaluate the energy shift experienced by the QD ensemble through the shift of its PL peak, as illustrated in Fig. 2.33(b). The PL peak shifts by approximately 60 meV between excitation densities of 0.13 and $1.2\,\mathrm{W \cdot cm^{-2}}$, but all QDs do not experience the same shift, as indicated by the reduction in the FWHM with increasing excitation power (see inset). Smaller QDs are less affected by the screening of the built-in field, resulting in a less pronounced blueshift at the high-energy end of the ensemble PL. A redshift is even anticipated above 3.8 eV when transitioning from exciton to biexciton PL, as the biexciton binding energy becomes positive, (see Subsect. 2.3.1). This is evidenced in Fig. 2.33 as a crossing between the normalized spectra recorded at high and low excitation powers, respectively.

Overall, the energy shift associated with the PL of multiexcitonic states increases with QD size. However, for high-energy QDs, this shift is sufficiently small to be disregarded. This holds particularly true for QDs emitting around 3.8 eV, which are further investigated in the subsequent section.

2.10.3 Evidence for multiexcitonic recombination

After initially focusing on the long-lived decay associated with exciton recombination, we now delve into the analysis of faster decay processes linked to multiexcitonic recombinations. In this regard, it is crucial to note that the formalism developed in Sect. 2.4 does not adequately reproduce experimental observations. As highlighted in Subsect. 2.4.2, the ensemble TRPL intensity is expected to exhibit a monoexponential decay at any excitation power within the linear scaling scenario ($\gamma_i = i\gamma_1$), a prediction contradicted by experimental data. Moreover, the persistent biexponential decay described in Subsect. 2.10.1 also deviates from the predictions of the simplified multiexcitonic model.

To address this discrepancy, we propose an empirical approach to assess the different recombination processes involved in the ensemble TRPL decay before refining our model. We adopt a subtractive procedure, as successfully experimented by Klimov *et al.* [164], to iteratively extract single exponential dynamics characteristic of each (multi-)excitonic state. This procedure, outlined in Figs. 2.34(a) and 2.34(b) for transients recorded at 3.80 eV, involves fitting the tail of each TRPL decay with a monoexponential function, subtracting its contribution from the raw dataset, and repeating the process to estimate the three first decay rates of the multiexcitonic cascade. Notably, decay rates extracted at different excitation power densities align well, indicating the power-insensitivity of the (multi-)excitonic lifetimes. The change in laser fluence primarily affects the contribution of each state to the ensemble PL, rather than

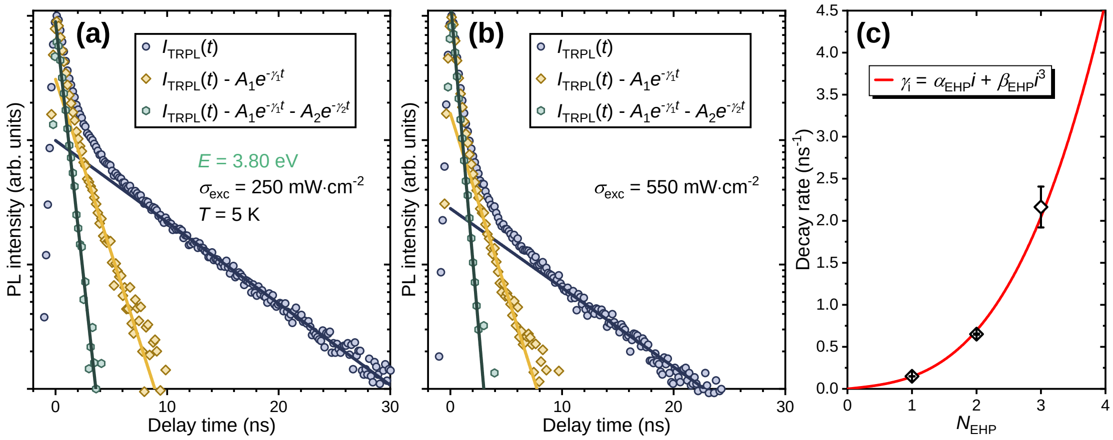

Figure 2.34: **(a)** Dynamics of the first (multi-)excitonic states extracted from TRPL transients around 3.80 eV and at excitation power densities of **(a)** 250 and **(b)** 550 mW·cm^{-2}. The blue circles represent the raw TRPL transients. The yellow and green transients are obtained after subtracting the contribution of the first and second decay components, respectively. **(c)** Evolution of the decay rates extracted from TRPL transients. Each data point is given as an average over the decay rates determined in (a) and (b), with error bars estimated as the difference between these two rates. Experimental decays are fitted with a cubic polynomial (refer to the legend).

the intrinsic physics of each state.

However, precision in the extracted decays decreases after each iteration, particularly approaching the temporal resolution limit of the experimental setup. In our case, this limit is reached after extracting the third decay component. Nonetheless, we attempt to estimate higher-order decay rates through a cubic fit, as shown in Fig. 2.34(c). While this estimation is inherently uncertain, subsequent analysis reveals that high-order multiexcitonic states minimally contribute to experimental transients. The choice of a cubic fit is also supported by previous studies on NC QDs [164, 172], attributing cubic scaling of recombination rates to non-radiative AM recombination. It is worth noting that the extracted decays in Fig. 2.34(c) are genuinely attributed to the recombination of excitons (1 EHP), biexcitons (2 EHPs) and triexcitons (3 EHPs), despite earlier conclusions in Subsect. 2.10.1 regarding the origin of the persistent short-lived decay (τ_S, attributed to γ_2^{-1} here). We address this inconsistency at the end of this subsection.

In order to reconstruct a theoretical framework that accounts for the observed multiexponential decay, we revisit the multiexcitonic model, discarding the linear scaling assumption. This entails describing the QD dynamics using the rate equations (Eq. 2.36) provided in Subsect. 2.4.2, from which we can retrieve an expression for the time-dependent occupancy probability of each state ($n_i(t)$). In the absence of a well-defined scaling law for the γ_i values, solving the system becomes complex. Through a step-by-step resolution, we can nevertheless obtain an approximate expression which reads (see Appendix B.3):

$$n_i(t) = \sum_{j=i}^{N} A_{ij} e^{-\gamma_j t}, \tag{2.97}$$

where the coefficients A_{ij} are expressed as:

$$A_{ij} = \frac{\gamma_j}{\gamma_i} \sum_{k=j}^{N} n_k(0) \left[\prod_{\substack{m=i \\ m\neq j}}^{k} \frac{\gamma_m}{\gamma_m - \gamma_j} \right]. \tag{2.98}$$

Here, N represents the highest multiexcitonic state considered in our computation ($|N\rangle$). Increasing N improves the model precision but also increases its complexity.

Under the simplified hypothesis that we generate a fixed number of EHPs in each QD at time $t = 0$[XXIX], Eq. 2.97 simplifies to:

$$n_i(t) = \left(\prod_{m=i+1}^{\overline{\mu}} \gamma_m \right) \sum_{k=i}^{\overline{\mu}} \frac{e^{-\gamma_k t}}{\prod_{\substack{m=i \\ m\neq k}}^{\overline{\mu}} (\gamma_m - \gamma_k)}. \tag{2.99}$$

This expression aligns with the findings of C. Kindel [162] under the same assumptions, validating our conjecture. However, in practice, the QD filling at $t = 0$ follows a Poisson distribution, (cf. Eq. 2.35), which significantly deviates from the above simplification. Specifically, the first multiexcitonic states $|i\rangle$ with $i > \overline{\mu}$ still contribute to the ensemble PL.

Without loss of generality, we can nonetheless express the ensemble TRPL intensity (I_{TRPL}) by summing the contribution of all multiexcitonic states:

$$I_{\mathrm{TRPL}}(t) = \sum_{i=1}^{N} \gamma_{\mathrm{i}}^{\mathrm{rad}} n_i(t) = \sum_{i=1}^{N} \sum_{j=i}^{N} \gamma_{\mathrm{i}}^{\mathrm{rad}} A_{ij} e^{-\gamma_j t} = \sum_{j=1}^{N} C_j e^{-\gamma_j t}, \tag{2.100}$$

with:

$$C_j = \sum_{i=1}^{j} \gamma_{\mathrm{i}}^{\mathrm{rad}} A_{ij}, \tag{2.101}$$

where $\gamma_{\mathrm{i}}^{\mathrm{rad}}$ represents the radiative recombination rate of multiexcitonic state $|i\rangle$.

Equation 2.100 presents an overparameterized form, rendering it unsuitable for directly assessing the fidelity of our model against experimental observations. However, by constraining all decay rates through the method outlined in Fig. 2.34, we effectively reduce the system to a single degree of freedom, $\overline{\mu}$, supplemented by a normalization parameter. This, however, necessitates knowledge of the expression for the rates $\gamma_{\mathrm{i}}^{\mathrm{rad}}$, representing the contribution of radiative processes to the overall recombination rates. While this task proves to be challeng-

---

[XXIX] This amounts to consider all QDs in the same Fock state $n_i(0) = \delta_{i\overline{\mu}}$ at $t = 0$.

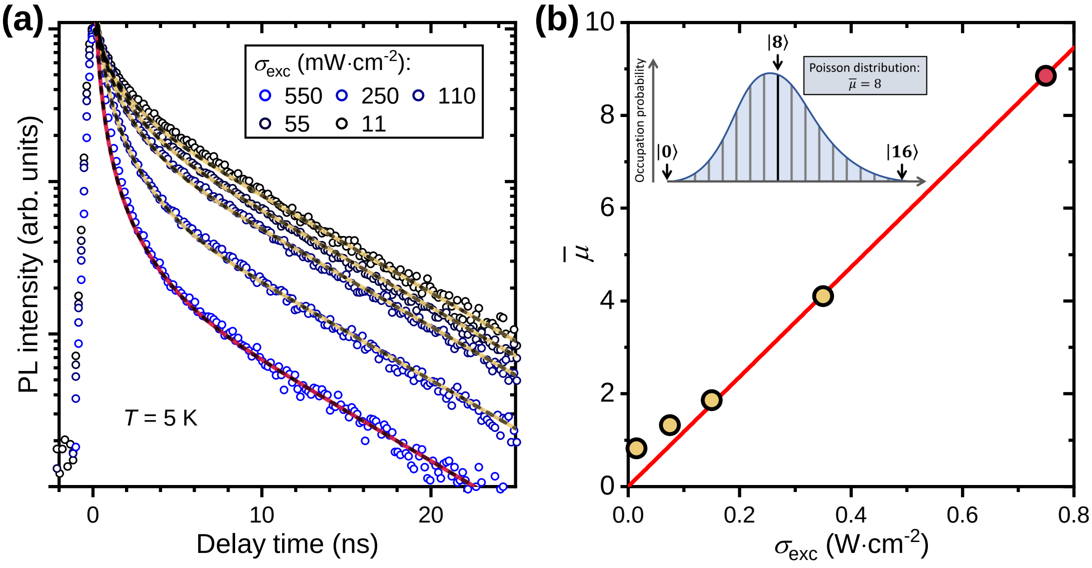

Figure 2.35: **(a)** TRPL decay curves recorded at 5 K and $E = 3.80$ eV, plotted against various excitation power densities. The first four transients (yellow lines) are fitted using Eq. 2.100 with fixed recombination rates. The values of $\overline{\mu}$ derived from the fitting process are reported in **(b)** as yellow dots. The red dot is extrapolated via a linear fit of the mean occupation number and subsequently employed to simulate the red curves in panel (a). The inset visualizes the initial occupancy probability for a Poisson distribution (with $\overline{\mu} = 8$), underscoring the importance of considering the contribution of higher multiexcitonic states. For this analysis, Eq. 2.100 with $N = 16$ is employed.

ing to achieve with our current dataset, another solution consists in formulating educated guesses. Initially assuming a linear relationship ($\gamma_{\text{i}}^{\text{rad}} = i\gamma_{1}^{\text{rad}} = \gamma_1$) failed to reproduce the experimental dataset satisfactorily. A more conclusive hypothesis emerged by disregarding non-radiative recombination processes, setting $\gamma_{\text{i}}^{\text{rad}} = \gamma_i$. The validity of this assumption is discussed subsequently.

To evaluate our model against experimental data, we attempted to fit the TRPL transients collected at 5 K and $E = 3.80$ eV (see Fig. 2.31(a)) using Eq. 2.100 with $N = 16$ and the hypotheses detailed above. The results of this fitting process are depicted in Fig. 2.35(a) as yellow lines, with the corresponding $\overline{\mu}$ values shown in Fig. 2.35(b) as yellow dots. The model demonstrates good agreement with experimental data up to an excitation power density of 250 mW · cm^{-2}. However, for the last transient recorded at 550 mW · cm^{-2}, the temporal resolution of the setup limits the applicability of the fitting procedure. Implementing a solution to account for the instrument response function (IRF) computationally proved to be too costly, given the low precision of the recombination rates γ_i for $i > 3$. As an alternative, we extrapolated the mean occupation number $\overline{\mu}$ at 250 mW · cm^{-2} using a linear fit (see Fig. 2.35(b)) and simulated the corresponding transient. The resulting curve, shown as a red line in Fig. 2.35(a), aligns well with the experimental decay. It is worth pointing out that for all fitted curves, the contribution of multiexcitonic states above $i = 3$ is significantly hindered by the duration of the laser pulse.

Their influence is primarily reflected in the variations of the occupancy probabilities $n_i(t)$ of the first three states. For instance, slight alterations to the $\overline{\mu}$ value by several units have minimal impact on the simulated red transient.

As a final remark, it is essential to highlight that the accuracy of the fit diminishes for the decay curve recorded at 11 $\mathrm{mW \cdot cm^{-2}}$, visually evidenced by the undershooting of the fitted curve between 2 and 6 ns. This decline in fit quality coincides with the saturation of the derived $\overline{\mu}$ values at low excitation powers densities, observed in Fig. 2.35(b), deviating from the expected linear trend. This discrepancy is closely related to the persistent biexponential decay revealed in Subsect. 2.10.1, which cannot be accounted for by Eq. 2.100. This observation confirms, if needed, that short- and long-lived decays (τ_S and τ_L) are not associated with multiexcitonic recombination processes.

Despite this inconsistency, the developed model exhibits a remarkable accuracy at large excitation power densities, strongly suggesting that non-radiative recombinations are weak or even negligible processes in GaN/AlN SAQDs, in contrast to, for example, NC QDs [167]. To corroborate this claim, it would be relevant to investigate the evolution of the integrated PL intensity with respect to excitation power density. However, the current dataset, acquired with arbitrary integration times, prevents us from performing a quantitative analysis.

2.10.4 Literature review on the exciton lifetime in GaN/AlN quantum dots

At this stage of the discussion, we have offered an exhaustive examination of the recombination dynamics observed across an ensemble of QDs. To further enrich our discussion, we now compare our findings with experimental and theoretical exciton lifetimes documented in the literature, focusing on GaN/AlN SAQDs and decay rates recorded at cryogenic temperatures [99, 113, 130, 163, 262, 266]. In Fig. 2.36, we present a summary of all these results, including the long-lived (τ_L, red circles) and short-lived decay times (τ_S, yellow circles) measured in our study.

The energy-dependent behavior of τ_L is compliant with prior observations. It exhibits an exponential decrease as QD size decreases within the 2.5 to 4 eV range, followed by a saturation at higher energies. This trend, as previously mentioned, primarily arises from the overlap of electron-hole wavefunctions along the c-axis, and is well-represented by approximating QDs as two-dimensional QWs subject to a perpendicular built-in electric field [113, 270]. A similar qualitative behavior is also observed for the short-lived component, with $\tau_\mathrm{L}/\tau_\mathrm{S} \sim 5$, and is anticipated for the lifetime of any multiexcitonic state.

While the datasets qualitatively follow a similar trend consistent with the wurtzite crystal structure, notable differences arise in the reported lifetimes across studies. Specifically, exciton lifetimes recorded for QDs grown on SiC [99, 163, 266] consistently appear to be about one order of magnitude shorter than τ_L values over a wide emission energy range. Conversely, lifetimes measured on Si(111) substrates seem to better align with our long-lived decays for

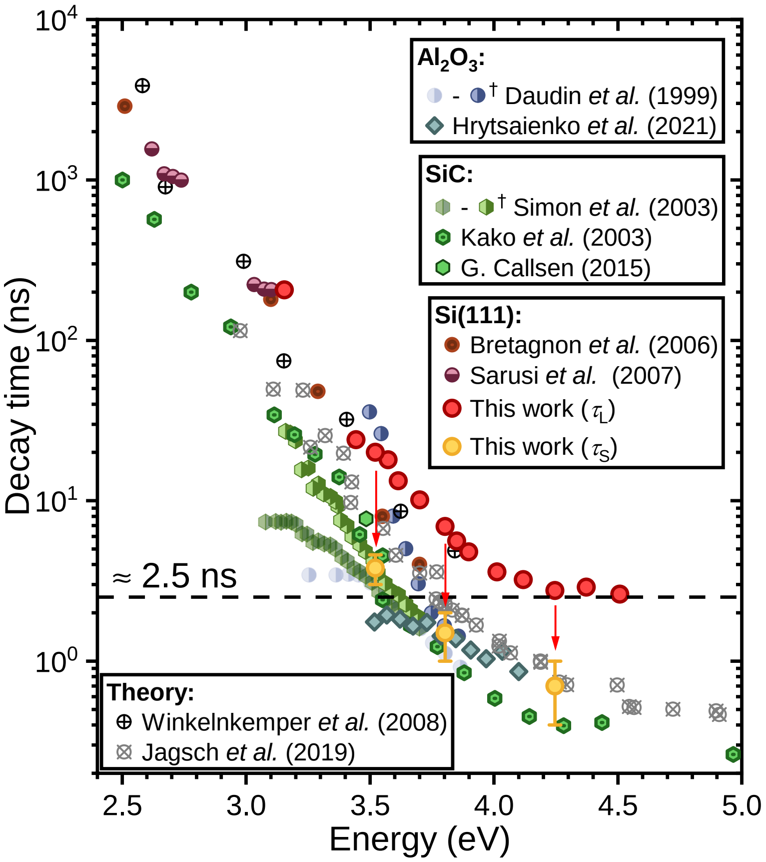

Figure 2.36: Exciton lifetimes measured at cryogenic temperatures for GaN/AlN SAQDs. Experimental results obtained with QD grown on Si(111) [130, 262, 268], sapphire [113], and SiC [99, 163, 266] are denoted by filled circles, diamonds, and hexagons, respectively. Theoretical calculations [116, 269] are represented by crossed-out circles and added here for the sake of completeness. Datasets marked with a dagger indicate corrections proposed by the authors to subtract the contribution from non-radiative recombinations from the raw data (shown in transparency).

larger QDs emitting above 3.5 eV [130, 268], but discrepancies arise at higher energies where the early saturation of our long-lived decays at approximately 2.5 ns appears as a singularity. However, lifetime measurements on Si(111) substrates are lacking at such energies, rendering this comparison more challenging. Finally, lifetimes measured on sapphire substrates by Hrytsaienko *et al.* [113] exhibit closer alignment with SiC-grown QDs, despite surprisingly minimal variations across the investigated energy range. At last, lifetimes recorded on sapphire substrates by Daudin *et al.* [262] substantially deviate from other findings.

Part of the explanation for the observed differences may stem from the impact of non-radiative recombination processes, which appeared to significantly influence early-grown QDs, as indicated by the need to correct raw lifetimes in studies such as those led by Daudin *et al.* [262] and Simon *et al.* [99]. Another source of variation could arise from differing interpretations of the complex time-dependent PL observed in each study. For instance, long-lived multiexponential decays observed in TRPL transients by Kako *et al.* and Hrytsaienko *et al.* were attributed to refilling of the exciton state via interface-related traps or free carriers in the QW [266] and to refilling from dark states [113], respectively. However, given the temperature-insensitivity of our measured lifetimes and our quasi-resonant excitation scheme, these scenarios cannot apply to our results. Additionally, the lack of temperature-dependent measurements in many studies makes it challenging to draw firm conclusions regarding the validity of each hypothesis. It is worth noting that the short-lived recombinations (τ_S) we measured, which also appear to be related to exciton dynamics, show strong agreement with high-energy exciton lifetimes reported on SiC and sapphire substrates. Therefore, the discrepancy between different datasets may also be attributed to the presence or absence of a dual recombination process, irrespective of its exact origin.

In summary, values reported in Fig. 2.36 underscore the variability of exciton lifetimes across GaN/AlN SAQDs, suggesting a notable disparity between datasets recorded on different substrates. The difference tends to reduce for larger QDs, whose properties are primarily influenced by the vertical separation of EHPs. For smaller QDs, horizontal confinement plays a more significant role potentially accounting for the larger fluctuations in the literature results. These fluctuations may stem, for instance, from variations in the AR.

Alternatively, relieving tensile strain in the AlN matrix via microcracks has been demonstrated to extend the excitonic lifetimes of GaN/AlN SAQDs on Si(111) substrates [268]. Thus, variations in strain fields among QDs grown under different conditions likely contribute to the spread in experimental results. Despite partial strain relaxation in the AlN matrix after growth of a few MLs, residual stress from the substrate persists. Consequently, GaN QDs on Si(111) are still subject to some degree of biaxial tensile strain [268]. In contrast, the shortest lifetimes were measured on c-plane sapphire and 6H-SiC substrates, where the AlN matrix is largely relaxed [271, 272]. Ultimately, the optical characteristics of SAQDs are also impacted by the properties of the GaN WL, with a thinner WL anticipated to increase the confinement of EHPs [273, 274]. In our case, the WL is about half thinner (~ 1.5 ML) than in earlier studies and may account for part of the observed differences.

In essence, alterations in the strain conditions between different samples, influenced by the substrates, and variations in the WL thickness could explain the observed discrepancies in exciton lifetimes. In this context, systematic micro-Raman spectroscopy measurements could serve as a valuable and complementary tool for establishing correlations between the strain experienced by QDs and the decay times measured.

2.11 Summary

Building upon the theoretical foundation laid out in Sect. 2.1 to 2.5, this chapter presents our experimental findings on the optical properties of GaN/AlN SAQDs. The results can be divided into two main parts: the investigation of individual, high-energy QDs through µ-PL, and the analysis of the luminescence properties of an ensemble of QDs using TRPL.

In the first part, we explored the impact of SD on the optical properties of such polar QDs at cryogenic temperatures, shedding light on the different timescales at which these features manifest themselves. Despite their potential drawbacks for device applications, we demonstrated how SD could serve as valuable indicators of the origin of various PL lines and the density of defects near SPEs, using a methodology which can naturally be extended to other systems featuring excited states with large permanent dipole moments.

We then delved into the power- and temperature-dependent behavior of high-energy QDs, revealing unique features such as a significant FSS coupled with a pronounced discrepancy between bright excitons. By comparing our findings to the 'multiexcitonic model' developed in the groundwork, we underscored its inherent limitations and identified areas where our experimental results deviated from 'basic' theoretical predictions.

These limitations were particularly evident in our analysis of second-order autocorrelation measurement performed on individual exciton lines which nevertheless confirmed the strong potential of GaN/AlN QDs for achieving bright RT single-photon emission, despite the challenges posed by phonon-related processes.

Given the shortcomings of our multiexcitonic model exposed through the analysis of μ-PL measurements, we supplemented our investigation with TRPL, focusing at first on the exciton recombination dynamics. While the biexponential decay observed in our PL transients presents challenges for a fully consistent framework, the proposed scenarios lay a solid foundation for future investigations. Additionally, investigating multiexcitonic processes under high excitation power density provided insights into potential refinements of the multiexcitonic model to better align with experimental observations.

As a final note, it is important to remind that many of the conclusions and insights discussed in this chapter are readily applicable to other SPE systems, as will be evident in the exploration of PD PL in Chap. 3.

3 Point defects acting as single-photon emitters in bulk GaN layers

While GaN/AlN QDs demonstrate promising RT properties presented throughout Chap. 2, their integration into photonic structures faces significant challenges due to their intrinsic characteristics. One major limitation is their peak efficiency occurring in the deep UV range, where the reduced impact of QCSE makes them the most effective. This UV range is ill-suited for any long-range application relying on an optical fiber infrastructure. To this end, it appears particularly desirable to achieve similar RT properties in the NIR to telecom range without departing from the industrially well-established GaN platform. In this regard, PDs embedded in bulk GaN layers have recently shown their potential to act as bright SPEs up to RT across wavelengths ranging from 500 nm to 1400 nm [30–32, 275].

The presence of PDs in GaN has been attested for a long time in III-Ns materials [276]. However, they have primarily been studied for their negative impact in light-emitting devices, where they act as non-radiative recombination centers [95, 277–279]. Their use as single-photon source represents a new and promising paradigm shift.

To effectively identify PDs exhibiting an SPE behavior, a thorough comprehension of the system dynamics is essential. This necessitates a brief exploration of relevant theoretical concepts in the literature to construct a comprehensive understanding of their formation mechanism and optical characteristics, which we summarize here in Sect. 3.1. It is important to clarify that our intention here is not to establish a fully consistent framework for rigorous first-principles modeling as such an approach goes beyond the scope of this study. Instead, our objective is to present an intuitive overview of the investigated systems, starting from theoretical concepts. This approach aims to bridge the gap between the physics of PDs and PL results. Experimental observations are then detailed throughout Sects. 3.2 to 3.5. It is also worth pointing out that the study of PDs is nascent within our laboratory and is rapidly evolving. Several concepts introduced here will serve as foundational principles for future endeavors, which will be highlighted in subsequent sections.

3.1 Theoretical framework

In contemporary theoretical calculations related to semiconductors, density functional theory (DFT) [280] serves as a prevalent method due to its computational efficiency. While alternative approaches, such as many-body perturbation theory, exist, they are computationally intensive and challenging to implement in a self-consistent manner [281]. Common approximations like the local density approximation (LDA) [282] and the general gradient approximation (GGA) [283] have historically been used but have faced challenges in delivering accurate quantitative results, particularly in predicting the bandgap [284–286].

The introduction of hybrid functionals [287], specifically the Heyd, Scuseria, and Ernzerhof screened hybrid functional (HSE) in the early 2000s [288, 289], has emerged as a refinement to existing methodologies. The HSE approach has demonstrated its efficacy in providing accurate structural and electronic results [290], as well as improved predictions for the bandgap and the band structure of dielectrics compared to LDA and GGA [285, 286]. As a result, it has become the standard approach for theoretical predictions in the field and examples and theoretical results that will be discussed below have been obtained in this framework, using a supercell geometry [291]. For the sake of clarity, we should additionally emphasize that the term "point defect (PD)" is used to refer to substitutional and interstitial native defects or impurities as well as vacancy defects.

3.1.1 Formation energy and thermodynamic transition levels

Properties associated with PDs are derived from their formation energy which, for a PD X in a charge state q is defined as [291]:

$$E^f[X^q] = E_{\text{tot}}[X^q] - E_{\text{tot}}[\text{bulk}] + \sum_i n_i \mu_i + qE_{\text{F}} + E_{\text{corr}}, \tag{3.1}$$

where $E_{\text{tot}}[X^q]$ represents the total energy of a supercell containing the defect. The term $E_{\text{tot}}[\text{bulk}] = E_{\text{tot}}[\text{GaN}]$ corresponds to the energy in an equivalent supercell without defect. μ_i denotes the chemical potential of atomic species of type i, which must be either added ($n_i < 0$) or removed ($n_i > 0$) to form the defect. n_i refers here to the number of atoms added/removed. E_{F} represents the Fermi level referenced to the VBM, essentially analog to the chemical potential of the electrons. E_{corr} serves as a correction factor used in theoretical computation to address the finite nature of the supercell. Although its rigorous definition is crucial for correcting long-range Coulomb interactions in charged states, technical details related to this factor will not be further addressed in this study, and we will ignore it. In essence, E^f is the energy required to incorporate a defect into the material and is necessarily positive for the stability of the GaN matrix. A higher formation energy of X^q indicates among other things a lower likelihood of forming this defect during growth.

A defect X may exist in various charge states, and its formation energy changes with the Fermi

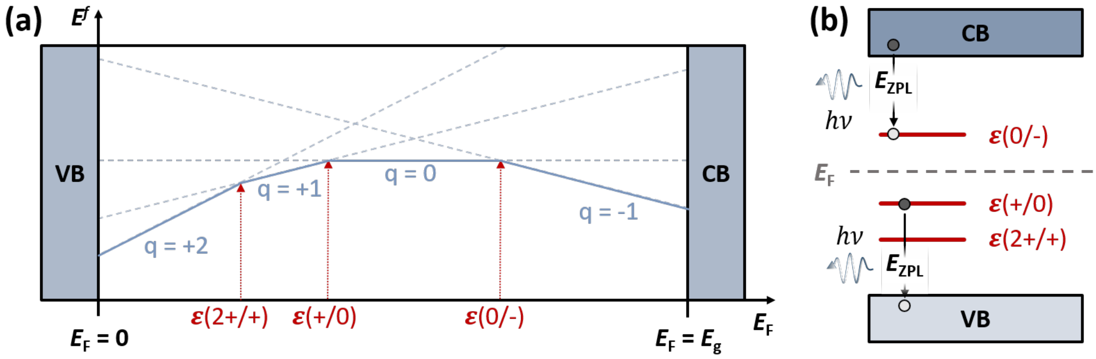

Figure 3.1: **(a)** Formation energy as a function of Fermi level E_F, for an amphoteric defect existing in charge states $q = -1, 0, 1, 2$. $E^f(E_F)$ lines are prolonged by dashed lines to emphasize the region where each charge defect becomes unstable. Freely adapted from Ref. [291]. The thermodynamic transition levels ($\epsilon(q/q')$) are reported in **(b)** with a hypothetical Fermi level E_F. ZPLs are depicted for an electron capture and a hole capture, respectively.

level as indicated by Eq. 3.1:

$$E^f[X^q] = E^f[X^q, E_F = 0] + qE_F. \tag{3.2}$$

Negatively charged states ($q < 0$) are thus more stable at higher Fermi energies (p-doped GaN) while positively charged states are favored when E_F is low (n-doped GaN). This relationship can be visually represented for an amphoteric defect by plotting E^f against E_F as illustrated in Fig. 3.1(a). The solid blue lines highlight the stable charge state at a given Fermi energy.

The term "defect level", denoted as $\epsilon(q/q')$, corresponds to the Fermi energy at which the formation energy of two different charged states (q and q') is equal. [286] This transition energy can be expressed using Eq. 3.1 with $E^f[X^q] = E^f[X^{q'}]$ such that:

$$E^f[X^q, E_F = 0] + q\epsilon(q/q') = E^f[X^{q'}, E_F = 0] + q'\epsilon(q/q'), \tag{3.3}$$

leading to:

$$\epsilon(q/q') = \frac{E^f[X^q, E_F = 0] - E^f[X^{q'}, E_F = 0]}{q' - q}. \tag{3.4}$$

The stable charge state of a given defect is determined by the Fermi level. For the amphoteric species considered in Fig. 3.1(a), the transition energies are reported in Fig. 3.1(b). In this example, the defect is stable in its neutral state X^0.

3.1.2 Optical transition in the configuration coordinate diagram

To understand intuitively how the transition level pertains to optical properties of a defect, let us consider a scenario where this defect is optically pumped out of equilibrium. Absorption can be described through one of the following processes[I]:

$$\begin{aligned} X^0 + h\nu &\rightarrow X^+ + e^-, \\ X^0 + h\nu &\rightarrow X^- + h^+, \end{aligned} \tag{3.5}$$

where $h\nu$ amounts to absorbed photon energy. Once elevated to an excited state, the defect can relax either radiatively or non-radiatively to its ground state. Radiative processes are denoted as:

$$X^+ + e^- \rightarrow X^0 + h\nu, \tag{3.6}$$

or:

$$X^- + h^+ \rightarrow X^0 + h\nu. \tag{3.7}$$

Such optical transitions are depicted in Fig. 3.1(b). Under a simplified view, the luminescence peaks are determined by the position of the transition level within the bandgap. However, it is important to note that optical transitions involving the capture of a hole or an electron do not occur with equal probability. The likelihood of each process requires thorough computation, although the details of these calculations are beyond the scope of this discussion.

Defect levels situated near the CBM or close to the VBM are commonly referred to as shallow donors and acceptors, respectively. Due to their proximity to the band edges, electrons from the VB efficiently ionize into the acceptor levels, while electrons from shallow donors ionize into the CB. This leads to the generation of populations of free carriers, resulting in p-type or n-type doping, respectively. Shallow donors and acceptors lead to excitonic features at cryogenic temperatures in PL experiments. They are however unsuited for SPE application and will not be further discussed in this section.

Other transitions are referred to as deep levels and are characterized by localized electronic wavefunctions, which can significantly impact how neighboring atoms arrange. As a result, these levels may exhibit different atomic configurations for various charge states, with the atomic reconfiguration during transitions occurring on a phonon emission/absorption (picosecond) timescale [291]. The optical transition from a state X^q to a state $X^{q'}$ is, however, often considered an instantaneous process (the so-called Franck-Condon approximation [292]) causing the atomic configuration to remain frozen in the defect initial state. Consequently, the formation energy of the final state differs from its relaxed configuration $E^f[X^{q'}]$,

---

[I] We should point out that while the following examples consider transitions involving a change in the charge state q, optical transitions can also occur without changing the defect charge ($X^q \leftrightarrow X^{q*}$). In this case, the theoretical framework developed here remains mostly valid.

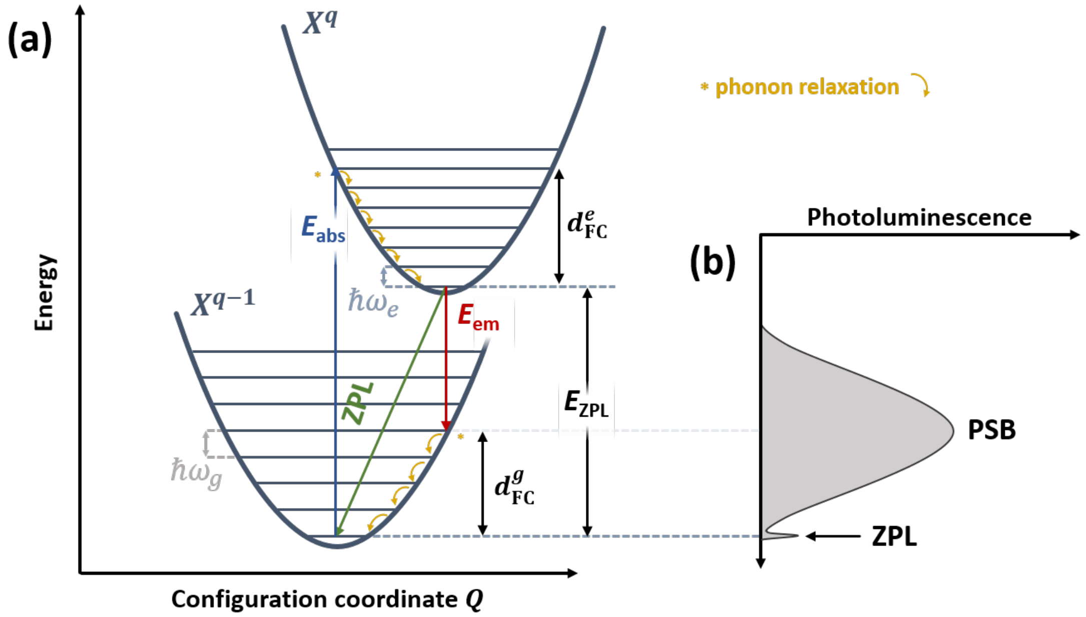

Figure 3.2: **(a)** Configuration-coordinate diagram for the exchange of an electron with the CB by a defect X^q. **(b)** A schematic luminescence spectrum associated to the e^- radiative capture by X^q is also depicted for a strong phonon coupling, for which both ZPL and PSB optical signatures are expected. Freely adapted from [281, 293].

and thermodynamic transition levels $\epsilon(q/q')$ defined by Eq. 3.4 are insufficient to describe such a transition. To capture the dynamics during an optical process, the concept of a configuration coordinate (CC) diagram needs to be introduced.

While transitions in charge states involve variations in a comprehensive set of configuration coordinates $\{R_i\}$, typically describing the displacement of all atoms surrounding the PD, they can often be uniquely linked to a 1D generalized CC (Q) [294]. This coordinate relates for instance to the magnitude of relaxation of the defect surrounding atoms [291]. The energy of each defect state is minimized for a different value of Q and follows a parabolic dependence ($E \propto Q^2$), assuming atomic bonds behave as harmonic springs. Figure 3.2(a) depicts the CC diagram for a defect X^q exchanging an electron with the CB. Vertical transitions in the diagram correspond to photon absorption (E_{abs}) and emission (E_{em}), respectively. After photo-induced ionization, the charge state X^q experiences rapid phonon relaxation to its configuration ground state, losing its excess energy d^e_{FC}. The same process applies to X^{q-1} after the radiative capture of an electron with an energy loss denoted d^g_{FC}. For simplicity, d^e_{FC} and d^g_{FC} are collectively referred to as Franck-Condon shifts (d_{FC}) in the following. This description reveals that the luminescence peak associated with the vertical transition (E_{em}) in Fig. 3.2(a) can differ significantly from the transition with photon energy E_{ZPL} depicted in Fig. 3.1(a). The luminescence peak energy decreases when the atomic equilibrium configuration of the ground and excited defect states diverges. In contrast, E_{ZPL} is associated with the energy difference between the ground state and excited state equilibrium configurations and is referred to as the zero-phonon line (ZPL).

In an effort to synthesize the physics, we can approximate the multiplicity of phonon modes which interact with the ground or excited defect state as single effective modes, with frequencies ω_g and ω_e, and assume $\omega_g = \omega_e = \omega_0$ [293]. The vibrational modes associated with the defect surrounding atoms manifest as multiples of $\hbar\omega_0$. Luminescence from a defect level does not solely result from a vertical transition (E_{em}) in the CC diagram. Instead, it encompasses the sum of all transitions from vibrational levels in the excited state to vibrational levels in the ground state [294]. This leads theoretically to multiple sharp emission lines. Thermal broadening tends to blurr this feature and experimental spectra typically exhibit a well-defined ZPL along with a broad PSB centered around E_{em}.

The phonon coupling strength is quantified by the Huang-Rhys factor S, which, in our simplified description, reads [281]:

$$S = \frac{d_{\mathrm{FC}}}{\hbar\omega_0}. \tag{3.8}$$

In essence, S provides the average number of phonons emitted during an optical process. Figure 3.2(b) illustrates the luminescence spectrum of a defect in the strong phonon coupling regime ($S >> 1$) where the broad PSB takes over the sharp ZPL. From Eq. 3.8, we understand that the electron-phonon coupling of a defect level is primarily driven by the discrepancy between the equilibrium configuration of the ground and excited charge states. This discrepancy causes the substantial broadening of the luminescence spectrum through the PSB. Phonon-coupling is a recurring feature in the investigation of SPE candidates, whether they are QDs or PDs. Its implications for PDs are further discussed below.

Experimentally, the phonon coupling is estimated experimentally by direct extraction of the ZPL photoluminescence relative intensity for a single defect. For NV centers in diamond it is commonly referred to as the Debye-Waller factor (w_{ZPL}) [295, 296] and is explicitly determined by [297]:

$$w_{\mathrm{ZPL}} = \frac{I_{\mathrm{ZPL}}}{I_{\mathrm{ZPL}} + I_{\mathrm{PSB}}}, \tag{3.9}$$

where I_{ZPL} and I_{PSB} represent the photoluminescence of the ZPL and PSB, respectively. The relationship between w_{ZPL} and the Huang-Rhys factor is commonly established through $w_{\mathrm{ZPL}} = e^{-S}$ [298]. However, this relation slightly overestimates the ZPL contribution with respect to the theoretically computed factor, as emphasized by Alkauskas *et al.* [298]. Hence, it is more appropriate to refer to the experimentally computed S factor as:

$$S_{\mathrm{exp}} = -\ln(w_{\mathrm{ZPL}}). \tag{3.10}$$

Optical absorption is conceptually similar to luminescence, involving transitions across all vibrational modes that contribute to smoothing the onset of absorption (E_{abs}). A substantial

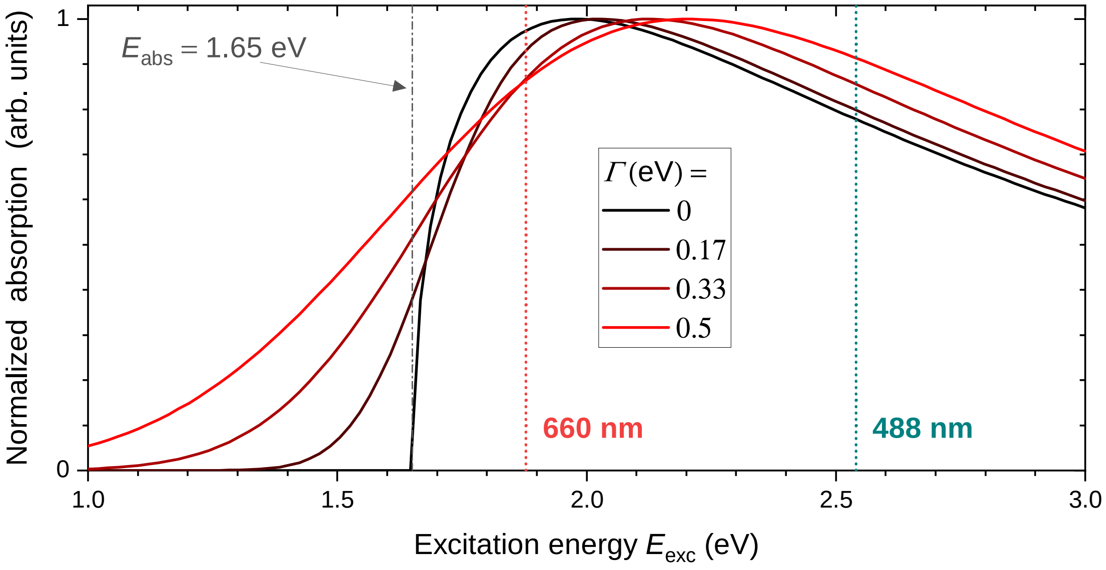

Figure 3.3: Normalized absorption curves for a set of broadening parameters Γ, according to Eq. 3.11. The absorption onset is chosen as $E_{\text{abs}} = 1.65\,\text{eV}$, ($\lambda_{\text{exc}} \sim 750\,\text{nm}$). The dotted lines illustrate the excitation energies for the two lasers: $\lambda_{\text{exc}} = 488\,\text{nm}$ and $\lambda_{\text{exc}} = 660\,\text{nm}$.

difference, however, arises in that a hole or an electron, released during the absorption of a photon, ends up in a continuum of VB or CB states, respectively. This results in sustained absorption well above E_{abs} as detailed by Alkauskas *et al.* [281], with an absorption cross-section σ approximated by:

$$\sigma(E_{\text{exc}}) = \int_0^\infty \frac{e^{-(E+E_{\text{abs}}-E_{\text{exc}})^2/\Gamma^2}\sqrt{E}\,\mathrm{d}E}{E_{\text{exc}}(E+E_{\text{abs}})^2}, \tag{3.11}$$

where E_{exc} represents the energy of the excitation light source and Γ is a broadening parameter proportional to $\sqrt{S}$. Figure 3.3 illustrates the absorption of a single PD for an absorption energy $E_{\text{abs}} = 1.65\,\text{eV}$, representative of the investigated PD SPEs . The vertical dotted lines correspond to the wavelengths of the two lasers which are the most systematically used in the present work, and highlight the relatively constant response expected from a defect when switching the pumping laser.

The 1D configuration coordinate diagram is not universal [294] and seems to particularly fail at describing quantitatively the phonon broadening in the weak phonon coupling regime $S << 1$ [281]. PDs perturb the crystal lattice and are anticipated to induce quasi-local phonon modes, distinct from the bulk optical and acoustic phonon branches [281]. A comprehensive description would require consideration of PD coupling to these modes and goes beyond the scope of our study. Nevertheless, such 1D diagram provides us with key concepts to approach phenomenologically the experimental µ-PL results detailed throughout this section.

3.1.3 Defect concentration

To ascertain the nature of a PD, a practical approach involves establishing a connection between experimentally measured defect concentrations and formation energies computed through DFT simulations for various defects. This connection is often established using the equilibrium defect concentration equation [299, 300]:

$$c^{\mathrm{eq}}(T) = N_{\mathrm{s}} N_{\mathrm{c}} e^{-E^f / k_{\mathrm{B}} T}, \tag{3.12}$$

where N_{s} represents the number of defect sites per unit volume and N_{c} denotes the count of comparable configurations in which a defect can be integrated [299]. However, there are certain limitations to this approach. In Eq. 3.12, it is implicitly assumed that E^f is temperature-independent, which is suitable for simulations performed at $T = 0\,\mathrm{K}$, where electronic and vibrational entropies, are readily neglected [291], but may not hold over a large temperature range. GaN layers are typically grown at elevated temperatures, and defects are formed during this growth process. Applying Eq. 3.12 to compare simulations conducted at 0 K with defect concentrations from samples grown at high temperatures may neglect non-Arrhenius behaviors, potentially impacting the accuracy of theoretical predictions.

Moreover, Eq. 3.12 only holds under thermodynamic equilibrium, requiring PDs to exhibit sufficiently high mobility at the growth temperature to reach this equilibrium. While this condition is believed to be met for MOVPE GaN layers [279, 301] typically grown between 900 and 1100 °C [302, 303], it may not hold for layers grown at lower temperatures (~ 800 °C) using MBE [299].

Additionally, the accuracy of formation energies, as defined by Eq. 3.1, is influenced by the choice of the chemical potential values for the species involved in the defect formation. E^f diagrams, such as the one illustrated in Fig. 3.1, can be adjusted to reflect experimental conditions [279].

In this study, one objective is to extract the density of SPE PDs characterized by sharp ZPLs. Due to their rarity, these emitters can be individually distinguished in hyperspectral μ-PL maps. This technically allows for a counting of these defects, providing a concentration denoted as c_{opt}. At this stage of the setup development, the counting procedure (detailed in Subsect. 3.2.3) still requires manual intervention, which restricts its applicability. However, an automated treatment of hyperspectral maps is currently in progress in our laboratory and is expected to enable a quantitative assessment of defect concentrations in a near future.

For this density to be directly comparable to theoretical predictions, an ideal scenario would require the efficient excitation of all defects in a single measurement, at a specific excitation wavelength λ_{exc}. According to Eq. 3.11, all emitters satisfying $\lambda_{\mathrm{SPE}} > \lambda_{\mathrm{exc}}$ should be excited simultaneously. However, this consideration does not address the coupling between the laser electric field and the SPE dipole moments, as explained in Section 1.3.2, which may result in the inability to detect PDs with an optical dipole moment aligned along the c-axis.

In case where only a fraction of defects of a given type X^q can be detected, we could leverage the concentrations extracted from hyperspectral µ-PL maps to infer the charge state q. This could be achieved by measuring c_{opt} in a set of samples with different doping levels, assuming all other parameters remain constant. Combining Eqs 3.2 and 3.12 we obtain, for a given defect X^q:

$$c^{\text{eq}}(E_{\text{F}}) = N_{\text{s}} N_{\text{c}} e^{-\left(E^f[X^q, E_{\text{F}}=0] + qE_{\text{F}}\right)/k_{\text{B}}T} = N_{\text{s}} N_{\text{c}} e^{-E^f[X^q, E_{\text{F}}=0]} e^{-qE_{\text{F}}/k_{\text{B}}T}. \tag{3.13}$$

Assuming that $c^{\text{eq}} \propto c_{\text{opt}}$, this relationship implies that $\ln(c_{\text{opt}}) \propto q$, providing us with insights into the charge state of the investigated defects. This protocol is currently in a prototype stage and this subsection mainly aims to present one of the potential avenues of our research. However, the conclusions presented here should aid in understanding the initial results discussed in Sect. 3.5.

It is worth emphasizing that achieving precise control over doping levels can be particularly challenging in many wide bandgap materials featuring RT defect SPEs, such as diamond [304]). In this regard, the maturity of III-Ns platforms, and more specifically GaN, offers a notable advantage in achieving this level of control.

3.1.4 Review of defect luminescence in GaN

Numerous luminescence features associated with defects in GaN layers have undergone extensive investigation and classification, as exemplified in Reshchikov and Morkoç [305]. These features are now comprehensively understood within the theoretical framework mentioned earlier, attributing many of them to various PDs. Notable candidates include for instance native defects like nitrogen V_{N} [293] and gallium V_{Ga} vacancies [285], impurities (such as C_{N} [293, 306]), and complexes such as $\text{Mg}_{\text{Ga}} - V_{\text{N}}$[II] [285, 307]. One prevalent feature, known as yellow luminescence (YL) [308, 309], is widely acknowledged to originate from the C_{N} acceptor impurity [310], despite the potential contributions from multiple defects. Our experimental results also confirm the presence of this luminescence band in our samples, as detailed in Subsect. 3.2.1.

It should be noted that all luminescent defects mentioned above share a common characteristic: they exhibit a broad PSB and a weak or nonexistent ZPL. This observation aligns with expectations, considering that localized electronic wavefunctions of deep levels usually transpose into distinct equilibrium configurations of different charge states. This feature leads to a pronounced phonon coupling as detailed in Sect. 3.1.2. However, these defects are ill-suited for photonic applications, which typically demand SPEs exhibiting bright as well as well-defined and narrow emission lines.

In contrast, defect levels featuring low phonon coupling would potentially align with these

---

[II] The notation X_{Y} refers to substitional defects, indicating that an atom X is located in the position typically occupied by the atom Y within the crystal lattice.

restrictive criteria. We expect such levels to showcase nearly cancelled offsets between ground and excited potential energy curves. This should alleviate competitive non-radiative multi-phonon emission (MPE) processes [281], ultimately enhancing the brightness of these defect levels.

Sharp SPE lines associated with defects had not been documented in the literature until recently, possibly due to various reasons: (i) initially, defects were primarily addressed concerning their adverse effects on the internal quantum efficiency (IQE) in LED active layers. (ii) Investigations of GaN layers were conducted using macro-PL, where defects with a low concentration might not have been discernible in photoluminescence spectra dominated by features like the YL. Only lately have GaN defects drawn attention for their potential as high-temperature SPEs in photonic applications. In previous μ-PL studies, SPEs with bright luminescence ZPLs were readily identified in GaN layers, first in the NIR range (600 nm to 800 nm), with $S_{\mathrm{exp}} \simeq 0.5$ at low temperature [30, 311], and later in the telecom range (1100 nm to 1400 nm) [31].

Initially, Berhane *et al.* and Zhou *et al.* proposed that the luminescence could originate from excitons localized at defect positions near stacking faults (SFs) [30, 31]. However, subsequent studies challenged this hypothesis, finding no evidence that the concentration of these emitters depended on the presence of SFs. Rather, they were observed in samples both with and without SFs, in both the NIR [275] and telecom ranges [312]. Nguyen *et al.* also reported samples with a high concentration of SFs and no SPE lines [275].

Numerous reports now document bright RT and narrow SPE lines in bulk GaN [255, 311, 313–315]. If their origin is still unknown, recent studies tend to support the idea that they stem from deep defect levels, potentially in the form of defect complexes [33], from various emitter types [314]. In parallel, recent DFT calculations have been proposed which yield defects with small d_{FC} shifts, such as $\mathrm{N_{Ga}V_N^0}$ with $E_{\mathrm{ZPL}} = 1.98\,\mathrm{eV}$ (NIR), $d_{\mathrm{FC}} = 0.23\,\mathrm{eV}$ and $\mathrm{N_{Ga}^0}$ with $E_{\mathrm{ZPL}} = 0.84\,\mathrm{eV}$ (telecom), $d_{\mathrm{FC}} = 0.09\,\mathrm{eV}$. The high energy of formation of these defects ($> 4\,\mathrm{eV}$ for all growth conditions) could align with the low densities observed in μ-PL maps. The large variety of peak energies has yet to be explained.

However, several trends already emerge from these studies. Defect SPEs are preferentially observed in GaN grown on sapphire, and there seems to be a correlation between the density of threading dislocations (TDs) and the density of defects, but no direct causality. These defects do not form directly in the vicinity of TDs. Defect SPEs seem to form predominantly in the bulk, and thus seem unrelated to surface-related defects. They have been reported in polar and semi-polar GaN but not in non-polar GaN. Details regarding their optical characteristics are discussed in the subsequent sections.

3.1.5 Modeling the recombination dynamics of defects states

Given the elusive origin of SPE PDs in GaN layers at this stage, accurately modeling the recombination dynamics of such emitters remains challenging. Nevertheless, valuable insights can be obtained by analysing $g^{(2)}(\tau)$ traces and TRPL transients recorded from single defects. As our NIR setup has not yet been adapted for TRPL measurements, we focus here on the perspective gained from $g^{(2)}(\tau)$ measurements. To do so, it is insightful to review the approaches adopted so far by the different groups who reported on RT single-photon emission from PDs in GaN.

Whether addressing NIR or telecom SPEs, most studies have identified a bunching phenomenon in $g^{(2)}(\tau)$ traces recorded from individual emission lines, indicating a recombination mechanism extending beyond the simplistic two-level system detailed in Subsection 2.2.4. As discussed in Subsect. 2.4.3 for QDs, this bunching phenomenon can be explained by considering additional electronic states analogous to the QD multiexcitonic and/or dark states. In the case of defect SPEs, these manifest themselves as shelving states typically originating from excited defect states characterized by a metastability attributed to spin-forbidden radiative recombination. Various models have been proposed in the literature to account for such features, starting with the general expression [312, 316]:

$$g^{(2)}_{\mathrm{PD}}(\tau) = 1 - C_1 e^{-|t|/\tau_1} + \sum_{i \neq 1} C_i e^{-|\tau|/\tau_i}. \tag{3.14}$$

Here, empirically introduced bunching terms with amplitudes C_i $(i > 1)$ and characteristic lifetimes τ_i account for the presence of undetermined shelving states.

In their precursor study, Berhane *et al.* [30] adopted a more specific model, previously applied to a wide range of SPEs, ranging from various dye molecules [317, 318] to Cr or SiV defects in diamond [12, 319, 320] or ZnO defects [321]. This model, numbered (i) in Fig. 3.4, considers a single metastable state $|m\rangle$, which offers an additional non-radiative recombination channel from the excited state (denoted as $|e\rangle$) to the ground state $|g\rangle$. Subsequent studies have consistently applied this approach to both NIR [314, 315] and telecom emitters [31].

While not explicitly applied, Berhane *et al.* [30] and Zhou *et al.* [31] evoked an alternative model, numbered (ii) in Fig. 3.4, initially proposed by Kurtsiefer *et al.* [322] to describe the recombination dynamics of NV centers in diamond. In this model, the de-shelving of the metastable state is bound to occur through repopulation of the excited state $|e\rangle$ rather than relaxation toward the ground state. Bishop *et al.* [313] modeled the bunching phenomenon by combining both scenarios (i + ii), assuming de-shelving of state $|m\rangle$ through both states $|e\rangle$ (rate γ^{e}_m) and $|g\rangle$ (rate γ^{r}_m) [313].

In all scenarios, the $g^{(2)}(\tau)$ of the system is derived by solving the associated rate equations,

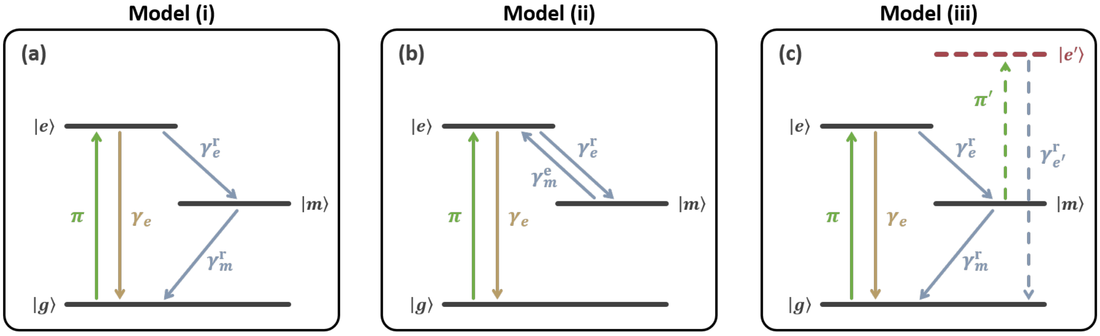

Figure 3.4: Modeling of the recombination dynamics in PDs acting as SPEs. Green arrows indicate power-dependent transitions (pump rates π and π'), while blue arrows represent non-radiative channels. Radiative transitions are highlighted by yellow arrows (rate γ_e). Dashed lines represent transitions that are not explicitly included in the modeling (see details in text).

considering:

$$g^{(2)}_{\mathrm{PD}}(\tau) = \frac{n_e(|\tau|)}{n_e(\infty)}, \tag{3.15}$$

where n_e represents the occupancy probability of state $|e\rangle$. The resolution process follows the same methodology outlined for the 'biexciton three-level model' developed in Subsect. 2.4.3 and yields ultimately a solution of the form, (see Appendices B.4 and B.5 for details):

$$g^{(2)}_{\mathrm{PD}}(\tau) = 1 - (1+a)e^{-\gamma_1^{\mathrm{d}}|\tau|} + ae^{-\gamma_2^{\mathrm{d}}|\tau|}, \tag{3.16}$$

where the amplitude a as well as the antibunching γ_1^{d} and bunching γ_2^{d} rates depend on the specific model employed. Thus, while all models yield a similar solution (Eq. 3.16) capable of reproducing experimental $g^{(2)}(\tau)$ traces satisfactorily, the true validity of a model in capturing the physics of the defect system can only be assessed by comparing the trends of fitting parameters with theoretical predictions. Notably, Berhane *et al.* proposed adapting model (i) to incorporate a power-dependent de-shelving mechanism of the metastable state, a concept previously applied to SiV defects by Neu *et al.* [12, 320]. In this revised model, designated as (iii) in Fig. 3.4, the de-shelving is assumed to occur simultaneously through state $|g\rangle$ and a higher excited state ($|e'\rangle$), resulting in an effective 'de-shelving rate' $\gamma_m^{\mathrm{r}}(\sigma_{\mathrm{exc}})$ [30, 323]:

$$\gamma_m^{\mathrm{r}}(\sigma_{\mathrm{exc}}) = \gamma_{\mathrm{m}}^{\mathrm{r},0} + \frac{\gamma_{\mathrm{m}}^{\mathrm{r},\infty}}{1+\sigma_{\mathrm{sat}}^{\mathrm{m}}/\sigma_{\mathrm{exc}}}, \tag{3.17}$$

where $\gamma_{\mathrm{m}}^{\mathrm{r},0}$, $\gamma_{\mathrm{m}}^{\mathrm{r},\infty}$ and $\sigma_{\mathrm{sat}}^{\mathrm{m}}$ depend on the transition rates π', γ_m^{r} and $\gamma_{\mathrm{e'}}^{\mathrm{r}}$ depicted in Fig. 3.4(c). It is crucial to note that increasing the number of fitting parameters mechanically improves the goodness of fit for a given dataset, thus directly impacting the relevance of conclusions drawn from using an overly complex model. Considering these factors, we provide a comparison of the various models with our experimental findings in Sect. 3.4.

In all proposed models, the presence of a shelving state also impacts the intensity of an SPE PL line (I_{SPE}), resulting in a saturation behavior described by:

$$I_{\mathrm{SPE}} = \frac{I_{\mathrm{sat}}}{1 + \sigma_{\mathrm{sat}}/\sigma_{\mathrm{exc}}}, \tag{3.18}$$

where the parameters I_{sat} and σ_{sat} vary depending on the model under consideration (refer to Appendix B.4). It is worth noting that this saturation is independent of 'vibrational relaxation' processes discussed in Subsect. 3.1.2, which occur on a much shorter timescale.

3.2 Methodology for investigating point defects

The following sections are dedicated to the presentation of our preliminary results on PD SPEs in GaN layers. Since this topic remains rather new for our laboratory, experimental protocols are still subject to further refinement. This first section details the standard procedures elaborated by the time of writing to address individual SPEs and intends at providing a general understanding of the investigated platform. While the 'QD community' is used to report PL results in energy units, prior publications on GaN PD SPEs have consistently adopted wavelength scales to represent PL spectra. For the sake of coherence, we will adhere to this standard in the following. All measurements described in this chapter were performed at RT. We should mention that while the actual confirmation of the SPE nature of the PDs under investigation is only provided in Sect. 3.4, we will assume it to be true throughout all sections of this chapter.

3.2.1 Yellow luminescence

All samples examined in this chapter consist of GaN layers grown on sapphire substrates. As mentioned in Subsect. 3.1.4 such bulk layers typically exhibit a broad defect-related PL band referred to as yellow luminescence (YL). The position, extent, and relative intensity of this band vary with the doping level and the growth recipes adopted. Its presence is usually detrimental as it constitutes the principal source of background luminescence and can significantly impact the single-photon purity of PD SPEs. This luminescence feature is illustrated in Fig. 3.5 for PL spectra recorded on a 4 µm n-doped GaN template grown by MOVPE at high temperature (1000 °C) on sapphire (labeled C3647). While typically much more intense when excited using an above-bandgap laser [324] (here, with a $\lambda_{\mathrm{exc}} = 355$ nm), its presence is still clearly evident when employing a 488 nm laser line. Although the YL peaks in the visible range, its low-energy tail still overlaps with the spectral range investigated in this chapter ($\gtrsim 700$ nm) and is consistently observed in most samples. While detrimental, it can have a practical use detailed in the next section. Unless stated otherwise, the measurements reported in the subsequent sections were all conducted on a p-doped GaN template with a thickness of 4 µm, grown on sapphire and labeled as A4365. Discussion regarding the selection of substrate and growth conditions is deferred to Subsection 3.5.

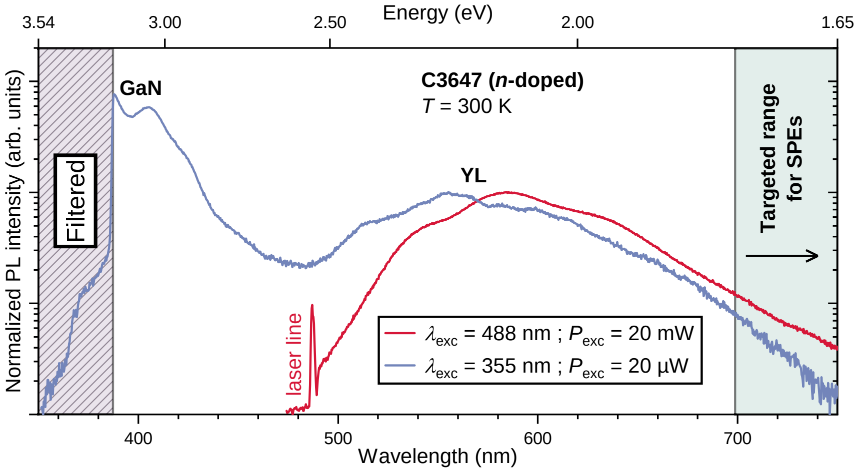

Figure 3.5: Normalized RT PL spectra recorded on an n-doped sample (C3647) at $\lambda_{\text{exc}} = 355$ nm and $\lambda_{\text{exc}} = 488$ nm. The tail of the YL overlaps with the spectral window investigated in this chapter. The GaN PL peak is largely attenuated by the long-pass filter used to eliminate the 355 nm laser line, which accounts for its redshift compared to the GaN-on-sapphire bandgap of $E_g \simeq 3.44$ eV ($\sim$ 360 nm) at 300 K. In practice, the YL is orders of magnitude weaker than the GaN bandedge luminescence.

3.2.2 Depth measurements and confocal microscopy

Studying individual SPEs via µ-PL measurements requires precise alignment of the microscope to achieve a focus with micrometer-level accuracy. The alignment procedure typically begins with a coarse positioning of the objective using the 'imaging assembly' depicted in Fig. 1.8. However, a more refined alignment can be achieved by monitoring the YL as a function of the 'vertical' or z-axis position of the microscope.

This alignment procedure is illustrated in Fig. 3.6 for a dataset acquired with the in-plane position of the objective aligned to an emitter labeled SPE$_1$. Figure 3.6(a) depicts a PL spectrum averaged from multiple spectra acquired around the peak intensity of the SPE. The two lines observed around 695 nm stem from the sapphire substrate and are attributed to the R$_1$ and R$_2$ lines of the Cr^{3+} ions [325] present in the substrate. The broad luminescence background otherwise originates from the tail of the YL. The sharp decline observed around 775 nm is a result of the dichroic mirror used to optimize the collection efficiency of our setup (cf. Sect. 1.1).

The PL intensity map displayed in Fig. 3.6(b) was generated by vertically scanning the sample over a distance of 10 µm. Such maps are used for the extraction of 'depth' profiles by integrating the PL intensity over specific spectral features. This is demonstrated in Fig. 3.6(c) for spectral windows centered on the SPE$_1$[III] line and on the lower-wavelength end of the YL, respectively. The maximum intensity of the YL luminescence is expected when the laser beam is focused in

---

[III] In practice, the integrated intensity of an SPE is better estimated by fitting the PL with a Lorentzian profile.

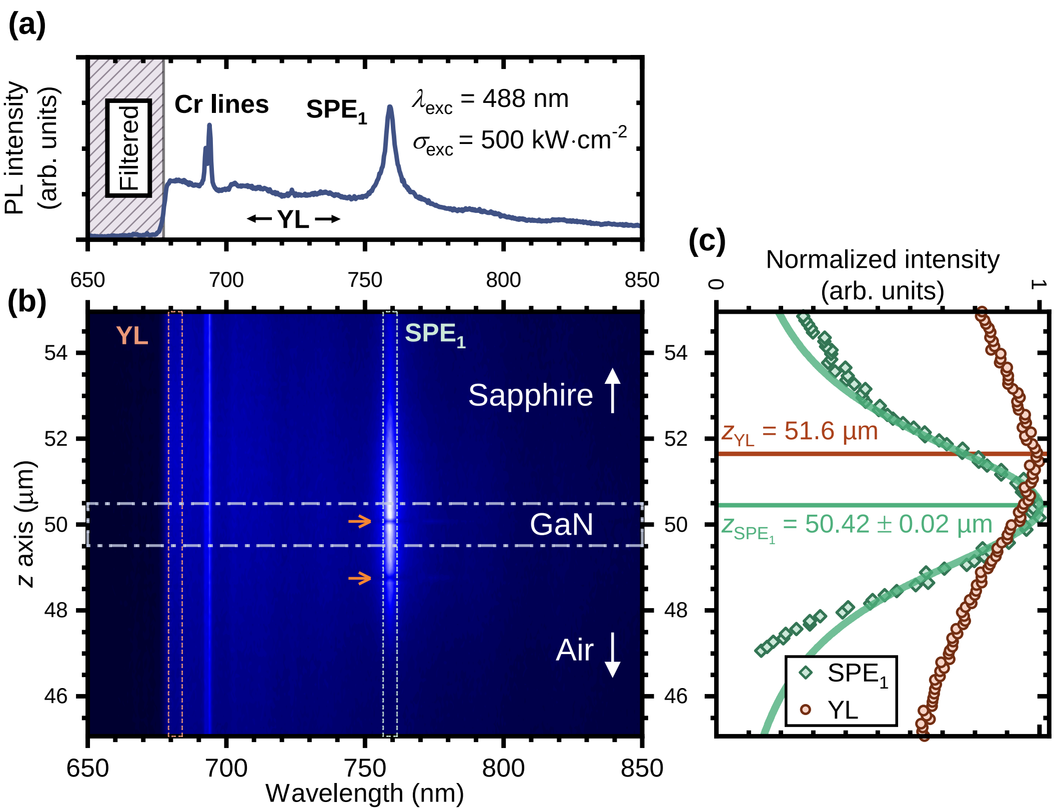

Figure 3.6: **(a)** PL spectrum of SPE$_1$ averaged over the region highlighted by the dash-dotted area in (b). **(b)** Intensity map acquired as a function of objective position along the z-axis. **(c)** Average normalized PL intensity over the regions indicated by dashed lines in (b). The integrated PL of SPE$_1$ is determined by fitting a Lorentzian function to the SPE line (green diamonds). The peak intensities are indicated by horizontal bars. The evolution of SPE PL in the z direction is fitted using Eq. 3.19.

the center of the GaN layer, which provides a rather accurate method for aligning our setup, despite the broad extent of the YL along the z-axis. Qualitatively, localized emission lines have consistently been observed within a $\pm 2\,\mu\text{m}$ range of the YL maximum, as discussed in Subsect. 3.5.2 and as exemplified in Fig. 3.6(c) for SPE$_1$.

In contrast to the YL, the SPE depth profile features a relatively-well defined maximum, consistent with the framework developed in Subsect. 1.1.3. Considering that the excitation power density along the z-axis follows a Lorentzian profile (cf. Eqs. 1.6 and 1.7) and assuming a linear dependence between σ_{exc} and the SPE intensity (I_{SPE}), we can derive the following relation:

$$I_{\text{SPE}}(z) = \frac{I_0}{1+\left(\frac{z-z_{\text{SPE}}}{z_{\text{R}}'}\right)^2}, \tag{3.19}$$

where z_{SPE} represents the vertical position of the emitter and I_0 is a fitting parameter. Although

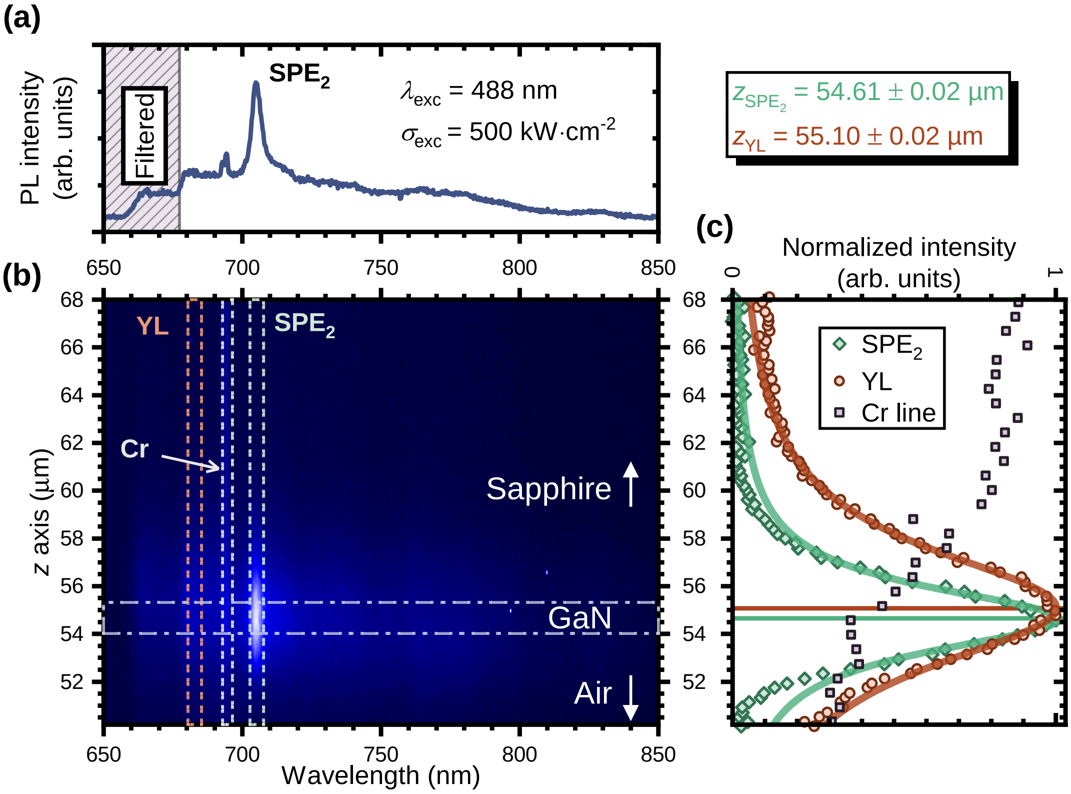

Figure 3.7: **(a)** PL spectrum of SPE$_3$ averaged over the region highlighted by the dash-dotted area in (b). **(b)** Intensity map acquired as a function of objective position along the z-axis. **(c)** Average PL intensity over the regions indicated by dashed lines in (b). The peak intensities are indicated by horizontal bars. The YL and SPE PL evolution in the z direction are fitted using Eq. 3.19.

the linear approximation ($I_{\mathrm{SPE}} \propto \sigma_{\mathrm{exc}}$) breaks down at high excitation power, Eq. 3.19 satisfactorily reproduces the SPE depth profile around z_{SPE} and provides a sub-micrometer precision on the relative position of the emitter, albeit *a priori* larger than the fitting uncertainty reported in Fig. 3.6(c)). It is worth remarking that the $z_R{}' = (2.21 \pm 0.05)\,\mu\mathrm{m}$ value obtained here does not significantly deviate from the theoretical limit of the Rayleigh range ($z_R{}' = 1.6\,\mu\mathrm{m}$) derived in Subsect. 1.1.3.

While an accurate determination of the relative position of an SPE is crucial for optimum alignment, an absolute determination of its position with respect to the GaN layer could provide insights into the formation mechanism of these quantum emitters, a concept further explored in Subsect. 3.5.2. To achieve this, we complemented the NIR setup with a confocal path (illustrated in Fig. 1.4). The depth scan of a second SPE (denoted as SPE$_2$) recorded using the confocal path is illustrated in Fig. 3.7.

The spatial filtering first results in an enhanced resolution on the emitter position, evidenced by a narrowing of the depth profile characterized by $z_R{}' = (1.67 \pm 0.04)\,\mu\text{m}$. More importantly, the depth profile associated with the YL now exhibits a peak comparable to that of the SPE, which is also well-approximated by Eq. 3.19, enabling us to measure the distance of the emitter to the center of the GaN layer[IV]. In confocal measurements, the Cr lines also show a notable increase as the objective approaches the sample (with increasing z). However, this transition is much less pronounced than that of the YL (cf. Fig. 3.7(c)) and does not serve as reliable reference point for determining the position of the emitters.

We should incidentally mention that the confocal setup is also intended to enhance the SNR of the investigated emitters. However, in its current configuration, the modest reduction in background luminescence comes at the expense of a substantial decrease in the collected PL signal and requires further adjustment to improve its effectiveness.

As an additional observation, SPE$_1$ displays a blinking behavior, visible in Fig. 3.6(b) as a sudden intensity drop at $z = 49$ and $50\,\mu\text{m}$. Such phenomena are fairly common for PD-like SPEs although the underlying mechanisms are not well understood yet. A section of this chapter (see Sect. 3.3) is dedicated to the study of such a blinking emitter.

3.2.3 Sample mapping

After the initial focusing of the objective on the GaN layer, the identification of SPEs is achieved by recording hyperspectral maps of the sample. This consists in raster scanning the sample in-plane, recording a PL spectrum at each x and y position. The resulting data are visualized by selecting specific spectral ranges to integrate each PL spectrum, thus generating intensity maps like those depicted in Figs. 3.8(a-e). These intensity maps, derived from the same hyperspectral data, exhibit localized intensity maxima that vary depending on the wavelengths of interest. Bright features appearing across multiple intensity maps are typically associated with fluctuations in the background luminescence and are disregarded. Likewise, isolated bright spots usually coincide with cosmic ray interference on one or a few CCD pixels and are easily distinguished ’by the eye’ from genuine SPE features[V].

The raster scanning step for creating large overview maps (covering tens of micrometers) is typically set between 0.1 and 0.4 µm to ensure that SPE features cover several pixels in the intensity maps while minimizing the acquisition time. The integration time for each PL spectrum usually lasts a few seconds, (e.g., 2 s in Fig. 3.8).

Following the careful elimination of spurious features, SPEs can be readily identified by

---

[IV] While the YL depth profile is well reproduced through Eq. 3.19, it seems reasonable to assume a better match by applying a convolution of the Lorentzian with a 4 µm boxcar function to account for the extent of the GaN layer. The resulting function, computed with Wolfram|Alpha, reads $I_{\text{YL}}(z) = I_0\left[\arctan\left(\frac{z - z_{\text{YL}} + 2\,\mu\text{m}}{z_R}\right) - \arctan\left(\frac{z - z_{\text{YL}} - 2\,\mu\text{m}}{z_R}\right)\right]$ and exhibits a similar behavior to the Lorentzian profile.

[V] Incidentally, an option for removing cosmic rays has been implemented in the LabVIEW software. This feature identifies erroneous events by comparing the intensity recorded on each CCD pixel with the values of its neighboring pixels in the hyperspectral map, both spatially and spectrally.

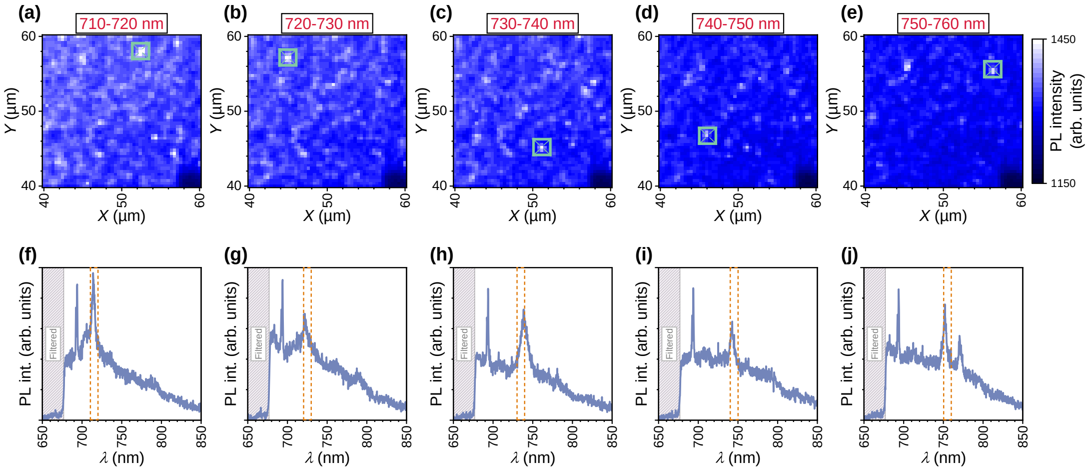

Figure 3.8: **(a-e)** $20 \times 20\,\mu\mathrm{m}^2$ RT PL intensity maps integrated over spectral intervals of 10 nm. The associated hyperspectral map was acquired by steps of 0.4 µm with 2 s integration time. **(f-j)** RT PL spectra associated with each pixel marked by a green square in intensity maps. Dashed rectangles highlight the integration window used for each intensity map. All data were recorded with $\lambda_{\mathrm{exc}} = 488\,\mathrm{nm}$ at $1.1\,\mathrm{MW \cdot cm^{-2}}$.

correlating bright spots detected in the intensity maps with their characteristic Lorentzian signature in PL spectra. Such spectra are shown for illustration in Figs. 3.8(f-i) and are associated with the pixels highlighted by green squares in Figs. 3.8(a-e). More details about the identification procedure and software capabilities are discussed in Appendix A.1.

At the current stage of the software development, the examination of individual emitters still relies on manual intervention, following the identification of positions of interest in the hyperspectral map. Achieving full automation of such measurements necessitates the establishment of robust criteria for distinguishing between genuine SPE features and spurious ones, as well as the implementation of a self-focusing procedure and represents a challenging tasks. Nevertheless, it constitutes and essential milestone toward extracting meaningful statistics from our samples and is currently under development as part of the PhD thesis of A. Bampis in our laboratory.

3.2.4 Polarization and power-dependent measurements

To investigate individual SPEs, high-resolution measurements that aim at determining the polarization, power, or temperature features are typically recorded. While our exploration into the temperature response of PD SPEs has yet to commence, the procedures for extracting information from other sets of measurements are already quite well-established and outlined in the following. The analysis of processed datasets will be covered in subsequent sections.

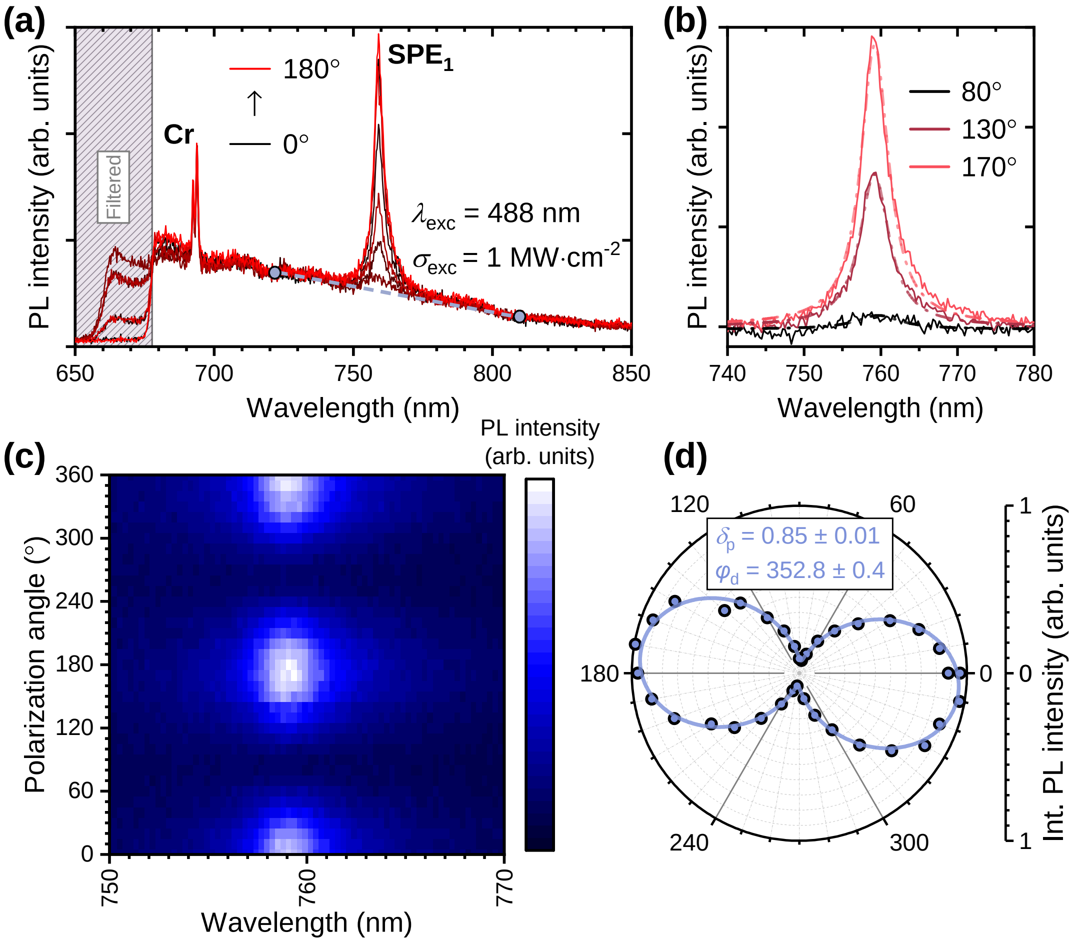

Figure 3.9: **(a)** Polarization-dependent RT PL spectra recorded on SPE$_1$. The grey dots represent the data points used for linear background correction. **(b)** Background-corrected polarization-dependent PL spectra. Lorentzian fits are represented by dash-dotted lines. **(c)** PL intensity map used to extract the integrated intensity values displayed in **(d)** the polar plot.

POLARIZATION-DEPENDENT MEASUREMENTS

Starting with polarization-dependent measurements, Fig. 3.9(a) illustrates the evolution of PL spectra acquired from SPE$_1$ for varying angles of the HWP (see Figs. 1.1 and 1.13). The actual polarization angle of the PL signal after passing through the polarizer is determined using the procedure outlined in Subsect. 1.4, with the vertical axis set to 0. To ensure the comparability of polarization-dependent measurements across different samples or after physical adjustments to the sample position, the polarization angle is ultimately referenced to the m-axis[VI] of the GaN layer. This axis is readily determined by acquiring an optical image of a sample edge, as GaN samples grown on sapphire are typically cleaved along the a-plane. Owing to the C_3 symmetry of wurtzite GaN and the C_2 symmetry of the polarized light, the in-plane dipole angle of each emitter (φ_d, cf. Sect. 1.3.2) is defined modulo 60.

[VI] Perpendicular to the m-plane.

For each PL spectrum, the simplest procedure to extract the integrated intensity of the SPE line consists in approximating the complex YL background through a linear correction, as illustrated in Fig. 3.9(a), and fitting the background-corrected plots with a Lorentzian profile, as shown in Fig. 3.9(b). This procedure was used here to derive the polar plot presented in Fig. 3.9(d) from the polarization-dependent intensity map presented in Fig. 3.9(c).

However, while this method is efficient for determining the in-plane dipole angles of PD SPEs, it can lead to large uncertainties when the luminescence of an SPE nearly cancels, especially for polarization angles close to $\varphi_\mathrm{d} \pm 90°$. This is particularly problematic for emitters with a DLP close to unity and is exacerbated by Fabry-Perot interference. The interference pattern, visible in Fig. 3.9(a), results in integrated intensities extracted from the fitting procedure being highly dependent on the data points chosen for baseline correction and on the position of the SPE relative to the Fabry-Perot interference pattern. This issue is evidenced in Fig. 3.9(b), where the Lorentzian fit obtained for a polarization angle of 80° primarily captures the Fabry-Perot intensity fluctuation. Since SPE_1 is located on a local maximum of the interference pattern, its DLP is underestimated and the protocol described here cannot properly assess it.

This issue becomes particularly problematic when attempting to derive the out-of-plane dipole orientation (θ_d) from the DLP. The sensitivity of this calculation is such that variations of a hundredth in δ_p can result in differences of tens of degrees in the calculated θ_d (cf. Fig. 1.19). While the NA of our objective currently hinders any true quantitative assessment of the out-of-plane dipole angle, it is worth discussing an alternative approach that could significantly improve the precision of our measurements. This approach is illustrated in Fig. 3.10, which depicts measurements performed on another emitter labeled SPE_3.

The key idea revolves around leveraging the polarization insensitivity of the YL, as observed in Fig. 3.9[VII] to record PL spectra distant by a few micrometers from an SPE and subtract these 'background' spectra from those obtained directly on the emitter. This procedure is demonstrated in Figs. 3.10(a) and 3.10(b), showcasing PL spectra acquired on and one micrometer away from SPE_3 with perpendicular polarization axes. The resulting subtracted spectra are depicted in Fig. 3.10(c).

The method shows promising results despite facing several limitations. As illustrated in Fig 3.8, one challenge arises from the non-uniformity of the YL, which can exhibit significant variations within a few micrometers, thus affecting the reliability of our approach. On the other hand, background spectra recorded in close proximity to the emitter may still contain residual contributions from the SPE luminescence, as evident in Fig. 3.10(a), thereby impacting the precision of our measurements. The most viable solution at this stage appears to be the acquisition of multiple background spectra around the emitter, captured with a polarization angle chosen to minimize the residual SPE signal (as shown in Fig. 3.10(b)), to form an averaged background spectrum.

[VII] The polarization-dependent intensity fluctuations observed between 650 and 680 nm result from the sensitivity of the dichroic mirror cut-on wavelength on the light polarization.

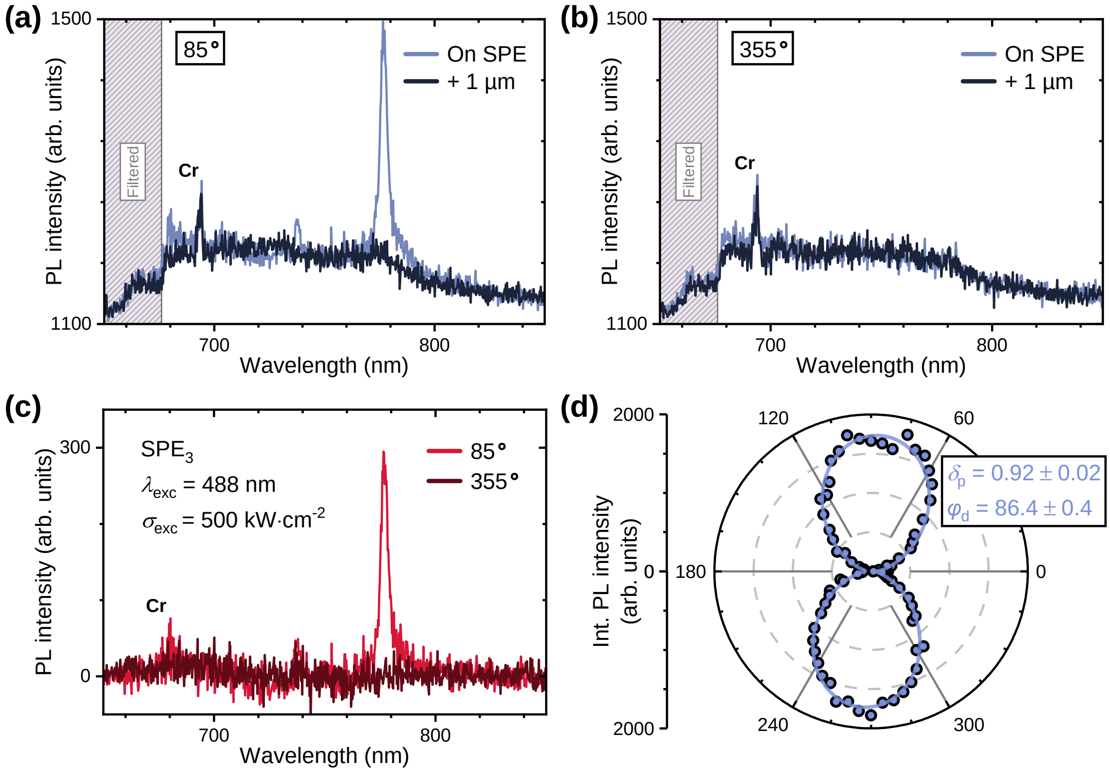

Figure 3.10: RT PL spectra recorded with a polarization angle of **(a)** 85° and **(b)** 355° on SPE$_3$ (blue lines) and 1 µm away, on the 'background' (black lines). **(c)** Background-subtracted PL curves. **(d)** Polar plot of the SPE$_3$ integrated intensities extracted from background-corrected spectra. All spectra were recorded with a 3 s integration time.

This method offers a promising alternative, as the background subtraction effectively eliminates the spectrally well-defined variations in the YL luminescence that result from Fabry-Perot interference. However, fluctuations in laser intensity and overall luminescence characteristics, which previously had a negligible impact, can significantly influence this approach, and seemingly necessitates longer integration times (~ tens of seconds per graph) to achieve satisfactory results. The method is currently undergoing further quantitative assessment.

POWER-DEPENDENT MEASUREMENTS

Compared to polarization-dependent measurements, power-dependent measurements are less challenging to implement and can be readily treated following the first method that consists in applying a linear baseline correction to the acquired spectra. The procedure is illustrated in Fig. 3.11 for measurements performed on SPE$_1$. The initial dataset is displayed in the intensity map (Fig. 3.11(a)) from which a set of spectra is illustrated in Fig. 3.11(b) after background correction. From a Lorentzian fit, we extracted the integrated intensity, center wavelength and FWHM of the SPE emission line, which are reported in Figs. 3.11(c) and 3.11(d).

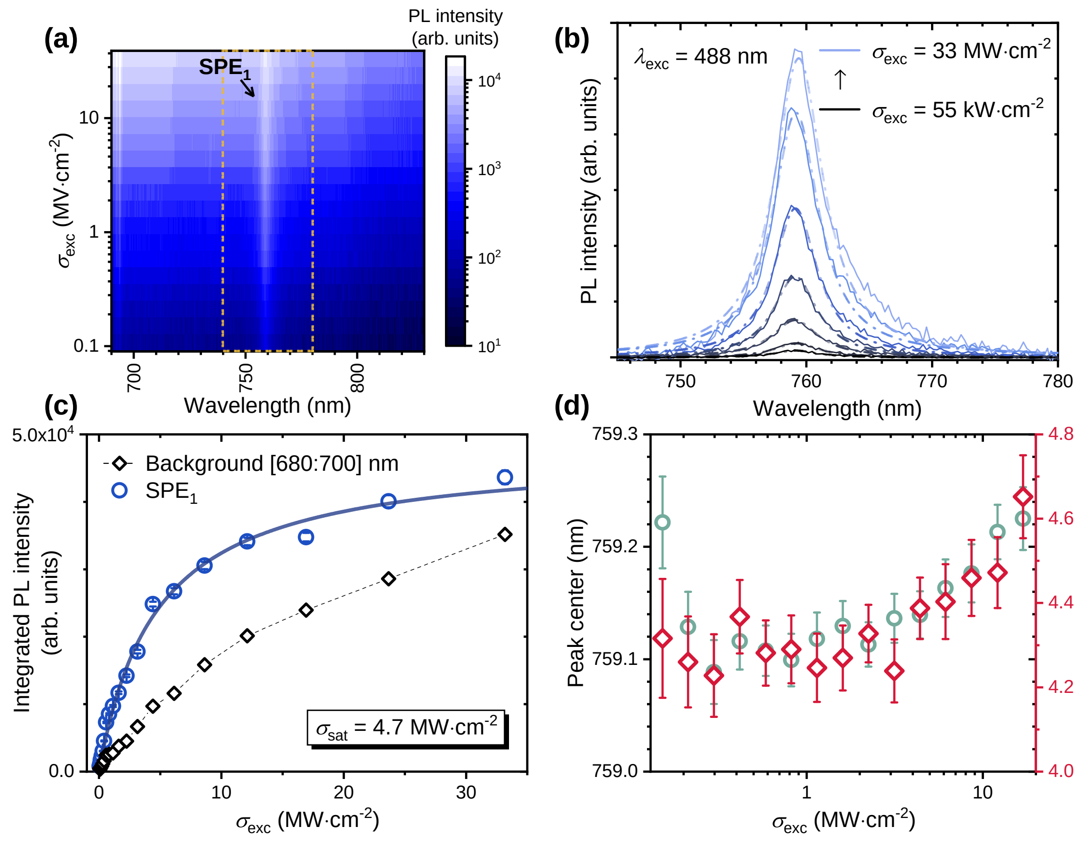

Figure 3.11: **(a)** Power-dependent RT PL intensity map recorded on $\mathrm{SPE_1}$. **(b)** Background-corrected RT PL spectra extracted from (a). Lorentzian fits are represented by dash-dotted lines. **(c)** Evolution of the integrated intensity of $\mathrm{SPE_1}$ as a function of excitation power density. The background intensity integrated between 680 and 700 nm is depicted for comparison. The solid blue line corresponds to the results obtained using Eq. 3.18, while the dashed line serves as a guide to the eye. **(d)** Evolution of the $\mathrm{SPE_1}$ peak position and FWHM with excitation power density.

As discussed in Subsect. 3.1.5, the SPE intensity follows a typical saturation behavior, well-reproduced using Eq. 3.18. However, this fitting procedure alone is insufficient to determine the various rates involved in the PD recombination dynamics, given the number of parameters involved and their intricate contribution to I_{sat} and σ_{sat} parameters (see Appendix B.4 for details). Nevertheless, it provides useful information to define the appropriate trade-off in excitation power densities needed when recording hyperspectral maps and performing $g^{(2)}(\tau)$ measurements.

For the latter, it is important to note that, while the background luminescence also follows a saturation of some sort (illustrated in Fig. 3.11(c)), its intensity relative to any SPE line consistently increases with excitation power density. This leads to a logical degradation of the single-photon purity values measured under high pumping conditions, as further discussed in Sect. 3.4.

Apart from a logical increase in intensity, the SPE PL line shows minimal variations in shape with increasing excitation power densities, as illustrated in Fig. 3.11(d). However, at sufficiently large σ_{exc} values, a slight redshift of the center wavelength can be observed along with a minor line broadening. Both features appear to coincide with a gradual deviation from a pure Lorentzian shape of the SPE line, as observed in Fig. 3.11(b) on the low-energy side of the PL peak at $\sigma_{\text{exc}} = 33\,\text{MW}\cdot\text{cm}^{-2}$. This asymmetry in the PL line is indicative of the PSB contribution. Its detailed study would require a better spectral resolution than that currently available, in conjunction with temperature-dependent measurements. Therefore, this aspect has been postponed for future investigations.

3.3 Photo-induced blinking behavior

3.3.1 Qualitative description

Many defect-based SPEs demonstrate long-term PL stability, as evidenced by the measurements detailed thus far. However, this is not universally observed, as blinking or bleaching phenomena have been reported in previous studies on GaN defects, spanning both NIR [314, 323] and telecom wavelengths [32, 312]. Despite their potential to hinder the attractiveness of otherwise highly promising RT SPEs, the complex power-dependence and non-reproducibility of such features often lead to their dismissal from in-depth study.

In our work, we encountered similar challenges when attempting to correlate instability features to the vertical position of emitters through the method developed in subsection 3.2.2. The highly variable frequency of blinking, jittering, or bleaching phenomena significantly hampers such investigations. For instance, the first occurrence of blinking from SPE_1 (Fig. 3.6(b)) manifested after days of investigation on an otherwise remarkably stable emitter. If any conclusion can be drawn at this stage, it is that high excitation power densities tend to amplify instability features, further exacerbating their complexity.

However, in certain cases, PL instabilities manifest themselves as a relatively simple process, as observed for the emitter labeled SPE_4, whose behavior is discussed in this section. This emitter exhibits a straightforward blinking pattern[VIII], with its PL peak switching over time between two discrete spectral positions, labeled as A and B, respectively, and separated by about 11 nm (or 24 meV). This phenomenon is illustrated by a time-dependent intensity map in Fig. 3.12(a). Associated RT PL spectra averaged over different time intervals to highlight peak_A and peak_B, are shown in Fig. 3.12(b). Additionally, both emission lines exhibit an equivalent in-plane dipole angle ($\sim \varphi_\text{d} = 136°$), as extracted from the polarization-dependent intensity map presented in Fig. 3.12(c) after careful attribution of each individual spectrum (1-second integration time) to either of the emitter configurations. The resulting polar plot is displayed in Fig. 3.12(d).

[VIII] Although the term ’blinking’ is often used to describe emitters presenting an ’on’ or bright and ’off’ or dark configuration, we shall use it in this context to describe the switch of the PL line between two distinct positions.

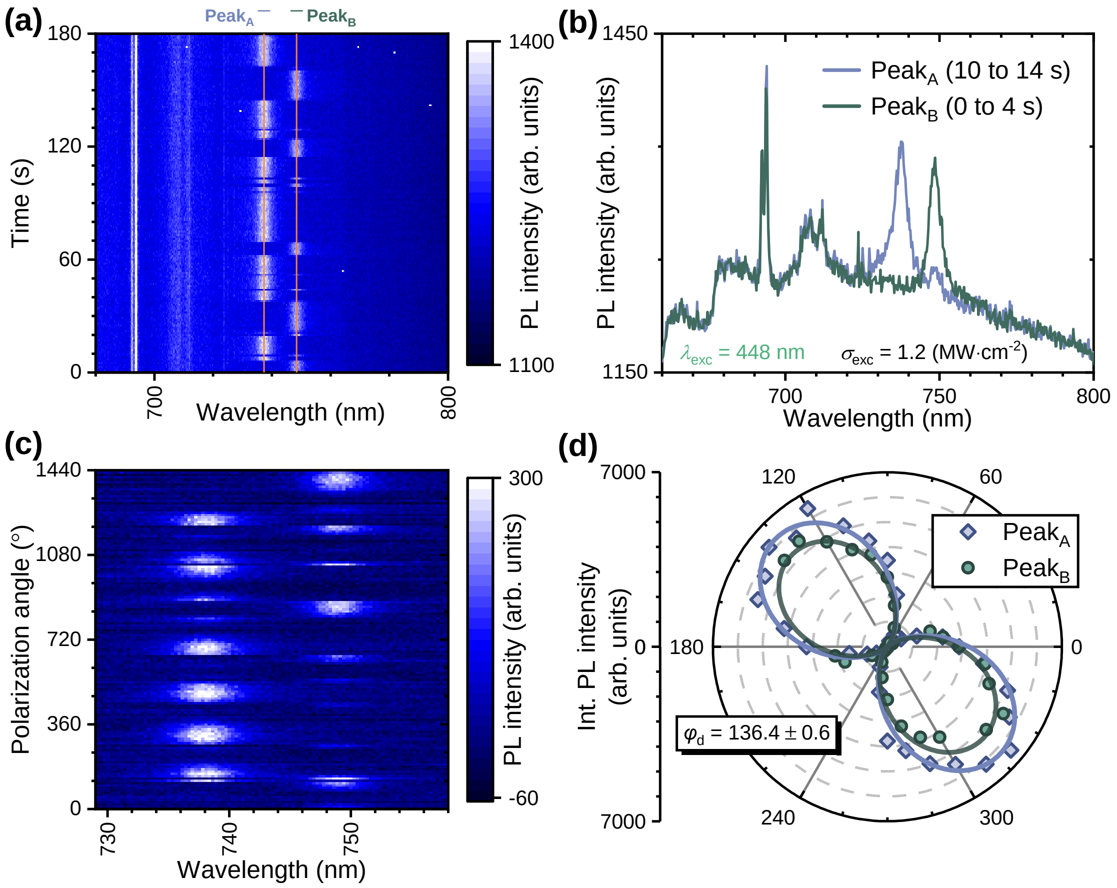

Figure 3.12: RT PL measurements acquired on an emitter (SPE$_4$) exhibiting a blinking behavior. **(a)** Time-dependent PL intensity map highlighting a dual PL feature (peaks A and B). Orange lines are used as a guide to the eye. **(b)** PL spectra of SPE$_4$ averaged over different time intervals to highlight peak$_A$ and peak$_B$. **(c)** Background-corrected, polarization-dependent PL intensity map used to extract the integrated intensity of each line, presented in **(d)** a polar plot. Both peaks feature a similar in-plane polarization angle $\varphi_d = (136.4 \pm 0.6)°$. All measurement were performed at $\sigma_{exc} = 1.2\,\mathrm{MW \cdot cm^{-2}}$ with $\lambda_{exc} = 488\,\mathrm{nm}$.

3.3.2 ’Binarization’ procedure

In the case of SPE$_4$, the blinking between each configuration occurs on a comparable second timescale. This makes it particularly suitable for a statistical investigation of the lifetimes associated with each state, as spectral transitions appear slow enough to acquire PL spectra with an adequate SNR and fast enough to record a statistically relevant number of transitions within several hours. To quantify the transitions between A and B, it is convenient to ’binarize’ the data by attributing each PL spectrum in a measurement set to either one of the emitter configurations. For this purpose, we tested different methods, illustrated in Fig. 3.13, on background-corrected time-dependent PL intensity maps akin to Fig. 3.12(a).

In a first approach (Fig. 3.13(a)), we extracted the wavelength corresponding to the maximum

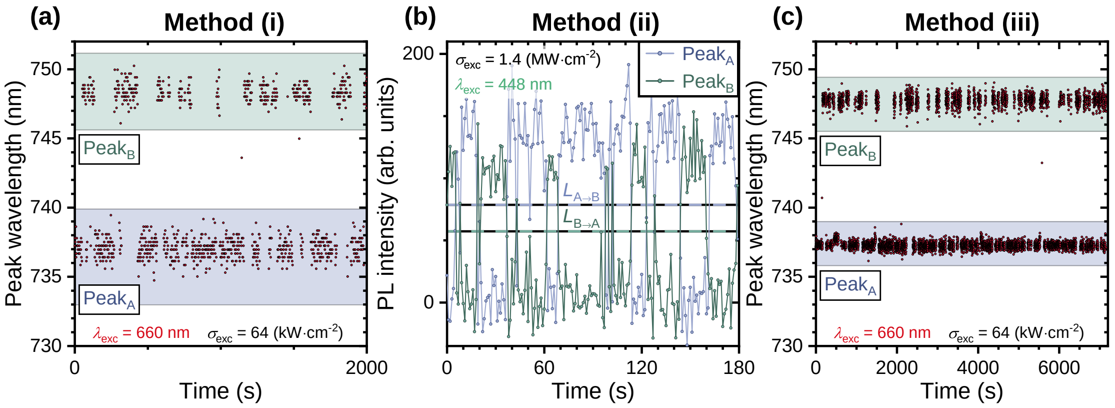

Figure 3.13: Illustration of the different binarization procedures. **(a)** Extraction of the peak wavelengths from background-corrected PL spectra. **(b)** Extraction of the PL intensity at peak positions. Horizontal bars denoted as $L_{\mathrm{A}\to\mathrm{B}}$ and $L_{\mathrm{B}\to\mathrm{A}}$ illustrate the threshold values discussed in the main text. **(c)** Extraction of the peak wavelengths after Lorentzian fitting of the PL lines. The third method is adopted in the following.

intensity in each PL spectrum and defined spectral ranges (illustrated by shaded areas) associated with each configuration. A data point in the blue (green, respectively) area is interpreted as an occurrence of peak$_\mathrm{A}$ (peak$_\mathrm{B}$, respectively). While yielding qualitatively good results, this method is particularly sensitive to spurious PL lines generated by cosmic rays, which can be challenging to discard. As an alternative, we tested a second method illustrated in Fig. 3.13(b) which consists in monitoring the PL intensity at the center of each peak. A transition is registered each time the intensity of the dominant line drops below an arbitrarily defined threshold (identified as $L_{\mathrm{A}\to\mathrm{B}}$ and $L_{\mathrm{B}\to\mathrm{A}}$ in the figure). While rather insensitive to cosmic rays, this method suffers from an inconsistent definition of said thresholds and loses precision when the SNR decreases.

As a third method, we can instead apply a Lorentzian fitting procedure on each PL spectrum, from which we derive the peak intensity wavelengths (see Fig. 3.13(c)). While similar to the first method, this approach is more robust with respect to spurious PL lines and generates a narrower distribution of center wavelengths. The few remaining outliers are by default considered equivalent to the previous data point.

By attributing a value ’zero’ (’one’, respectively) to PL spectra associated with peak$_\mathrm{A}$ (peak$_\mathrm{B}$, respectively), we construct a ’binarized’ dataset (see Fig. 3.14(a) for illustration) from which it is now possible to extract a lifetime statistics. Each series of consecutive zeros or ones yields a single ’transition delay’ ($\tau_{\mathrm{A}\to\mathrm{B}}$ or $\tau_{\mathrm{B}\to\mathrm{A}}$). Decay transients are ultimately constructed upon building a histogram for each set of transitions delays, as illustrated in Figs. 3.14(b) and 3.14(c).

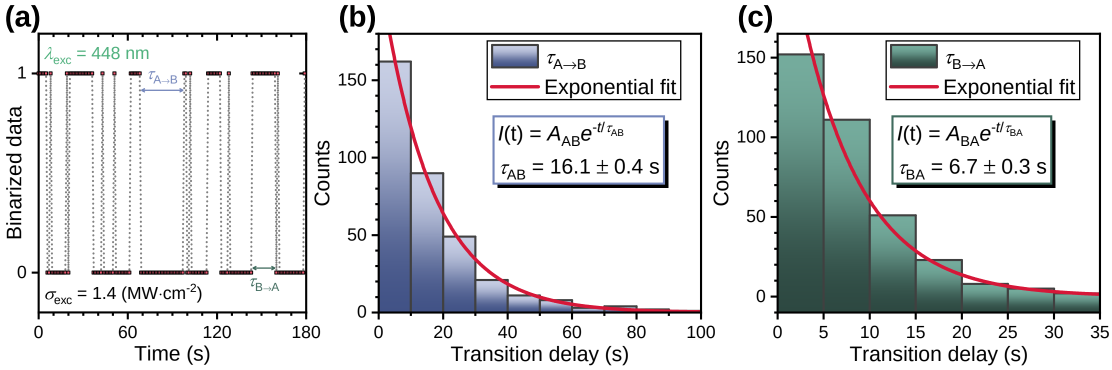

Figure 3.14: **(a)** Binarized dataset. Transition delays $\tau_{A\to B}$ ($\tau_{B\to A}$, respectively) are extracted after each streak of zeros (of ones, respectively). The associated histograms are displayed in **(b)** and **(c)** and fitted with monoexponential curves (red lines, see legends for fitting results).

3.3.3 Power-dependent behavior

For results obtained using a 488 nm laser, the experimental transients exhibit a close match to a single monoexponential decay, represented by solid red lines on the histograms. The validity of these monoexpoential decays is further assessed by considering a simplistic model where the blinking emitter alternates between two states, denoted as $|A\rangle$ and $|B\rangle$, each characterized by respective lifetimes denoted as τ_{AB} and τ_{BA} and occupancy probabilities $n_{A,B}$. In the steady state, the equations associated to this system:

$$\begin{cases} \frac{\mathrm{d}n_A}{\mathrm{d}t} = -\frac{n_A}{\tau_{AB}} + \frac{n_B}{\tau_{BA}}, \\ n_A + n_B = 1, \end{cases} \tag{3.20}$$

yield the solutions:

$$\begin{cases} n_A = \frac{\tau_{AB}}{\tau_{AB}+\tau_{BA}}, \\ n_B = \frac{\tau_{BA}}{\tau_{AB}+\tau_{BA}}. \end{cases} \tag{3.21}$$

The values of $n_{A,B}$ can be readily determined from the lifetimes obtained from the fitted histograms (Figs. 3.14(b) and 3.14(c)) and compared with those directly derived from binarized data[IX]. The results obtained at two different excitation power densities with a 488 nm laser are presented in Table 3.1 and show remarkable agreement between the occupancy probabilities extracted from the decay histograms and those from binarized data.

More interesting, the measurements reveal a clear conservation of occupancy probability for each defect configuration under varying pumping conditions. This result stems from the apparent linear scaling of the transitions rates ($\gamma_{AB} = \tau_{AB}{}^{-1}$ and $\gamma_{BA} = \tau_{BA}{}^{-1}$) with excitation power density, where γ_{AB} and γ_{AB} increase by an average factor of 4.6 as the excitation power

---

[IX] By summing up all zeros (total N_0) and ones (total N_1) from the binarized dataset (cf. Fig. 3.14(a)), we derive $n_{A,B}$ through $n_A = N_0/(N_0+N_1)$ and $n_B = N_1/(N_0+N_1)$.

σ_{exc} (MW·cm^{-2})	τ_{AB} (s)	τ_{BA} (s)	n_{A}	n_{B}
1.4	16.1	6.7	71 ; 70†	29 ; 30†
6.6	3.5	1.47	70 ; 30†	70 ; 30†

Table 3.1: Lifetimes (τ_{AB}, τ_{BA}) and occupancy probabilities ($n_{\mathrm{A,B}}$) measured on SPE$_4$ at two distinct excitation power densities, using λ_{exc} = 488 nm. The values indicated by a † are extracted from the binarized data.

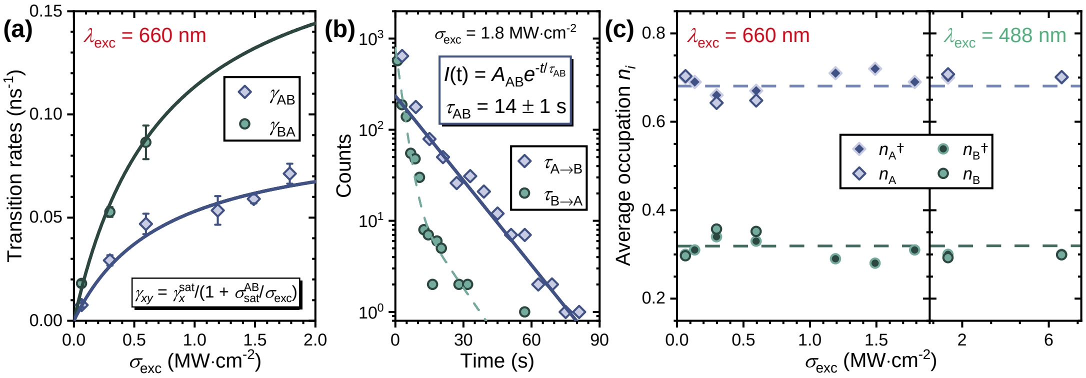

Figure 3.15: **(a)** Evolution of transition rates as a function of excitation power density. The data are fitted using Eq. 3.22 an a shared saturation parameter $\sigma_{\mathrm{sat}}^{\mathrm{AB}} = 6\,\mathrm{MW\cdot cm^{-2}}$. **(b)** Decay transients recorded at 1.8 MW·cm^{-2}. The legend displays the τ_{AB} lifetime derived from a monoexpoential fit (blue line). The green dashed line is used only as a guide for the eye. **(c)** Evolution of the occupancy probability of each defect configuration (A and B) as a function of excitation power density and for λ_{exc} = 488 and 660 nm. The values indicated by a † are extracted from the binarized data.

density is raised by the same factor.

To test the dependence of the blinking behavior on the excitation energy, we conducted similar time-dependent PL measurements with a 660 nm laser and for excitation power densities ranging from 0.22 to 1.8 MW·cm^{-2}. The transition rates determined from this set of measurements are depicted in Fig. 3.15(a). In contrast to the linear trend observed earlier, the transition rates showcased here exhibit a saturation behavior, well reproduced using the following relation:

$$\gamma_{xy} = \frac{\gamma_x^{\mathrm{sat}}}{1 + \sigma_{\mathrm{sat}}^{\mathrm{AB}}/\sigma_{\mathrm{exc}}}, \tag{3.22}$$

with $x, y \in \{\mathrm{A}, \mathrm{B}\}$. $\gamma_{\mathrm{A,B}}^{\mathrm{sat}}$ and $\sigma_{\mathrm{sat}}^{\mathrm{AB}}$ are fitting parameters analogous to all previous 'saturation-associated' parameters, with $\sigma_{\mathrm{sat}}^{\mathrm{AB}}$ identical for both A→B and B→A transitions.

Another notable difference with the measurements performed at $\lambda_{\mathrm{exc}} = 488$ nm pertains to the trends observed from the recorded transients. At $\lambda_{\mathrm{exc}} = 660$ nm, the histograms feature a pronounced rapid initial decay followed by a slow decay, from which we specifically extract τ_{AB} and τ_{BA}. At high excitation power, the fast and slow processes are no longer properly resolved for the transition from state |A⟩ to state |B⟩, which explains the missing data points in Fig. 3.15(a). This observation is illustrated in Fig. 3.15(b) for a dataset recorded at 1.8 $\mathrm{MW \cdot cm^{-2}}$. The solid blue lines represents the exponential fit from which we extracted the $\tau_{\mathrm{AB}} = (14 \pm 1)$ nm value reported in Fig. 3.15(a). The green dashed line is used only as a guide for the eye and does not constitute a viable fit. Despite the fast initial decay evidenced in Fig. 3.15(b), the occupancy of each defect configuration is still satisfactorily reproduced through Eq. 3.21 as confirmed by the adequacy between $n_{\mathrm{A,B}}$ values derived from the τ_{AB} and τ_{BA} lifetimes and those extracted from the binarized data. See for this purpose the values reported in Fig. 3.15(c). The dashed lines represent the occupancy probabilities derived after combining Eqs. 3.21 and 3.22 to obtain:

$$\begin{cases} n_{\mathrm{A}} = \frac{\gamma_{\mathrm{B}}^{\mathrm{sat}}}{\gamma_{\mathrm{A}}^{\mathrm{sat}} + \gamma_{\mathrm{B}}^{\mathrm{sat}}}, \\ n_{\mathrm{B}} = \frac{\gamma_{\mathrm{A}}^{\mathrm{sat}}}{\gamma_{\mathrm{A}}^{\mathrm{sat}} + \gamma_{\mathrm{B}}^{\mathrm{sat}}}. \end{cases} \tag{3.23}$$

3.3.4 Interpretation and prospects

The results summarized in Fig. 3.15(c) highlight the fact that, despite apparent disparities in the transients recorded at 488 and 660 nm, the occupancy of each defect configuration appears insensitive to variations in excitation power density and excitation energy. Instead, these parameters uniformly affect the lifetimes of |A⟩ and |B⟩, leaving the overall distribution unaffected. This photoinduced behavior especially contrasts with the findings by Berhane *et al.* [323], who reported on a blinking SPE featuring a power-dependent 'off' time and a power-insensitive 'on' time, tentatively attributed to a photo-assisted de-shelving process. In our case, the power-insensitive $n_{\mathrm{A,B}}$ values positively point toward the presence of a 'double-well potential', where transitions between stable configurations would be activated by photon absorption. Our results further suggest that in absence of laser excitation, SPE_4 could remain 'frozen' in either state |A⟩ or state |B⟩, a hypothesis which requires further investigation.

Despite these exhaustive results, it still remains unclear whether the blinking phenomenon is intrinsic to the emitter or arises instead from an exogenous factor, akin, for example, to the SD processes discussed in Chap. 2. We should nevertheless remark that the observed power-insensitivity seems hardly compatible with the charging/discharging process of a trap state as detailed in Subsect. 2.7.2. Besides, while the variation in PL intensity between $\mathrm{peak_A}$ and $\mathrm{peak_B}$ remains relatively discrete here, blinking phenomena are usually accompanied by a significant intensity variation that cannot be reconciled with the simple variations of the emitter dipole potential that result from SD.

This further raises the question of how representative the phenomenon described in this section is of the photo-instabilities typically exhibited by PD SPEs embedded in bulk GaN and opens up a line of study for the near future. In addition to this, alternative measurements conducted on SPE_4 could help identify the origin of the blinking process. These may include temperature-dependent measurements, a comparative analysis of PL and blinking saturation processes, or investigations into the radiative lifetime of each defect configuration. To this end, it is important to emphasize that SPE_4, as well as other emitters studied in this chapter, are still active months after their initial investigation an show no sign of a long-term bleaching behavior.

3.4 Second-order auto-correlation measurements

3.4.1 Room-temperature single photon emission

Up to this point, we have consistently presumed the SPE-like behavior of PD emitters without providing explicit evidence. While conducting $g^{(2)}(\tau)$ measurements on all emitters is impractical due to obvious time constraints, all such measurements conducted thus far have consistently verified the quantum characteristics of these emitters. An example of this confirmation is depicted in Fig. 3.16(a) for SPE_1. However, in the case of emission lines examined in sample A4365, the YL is typically too dominant to achieve high single-photon purity values. To showcase the potential of the GaN platform, we turned to an alternative sample denoted as TDC, which consists of a 4 μm thick non-intentionally doped GaN layer grown on sapphire at 1000 °C using MOVPE[X].

Taking advantage of the relatively low YL features in this sample, we were able to achieve a record-high single-photon purity of $g^{(2)}(0) = (0.06 \pm 0.01)$ at RT for such GaN epilayers on an emitter labeled SPE_5, as shown in Fig. 3.16(b). The corresponding $g^{(2)}(\tau)$ trace, depicted in Fig. 3.16(c), was obtained after spectral filtering of the ZPL using a 10 nm bandpass filter, simultaneously reducing the contribution of the PSB, notably bright for this emitter. A comparison with previously reported RT $g^{(2)}(0)$ from GaN defects is provided in Table 3.2 for the reader's reference. The table highlights that achieving high single-photon purity seems commonly more challenging in the NIR compared to the telecom range, likely due to the detrimental impact of the YL.

Incidentally, the bright PSB exhibited by SPE_5, compared to SPE_3 for instance,[XI] is characteristic of the large disparity of spectral signatures observed among the various emitters investigated. This disparity is also observed in the recombination dynamics of these emitters as illustrated by the RT $g^{(2)}(\tau)$ traces shown in Figs. 3.16(a) and 3.16(c), with SPE_1 showcasing anti-bunching and bunching rates about one order of magnitude larger than SPE_5 under similar excitation conditions. However, part of this difference can be attributed to variations in laser absorption efficiency among the different SPEs.

[X] This sample was not grown for SPE investigation and features some additional patterning. However, we deem this patterning irrelevant for the present discussion, provided we have ensured that all emitters originate from the primarily grown GaN layer.

[XI] In sample A4365, distinguishing the PSB from the background is challenging due to the predominance of YL in PL spectra recorded without background subtraction, hence the comparison to SPE_3.

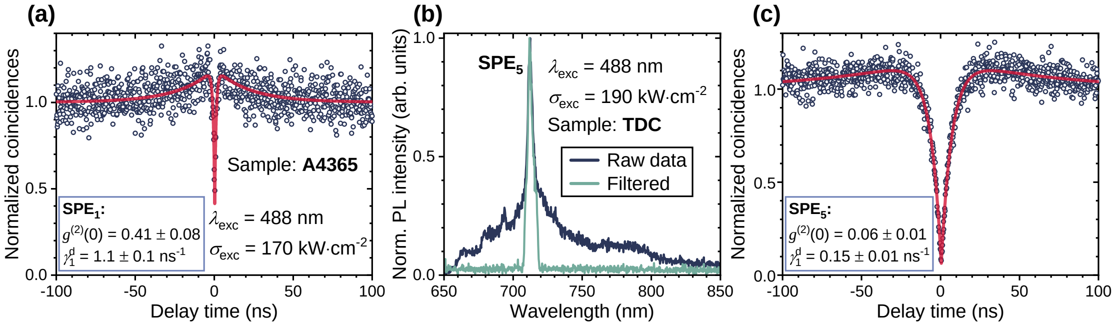

Figure 3.16: **(a)** RT $g^{(2)}(\tau)$ trace recorded on SPE$_1$ shown with a channel resolution of 200 ps/channel. **(b)** RT PL spectrum acquired on SPE$_5$ with (green line) and without band-pass filter (black line). **(c)** RT $g^{(2)}(\tau)$ trace recorded on SPE$_5$ with a 200 ps/channel resolution, demonstrating a record-high RT single-photon purity of (0.06 ± 0.01) for the GaN platform. $g^{(2)}(\tau)$ traces are fitted using Eq. 3.16. Courtesy of A. Bampis for performing the measurements on SPE$_5$.

Publication	$g^{(2)}(0)$ values	Spectral range
Berhane *et al.* [323]	0.24	NIR
Nguyen *et al.* [275]	0.38	NIR
Yuan *et al.* [326]	0.21	NIR
Luo *et al.* [314]	0.3	NIR
This work	0.06	NIR
Zhou *et al.* [31]	0.05	telecom
Meunier *et al.* [312]	0.29 ; 0.01†	telecom

Table 3.2: Review of RT single-photon purity values reported from GaN defects in the NIR (< 800 nm) and telecom (> 1100 nm) range. The value indicated by a † was acquired from an emitter embedded in a bullseye structure.

3.4.2 Power-dependent measurements

To assess the conformity of PD SPEs with the various models discussed in Subsect. 2.4.3, we can additionally examine the evolution of $g^{(2)}(\tau)$ traces with excitation power density. Figure 3.17(a) presents such traces for another emitter (SPE$_6$) from sample TDC. The data are fitted using Eq. 3.16 and reveal a significant disparity between anti-bunching and bunching rates ($\gamma_1^{\mathrm{d}} \gg \gamma_2^{\mathrm{d}}$), a behavior commonly observed in the literature [311, 312, 314]. This suggests that transitions to and from the metastable state $|m\rangle$ occur on a slower timescale than optical transitions, particularly $\gamma_e \gg \gamma_e^{\mathrm{r}}, \gamma_m^{\mathrm{r}}$ in models (i, iii) and $\gamma_e \gg \gamma_e^{\mathrm{r}}, \gamma_m^{\mathrm{e}}$. Under these circumstances, the expressions obtained for the fitting parameters simplify as follows (see Appendices B.4 and B.5 for computational details):

$$\begin{cases} \gamma_1^{\mathrm{d}} & = \pi + \gamma_e, \\ \gamma_2^{\mathrm{d}} & = \gamma_m^i + \frac{\gamma_e^{\mathrm{r}}}{1+\gamma_e/\pi}, \\ a & = \frac{\gamma_e^{\mathrm{r}}}{\gamma_m^i(1+\gamma_e/\pi)}, \end{cases} \tag{3.24}$$

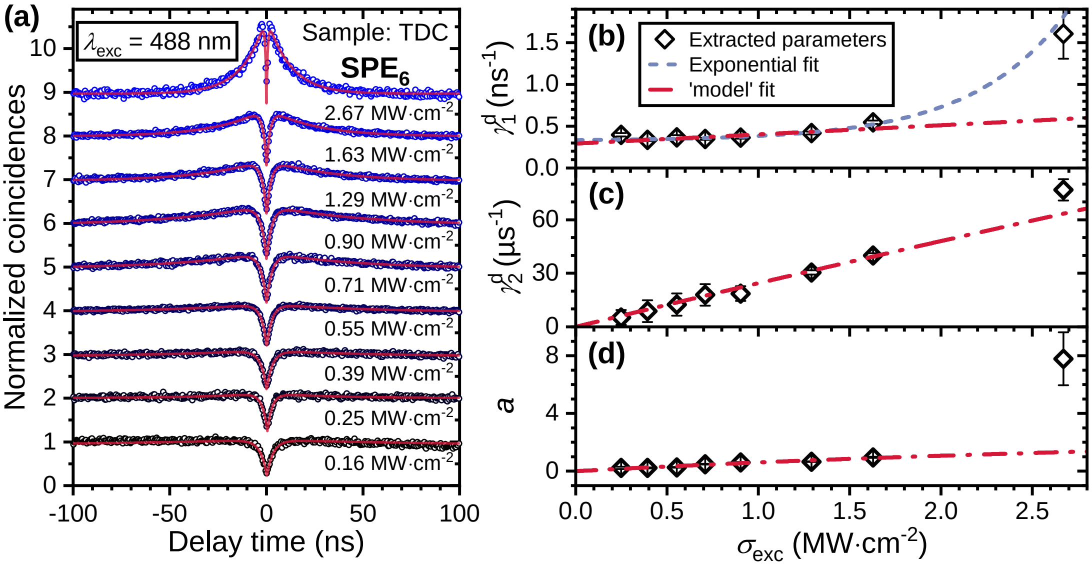

Figure 3.17: **(a)** $g^{(2)}(\tau)$ traces recorded on SPE$_6$ as a function of excitation power density, displayed with a resolution of 50 ps/channel for better qualitative appraisal. Solid red lines represent fits to the data obtained using Eq. 3.16. The evolution of the anti-bunching rate (γ_1^{d}), bunching rate (γ_2^{d}) and bunching amplitude a as a function of excitation power density are shown in **(b)**, **(c)** and **(d)**, respectively. Dash-dotted red lines depict fits to the parameters obtained using Eq. 3.24. The blue dashed line represents an empirical exponential fit. Courtesy of A. Bampis for recording the $g^{(2)}(\tau)$ traces.

where $\gamma_m^i = \gamma_m^{\mathrm{r}}$ in models (i) and (iii) and $\gamma_m^i = \gamma_m^{\mathrm{e}}$ in model (ii). These relations notably imply that when $\gamma_1^{\mathrm{d}} \gg \gamma_2^{\mathrm{d}}$, there exists no mathematical difference between the solutions computed in models (i) and (ii), making it necessary to either support or refute both hypotheses simultaneously.

Eq. 3.24 is applied under the assumption of a linear relationship between excitation power density and pump rate ($\pi = \alpha_{\mathrm{abs}}\sigma_{\mathrm{exc}}$), and the fitting parameters derived for SPE$_6$ are presented in Figs. 3.17(b), 3.17(c), and 3.17(d). In theory, Eq. 3.24 predicts a linear scaling for parameter γ_1^{d} and a saturation behavior for both parameters γ_2^{d} and a. However, these forecasts are not supported by our measurements. The best fits –essentially linear functions depicted as red dash-dotted lines– fail to replicate experimental trends. Instead all parameters exhibit a supralinear scaling behavior, particularly evident[XII] in the $g^{(2)}(\tau)$ trace recorded at 2.67 MW · cm^{-2}.

At this stage, the results obtained on SPE$_6$ seem hard to reconcile with a simple de-shelving mechanism. The alternative model (iii) proposed by Berhane *et al.* [30] is also incompatible,

---

[XII] The uncertainty associated with parameters a and γ_1^{d} escalates as the anti-bunching dip narrows, leading to a decrease in precision over the anti-bunching amplitude. This reduction in precision stems from the limited temporal resolution of the SPDs but does not invalidate the substantial increase of a and γ_1^{d} values at 2.67 MW · cm^{-2}.

as the power-dependence of the de-shelving rate (γ_m^{r}) suggested in Eq. 3.17 only introduces sublinear factors that cannot account for the convex trends observed.

It remains to be determined whether this pattern is consistent across all emitters or if it represents an exception. However, we should point out that such a $g^{(2)}(\tau)$ dataset takes approximately a week to acquire, rendering it impractical for large-scale studies. In this regard, TRPL measurements would be a more suitable alternative.

3.5 Preliminary statistical results

In earlier sections, we have highlighted the potential of µ-PL measurements in elucidating the properties of individual SPEs. Yet, the long-term objective of this research is to conduct large-scale measurements on purposefully designed samples, aimed at elucidating the nature and formation processes of the defect SPEs observed in GaN layers. In this section, we present a preliminary set of statistics collected from sample A4365. The current dataset is constrained by the manual data collection process, which inherently introduces bias as brighter emitters are more readily investigated and thus prioritized. Therefore, it is important to interpret the results with these limitations in mind.

3.5.1 Defect energies and dipole orientations

As an initial result, we ought to emphasize a point already implied by the variability of PL demonstrated thus far: as further illustrated in Fig. 3.18(a), the PL lines of PD SPEs in GaN do not appear to cluster around any particular wavelength, contrary to what might be expected from a PD characterized by distinct electronic transitions[XIII]. Instead, they seem to span a considerably wide spectral range. Our analysis includes numerous emitters ranging between 700 and 800 nm, complementing earlier reports on emitters found between 600 and 750 nm [30, 275, 327]. Furthermore, telecom emitters have been extensively documented between 1000 and 1400 nm by Meunier *et al.* [312] and there is no indication that the remaining gap (between 800 and 1000 nm) should be devoid of such emitters.

As an additional observation, we can mention that the RT PL linewidths, derived through fitting of the Lorentzian-shaped ZPL, distribute over a substantially large range (here, from 2 to 6 nm) with an average linewidth of 4.1 nm. This average amounts to 9 meV at 750 nm, a value comparable to the average linewidths reported for emitters in the telecom range [312]. PL spectra recorded on PDs with narrow (FWHM = 2 nm, SPE_7) and large linewidths (FWHM = 2 nm, SPE_8) are displayed in Fig. 3.18(b) for illustration.

The significant variability in PL emission energies and linewidths seems hardly attributable to a unique type of PDs and raises the question of how to discern between SPEs of various origin.

[XIII] This is incidentally the case for the Cr R_1 and R_2 lines consistently observed in the sapphire substrate, which align with well-defined electronic transitions of the Cr^{3+} ions [85].

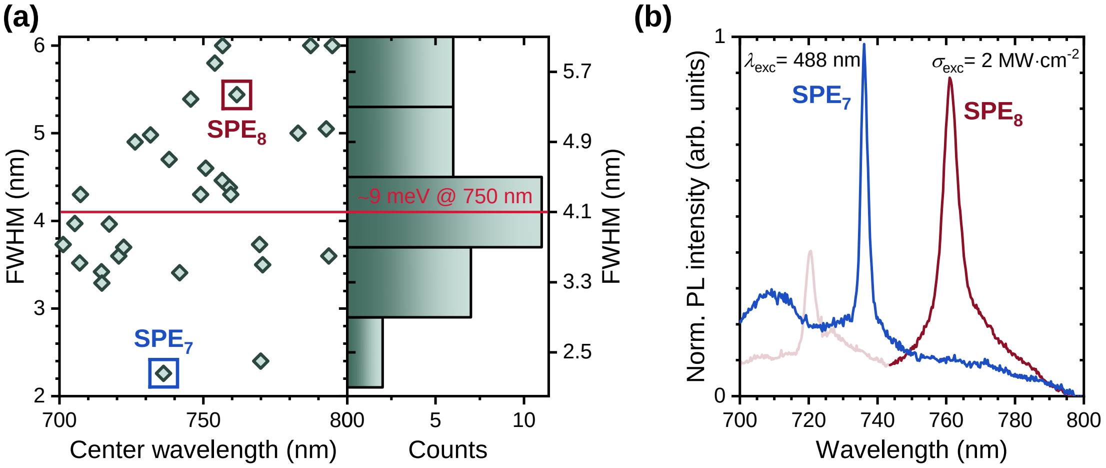

Figure 3.18: **(a)** Linewidth distribution of SPE RT PL lines recorded between 700 and 800 nm on sample A4365. **(b)** PL spectra recorded on SPEs for SPE$_7$ and SPE$_8$ as labeled in (a). An additional emitter is present in the PL spectrum featuring SPE$_8$.

As discussed in Sect. 1.4, measuring the 3D dipole orientation of SPE emitters could help in identifying their origin, as their polarization is expected to align with structural features [63]. Although the out-of-plane dipole angle cannot be reliably ascertained at this stage, it is anticipated to approach 90° for 'bright emitters' as discussed in Sec. 1.3 and according to earlier studies [33]. Extraction of the in-plane φ_d angle is more feasible and is presented in Fig. 3.19(a) for a dataset encompassing 51 SPEs.

Figure 3.19 reveals a broad angular distribution that appears non-isotropic. Notably, there is an absence of occurrences around angles of 0 and 30°, which contradicts findings by Geng *et al.* [33], who reported a predominant emitter orientation along these axes. This discrepancy urges us to interpret these preliminary results with caution and awaits further validation. The large number of occurrences around 21 and 54°, which does not align with any high-symmetry axis, is equally puzzling.

3.5.2 Defect position and defect densities

As a final result, we should discuss how depth scans can help determining the location of emitters within the GaN layer, using again sample A4365 as example. To this end we need to detail further the sample structure and growth conditions, which have been purposely omitted earlier for the sake of concision. The sample structure is shown in Fig. 3.20(a).

The growth process of GaN on sapphire typically starts with the deposition of a thin layer of GaN, typically a few tens of nanometer thick, onto a sapphire substrate. Subsequent high-temperature (~ 1100 °C) annealing of this thin layer prompts the nucleation of GaN, leading to the formation of 3D islands. These grains serve as preferential sites for subsequent GaN growth, with the material expanding outward from these nuclei until coalescence is achieved.

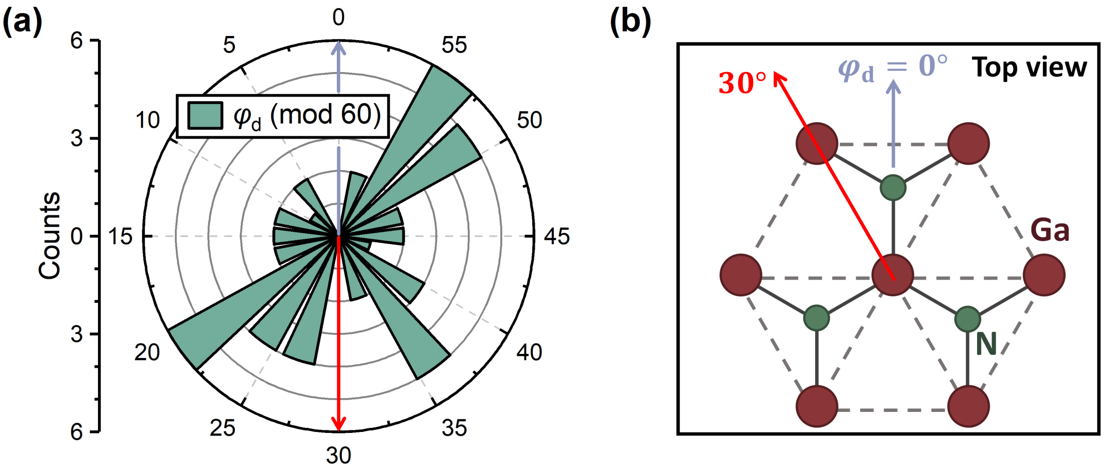

Figure 3.19: **(a)** Distribution of in-plane dipole angles recorded from NIR SPEs in sample A4365. **(b)** illustrates the correspondence between the 0 and 30° angles and the crystal structure. Courtesy of V. Gillioz for recording part of the statistics.

For reasons that extend beyond the scope of this thesis, p-doped GaN ([Mg] = $3 \times 10^{18}\,\mathrm{cm}^{-3}$) is not directly grown from the nucleation layer and typically requires an intermediate layer of undoped or n-doped GaN. In our case, a 1.4 µm thick n-doped GaN layer ([Si] = $3 \times 10^{18}\,\mathrm{cm}^{-3}$) was formed on top of a 1.2 µm thick unintentionally doped layer. The 1.4 µm thick p-GaN layer itself was grown after a growth interruption and exposure to air, for reasons that do not relate to the investigation of SPEs. p-GaN is activated by rapid thermal annealing at 700 °C of an Mg-doped layer in a oxygen environment that breaks Mg-H bonds and allows hydrogen atoms to diffuse out of the p-type region [328, 329]. It is worth noting that measurements carried out on sample A4365 before and after annealing did not reveal measurable changes in the density of PD SPEs, suggesting that their formation is not related to Mg impurity complexes.

Despite the complex structure of the investigated sample, the precision reached through confocal measurements is enough to determine with precision the position of SPEs with respect to the maximum of the YL, and by extension, with respect to the sample structure. Figure 3.20(b) illustrates the distribution of 9 SPEs investigated by confocal measurements assuming the YL maximum (z_{YL}) aligns with the center of the GaN stack. The distances (z_{SPE}) are referenced to the GaN/sapphire interface.

The data points were gathered from different regions of the sample, and emitters were chosen after conducting hyperspectral maps at the depth corresponding to the peak intensity of the YL. This approach should mitigate the bias resulting from selecting the investigated SPEs by hand. Strikingly, SPEs are predominantly situated 'above' the YL maximum, i.e., toward the GaN/air interface, which suggests that the emitters primarily originate within the p-doped layer[XIV]. Let us note that sample A4365 was selected for preliminary investigations due to

---

[XIV] The assumption that the YL is centered within the GaN layer is somewhat speculative, given the limited

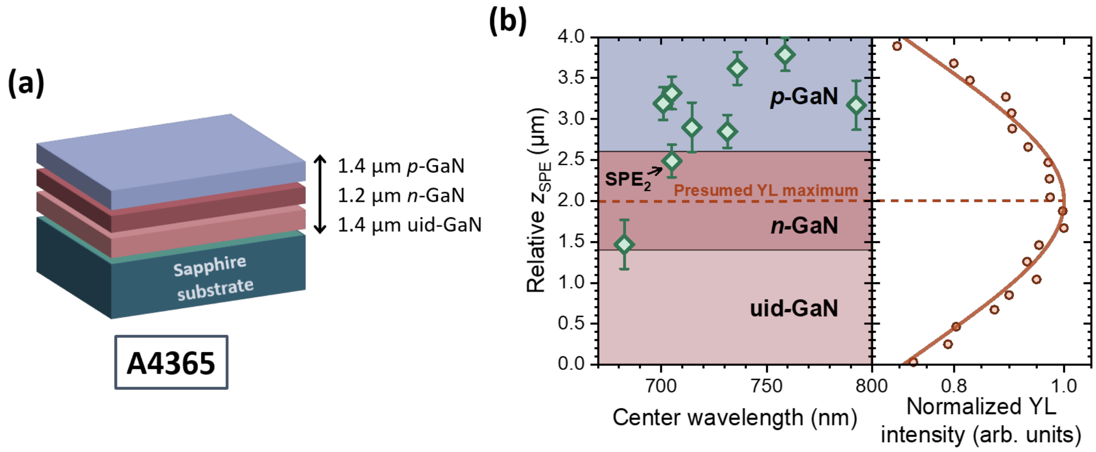

Figure 3.20: **(a)** Illustration of the A4365 sample structure. **(b)** Spatial distribution of SPEs within this sample along the c-axis. z_{SPE} distances are measured with respect to the peak position of the YL signal, which is assumed to align with the center of the GaN layer. The YL depth profile recorded on SPE_2 (see Fig. 3.7(c)) is reproduced for clarity.

its relatively high emitter density[XV], approximately $8 \times 10^6\,\mathrm{cm}^{-2}$. In comparison, the purely n-doped sample C3647 discussed in Subsection 3.2.1 exhibited a density emitters of about $2 \times 10^6\,\mathrm{cm}^{-2}$, a level similar to that observed for sample TDC. The higher density observed in sample A4365 could potentially be associated with the presence of the p-doped region, consistent with the findings from the depth statistics presented in Fig. 3.20(b).

However, it is important to acknowledge that, at this stage, these results should be primarily considered as a proof of concept rather than solid statistical findings. The limited number of data points, combined with uncertainties regarding the homogeneity of the YL, only allows for qualitative interpretations, which need to be complemented by a robust experimental protocol. Additionally, it should be noted that these preliminary results were obtained from a heterogeneous set of samples initially grown for other applications, with variations in growth procedures beyond the doping level. A more systematic study has now to be implemented.

3.6 Summary

Upon reading this chapter, it must have become apparent to the reader that the investigation of PD SPEs in GaN represents a novel and largely uncharted area of study. Despite drawing comparisons with various other defect systems, the precise nature of these emitters remains

---

information available about its relative intensity within each sub-layer. However, the distribution of z_{SPE} sets boundary conditions, as emitters cannot be located within the air or the substrate. As such, the position of z_{YL} cannot be shifted toward the p-GaN layer. If the YL primarily originates from the n-GaN layer, z_{YL} would remain unchanged, supporting the idea that emitters are predominantly situated within the p-doped region.

[XV] We extract 2D densities from hyperspectral maps. It is assumed that these densities are comparable across the different samples investigated here, all having a similar thickness of about 4 µm.

largely unraveled and is likely to necessitate numerous additional contributions to achieve a comprehensive understanding. Throughout this thesis, a significant portion of time has been dedicated to the development and implementation of a newly-built setup capable of delivering high-quality μ-PL results. This, combined with the resources of a well-established MOVPE facility, holds the promise of yielding rapid progress in this field.

To support this objective, the first section of this chapter aimed to provide an intuitive grasp of the physics behind defect formation, while also offering a comprehensive review of the current state of knowledge regarding the GaN platform. While certain concepts introduced in this section, such as the discussions on the optical signatures of PDs or the protocols aimed at correlating the defect concentrations with their formation energies, have not yet been practically applied, they are intended to offer insights for future investigations.

Building upon the theoretical framework established in Section 3.1, Sect. 3.2 provided a hands-on overview of the methodology employed to investigate individual SPEs through μ-PL measurements. Additionally, it outlined the current experimental limitations faced and proposed potential avenues for improvement. This methodology was then applied to a case study on photo-induced blinking in Sect. 3.3, followed by the formal confirmation of the SPE-like behavior of the investigated defects through the $g^{(2)}(\tau)$ measurements presented in Sect. 3.4. Subsequently, Sect. 3.5 introduced prospective results gathered from a larger set of emitters, offering an overview of the various indicators that will be utilized for statistical analysis once the setup automation is completed.

Conclusion

In the near future, RT SPEs could play a significant role over the large-scale development of quantum photonics applications. In this thesis, we have investigated the optical properties of two types of such emitters: GaN/AlN SAQDs and PDs in GaN. Both exhibit comparable features inherited from the III-N platform.

Investigating individual SPEs can pose significant experimental challenges. Having emphasized spatial resolution and stability requirements for µ-PL investigation, we pursued the review of our setup implementation, highlighting the critical role of collection efficiency on its overall performance. By deriving the maximum efficiency expected for different dipole orientations, we notably outlined how PDs with an optical dipole aligned with the wurtzite c-axis could appear undetectable with our current configuration, indicating a substantial limitation of our setup configuration. We complemented our analysis with simulations of Fabry-Perot interference in micrometer-thick III-N layers to gauge its impact on PL spectra. We exposed how such interference, which adds to the limited resolution of our microscope objective, could affect the determination of the 3D orientation of PDs in bulk GaN epilayers.

Drawing from our experimental insights, we presented an exhaustive analysis of the dynamics of GaN/AlN SAQDs. Starting with an exploration of the unique characteristics of the III-N platform, we investigated the significant influence of SD on the PL of polar zero-dimensional structures. We outlined the potential of SD as a local probe for defect concentrations and as a marker of the spatial origin of PL lines despite its detrimental aspect for quantum applications. We further delved into the optical properties of high-energy QDs ($> 4\,\mathrm{eV}$), analyzing their PL response to temperature and excitation power variations. Our experimental results were compared with a model of biexciton and exciton recombination processes, revealing the limitations of the model commonly adopted in the literature and the critical role of phonon-assisted transitions on the QD dynamics. Our investigation of individual QDs culminated in the analysis of second-order photon autocorrelation measurements recorded on exciton PL lines over temperatures ranging from 5 to 300 K. These measurements outlined the potential of III-N QDs for RT single-photon emission and shed light on the influence of the biexciton luminescence on photon statistics. At last, we supplemented our µ-PL study with TRPL measurements performed on an ensemble of QDs, enabling a better understanding of (multi-)excitonic recombination. Notably, we observed a persistent biexponential behavior in PL decay curves, which exhibited strong thermal insensitivity. We also revisited prior findings obtained on GaN/AlN SAQDs, which suggested a significant influence of the substrate on QD optical properties, thus providing valuable insights for a more systematic analysis of growth condition effects. Additionally, preliminary investigations of TRPL transients acquired under high power excitation hinted at a strong supralinear scaling of multiexcitonic recombination rates, which further suggests the dominant contribution of the radiative process over the lifetime of multiexcitonic states.

In our final discussion, we presented preliminary results acquired on PDs in GaN behaving as RT SPEs. Here, our emphasis was placed on the potential of a recently developed setup for forthcoming investigations, along with key aspects of the theoretical framework tailored to support this research endeavor. After introducing the general methodology employed to address randomly distributed defects, we dedicated a section to the study of an individual PD featuring a blinking behavior. This analysis underpinned its unique power-dependence characteristics and served as a compelling case study to illustrate the capabilities of the μ-PL setup. We then showcased the potential of the investigated SPEs by achieving a record-high RT single-photon purity with $g^{(2)}(0) = (0.06 \pm 0.01)$, obtained on a NIR emitter ($\lambda = 712\,\mathrm{nm}$). We complemented this result with power-dependent photon statistics acquired from another SPE, providing insights into their recombination dynamics. We concluded this chapter by providing an overview of statistics concerning the energy and spatial distribution, as well as the dipole orientation, of a selected set of PDs. These qualitative findings illustrate the key metrics that we intend to employ in establishing the origin and nature of defect-related RT SPEs in GaN. We anticipate a further elucidation of these aspects upon the completion of our ongoing protocol, designed to extract defect densities from hyperspectral maps.

Outlook

Through our investigation of GaN/AlN SAQDs, we have clearly demonstrated their potential as bright SPEs up to RT, boasting a relatively high single-photon purity ($g^{(2)}(0) = (0.17 \pm 0.08)$) enabled by the large biexciton binding energies exhibited by the high-energy emitters under study. However, this achievement comes with the significant caveat of operating in the UV range, primarily due to the critical impact of QCSE on lifetime and broadening characteristics as the QD size increases. In the UV spectral domain, achieving reliable photonic structures is notably hard due to the wavelength-scale structural features, material degradation at high energies, and reduced detector sensitivity. Although some successful integrations have been demonstrated [330] the inherent incompatibility with optical fiber infrastructures for long-range transmission further complicates matters, contributing to the limited development of such applications thus far.

Besides the 'UV challenge', the difficulty in realizing efficient p-doping of the AlN matrix material [331] poses an obstacle to achieving electrical injection, a desirable milestone for practical applications. In this regard, InGaN/GaN QDs may constitute an alternative although convincing results are still awaited. Nevertheless GaN/AlN QDs remain key for more fundamental investigations. To this end, we can only encourage further research on the QD dynamics with a special focus on TRPL measurements performed on individual emitters.

To achieve RT SPE in the NIR and telecom, which is more suitable for industrial applications, defect-based SPEs in GaN emerged as a thrilling new prospect. For this purpose, unravelling the origins of the PL 'zoo' observed across the visible to telecom range is remains a challenge but should significantly benefit from the maturity of the III-N platform and insights gleaned from research on defects in other materials. In particular, the tunability of the doping levels in GaN is expected to facilitate precise control over the density of SPE-like defects, since the formation energy of defects with a non-zero charged state relies on the position of the Fermi level.

In parallel to this core objective, it is equally decisive to identify the mechanisms underlying the photoinstabilities we observed, which are also reported in the existing literature, to establish protocols to mitigate or conveniently tailor blinking phenomena. Electrical manipulation of blinking, as demonstrated in other platforms, such as CdSe/CdS NCs or defects in hBN layers [332–334], presents a promising avenue.

While 'high-end' applications for this nascent platform have yet to be demonstrated, recent advancements are worth being emphasized. In this regard, Meunier *et al.* [312] recently achieved integration of telecom single-photon emitters into bullseye antennas, paving the way toward more sophisticated structures. Achieving RT single-photon emission though electrical injection represents another milestone to strive for.

A Software description

The effectiveness of the µ-PL setup developed for the investigation of NIR and telecom PDs largely relies on the software created during this thesis. This software facilitates communication among multiple devices and includes various routines to streamline the measurement process. Although it is under constant development, its main functionalities are already well-established and summarized in this appendix. Appendix A.1 provides an overview of the software functionality while Appendix A.2 outlines the key aspects of the scanning procedure employed during $g^{(2)}(\tau)$ measurements.

A.1 Overview of the software working principles

For the sake of clarity, the software can be broken down into four main panels highlighted in Fig. A.1 and detailed below. These comprise:

- A 'Device Control' panel: used to manually communicate with all devices outside the measurement routines and to adjust the instruments settings.
- An 'Acquisition' panel: featuring the real-time charts during experimental routines and allowing adjustment of the graphical settings.
- A 'Parameterization' panel: used to define acquisition settings for experimental routines.
- A 'Naming' panel: used to standardize the data file labels for further use in Python scripts, among other functions.

DEVICE CONTROL PANEL

The 'Device Control' panel, depicted in Fig. A.2, encompasses various subpanels. These subpanels include controls for the piezostack and motorized linear stages, facilitating coarse and smooth positioning and focusing on the investigated samples, which can be used during live spectra acquisitions for swift manual alignment. Additionally, the 'Powermeter and filter

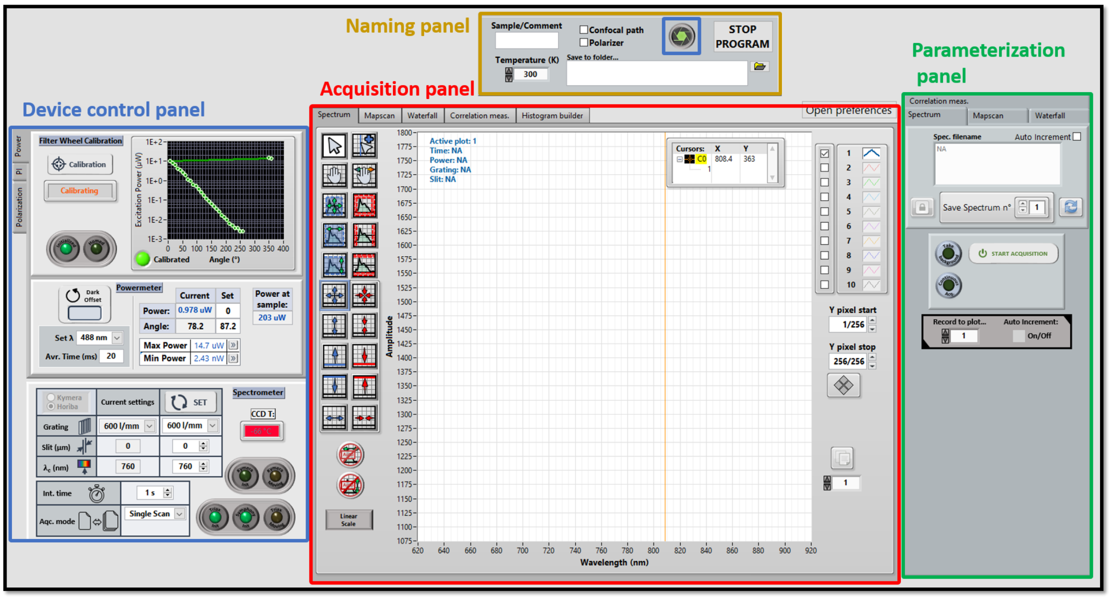

Power: 0.978 uW 0
Angle: 78.2 87.2
Power at sample: 203 uW
Set λ 488 nm
Avr. Time (ms) 20
Max Power 14.7 uW
Min Power 2.43 nW
Temperature (K) 300
Active plot: 1
Time: NA
Power: NA
Grating: NA
Slit: NA
Cursors: X 808.4 Y 363
Y pixel start 1/256
Y pixel stop 256/256

Figure A.1: Screenshot of the software front-end. The four main panels are delimited by rectangles.

wheel' control panel enables adjustment of the excitation power density as required. The powermeter calibration interface is used when restarting the software to recalibrate the laser fluence at each position of the filter wheel. The spectrometers CCDs and grating turrets are managed through the last subpanel. An external shutter on the laser excitation path offers further control over the exposure time.

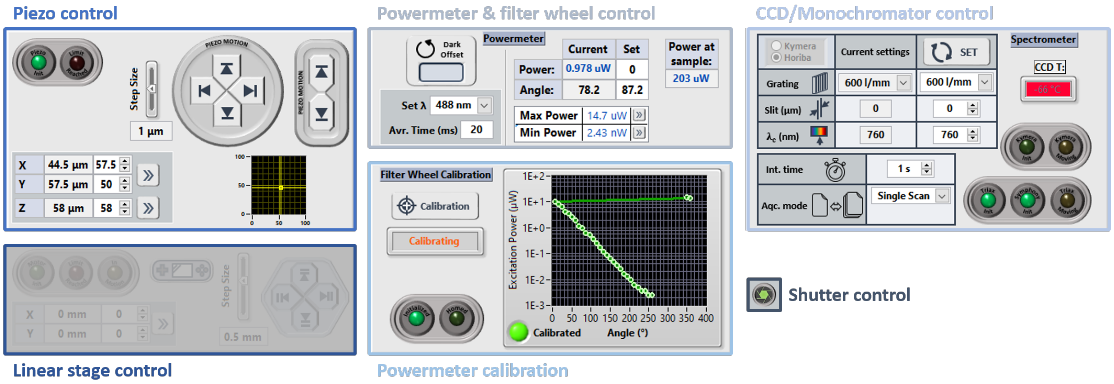

Step Size 1 µm
X 44.5 µm 57.5
Y 57.5 µm 50
Z 58 µm 58
Power: 0.978 uW 0
Angle: 78.2 87.2
Power at sample: 203 uW
Set λ 488 nm
Avr. Time (ms) 20
Max Power 14.7 uW
Min Power 2.43 nW
Grating 600 l/mm 600 l/mm
Slit (µm) 0 0
λc (nm) 760 760
Int. time 1 s
Aqc. mode Single Scan
X 0 mm 0
Y 0 mm 0
Step Size 0.5 mm

Figure A.2: Screenshots of the various subpanels constitutive of the instrument control.

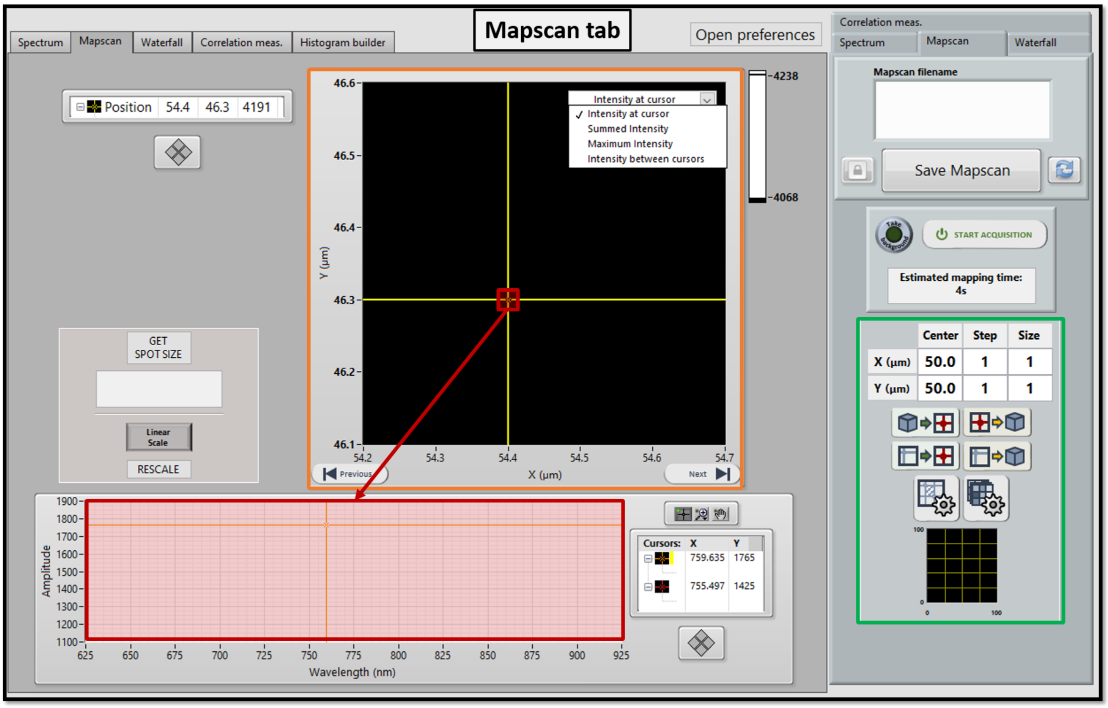

Position 54.4 46.3 4191

Estimated mapping time: 4s

Cursors:	X	Y
	759.635	1765
	755.497	1425

	Center	Step	Size
X (µm)	50.0	1	1
Y (µm)	50.0	1	1

Figure A.3: Screenshot of the 'Mapscan Routine' tab. 2D intensity maps are visualized in the chart highlighted by an orange rectangle. The cursor position in this chart determines the PL spectrum displayed in the second chart (red rectangle). Mapscan settings can be adjusted in the dedicated tab within the parameterization panel (green rectangle).

EXPERIMENTAL ROUTINES

Experimental routines form the core of the software architecture and constitute its primary interests. Each routine comes with a dedicated tab in the 'Acquisition' and 'Parameterization' panels, whose main features are highlighted by orange red and green rectangles in Figs. A.3, A.4 and A.5, and summarized below.

'Mapscan routine': this routine is used to record hyperspectral maps and features several tools for preliminary analysis of the recorded datasets. It includes a main chart (orange rectangle in Fig. A.3) used to display 2D intensity maps and a secondary chart (red rectangle) that helps visualizing the PL spectra recorded at each X and Y spatial coordinates. Mapping settings are adjusted though the associated tab in the 'Parameterization' panel.

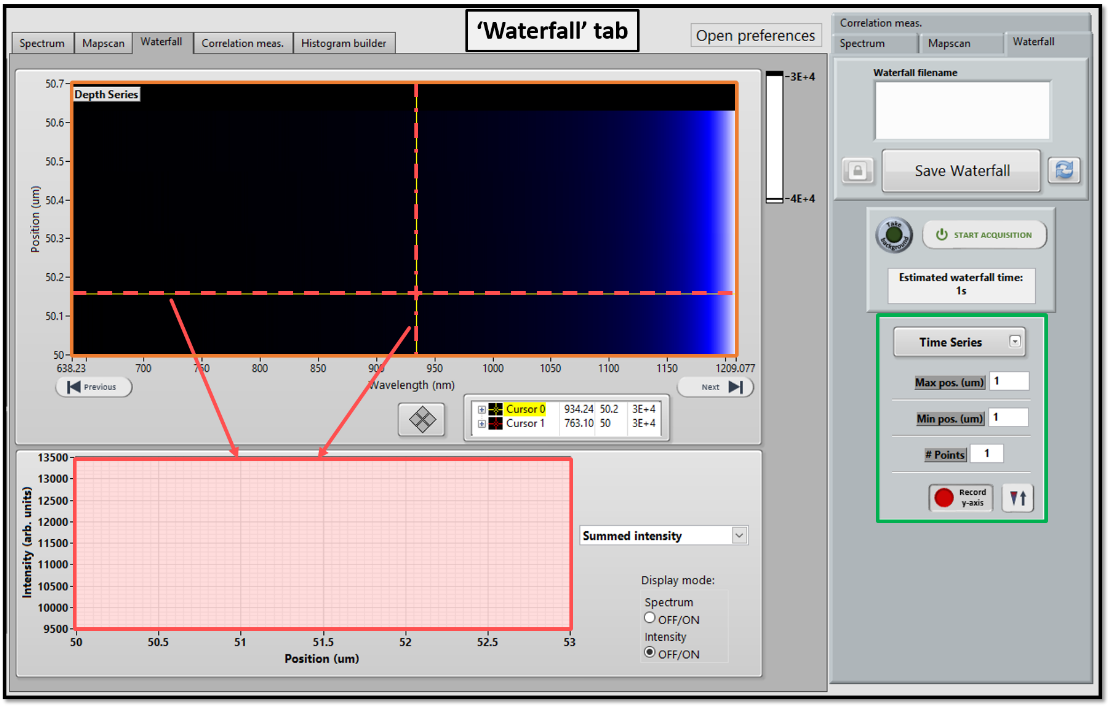

Cursor 0	934.24	50.2	3E+4
Cursor 1	763.10	50	3E+4

Summed intensity

Display mode:
Spectrum
○ OFF/ON
Intensity
● OFF/ON

Estimated waterfall time: 1s

Time Series

Max pos. (um) 1

Min pos. (um) 1

Points 1

Figure A.4: Screenshot of the 'Waterfall Routine' tab. 2D intensity maps are visualized in the chart highlighted by an orange rectangle. The x and y coordinates of the cursor in this chart allow for two functions: (i) displaying a PL spectrum at a specific y-axis value (indicated by the horizontal dashed line) or (ii) performing a y-axis scan at a specific wavelength (indicated by the vertical dash-dotted line) or over a specific wavelength range. The associated graphs are displayed in the second chart (red rectangle). Waterfall settings can be adjusted in the dedicated tab within the parameterization panel (green rectangle).

'Waterfall routine': this routine is used to record 2D datasets where one axis represents the wavelength of each CCD pixel, while the other axis (y-axis) corresponds to various experimental parameters, such as time, power, or polarization. The associated intensity maps are visualized in the main chart (orange rectangle in Fig. A.4). The vertical cursor coordinate in this chart serves for displaying a PL spectrum at a specific y-axis value (horizontal dashed line), while the horizontal coordinate enables visualisation of y-axis PL intensity scans at a specific wavelength (vertical dash-dotted line) or across a specific wavelength range.

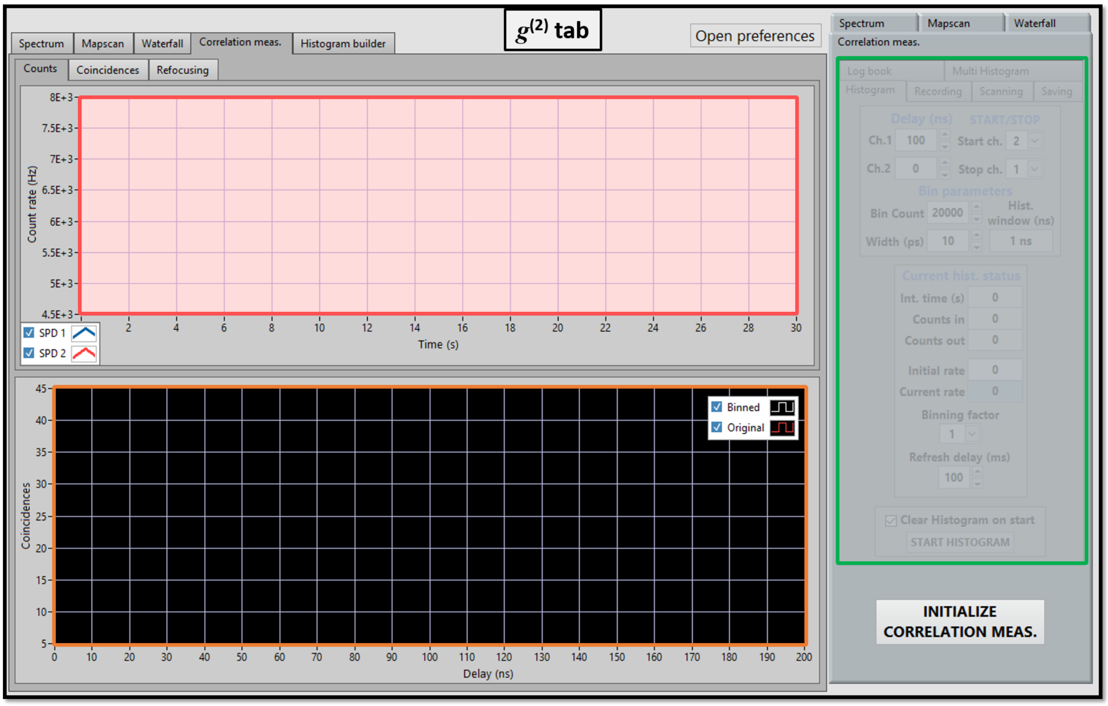

☑ SPD 1
☑ SPD 2
☑ Binned
☑ Original

Ch.1 100
Start ch. 2
Ch.2 0
Stop ch. 1
Bin Count 20000
Hist. window (ns) 1 ns
Width (ps) 10
Int. time (s) 0
Counts in 0
Counts out 0
Initial rate 0
Current rate 0
Binning factor 1
Refresh delay (ms) 100
☑ Clear Histogram on start

Figure A.5: Screenshot of the '$g^{(2)}(\tau)$ Routine' tab. Live $g^{(2)}(\tau)$ histograms are displayed in the chart highlighted by an orange rectangle. The counts and coincidences are also displayed live in the second chart (red rectangle), which additionally visualizes count rates during refocusing procedures (cf. Appendix A.2). SPD and histogram acquisition settings can be adjusted in the dedicated tab within the parametrization panel (green rectangle).

'$g^{(2)}(\tau)$ routine': this routine is designed for recording $g^{(2)}(\tau)$ histograms (see orange rectangle in Fig. A.5). It also includes a secondary chart used to monitor count rates on each SPD and the coincidence rate within the specified time interval. The associated tab in the 'Parameterization' panel offers a range of controls, including histogram settings, SPD calibration, time-tagger delay and memory settings, and options for the refocusing procedure.

A.2 $g^{(2)}(\tau)$ measurements – Scanning procedure

The acquisition of high-resolution $g^{(2)}(\tau)$ traces is a tedious procedure that often requires hours of continuous data acquisition, particularly when working with very low excitation power densities. During this extended duration, even minor micrometric shifts in the sample or the objective can significantly impact the coincidence rate, consequently affecting the SNR and the overall quality of the results. It thus appears crucial to implement an automated repositioning procedure to mitigate these effects without the need for manual intervention.

To address this concern, we integrated this functionality into the LabVIEW software designed for the NIR setup, in a structure that is highlighted in Fig. A.6. While recording photon

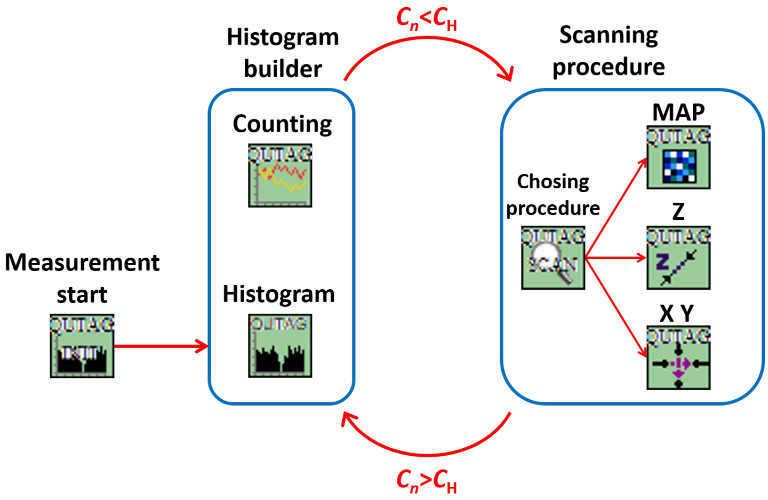

Figure A.6: Simplified illustration of the procedure followed to record $g^{(2)}(\tau)$ histograms. Each icon represents a LabVIEW high-level sub-VI.

coincidences to construct the $g^{(2)}(\tau)$ histogram in real-time, we concurrently monitor the average count rate on each detector to ensure it remains above a predefined threshold value, denoted as C_H. By default, this threshold is set to 90% of the initial count rate, represented as C_0. Whenever the count rate drops below this lower limit, the histogram acquisition is paused to launch the automatic repositioning procedure. Histogram acquisition resumes once $C_n > C_\mathrm{H}$. Here, C_n refers to the 'current' average count rate, following the n^{th} iteration of the procedure.

Depending on various parameters, the repositioning procedure is performed either by scanning the sample along two orthogonal in-plane directions ('light' procedure) or by recording a 2D map of the average count rate ('heavy' procedure). This procedure may also include refocusing of the objective by scanning along the out-of-plane axis. In most cases, when investigating a stable SPE, a single iteration is sufficient to recover an optimum count rate. However, in certain cases, such as when investigating a blinking or jittering emitter, a more sophisticated approach is required to account for the 'off' times during which its PL signal is not detected. For a detailed representation of the acquisition procedure, please refer to the state diagram shown in Fig. A.2.

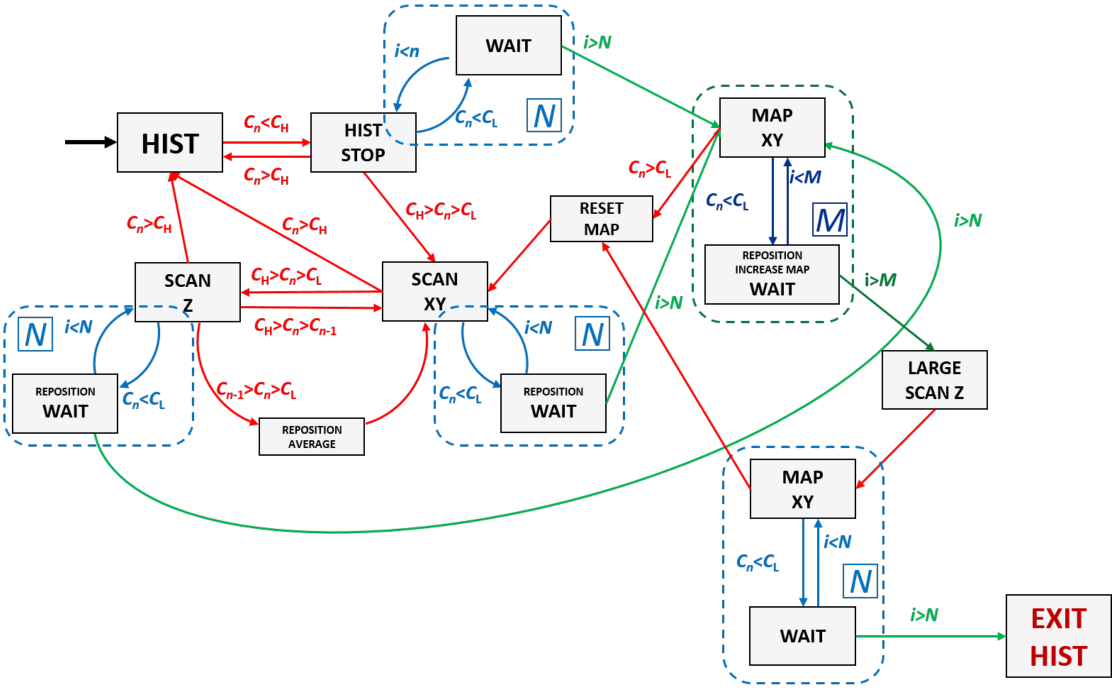

Figure A.7: State diagram depicting the histogram acquisition and repositioning procedure. In typical operation, the system transitions primarily between the 'Hist' (histogram acquisition), 'Hist stop', 'Scan XY', and 'Scan Z' states. C_L is a second 'low' threshold value used to identify if the emitter is temporarily off.

B Mathematical complement

B.1 Numerical resolution under CW excitation

With the objective of simulating the PL signature of high-energy QDs under various exciton power densities and temperature conditions, we numerically solved the rate equations associated with the system described in Fig. 2.14(a). In addition to the ground state, bright states ($|B_1\rangle$ and $|B_2\rangle$) combined dark state ($|D_{1-2}\rangle$) and biexciton states ($|XX_c\rangle$ and $|XX_h\rangle$), we also included higher multiexcitonic states ($|3\rangle$, $|4\rangle$, $|5\rangle$ and $|6\rangle$), which primarily act as a reservoir under high pumping conditions. They are included to prevent an overestimation of the biexciton populations but have minimal influence on the simulated results. It is worth noting that under reasonably low pumping conditions ($\pi \leq \gamma_3$) , multiexcitonic states above the triexciton have no perceptible influence.

For CW excitation, we considered the steady-state solutions of our system of equations, which amounts to solving the following relation:

$$\begin{pmatrix} 0 \\ \vdots \\ 0 \\ 1 \end{pmatrix} = \boldsymbol{M}_{\text{multi}} \cdot \mathbf{n}_{\text{multi}}, \tag{B.1}$$

where the matrix $\boldsymbol{M}_{\text{multi}}$ reads:

$$\boldsymbol{M}_{\text{multi}} = \begin{pmatrix} -\pi & \gamma_1^{B_1} & \gamma_1^{B_2} & 0 & 0 & 0 & 0 & 0 & 0 \\ \pi/2 & -(\gamma_1^{B_1}+\pi+\gamma_{\searrow}^{B_1}) & 0 & \gamma_{\nwarrow}^{B_1} & \gamma_2/2 & 0 & 0 & 0 & 0 \\ \pi/2 & 0 & -(\gamma_1^{B_2}+\pi+\gamma_{\searrow}^{B_2}) & \gamma_{\nwarrow}^{B_2} & \gamma_2/2 & 0 & 0 & 0 & 0 \\ 0 & \gamma_{\searrow}^{B_1} & \gamma_{\searrow}^{B_2} & -(\pi+\gamma_{\nwarrow}^{B_1}+\gamma_{\nwarrow}^{B_2}) & 0 & \gamma_2 & 0 & 0 & 0 \\ 0 & \pi & \pi & 0 & -(\pi+\gamma_2+\gamma_{\searrow}^{XX}) & \gamma_{\nwarrow}^{XX} & \gamma_3/2 & 0 & 0 \\ 0 & 0 & 0 & \pi & \gamma_{\searrow}^{XX} & -(\pi+\gamma_2+\gamma_{\nwarrow}^{XX}) & \gamma_3/2 & 0 & 0 \\ 0 & 0 & 0 & 0 & \pi & \pi & -(\pi+\gamma_3) & \gamma_4 & 0 \\ 0 & 0 & 0 & 0 & 0 & 0 & \pi & -(\gamma_4+\pi) & \gamma_5 \\ 1 & 1 & 1 & 1 & 1 & 1 & 1 & 1 & 1 \end{pmatrix}.$$

$\mathbf{n}_{\text{multi}}$ represents the occupancy numbers of all considered states. It should be noted that the last line in $\boldsymbol{M}_{\text{multi}}$ is used for normalization, ensuring the condition:

$$\sum n_i = 1. \tag{B.2}$$

The various decay parameters were adjusted based on the considerations developed throughout Chap. 2. Numerical resolution is performed using Python.

B.2 Cross-correlation $g^{(2)}(\tau)$ function in the three-level system

The detrimental impact of biexciton PL on the single-photon purity of the exciton line (X_2 at RT) is assessed using Eq. 2.89, which involves the biexciton-to-exciton second-order cross-correlation function ($g^{(2)}_{\mathrm{XX}\to\mathrm{X}_2}(\tau)$) evaluated at zero delay. In the three-level model, this function can be analytically expressed after noticing that:

$$g^{(2)}_{\mathrm{XX}\to\mathrm{X}_2}(\tau) = \frac{n_1(|\tau|)}{n_1(+\infty)}, \tag{B.3}$$

with the initial conditions:

$$\begin{cases} n_1(0) = 1, \\ \mathrm{d}_t n_1(0) = \pi n_0(0) - \gamma_1 n_1(0) = -\gamma_1. \end{cases} \tag{B.4}$$

Following the formalism introduced in Subsect. 2.4.3, we derive:

$$g^{(2)}_{\mathrm{XX}\to\mathrm{X}_2}(\tau) = 1 + C_1' e^{-\gamma_1^{\mathrm{d}}|\tau|} + C_2' e^{-\gamma_2^{\mathrm{d}}|\tau|}, \tag{B.5}$$

where:

$$\begin{aligned} C_1' &= \frac{(\gamma_1/\pi + \pi/\gamma_2)/(\gamma_1 - \gamma_2^{\mathrm{d}}) + \gamma_1}{B'} \\ C_2' &= \frac{(\gamma_1/\pi + \pi/\gamma_2)/(\gamma_1^{\mathrm{d}} - \gamma_1) - \gamma_1}{B'}. \end{aligned} \tag{B.6}$$

At $\tau = 0$, we retrieve Eq. 2.91:

$$g^{(2)}_{\mathrm{XX}\to\mathrm{X}_2}(0) = C_1' + C_2' + 1 = \gamma_1/\pi + 1 + \pi/\gamma_2, \tag{B.7}$$

where $\gamma_1 = \gamma_1^{\mathrm{B}_2}$ for the X_2 line. This model, by design, does not account for the various exciton and biexciton states.

B.3 Refinement of the multiexcitonic model

When we relax the assumption of linear scaling for the recombination rates ($\gamma_i = i\gamma_1$), solving the system of equations that defines the multiexcitonic model under pulsed excitation (see Eq.

2.36) becomes more complex. The system of equations is given by:

$$\begin{cases} \frac{\mathrm{d}n_i}{\mathrm{d}t} = -\gamma_i n_i + \gamma_{i+1} n_{i+1} \; \forall \; i \geq 1, \\ \frac{\mathrm{d}n_0}{\mathrm{d}t} = -\gamma_1 n_1, \\ \sum_{i=0}^{+\infty} n_i = 1. \end{cases} \tag{B.8}$$

To obtain general solutions (Eq. 2.97), we solved the system of equations 2.36 up to the fourth order[I] and inferred a general solution from this particular case. It is important to note that this method does not provide a rigorous mathematical proof, which still needs to be completed. Nonetheless, this approach may offer valuable insights into a more rigorous demonstration in the future.

By postulating:

$$n_i(t) = \sum_{j=i}^{N=4} A_{ij} e^{-\gamma_j t}, \tag{B.9}$$

with $i \in [1,4]$, we can compute the A_{ij} coefficients step-by-step, starting with A_{44} evaluated through the initial condition $A_{44} = n_4(0)$. A_{34} is then inferred by injecting:

$$n_3(t) = A_{33} e^{-\gamma_3 t} + A_{34} e^{-\gamma_4 t} \tag{B.10}$$

in:

$$\frac{\mathrm{d}n_3}{\mathrm{d}t} = -\gamma_3 n_3 + \gamma_4 n_4 \tag{B.11}$$

and yields $A_{34} = n_4(0)\frac{\gamma_4}{\gamma_3-\gamma_4}$. $A_{33} = n_3(0) + n_4(0)\frac{\gamma_4}{\gamma_4-\gamma_3}$ follows from $n_3(0) = A_{33} + A_{34}$. Using the same procedure for n_2 and n_1, we derive:

$$\begin{cases} A_{22} = n_2(0) + n_3(0)\frac{\gamma_3}{\gamma_3-\gamma_2} + n_4(0)\frac{\gamma_3\gamma_4}{(\gamma_3-\gamma_2)(\gamma_4-\gamma_2)}, \\ A_{23} = n_3(0)\frac{\gamma_3}{\gamma_2-\gamma_3} + n_4(0)\frac{\gamma_3\gamma_4}{(\gamma_2-\gamma_3)(\gamma_4-\gamma_3)}, \\ A_{24} = n_4(0)\frac{\gamma_3\gamma_4}{(\gamma_2-\gamma_4)(\gamma_3-\gamma_4)} \end{cases} \tag{B.12}$$

and:

$$\begin{cases} A_{11} = n_1(0) + n_2(0)\frac{\gamma_2}{\gamma_2-\gamma_1} + n_3(0)\frac{\gamma_2\gamma_3}{(\gamma_2-\gamma_1)(\gamma_3-\gamma_1)} + n_4(0)\frac{\gamma_2\gamma_3\gamma_4}{(\gamma_2-\gamma_1)(\gamma_3-\gamma_1)(\gamma_4-\gamma_1)}, \\ A_{23} = n_2(0)\frac{\gamma_2}{\gamma_1-\gamma_2} + n_3(0)\frac{\gamma_2\gamma_3}{(\gamma_1-\gamma_2)(\gamma_3-\gamma_2)} + n_4(0)\frac{\gamma_2\gamma_3\gamma_4}{(\gamma_1-\gamma_2)(\gamma_3-\gamma_2)(\gamma_4-\gamma_2)}, \\ A_{23} = n_3(0)\frac{\gamma_2\gamma_3}{(\gamma_1-\gamma_3)(\gamma_2-\gamma_3)} + n_4(0)\frac{\gamma_2\gamma_3\gamma_4}{(\gamma_1-\gamma_3)(\gamma_2-\gamma_3)(\gamma_4-\gamma_3)}, \\ A_{24} = n_4(0)\frac{\gamma_2\gamma_3\gamma_4}{(\gamma_1-\gamma_4)(\gamma_2-\gamma_4)(\gamma_3-\gamma_4)}. \end{cases} \tag{B.13}$$

[I] We define the fourth order by considering up to four multiexcitonic states, with $|4\rangle$ representing the highest-order state.

All the A_{ij} coefficients can than be expressed in the compact form (Eq. 2.98):

$$A_{ij} = \frac{\gamma_j}{\gamma_i} \sum_{k=j}^{N=4} n_k(0) \left[\prod_{\substack{m=i \\ m\neq j}}^{k} \frac{\gamma_m}{\gamma_m - \gamma_j} \right]. \tag{B.14}$$

We assume this expression also applies for any $N > 4$.

B.4 Solving the three-level system associated to point defects

Akin to the methodology adopted to derive the exciton second-order auto-correlation function in Subsect. 2.4.3, the PD $g^{(2)}(\tau)$ function is obtained for each scenario (refer to Subsect. 3.1.5) by solving the associated system of equations. In model (i) and (iii), the dynamics are described by:

$$\mathrm{d}_t \mathbf{n}_{\mathrm{pd}} = \mathrm{d}_t \begin{pmatrix} n_g \\ n_e \\ n_m \end{pmatrix} = \begin{pmatrix} -\pi & \gamma_e & \gamma_m^{\mathrm{r}} \\ \pi & -(\gamma_e + \gamma_e^{\mathrm{r}}) & 0 \\ 0 & \gamma_e^{\mathrm{r}} & -\gamma_m^{\mathrm{r}} \end{pmatrix} \cdot \mathbf{n}_{\mathrm{pd}}, \tag{B.15}$$

and in model (ii), by:

$$\mathrm{d}_t \mathbf{n}_{\mathrm{pd}} = \mathrm{d}_t \begin{pmatrix} n_g \\ n_e \\ n_m \end{pmatrix} = \begin{pmatrix} -\pi & \gamma_e & 0 \\ \pi & -(\gamma_e + \gamma_e^{\mathrm{r}}) & \gamma_m^{\mathrm{e}} \\ 0 & \gamma_e^{\mathrm{r}} & -\gamma_m^{\mathrm{e}} \end{pmatrix} \cdot \mathbf{n}_{\mathrm{pd}}. \tag{B.16}$$

In all the models, the $g^{(2)}(\tau)$ function of the system is obtained by deriving n_e and using:

$$g^{(2)}_{\mathrm{PD}}(\tau) = \frac{n_e(|\tau|)}{n_e(\infty)}, \tag{B.17}$$

with $n_g(0) = 1$. The solution takes the form:

$$g^{(2)}_{\mathrm{PD}}(\tau) = 1 - (1+a) e^{-\gamma_1^{\mathrm{d}}|\tau|} + a e^{-\gamma_2^{\mathrm{d}}|\tau|}, \tag{B.18}$$

where the antibunching (γ_1^{d}) and bunching (γ_2^{d}) rates are given by:

$$\gamma_{1,2}^{\mathrm{d}} = \frac{A_{\mathrm{PD}} \pm \sqrt{A_{\mathrm{PD}}^2 - 4B_{\mathrm{PD}}}}{2}. \tag{B.19}$$

In model (i) and (iii):

$$\begin{cases} A_{\mathrm{PD}} &= \pi + \gamma_e + \gamma_e^{\mathrm{r}} + \gamma_m^{\mathrm{r}}, \\ B_{\mathrm{PD}} &= \gamma_m^{\mathrm{r}} \left[\pi + \gamma_e + \gamma_e^{\mathrm{r}} \right] + \pi \gamma_e^{\mathrm{r}}, \\ a &= \frac{\gamma_2^{\mathrm{d}} - \gamma_m^{\mathrm{r}}}{\gamma_m^{\mathrm{r}} (1 - \gamma_2^{\mathrm{d}} / \gamma_1^{\mathrm{d}})}. \end{cases} \tag{B.20}$$

In model (ii):

$$\begin{cases} A_{\text{PD}} & = \pi + \gamma_e + \gamma_e^{\text{r}} + \gamma_m^{\text{e}}, \\ B_{\text{PD}} & = \pi\gamma_e^{\text{r}} + \pi\gamma_m^{\text{e}} + \gamma_e\gamma_m^{\text{e}}, \\ a & = \frac{\gamma_2^{\text{d}} - \gamma_m^{\text{e}}}{\gamma_m^{\text{e}}(1-\gamma_2^{\text{d}}/\gamma_1^{\text{d}})}. \end{cases} \tag{B.21}$$

In all the models, the PL intensity of a defect line (I_{SPE}) under CW excitation is expressed by deriving the steady-state solutions of the system of equations, knowing:

$$I_{\text{SPE}} = \eta_{\text{setup}}\gamma_e n_e(\infty) = \eta_{\text{setup}}\gamma_e n_e^{\text{ss}}. \tag{B.22}$$

In each case, this results in a saturation behavior:

$$I_{\text{SPE}} = \frac{I_{\text{sat}}}{1 + \sigma_{\text{sat}}/\sigma_{\text{exc}}}, \tag{B.23}$$

with $I_{\text{sat}} = \eta_{\text{setup}}\gamma_e$[II]. In model (i) and (ii), the saturation intensity (I_{sat}) and saturation excitation power density (σ_{sat}) are respectively given by:

$$\begin{cases} I_{\text{sat}} & = \frac{\eta_{\text{setup}}\gamma_e\gamma_m^{\text{r}}}{\gamma_e^{\text{r}} + \gamma_m^{\text{r}}}, \\ \\ \sigma_{\text{sat}} & = \frac{\gamma_m^{\text{r}}(\gamma_e + \gamma_e^{\text{r}})}{\alpha_{\text{abs}}(\gamma_e^{\text{r}} + \gamma_m^{\text{r}})} \end{cases} \tag{B.24}$$

and:

$$\begin{cases} I_{\text{sat}} & = \frac{\eta_{\text{setup}}\gamma_e\gamma_m^{\text{e}}}{\gamma_e^{\text{r}} + \gamma_m^{\text{e}}}, \\ \\ \sigma_{\text{sat}} & = \frac{\gamma_e\gamma_m^{\text{e}}}{\alpha_{\text{abs}}(\gamma_e^{\text{r}} + \gamma_m^{\text{e}})}. \end{cases} \tag{B.25}$$

The expression obtained in model (iii) is more complex and is not elaborated any further here.

B.5 Simplification under slow bunching rates

The expressions (Eqs. B.19, B.20 and B.21) derived for the parameters governing the recombination dynamics of SPEs are quite intricate and challenging to comprehend. However, in many scenarios, such as the one elaborated in Sect. 3.4, the bunching rate is significantly smaller than its antibunching counterpart ($\gamma_2^{\text{d}} \ll \gamma_1^{\text{d}}$), which substantially simplifies the relations derived above, as elucidated below.

The condition $\gamma_2^{\text{d}} \ll \gamma_1^{\text{d}}$ implies that $B_{\text{PD}} \ll A_{\text{PD}}$, which in turns suggests that $\gamma_e \gg \gamma_e^{\text{r}}, \gamma_m^{\text{r}}$

[II] σ_{sat} is analogous to the excitation power density discussed in the chapter dedicated to QDs. Therefore, we have chosen to maintain the same notation.

in models (i, iii) and $\gamma_e \gg \gamma_e^{\mathrm{r}}, \gamma_m^{\mathrm{e}}$ in model (ii), respectively, indicating that transitions from and toward the metastable state are slow compared to optical transitions. This leads to the following relations:

$$\begin{aligned} &\gamma_1^{\mathrm{d}} = A_{\mathrm{PD}}, \\ &\gamma_2^{\mathrm{d}} = B_{\mathrm{PD}}/A_{\mathrm{PD}}, \end{aligned} \tag{B.26}$$

which yields:

$$\begin{cases} \gamma_1^{\mathrm{d}} & = \pi + \gamma_e, \\ \gamma_2^{\mathrm{d}} & = \gamma_m^{\mathrm{r}} + \frac{\gamma_e^{\mathrm{r}}}{1+\gamma_e/\pi}, \\ a & = \frac{\gamma_e^{\mathrm{r}}}{\gamma_m^{\mathrm{r}}(1+\gamma_e/\pi)}, \end{cases} \tag{B.27}$$

for models (i, iii) and:

$$\begin{cases} \gamma_1^{\mathrm{d}} & = \pi + \gamma_e, \\ \gamma_2^{\mathrm{d}} & = \gamma_m^{\mathrm{e}} + \frac{\gamma_e^{\mathrm{r}}}{1+\gamma_e/\pi}, \\ a & = \frac{\gamma_e^{\mathrm{r}}}{\gamma_m^{\mathrm{e}}(1+\gamma_e/\pi)}, \end{cases} \tag{B.28}$$

for model (ii). Notably, we observed that models (i) and (ii) yield fitting parameters that are mathematically equivalent, with γ_m^{e} and γ_m^{r} coefficients being interchangeable. Under such circumstances, CW $g^{(2)}(\tau)$ measurements are insufficient to distinguish between these two scenarios. In model (iii), incorporating the power-dependent de-shelving rate $\gamma_m^{\mathrm{r}}(\sigma_{\mathrm{exc}})$ (Eq. 3.17) into Eq. B.27 influences the projected trend, although the specific impact is not elaborated upon in this study.

Bibliography

[1] J. P. Dowling and G. J. Milburn, “Quantum technology: the second quantum revolution”, Philosophical Transactions of the Royal Society of London. Series A: Mathematical, Physical and Engineering Sciences **361**, 1655–1674 (2003).

[2] J. L. O’Brien, A. Furusawa, and J. Vučković, “Photonic quantum technologies”, Nature Photonics **3**, 687–695 (2009).

[3] P. Senellart, G. Solomon, and A. White, “High-performance semiconductor quantum-dot single-photon sources”, Nature Nanotechnology **12**, 1026–1039 (2017).

[4] Y. Arakawa and M. J. Holmes, “Progress in quantum-dot single photon sources for quantum information technologies: A broad spectrum overview”, Applied Physics Reviews **7**, 021309 (2020).

[5] M. H. Appel *et al.*, “Entangling a Hole Spin with a Time-Bin Photon: A Waveguide Approach for Quantum Dot Sources of Multiphoton Entanglement”, Physical Review Letters **128**, 233602 (2022).

[6] N. Coste *et al.*, “High-rate entanglement between a semiconductor spin and indistinguishable photons”, Nature Photonics **17**, 582–587 (2023).

[7] X. Wang *et al.*, “III–V compounds as single photon emitters”, Journal of Semiconductors **40**, 071906 (2019).

[8] I. Aharonovich, D. Englund, and M. Toth, “Solid-state single-photon emitters”, Nature Photonics **10**, 631–641 (2016).

[9] J. Y. Cheung *et al.*, “The quantum candela: a re-definition of the standard units for optical radiation”, Journal of Modern Optics **54**, 373–396 (2007).

[10] A. G. White *et al.*, ““Interaction-free” imaging”, Physical Review A **58**, 605–613 (1998).

[11] H.-K. Lo, M. Curty, and K. Tamaki, “Secure quantum key distribution”, Nature Photonics **8**, 595–604 (2014).

[12] E. Neu *et al.*, “Single photon emission from silicon-vacancy colour centres in chemical vapour deposition nano-diamonds on iridium”, New Journal of Physics **13**, 025012 (2011).

[13] S. I. Bogdanov *et al.*, “Ultrabright Room-Temperature Sub-Nanosecond Emission from Single Nitrogen-Vacancy Centers Coupled to Nanopatch Antennas”, Nano Letters **18**, 4837–4844 (2018).

[14] I. Aharonovich and E. Neu, “Diamond Nanophotonics”, Advanced Optical Materials **2**, 911–928 (2014).

[15] I. Aharonovich *et al.*, “Two-Level Ultrabright Single Photon Emission from Diamond Nanocrystals”, Nano Letters **9**, 3191–3195 (2009).

[16] T. T. Tran *et al.*, “Quantum emission from hexagonal boron nitride monolayers”, Nature Nanotechnology **11**, 37–41 (2016).

[17] S. Castelletto *et al.*, “Hexagonal boron nitride: a review of the emerging material platform for single-photon sources and the spin–photon interface”, Beilstein Journal of Nanotechnology **11**, 740–769 (2020).

[18] D. M. Lukin, M. A. Guidry, and J. Vuckovic, “Integrated Quantum Photonics with Silicon Carbide: Challenges and Prospects”, PRX Quantum **1**, 020102 (2020).

[19] J. Wang *et al.*, “Bright room temperature single photon source at telecom range in cubic silicon carbide”, Nature Communications **9**, 4106 (2018).

[20] M. J. Holmes *et al.*, “Room-Temperature Triggered Single Photon Emission from a III-Nitride Site-Controlled Nanowire Quantum Dot”, Nano Letters **14**, 982–986 (2014).

[21] M. J. Holmes *et al.*, “Single Photons from a Hot Solid-State Emitter at 350 K”, ACS Photonics **3**, 543–546 (2016).

[22] S. Deshpande *et al.*, “Electrically driven polarized single-photon emission from an InGaN quantum dot in a GaN nanowire”, Nature Communications **4**, 1675 (2013).

[23] S. Deshpande *et al.*, “Electrically pumped single-photon emission at room temperature from a single InGaN/GaN quantum dot”, Applied Physics Letters **105**, 141109 (2014).

[24] S. Tamariz *et al.*, “Toward Bright and Pure Single Photon Emitters at 300 K Based on GaN Quantum Dots on Silicon”, ACS Photonics **7**, 1515–1522 (2020).

[25] L. Chen *et al.*, “Room Temperature Triggered Single Photon Emission from Self-Assembled GaN/AlN Quantum Dot in Nanowire”, Advanced Functional Materials **32**, 2208340 (2022).

[26] B. Damilano *et al.*, “From visible to white light emission by GaN quantum dots on Si(111) substrate”, Applied Physics Letters **75**, 962–964 (1999).

[27] T. Frost *et al.*, “Temperature-dependent measurement of Auger recombination in $In_{0.40}Ga_{0.60}N$/GaN red-emitting ($\lambda = 630$ nm) quantum dots”, Applied Physics Letters **104**, 081121 (2014).

[28] J. Verma *et al.*, “Tunnel-injection quantum dot deep-ultraviolet light-emitting diodes with polarization-induced doping in III-nitride heterostructures”, Applied Physics Letters **104**, 021105 (2014).

[29] C. E. Reilly *et al.*, “Infrared luminescence from N-polar InN quantum dots and thin films grown by metal organic chemical vapor deposition”, Applied Physics Letters **114**, 241103 (2019).

[30] A. M. Berhane *et al.*, “Bright Room-Temperature Single-Photon Emission from Defects in Gallium Nitride”, Advanced Materials **29**, 1605092 (2017).

[31] Y. Zhou *et al.*, “Room temperature solid-state quantum emitters in the telecom range”, Sci. Adv. **4**, eaar3580 (2018).

[32] M. Meunier, “GaN-based single-photon emitters at telecom wavelengths: electrical injection and room-temperature operation”, PhD thesis (Université Côte d’Azur, Nice, 2023).

[33] Y. Geng *et al.*, “Optical Dipole Structure and Orientation of GaN Defect Single-Photon Emitters”, ACS Photonics **10**, 3723–3729 (2023).

[34] Y. Xue *et al.*, “Single-Photon Emission from Point Defects in Aluminum Nitride Films”, The Journal of Physical Chemistry Letters **11**, 2689–2694 (2020).

[35] J. K. Cannon *et al.*, “Polarization study of single color centers in aluminum nitride”, Applied Physics Letters **122**, 172104 (2023).

[36] J. E. Greivenkamp, *Field guide to geometrical optics*, SPIE field guides v. FG01 (SPIE Press, Bellingham, Washington USA, 2004).

[37] I. M. Rousseau, “III-Nitride Semiconductor Photonic Nanocavities on Silicon”, PhD thesis (EPFL, Lausanne, 2018).

[38] M. Born and E. Wolf, *Principles of Optics: Electromagnetic Theory of Propagation, Interference and Diffraction of Light*, 7th ed. (Cambridge University Press, Cambridge, Oct. 1999).

[39] G. B. Airy, “On the Diffraction of an Object-glass with Circular Aperture”, Transactions of the Cambridge Philosophical Society **5**, 283 (1835).

[40] Lord Rayleigh F.R.S., “Investigations in optics, with special reference to the spectroscope”, The London, Edinburgh, and Dublin Philosophical Magazine and Journal of Science **8**, 261–274 (1879).

[41] O. Svelto, *Principles of Lasers* (Springer US, Boston, MA, 2010).

[42] B. Cagnac and J.-P. Faroux, *Lasers. Interaction lumière - atomes* (CNRS Éditions, Paris, 2002).

[43] S. A. Self, “Focusing of spherical Gaussian beams”, Applied Optics **22**, 658 (1983).

[44] B. Zhang, J. Zerubia, and J.-C. Olivo-Marin, “Gaussian approximations of fluorescence microscope point-spread function models”, Applied Optics **46**, 1819 (2007).

[45] T. S. Tkaczyk, *Field Guide to Microscopy v. FG13* (SPIE Press, Bellingham, Washington USA, May 2010).

[46] K. Parto *et al.*, “Cavity-Enhanced 2D Material Quantum Emitters Deterministically Integrated with Silicon Nitride Microresonators”, Nano Letters **22**, 9748–9756 (2022).

[47] C. M. Natarajan, M. G. Tanner, and R. H. Hadfield, “Superconducting nanowire single-photon detectors: physics and applications”, Superconductor Science and Technology **25**, 063001 (2012).

[48] D. Brunner *et al.*, “Optical constants of epitaxial AlGaN films and their temperature dependence”, Journal of Applied Physics **82**, 5090–5096 (1997).

[49] M. E. Lin *et al.*, “Refractive indices of wurtzite and zincblende GaN”, Electronics Letters **29**, 1759–1760 (1993).

[50] A. S. Barker and M. Ilegems, “Infrared Lattice Vibrations and Free-Electron Dispersion in GaN”, Physical Review B **7**, 743–750 (1973).

[51] T. Kawashima *et al.*, “Optical properties of hexagonal GaN”, Journal of Applied Physics **82**, 3528–3535 (1997).

[52] E. Hecht, *Optics, Global Edition* (Pearson Education, Limited, Harlow, UK, 2016).

[53] D. W. Lynch and W. Hunter, “Refractive Index”, in *Handbook of Optical Constants of Solids* (Elsevier Academic Press, Amsterdam, 1997), pp. 5–114.

[54] C. Hums *et al.*, “Fabry-Perot effects in InGaN/GaN heterostructures on Si-substrate”, Journal of Applied Physics **101**, 033113 (2007).

[55] P. Lottigier *et al.*, “Investigation of the Impact of Point Defects in InGaN/GaN Quantum Wells with High Dislocation Densities”, Nanomaterials **13**, 2569 (2023).

[56] L. Y. Beliaev *et al.*, “Thickness-dependent optical properties of aluminum nitride films for mid-infrared wavelengths”, Journal of Vacuum Science & Technology A: Vacuum, Surfaces, and Films **39**, 043408 (2021).

[57] J. T. Fourkas, “Rapid determination of the three-dimensional orientation of single molecules”, Optics Letters **26**, 211 (2001).

[58] C. Lethiec *et al.*, “Measurement of Three-Dimensional Dipole Orientation of a Single Fluorescent Nanoemitter by Emission Polarization Analysis”, Physical Review X **4**, 021037 (2014).

[59] L. Novotny and B. Hecht, *Principles of nano-optics*, 2nd ed (Cambridge University Press, Cambridge, 2012).

[60] K. Fujito, S. Kubo, and I. Fujimura, “Development of Bulk GaN Crystals and Nonpolar/Semipolar Substrates by HVPE”, MRS Bulletin **34**, 313–317 (2009).

[61] D. F. Feezell *et al.*, “Development of Nonpolar and Semipolar InGaN/GaN Visible Light-Emitting Diodes”, MRS Bulletin **34**, 318–323 (2009).

[62] T. Ha *et al.*, “Polarization Spectroscopy of Single Fluorescent Molecules”, The Journal of Physical Chemistry B **103**, 6839–6850 (1999).

[63] N. R. Jungwirth and G. D. Fuchs, “Optical Absorption and Emission Mechanisms of Single Defects in Hexagonal Boron Nitride”, Physical Review Letters **119**, 057401 (2017).

[64] N. Vukmirović *et al.*, “Symmetry-based calculation of single-particle states and intraband absorption in hexagonal GaN/AlN quantum dot superlattices”, Journal of Physics: Condensed Matter **18**, 6249–6262 (2006).

[65] C. Palmer, “Diffraction Grating Handbook, 8th edition”, MKS Instruments (2020).

[66] M. Böhmer and J. Enderlein, “Orientation imaging of single molecules by wide-field epifluorescence microscopy”, Journal of the Optical Society of America B **20**, 554–559 (2003).

[67] D. Patra, I. Gregor, and J. Enderlein, “Image Analysis of Defocused Single-Molecule Images for Three-Dimensional Molecule Orientation Studies”, The Journal of Physical Chemistry A **108**, 6836–6841 (2004).

[68] D. Patra *et al.*, “Defocused imaging of quantum-dot angular distribution of radiation”, Applied Physics Letters **87**, 101103 (2005).

[69] C. Lethiec *et al.*, “Polarimetry-based analysis of dipolar transitions of single colloidal CdSe/CdS dot-in-rods”, New Journal of Physics **16**, 093014 (2014).

[70] S. A. Empedocles, R. Neuhauser, and M. G. Bawendi, “Three-dimensional orientation measurements of symmetric single chromophores using polarization microscopy”, Nature **399**, 126–130 (1999).

[71] I. Chung, K. T. Shimizu, and M. G. Bawendi, “Room temperature measurements of the 3D orientation of single CdSe quantum dots using polarization microscopy”, Proceedings of the National Academy of Sciences **100**, 405–408 (2003).

[72] W. Becker, *Advanced time-correlated single photon counting techniques*, Springer series in chemical physics 81 (Springer, Berlin Heidelberg New York, 2005).

[73] R. H. Hadfield, “Single-photon detectors for optical quantum information applications”, Nature Photonics **3**, 696–705 (2009).

[74] M. D. Eisaman *et al.*, “Invited Review Article: Single-photon sources and detectors”, Review of Scientific Instruments **82**, 071101 (2011).

[75] I. Esmaeil Zadeh *et al.*, “Superconducting nanowire single-photon detectors: A perspective on evolution, state-of-the-art, future developments, and applications”, Applied Physics Letters **118**, 190502 (2021).

[76] J. Chang *et al.*, “Detecting telecom single photons with 99.5-2.07+0.5% system detection efficiency and high time resolution”, APL Photonics **6**, 036114 (2021).

[77] Z. Lin *et al.*, “Efficient and versatile toolbox for analysis of time-tagged measurements”, Journal of Instrumentation **16**, T08016 (2021).

[78] J. Arlt *et al.*, “A study of pile-up in integrated time-correlated single photon counting systems”, Review of Scientific Instruments **84**, 103105 (2013).

[79] S. Thomson, “IRF Width & Minimum Measurable Lifetime in the FLS1000”, Edimburgh Instruments **TN_P81** (2023).

[80] A. Visco *et al.*, “Temporal dispersion of a spectrometer”, Review of Scientific Instruments **79**, 10F545 (2008).

[81] D. V. O’Connor, W. R. Ware, and J. C. Andre, “Deconvolution of fluorescence decay curves. A critical comparison of techniques”, The Journal of Physical Chemistry **83**, 1333–1343 (1979).

[82] A. Cross and G. Fleming, “Analysis of time-resolved fluorescence anisotropy decays”, Biophysical Journal **46**, 45–56 (1984).

[83] J. Léonard *et al.*, “High-throughput time-correlated single photon counting”, Lab Chip **14**, 4338–4343 (2014).

[84] M. J. Stevens *et al.*, “Third-order antibunching from an imperfect single-photon source”, Optics Express **22**, 3244 (2014).

[85] V. S. Arakelyan *et al.*, “Structure of the R_1 and R_2 Bands of Isotopes of Cr^{3+} Ion in a Single Crystal of Ruby at Room Temperature”, Optics and Spectroscopy **129**, 440–451 (2021).

[86] E. Wijerathna *et al.*, “Correcting etaloning fringes in hyperspectral image cubes of Jupiter using sensor thickness modeling with flat-field data fitting”, Journal of Astronomical Telescopes, Instruments, and Systems **6**, 10.1117/1.JATIS.6.2.028002 (2020).

[87] C. Massie, K. Chen, and A. J. Berger, “Calibration Technique for Suppressing Residual Etalon Artifacts in Slit-Averaged Raman Spectroscopy”, Applied Spectroscopy **76**, 255–261 (2022).

[88] I. Vurgaftman and J. R. Meyer, “Band parameters for nitrogen-containing semiconductors”, Journal of Applied Physics **94**, 3675–3696 (2003).

[89] S. Limpijumnong and W. R. L. Lambrecht, “Homogeneous Strain Deformation Path for the Wurtzite to Rocksalt High-Pressure Phase Transition in GaN”, Physical Review Letters **86**, 91–94 (2001).

[90] M. Sumiya and S. Fuke, “Review of polarity determination and control of GaN”, MRS Internet Journal of Nitride Semiconductor Research **9**, e1 (2004).

[91] F. Bernardini, V. Fiorentini, and D. Vanderbilt, “Spontaneous polarization and piezoelectric constants of III-V nitrides”, Physical Review B **56**, R10024–R10027 (1997).

[92] M. Suzuki, T. Uenoyama, and A. Yanase, “First-principles calculations of effective-mass parameters of AlN and GaN”, Physical Review B **52**, 8132–8139 (1995).

[93] J. Wu *et al.*, “Temperature dependence of the fundamental band gap of InN”, Journal of Applied Physics **94**, 4457–4460 (2003).

[94] M. Feneberg *et al.*, “Sharp bound and free exciton lines from homoepitaxial AlN”, physica status solidi (a) **208**, 1520–1522 (2011).

[95] C. Haller *et al.*, “GaN surface as the source of non-radiative defects in InGaN/GaN quantum wells”, Applied Physics Letters **113**, 111106 (2018).

[96] B. Gil, O. Briot, and R.-L. Aulombard, "Valence-band physics and the optical properties of GaN epilayers grown onto sapphire with wurtzite symmetry", Physical Review B **52**, R17028–R17031 (1995).

[97] W. Shan *et al.*, "Strain effects on excitonic transitions in GaN: Deformation potentials", Physical Review B **54**, 13460–13463 (1996).

[98] H. Lahrèche *et al.*, "Buffer free direct growth of GaN on 6H–SiC by metalorganic vapor phase epitaxy", Journal of Applied Physics **87**, 577–583 (2000).

[99] J. Simon *et al.*, "Direct comparison of recombination dynamics in cubic and hexagonal GaN/AlN quantum dots", Physical Review B **68**, 035312 (2003).

[100] R. Pässler, "Moderate phonon dispersion shown by the temperature dependence of fundamental band gaps of various elemental and binary semiconductors including wide-band gap materials", Journal of Applied Physics **88**, 2570–2577 (2000).

[101] Y. P. Varshni, "Temperature dependence of the energy gap in semiconductors", Physica **34**, 149–154 (1967).

[102] R. Pässler, "Dispersion-related assessments of temperature dependences for the fundamental band gap of hexagonal GaN", Journal of Applied Physics **90**, 3956–3964 (2001).

[103] R. Warburton, "SEMICONDUCTOR MATERIALS | Quantum Dots", in *Encyclopedia of Modern Optics* (Elsevier, Amsterdam, 2005), pp. 408–417.

[104] D. Simeonov, "Synthesis and optical investigation of single polar GaN/AlN quantum dots", PhD thesis (EPFL, Lausanne, 2008).

[105] A. Kasic *et al.*, "Free-carrier and phonon properties of n- and p-type hexagonal GaN films measured by infrared ellipsometry", Physical Review B **62**, 7365–7377 (2000).

[106] D. P. Williams, A. D. Andreev, and E. P. O'Reilly, "Dependence of exciton energy on dot size in GaN/AlN quantum dots", Physical Review B **73**, 241301 (2006).

[107] M. Arlery *et al.*, "Quantitative characterization of GaN quantum-dot structures in AlN by high-resolution transmission electron microscopy", Applied Physics Letters **74**, 3287–3289 (1999).

[108] A. D. Andreev and E. P. O'Reilly, "Theory of the electronic structure of GaN/AlN hexagonal quantum dots", Physical Review B **62**, 15851–15870 (2000).

[109] F. Widmann *et al.*, "Blue-light emission from GaN self-assembled quantum dots due to giant piezoelectric effect", Physical Review B **58**, R15989–R15992 (1998).

[110] K. Hoshino, S. Kako, and Y. Arakawa, "Formation and optical properties of stacked GaN self-assembled quantum dots grown by metalorganic chemical vapor deposition", Applied Physics Letters **85**, 1262–1264 (2004).

[111] J. Coraux *et al.*, "Mechanism of GaN quantum dots capped with AlN : An AFM, electron microscopy, and x-ray anomalous diffraction study", Physical Review B **74**, 195302 (2006).

[112] B. Daudin, “Polar and nonpolar GaN quantum dots”, Journal of Physics: Condensed Matter **20**, 473201 (2008).

[113] M. Hrytsaienko *et al.*, “Dark-level trapping, lateral confinement, and built-in electric field contributions to the carrier dynamics in c-plane GaN/AlN quantum dots emitting in the UV range”, Journal of Applied Physics **129**, 054301 (2021).

[114] P. Michler, ed., *Single quantum dots: fundamentals, applications, and new concepts*, Topics in applied physics v. 90 (Springer-Verlag, Berlin ; New York, 2003).

[115] B. Santic, “On the hole effective mass and the free hole statistics in wurtzite GaN”, Semiconductor Science and Technology **18**, 219–224 (2003).

[116] M. Winkelnkemper *et al.*, “GaN/AlN quantum dots for single qubit emitters”, Journal of Physics: Condensed Matter **20**, 454211 (2008).

[117] M. J. Holmes *et al.*, “Probing the Excitonic States of Site-Controlled GaN Nanowire Quantum Dots”, Nano Letters **15**, 1047–1051 (2015).

[118] M. I. Dyakonov, *Spin physics in semiconductors*, Springer series in solid-state sciences 157 (Springer, New York, 2008).

[119] E. L. Ivchenko, “Fine Structure of Excitonic Levels in Semiconductor Nanostructures”, physica status solidi (a) **164**, 487–492 (1997).

[120] R. Seguin, “Electronic Fine Structure and Recombination Dynamics in Single InAs Quantum Dots”, PhD thesis (TU Berlin, Berlin, 2008).

[121] C. Kindel *et al.*, “Exciton fine-structure splitting in GaN/AlN quantum dots”, Physical Review B **81**, 241309 (2010).

[122] M. Arita *et al.*, “Ultraclean Single Photon Emission from a GaN Quantum Dot”, Nano Letters **17**, 2902–2907 (2017).

[123] R. Seguin *et al.*, “Size-Dependent Fine-Structure Splitting in Self-Organized InAs / GaAs Quantum Dots”, Physical Review Letters **95**, 257402 (2005).

[124] S. Rodt *et al.*, “Size-dependent binding energies and fine-structure splitting of excitonic complexes in single InAs/GaAs quantum dots”, Journal of Luminescence **122-123**, 735–739 (2007).

[125] V. Ranjan *et al.*, “Self-consistent calculations of the optical properties of GaN quantum dots”, Physical Review B **68**, 115305 (2003).

[126] J. Gleize *et al.*, “Signature of GaN–AlN quantum dots by nonresonant Raman scattering”, Applied Physics Letters **77**, 2174–2176 (2000).

[127] D. Simeonov *et al.*, “Stranski-Krastanov GaN/AlN quantum dots grown by metal organic vapor phase epitaxy”, Journal of Applied Physics **99**, 083509 (2006).

[128] J. Gleize *et al.*, “Inelastic Light Scattering by Phonons in Hexagonal GaN-AlN Nanostructures”, physica status solidi (a) **183**, 157–161 (2001).

[129] R. Butté and N. Grandjean, “Effects of Polarization in Optoelectronic Quantum Structures”, in *Polarization Effects in Semiconductors*, edited by C. Wood and D. Jena (Springer US, Boston, MA, 2008), pp. 467–511.

[130] T. Bretagnon *et al.*, “Radiative lifetime of a single electron-hole pair in GaN/AlN quantum dots”, Physical Review B **73**, 113304 (2006).

[131] C. Adelmann *et al.*, “Nucleation and growth of GaN/AlN quantum dots”, Physical Review B **70**, 125427 (2004).

[132] N. Bohr, “XXXVII. On the constitution of atoms and molecules”, Philos. Mag. **26**, 476–502 (1913).

[133] D. C. Reynolds *et al.*, “Ground and excited state exciton spectra from GaN grown by molecular-beam epitaxy”, Journal of Applied Physics **80**, 594–596 (1996).

[134] P. Ramvall *et al.*, “Optical properties of GaN quantum dots”, Journal of Applied Physics **87**, 3883–3890 (2000).

[135] A. Thränhardt *et al.*, “Relation between dipole moment and radiative lifetime in interface fluctuation quantum dots”, Physical Review B **65**, 035327 (2002).

[136] J. R. Guest *et al.*, “Measurement of optical absorption by a single quantum dot exciton”, Physical Review B **65**, 241310 (2002).

[137] M. Holmes *et al.*, “Spectral diffusion and its influence on the emission linewidths of site-controlled GaN nanowire quantum dots”, Physical Review B **92**, 115447 (2015).

[138] S. Buckley, K. Rivoire, and J. Vučković, “Engineered quantum dot single-photon sources”, Reports on Progress in Physics **75**, 126503 (2012).

[139] R. Brouri *et al.*, “Photon antibunching in the fluorescence of individual color centers in diamond”, Optics Letters **25**, 1294 (2000).

[140] O. Benson *et al.*, “Regulated and Entangled Photons from a Single Quantum Dot”, Physical Review Letters **84**, 2513–2516 (2000).

[141] N. Akopian *et al.*, “Entangled Photon Pairs from Semiconductor Quantum Dots”, Physical Review Letters **96**, 130501 (2006).

[142] S. Kako *et al.*, “Exciton and biexciton luminescence from single hexagonal GaN/AlN self-assembled quantum dots”, Applied Physics Letters **85**, 64–66 (2004).

[143] S. Kako *et al.*, “A gallium nitride single-photon source operating at 200 K”, Nature Materials **5**, 887–892 (2006).

[144] J. Renard *et al.*, “Exciton and Biexciton Luminescence from Single GaN/AlN Quantum Dots in Nanowires”, Nano Letters **8**, 2092–2096 (2008).

[145] D. Simeonov *et al.*, “Complex behavior of biexcitons in GaN quantum dots due to a giant built-in polarization field”, Physical Review B **77**, 075306 (2008).

[146] S. Amloy *et al.*, “Size dependent biexciton binding energies in GaN quantum dots”, Applied Physics Letters **99**, 251903 (2011).

[147] K. Choi *et al.*, “Strong exciton confinement in site-controlled GaN quantum dots embedded in nanowires”, Applied Physics Letters **103**, 171907 (2013).

[148] G. Hönig *et al.*, “Manifestation of unconventional biexciton states in quantum dots”, Nature Communications **5**, 5721 (2014).

[149] T. Bretagnon *et al.*, “Time dependence of the photoluminescence of GaN/AlN quantum dots under high photoexcitation”, Physical Review B **68**, 205301 (2003).

[150] G. Salviati *et al.*, “Optical and structural characterization of self-organized stacked GaN/AlN quantum dots”, Journal of Physics: Condensed Matter **16**, S115–S126 (2004).

[151] R. Seguin *et al.*, “Size-dependence of anisotropic exchange interaction in InAs/GaAs quantum dots”, physica status solidi (b) **243**, 3937–3941 (2006).

[152] A. Orieux *et al.*, “Semiconductor devices for entangled photon pair generation: a review”, Reports on Progress in Physics **80**, 076001 (2017).

[153] T. M. Stace, G. J. Milburn, and C. H. W. Barnes, “Entangled two-photon source using biexciton emission of an asymmetric quantum dot in a cavity”, Physical Review B **67**, 085317 (2003).

[154] C. Santori *et al.*, “Polarization-correlated photon pairs from a single quantum dot”, Physical Review B **66**, 045308 (2002).

[155] G. Callsen *et al.*, “Steering photon statistics in single quantum dots: From one- to two-photon emission”, Physical Review B **87**, 245314 (2013).

[156] M. E. Reimer *et al.*, *Voltage Induced Hidden Symmetry and Photon Entanglement Generation in a Single, Site-Selected Quantum Dot*, arXiv:0706.1075 [quant-ph], June 2007.

[157] J. E. Avron *et al.*, “Entanglement on Demand through Time Reordering”, Physical Review Letters **100**, 120501 (2008).

[158] C. H. Bennett and G. Brassard, “Public Key Distribution and Coin Tossing”, Proceedings of the IEEE International Conference on Computers, Systems and Signal Processing, Bangalore **1**, 175–179 (1984).

[159] C. Santori *et al.*, “Time-resolved spectroscopy of multiexcitonic decay in an InAs quantum dot”, Physical Review B **65**, 073310 (2002).

[160] M. Wimmer, S. V. Nair, and J. Shumway, “Biexciton recombination rates in self-assembled quantum dots”, Physical Review B **73**, 165305 (2006).

[161] G. Bacher *et al.*, “Biexciton versus Exciton Lifetime in a Single Semiconductor Quantum Dot”, Physical Review Letters **83**, 4417–4420 (1999).

[162] C. H. Kindel, “Study on Optical Polarization in Hexagonal Gallium Nitride Quantum Dots”, PhD thesis (University of Tokyo, Tokyo, 2010).

[163] G. Callsen, “Advanced optical signatures of single, wurtzite GaN quantum dots: From fundamental exciton coupling mechanisms towards tunable photon statistics and hybrid-quasiparticles”, PhD thesis (University of Technology, Sydney, 2015).

[164] V. I. Klimov *et al.*, “Quantization of Multiparticle Auger Rates in Semiconductor Quantum Dots”, Science **287**, 1011–1013 (2000).

[165] R. J. Ellingson *et al.*, “Highly Efficient Multiple Exciton Generation in Colloidal PbSe and PbS Quantum Dots”, Nano Letters **5**, 865–871 (2005).

[166] K. E. Shulenberger *et al.*, “Multiexciton Lifetimes Reveal Triexciton Emission Pathway in CdSe Nanocrystals”, Nano Letters **18**, 5153–5158 (2018).

[167] C. Melnychuk and P. Guyot-Sionnest, “Multicarrier Dynamics in Quantum Dots”, Chemical Reviews **121**, 2325–2372 (2021).

[168] L. Meitner, “Über den Zusammenhang zwischen β- und α-Strahlen”, Zeitschrift für Physik **9**, 145–152 (1922).

[169] P. Auger, “Sur les rayons β secondaires produits dans un gaz par des rayons X”, C. R. Acad. Sci. **177**, 169 (1923).

[170] D. Matsakis *et al.*, “A renaming proposal: “The Auger–Meitner effect””, Physics Today **72**, 10–11 (2019).

[171] A. V. Barzykin and M. Tachiya, “Stochastic models of charge carrier dynamics in semiconducting nanosystems”, Journal of Physics: Condensed Matter **19**, 065105 (2007).

[172] V. I. Klimov *et al.*, “Scaling of multiexciton lifetimes in semiconductor nanocrystals”, Physical Review B **77**, 195324 (2008).

[173] U. Mizrahi *et al.*, “Non-classical light generated by a quantum dot: multi-color photons with tunable statistics”, Synthetic Metals **139**, 711–714 (2003).

[174] D. Regelman *et al.*, “Semiconductor Quantum Dot: A Quantum Light Source of Multicolor Photons with Tunable Statistics”, Physical Review Letters **87**, 257401 (2001).

[175] L. Nevou *et al.*, “Intraband emission at λ=1.48 μm from GaN/AlN quantum dots at room temperature”, Applied Physics Letters **92**, 161105 (2008).

[176] U. Bockelmann and G. Bastard, “Phonon scattering and energy relaxation in two-, one-, and zero-dimensional electron gases”, Physical Review B **42**, 8947–8951 (1990).

[177] H. Benisty, C. M. Sotomayor-Torrès, and C. Weisbuch, “Intrinsic mechanism for the poor luminescence properties of quantum-box systems”, Physical Review B **44**, 10945–10948 (1991).

[178] T. Inoshita and H. Sakaki, “Electron relaxation in a quantum dot: Significance of multiphonon processes”, Physical Review B **46**, 7260–7263 (1992).

[179] B. Ohnesorge *et al.*, “Rapid carrier relaxation in self-assembled $In_xGa_{1-x}As$/GaAs quantum dots”, Physical Review B **54**, 11532–11538 (1996).

[180] U. Woggon *et al.*, “Ultrafast energy relaxation in quantum dots”, Physical Review B **54**, 17681–17690 (1996).

[181] U. Bockelmann and T. Egeler, “Electron relaxation in quantum dots by means of Auger processes”, Physical Review B **46**, 15574–15577 (1992).

[182] R. Ferreira and G. Bastard, “Phonon-assisted capture and intradot Auger relaxation in quantum dots”, Applied Physics Letters **74**, 2818–2820 (1999).

[183] X.-Q. Li, H. Nakayama, and Y. Arakawa, “Phonon bottleneck in quantum dots: Role of lifetime of the confined optical phonons”, Physical Review B **59**, 5069–5073 (1999).

[184] S. Hameau *et al.*, “Strong Electron-Phonon Coupling Regime in Quantum Dots: Evidence for Everlasting Resonant Polarons”, Physical Review Letters **83**, 4152–4155 (1999).

[185] O. Verzelen, R. Ferreira, and G. Bastard, “Polaron lifetime and energy relaxation in semiconductor quantum dots”, Physical Review B **62**, R4809–R4812 (2000).

[186] E. A. Zibik *et al.*, “Intraband relaxation via polaron decay in InAs self-assembled quantum dots”, Physical Review B **70**, 161305 (2004).

[187] T. Grange, R. Ferreira, and G. Bastard, “Polaron relaxation in self-assembled quantum dots: Breakdown of the semiclassical model”, Physical Review B **76**, 241304 (2007).

[188] N. Bouarissa and H. Aourag, “Effective masses of electrons and heavy holes in InAs, InSb, GaSb, GaAs and some of their ternary compounds”, Infrared Physics & Technology **40**, 343–349 (1999).

[189] G. Callsen *et al.*, “Analysis of the exciton–LO-phonon coupling in single wurtzite GaN quantum dots”, Physical Review B **92**, 235439 (2015).

[190] J. Lee, E. S. Koteles, and M. O. Vassell, “Luminescence linewidths of excitons in GaAs quantum wells below 150 K”, Physical Review B **33**, 5512–5516 (1986).

[191] A. J. Fischer *et al.*, “Femtosecond four-wave-mixing studies of nearly homogeneously broadened excitons in GaN”, Physical Review B **56**, 1077–1080 (1997).

[192] R. Seguin *et al.*, “Multi-excitonic complexes in single InGaN quantum dots”, Applied Physics Letters **84**, 4023–4025 (2004).

[193] H. Esmaielpour *et al.*, “Role of Exciton Binding Energy on LO Phonon Broadening and Polaron Formation in $(BA)_2PbI_4$ Ruddlesden–Popper Films”, The Journal of Physical Chemistry C **124**, 9496–9505 (2020).

[194] M. Bayer and A. Forchel, “Temperature dependence of the exciton homogeneous linewidth in $In_{0.60}Ga_{0.40}As/GaAs$ self-assembled quantum dots”, Physical Review B **65**, 041308 (2002).

[195] V. Y. Davydov *et al.*, “Phonon dispersion and Raman scattering in hexagonal GaN and AlN”, Physical Review B **58**, 12899–12907 (1998).

[196] J. Stachurski *et al.*, “Single photon emission and recombination dynamics in self-assembled GaN/AlN quantum dots”, Light: Science & Applications **11**, 114 (2022).

[197] F. Demangeot *et al.*, “Homogeneous and inhomogeneous linewidth broadening of single polar GaN/AlN quantum dots”, physica status solidi c **6**, S598–S601 (2009).

[198] R. Heitz *et al.*, “Enhanced Polar Exciton-LO-Phonon Interaction in Quantum Dots”, Physical Review Letters **83**, 4654–4657 (1999).

[199] L. Besombes *et al.*, “Few-particle effects in single CdTe quantum dots”, Physical Review B **65**, 121314 (2002).

[200] I. A. Ostapenko *et al.*, “Exciton acoustic-phonon coupling in single GaN/AlN quantum dots”, Physical Review B **85**, 081303 (2012).

[201] T. Wang, R. A. Oliver, and R. A. Taylor, “Non-polar nitride single-photon sources”, Journal of Optics **22**, 073001 (2020).

[202] R. Hanson *et al.*, “Spins in few-electron quantum dots”, Reviews of Modern Physics **79**, 1217–1265 (2007).

[203] K. Gawarecki and P. Machnikowski, “Phonon-assisted relaxation between triplet and singlet states in a self-assembled double quantum dot”, Scientific Reports **11**, 15256 (2021).

[204] M. Paillard *et al.*, “Spin Relaxation Quenching in Semiconductor Quantum Dots”, Physical Review Letters **86**, 1634–1637 (2001).

[205] W. Langbein *et al.*, “Radiatively limited dephasing in InAs quantum dots”, Physical Review B **70**, 033301 (2004).

[206] T. Flissikowski *et al.*, “Photon Beats from a Single Semiconductor Quantum Dot”, Physical Review Letters **86**, 3172–3175 (2001).

[207] O. Labeau, P. Tamarat, and B. Lounis, “Temperature Dependence of the Luminescence Lifetime of Single CdSe/ZnS Quantum Dots”, Physical Review Letters **90**, 257404 (2003).

[208] I. Favero *et al.*, “Fast exciton spin relaxation in single quantum dots”, Physical Review B **71**, 233304 (2005).

[209] H. Tong and M. W. Wu, “Theory of excitons in cubic III-V semiconductor GaAs, InAs and GaN quantum dots: Fine structure and spin relaxation”, Physical Review B **83**, 235323 (2011).

[210] B. Patton, W. Langbein, and U. Woggon, “Trion, biexciton, and exciton dynamics in single self-assembled CdSe quantum dots”, Physical Review B **68**, 125316 (2003).

[211] S. Tamariz, “GaN Quantum Dots for Room Temperature Excitonic Physics”, PhD thesis (EPFL, Lausanne, 2019).

[212] S. Tamariz, D. Martin, and N. Grandjean, “AlN grown on Si(1 1 1) by ammonia-molecular beam epitaxy in the 900–1200 °C temperature range”, Journal of Crystal Growth **476**, 58–63 (2017).

[213] S. Tamariz, G. Callsen, and N. Grandjean, “Density control of GaN quantum dots on AlN single crystal”, Applied Physics Letters **114**, 082101 (2019).

[214] M. A. Herman, W. Richter, and H. Sitter, *Epitaxy: Physical Principles and Technical Implementation*, Vol. 62, Springer Series in MATERIALS SCIENCE (Springer, Berlin, 2004).

[215] D. Simeonov *et al.*, “Strain relaxation of AlN epilayers for Stranski–Krastanov GaN/AlN quantum dots grown by metal organic vapor phase epitaxy”, Journal of Crystal Growth **299**, 254–258 (2007).

[216] B. Alloing *et al.*, “Growth and characterization of single quantum dots emitting at 1300 nm”, Applied Physics Letters **86**, 101908 (2005).

[217] B. Daudin *et al.*, “Stranski-Krastanov growth mode during the molecular beam epitaxy of highly strained GaN”, Physical Review B **56**, R7069–R7072 (1997).

[218] M. Miyamura, K. Tachibana, and Y. Arakawa, “High-density and size-controlled GaN self-assembled quantum dots grown by metalorganic chemical vapor deposition”, Applied Physics Letters **80**, 3937–3939 (2002).

[219] J. Brown *et al.*, “GaN quantum dot density control by rf-plasma molecular beam epitaxy”, Applied Physics Letters **84**, 690–692 (2004).

[220] N. Gmeinwieser and U. T. Schwarz, “Pattern formation and directional and spatial ordering of edge dislocations in bulk GaN: Microphotoluminescence spectra and continuum elastic calculations”, Physical Review B **75**, 245213 (2007).

[221] J. L. Rouvière *et al.*, “Preferential nucleation of GaN quantum dots at the edge of AlN threading dislocations”, Applied Physics Letters **75**, 2632–2634 (1999).

[222] D. Alden *et al.*, “Point-Defect Nature of the Ultraviolet Absorption Band in AlN”, Physical Review Applied **9**, 054036 (2018).

[223] C. Liu *et al.*, “234 nm and 246 nm AlN-Delta-GaN quantum well deep ultraviolet light-emitting diodes”, Applied Physics Letters **112**, 011101 (2018).

[224] I. A. Ostapenko *et al.*, “Large internal dipole moment in InGaN/GaN quantum dots”, Applied Physics Letters **97**, 063103 (2010).

[225] G. Hönig *et al.*, “Identification of electric dipole moments of excitonic complexes in nitride-based quantum dots”, Physical Review B **88**, 045309 (2013).

[226] J. W. Robinson *et al.*, “Quantum-confined Stark effect in a single InGaN quantum dot under a lateral electric field”, Applied Physics Letters **86**, 213103 (2005).

[227] S. A. Empedocles and M. G. Bawendi, “Influence of Spectral Diffusion on the Line Shapes of Single CdSe Nanocrystallite Quantum Dots”, The Journal of Physical Chemistry B **103**, 1826–1830 (1999).

[228] P. Blome *et al.*, “Spectral Diffusion of Single InP/$Ga_xIn_{1-x}P$ Quantum Dot Luminescence”, physica status solidi (b) **221**, 31–35 (2000).

[229] M. J. Fernée *et al.*, “Charge hopping revealed by jitter correlations in the photoluminescence spectra of single CdSe nanocrystals”, Physical Review B **81**, 155307 (2010).

[230] M. Abbarchi *et al.*, “Bunched photon statistics of the spectrally diffusive photoluminescence of single self-assembled GaAs quantum dots”, Physical Review B **86**, 115330 (2012).

[231] C. Kindel *et al.*, “Spectral diffusion in nitride quantum dots: Emission energy dependent linewidths broadening via giant built-in dipole moments”, physica status solidi (RRL) – Rapid Research Letters **8**, 408–413 (2014).

[232] K. Gao *et al.*, “Nanosecond-scale spectral diffusion in the single photon emission of a GaN quantum dot”, AIP Advances **7**, 125216 (2017).

[233] M. J. Holmes, M. Arita, and Y. Arakawa, “III-nitride quantum dots as single photon emitters”, Semiconductor Science and Technology **34**, 033001 (2019).

[234] X. Dong-Juan *et al.*, “Interfacial Properties of AlN/Si (111) Grown by Metal-Organic Chemical Vapour Deposition”, Chinese Physics Letters **19**, 543–545 (2002).

[235] V. Bonito Oliva *et al.*, “Silicon diffusion in AlN”, Journal of Applied Physics **134**, 095103 (2023).

[236] Q. Yan *et al.*, “Origins of optical absorption and emission lines in AlN”, Applied Physics Letters **105**, 111104 (2014).

[237] A. Mogilatenko *et al.*, “Crystal defect analysis in AlN layers grown by MOVPE on bulk AlN”, Journal of Crystal Growth **505**, 69–73 (2019).

[238] D. Koleske *et al.*, “Influence of MOVPE growth conditions on carbon and silicon concentrations in GaN”, Journal of Crystal Growth **242**, 55–69 (2002).

[239] J. Neugebauer and C. G. Van De Walle, “Role of hydrogen in doping of GaN”, Applied Physics Letters **68**, 1829–1831 (1996).

[240] O. Ambacher *et al.*, “Hydrogen in Gallium Nitride Grown by MOCVD”, physica status solidi (a) **159**, 105–119 (1997).

[241] A. Berthelot, “Diffusion spectrale et rétrécissement par le mouvement dans les boîtes quantiques”, PhD thesis (Université Paris VI, Paris, 2008).

[242] A. Lohner *et al.*, “Picosecond capture of photoexcited holes by shallow acceptors in *p*-type GaAs”, Physical Review Letters **68**, 3920–3923 (1992).

[243] A. Berthelot *et al.*, “Unconventional motional narrowing in the optical spectrum of a semiconductor quantum dot”, Nature Physics **2**, 759–764 (2006).

[244] K. Gao *et al.*, “Spectral diffusion time scales in InGaN/GaN quantum dots”, Applied Physics Letters **114**, 112109 (2019).

[245] J. H. Rice *et al.*, “Temporal variation in photoluminescence from single InGaN quantum dots”, Applied Physics Letters **84**, 4110–4112 (2004).

[246] R. Bardoux *et al.*, “Photoluminescence of single GaN/AlN hexagonal quantum dots on Si (111) : Spectral diffusion effects”, Physical Review B **74**, 195319 (2006).

[247] J. D. Evans, *Straightforward statistics for the behavioral sciences* (Brooks/Cole Pub. Co., Pacific Grove, 1996).

[248] G. Sallen *et al.*, “Subnanosecond spectral diffusion measurement using photon correlation”, Nature Photonics **4**, 696–699 (2010).

[249] G. Sallen *et al.*, “Exciton dynamics of a single quantum dot embedded in a nanowire”, Physical Review B **80**, 085310 (2009).

[250] G. Sallen *et al.*, “Subnanosecond spectral diffusion of a single quantum dot in a nanowire”, Physical Review B **84**, 041405 (2011).

[251] K. Ota, N. Usami, and Y. Shiraki, “Temperature dependence of microscopic photoluminescence spectra of quantum dots and quantum wells”, Physica E: Low-dimensional Systems and Nanostructures **2**, 573–577 (1998).

[252] P. Borri *et al.*, “Ultralong Dephasing Time in InGaAs Quantum Dots”, Physical Review Letters **87**, 157401 (2001).

[253] V. M. Axt *et al.*, “Phonon-induced pure dephasing in exciton-biexciton quantum dot systems driven by ultrafast laser pulse sequences”, Physical Review B **72**, 125309 (2005).

[254] K. E. Dorfman and S. Mukamel, “Indistinguishability and correlations of photons generated by quantum emitters undergoing spectral diffusion”, Scientific Reports **4**, 3996 (2014).

[255] Y. Geng and K. Nomoto, “Ultrafast spectral diffusion of GaN defect single photon emitters”, Applied Physics Letters **123**, 174002 (2023).

[256] M. Bayer *et al.*, “Hidden symmetries in the energy levels of excitonic ‘artificial atoms’”, Nature **405**, 923–926 (2000).

[257] S. Rodt *et al.*, “Repulsive exciton-exciton interaction in quantum dots”, Physical Review B **68**, 035331 (2003).

[258] M. Zieliński *et al.*, “Excitonic complexes in natural InAs/GaAs quantum dots”, Physical Review B **91**, 085303 (2015).

[259] D. Rivas *et al.*, “Two-Color Single-Photon Emission from InAs Quantum Dots: Toward Logic Information Management Using Quantum Light”, Nano Letters **14**, 456–463 (2014).

[260] S. M. Ulrich *et al.*, “Correlated photon-pair emission from a charged single quantum dot”, Physical Review B **71**, 235328 (2005).

[261] C.-W. Hsu *et al.*, “The charged exciton in an InGaN quantum dot on a GaN pyramid”, Applied Physics Letters **103**, 013109 (2013).

[262] B. Daudin *et al.*, “Piezoelectric Properties of GaN Self-Organized Quantum Dots”, MRS Internet Journal of Nitride Semiconductor Research **4**, 846–851 (1999).

[263] S. Kako *et al.*, “Long-lived excitons up to 1 μs in GaN/AlN self-assembled quantum dots”, physica status solidi (b) **240**, 388–391 (2003).

[264] X. Sun *et al.*, “Excitation and emission dynamics of a single photon emitting InGaN quantum dot in a photonic horn structure”, Superlattices and Microstructures **145**, 106575 (2020).

[265] P. Podemski *et al.*, “Photoluminescence Excitation Spectroscopy on Single GaN Quantum Dots”, Applied Physics Express **6**, 012102 (2013).

[266] S. Kako *et al.*, “Size-dependent radiative decay time of excitons in GaN/AlN self-assembled quantum dots”, Applied Physics Letters **83**, 984–986 (2003).

[267] J. Renard *et al.*, “Suppression of nonradiative processes in long-lived polar GaN/AlN quantum dots”, Applied Physics Letters **95**, 131903 (2009).

[268] G. Sarusi *et al.*, “Microcrack-induced strain relief in GaN/AlN quantum dots grown on Si(111)”, Physical Review B **75**, 075306 (2007).

[269] S. T. Jagsch *et al.*, “Ground-state resonant two-photon transitions in wurtzite GaN/AlN quantum dots”, Physical Review B **99**, 245303 (2019).

[270] M. Hrytsaienko, “Dynamique de relaxation dans des boîtes quantiques GaN/AlN: étude par photoluminescence et transmission différentielle pompe-sonde résolues en temps”, PhD thesis (Université de Strasbourg, Strasbourg, 2023).

[271] F. A. Ponce *et al.*, “Crystalline structure of AlGaN epitaxy on sapphire using AlN buffer layers”, Applied Physics Letters **65**, 2302–2304 (1994).

[272] F. A. Ponce *et al.*, “Microstructure of GaN epitaxy on SiC using AlN buffer layers”, Applied Physics Letters **67**, 410–412 (1995).

[273] S. Sanguinetti *et al.*, “Modified droplet epitaxy GaAs/AlGaAs quantum dots grown on a variable thickness wetting layer”, Journal of Crystal Growth **253**, 71–76 (2003).

[274] C. Sun *et al.*, “Wetting layers effect on InAs/GaAs quantum dots”, Physica B: Condensed Matter **407**, 4440–4445 (2012).

[275] M. Nguyen *et al.*, “Effects of microstructure and growth conditions on quantum emitters in gallium nitride”, APL Materials **7**, 081106 (2019).

[276] T. L. Tansley and R. J. Egan, “Point-defect energies in the nitrides of aluminum, gallium, and indium”, Physical Review B **45**, 10942–10950 (1992).

[277] C. Haller *et al.*, “Burying non-radiative defects in InGaN underlayer to increase InGaN/-GaN quantum well efficiency”, Applied Physics Letters **111**, 262101 (2017).

[278] T. F. K. Weatherley *et al.*, “Imaging Nonradiative Point Defects Buried in Quantum Wells Using Cathodoluminescence”, Nano Letters **21**, 5217–5224 (2021).

[279] Y. Chen *et al.*, “GaN buffer growth temperature and efficiency of InGaN/GaN quantum wells: The critical role of nitrogen vacancies at the GaN surface”, Applied Physics Letters **118**, 111102 (2021).

[280] P. Hohenberg and W. Kohn, “Inhomogeneous Electron Gas”, Physical Review **136**, B864–B871 (1964).

[281] A. Alkauskas, M. D. McCluskey, and C. G. Van De Walle, “Tutorial: Defects in semiconductors—Combining experiment and theory”, Journal of Applied Physics **119**, 181101 (2016).

[282] W. Kohn and L. J. Sham, “Self-Consistent Equations Including Exchange and Correlation Effects”, Physical Review **140**, A1133–A1138 (1965).

[283] J. P. Perdew, K. Burke, and M. Ernzerhof, “Generalized Gradient Approximation Made Simple”, Physical Review Letters **77**, 3865–3868 (1996).

[284] J. L. Lyons, A. Janotti, and C. G. Van De Walle, “Effects of carbon on the electrical and optical properties of InN, GaN, and AlN”, Physical Review B **89**, 035204 (2014).

[285] J. L. Lyons *et al.*, “First-principles theory of acceptors in nitride semiconductors”, physica status solidi (b) **252**, 900–908 (2015).

[286] J. L. Lyons and C. G. Van De Walle, “Computationally predicted energies and properties of defects in GaN”, npj Computational Materials **3**, 12 (2017).

[287] A. D. Becke, “A new mixing of Hartree–Fock and local density-functional theories”, The Journal of Chemical Physics **98**, 1372–1377 (1993).

[288] J. Heyd, G. E. Scuseria, and M. Ernzerhof, “Hybrid functionals based on a screened Coulomb potential”, The Journal of Chemical Physics **118**, 8207–8215 (2003).

[289] J. E. Peralta *et al.*, “Spin-orbit splittings and energy band gaps calculated with the Heyd-Scuseria-Ernzerhof screened hybrid functional”, Physical Review B **74**, 073101 (2006).

[290] M. A. Caro, S. Schulz, and E. P. O’Reilly, “Hybrid functional study of the elastic and structural properties of wurtzite and zinc-blende group-III nitrides”, Physical Review B **86**, 014117 (2012).

[291] C. Freysoldt *et al.*, “First-principles calculations for point defects in solids”, Reviews of Modern Physics **86**, 253–305 (2014).

[292] M. Lax, “The Franck-Condon Principle and Its Application to Crystals”, The Journal of Chemical Physics **20**, 1752–1760 (1952).

[293] A. Alkauskas *et al.*, “First-Principles Calculations of Luminescence Spectrum Line Shapes for Defects in Semiconductors: The Example of GaN and ZnO”, Physical Review Letters **109**, 267401 (2012).

[294] J. J. Markham, “Interaction of Normal Modes with Electron Traps”, Reviews of Modern Physics **31**, 956–989 (1959).

[295] C. Santori *et al.*, “Nanophotonics for quantum optics using nitrogen-vacancy centers in diamond”, Nanotechnology **21**, 274008 (2010).

[296] H.-Q. Zhao, M. Fujiwara, and S. Takeuchi, “Suppression of fluorescence phonon sideband from nitrogen vacancy centers in diamond nanocrystals by substrate effect”, Optics Express **20**, 15628–15635 (2012).

[297] H.-Q. Zhao, M. Fujiwara, and S. Takeuchi, “Effect of Substrates on the Temperature Dependence of Fluorescence Spectra of Nitrogen Vacancy Centers in Diamond Nanocrystals”, Japanese Journal of Applied Physics **51**, 090110 (2012).

[298] A. Alkauskas *et al.*, “First-principles theory of the luminescence lineshape for the triplet transition in diamond NV centres”, New Journal of Physics **16**, 073026 (2014).

[299] C. G. Van De Walle and J. Neugebauer, “First-principles calculations for defects and impurities: Applications to III-nitrides”, Journal of Applied Physics **95**, 3851–3879 (2004).

[300] J. Buckeridge, “Equilibrium point defect and charge carrier concentrations in a material determined through calculation of the self-consistent Fermi energy”, Computer Physics Communications **244**, 329–342 (2019).

[301] S. Limpijumnong and C. Van De Walle, “Diffusivity of native defects in GaN”, Physical Review B **69**, 035207 (2004).

[302] H. Amano *et al.*, “Metalorganic vapor phase epitaxial growth of a high quality GaN film using an AlN buffer layer”, Applied Physics Letters **48**, 353–355 (1986).

[303] S. Nakamura, “GaN Growth Using GaN Buffer Layer”, Japanese Journal of Applied Physics **30**, L1705 (1991).

[304] N. Gao, L. Gao, and H. Yu, “First-principles study of N and S co-doping in diamond”, Diamond and Related Materials **132**, 109651 (2023).

[305] M. A. Reshchikov and H. Morkoç, “Luminescence properties of defects in GaN”, Journal of Applied Physics **97**, 061301 (2005).

[306] J. L. Lyons, A. Janotti, and C. G. Van De Walle, “Carbon impurities and the yellow luminescence in GaN”, Applied Physics Letters **97**, 152108 (2010).

[307] Q. Yan *et al.*, “Role of nitrogen vacancies in the luminescence of Mg-doped GaN”, Applied Physics Letters **100**, 142110 (2012).

[308] T. Ogino and M. Aoki, “Mechanism of Yellow Luminescence in GaN”, Japanese Journal of Applied Physics **19**, 2395–2405 (1980).

[309] C. Seager *et al.*, “Luminescence in GaN co-doped with carbon and silicon”, Journal of Luminescence **106**, 115–124 (2004).

[310] M. A. Reshchikov, “On the Origin of the Yellow Luminescence Band in GaN”, physica status solidi (b) **260**, 2200488 (2023).

[311] A. M. Berhane *et al.*, “Photophysics of GaN single-photon emitters in the visible spectral range”, Physical Review B **97**, 165202 (2018).

[312] M. Meunier *et al.*, “Telecom single-photon emitters in GaN operating at room temperature: embedment into bullseye antennas”, Nanophotonics **12**, 1405–1419 (2023).

[313] S. G. Bishop *et al.*, “Enhanced light collection from a gallium nitride color center using a near index-matched solid immersion lens”, Applied Physics Letters **120**, 114001 (2022).

[314] J. Luo *et al.*, “Room temperature optically detected magnetic resonance of single spins in GaN”, Nature Materials, 10.1038/s41563-024-01803-5 (2024).

[315] Y. Geng *et al.*, “Dephasing by optical phonons in GaN defect single-photon emitters”, Scientific Reports **13**, 8678 (2023).

[316] R. N. Patel *et al.*, “Probing the Optical Dynamics of Quantum Emitters in Hexagonal Boron Nitride”, PRX Quantum **3**, 030331 (2022).

[317] S. C. Kitson *et al.*, “Intensity fluctuation spectroscopy of small numbers of dye molecules in a microcavity”, Physical Review A **58**, 620–627 (1998).

[318] L. Fleury *et al.*, “Nonclassical Photon Statistics in Single-Molecule Fluorescence at Room Temperature”, Physical Review Letters **84**, 1148–1151 (2000).

[319] I. Aharonovich *et al.*, “Photophysics of chromium-related diamond single-photon emitters”, Physical Review A **81**, 043813 (2010).

[320] E. Neu, M. Agio, and C. Becher, “Photophysics of single silicon vacancy centers in diamond: implications for single photon emission”, Optics Express **20**, 19956 (2012).

[321] N. R. Jungwirth *et al.*, “A single-molecule approach to ZnO defect studies: Single photons and single defects”, Journal of Applied Physics **116**, 043509 (2014).

[322] C. Kurtsiefer *et al.*, “Stable Solid-State Source of Single Photons”, Physical Review Letters **85** (2000).

[323] A. M. Berhane, C. Bradac, and I. Aharonovich, “Photoinduced blinking in a solid-state quantum system”, Physical Review B **96**, 041203 (2017).

[324] J. Colton *et al.*, “Selective excitation of the yellow luminescence of GaN”, Physica B: Condensed Matter **273-274**, 75–79 (1999).

[325] H. H. Kusuma, B. Astuti, and Z. Ibrahim, “Absorption and emission properties of ruby (Cr:Al_2O_3) single crystal”, Journal of Physics: Conference Series **1170**, 012054 (2019).

[326] J. Yuan *et al.*, “GaN as a Material Platform for Single-Photon Emitters: Insights from Ab Initio Study”, Advanced Optical Materials **11**, 2202158 (2023).

[327] M. A. P. Nguyen *et al.*, “Site control of quantum emitters in gallium nitride by polarity”, Applied Physics Letters **118**, 021103 (2021).

[328] S. Nakamura *et al.*, “Hole Compensation Mechanism of P-Type GaN Films”, Japanese Journal of Applied Physics **31**, 1258 (1992).

[329] J. Neugebauer and C. G. Van De Walle, “Hydrogen in GaN: Novel Aspects of a Common Impurity”, Physical Review Letters **75**, 4452–4455 (1995).

[330] S. Xia *et al.*, “Enhanced Single-Photon Emission from GaN Quantum Dots in Bullseye Structures”, ACS Photonics **8**, 1656–1661 (2021).

[331] H. Ahmad *et al.*, “Substantial P-Type Conductivity of AlN Achieved via Beryllium Doping”, Advanced Materials **33**, 2104497 (2021).

[332] C. Galland *et al.*, “Two types of luminescence blinking revealed by spectroelectrochemistry of single quantum dots - SI”, Nov. 2011.

[333] S. Morozov *et al.*, “Electrical control of single-photon emission in highly charged individual colloidal quantum dots”, Science Advances **6**, eabb1821 (2020).

[334] S. J. U. White *et al.*, “Electrical control of quantum emitters in a Van der Waals heterostructure”, Light: Science & Applications **11**, 186 (2022).

List of acronyms and symbols

Acronyms

μ-PL micro-photoluminescence
AFM atomic force microscopy
AM Auger-Meitner
AR aspect ratio
BS beam splitter
CB conduction band
CBM conduction band minimum
CC configuration coordinate
CCD charge coupled device
CL cathodoluminescence
Cor Pearson correlation coefficient
CW continuous-wave
DFT density functional theory
DLP degree of linear polarization
EBL electron beam lithography
EHP electron-hole pair
FM Frank-van der Merwe
FSS fine structure splitting
FWHM full width at half-maximum
GGA general gradient approximation
HBT Hanbury Brown and Twiss intensity interferometer
HSE screened hybrid functional
HWP half-wave plate
III-N III-nitride
IQE internal quantum efficiency
IRF instrument response function
LDA local density approximation
MBE molecular beam epitaxy
ML monolayer
MOVPE metalorganic vapor-phase epitaxy
MPE multi-phonon emission
NC nanocrystal
NIR near infrared
OD optical density
PD point defect
PDE photon detection efficiency
PDF probability distribution function
PL photoluminescence
PLE photoluminescence excitation
PMT photomultiplier tube
PSB phonon sideband
QCSE quantum confined Stark effect
QD quantum dot
QKD quantum key distribution
QW quantum well
RMS root mean square
RT room temperature
SA self-assembled
SC semiconductor
SD spectral diffusion
SE secondary electron
SF stacking fault
SK Stranski-Krastanov
SNR signal-to-noise ratio
SNSPD superconducting nanowire single-photon detector
SPAD single-photon avalanche diode
SPD single-photon detector
SPE single-photon emitter

TAM total angular momentum
TCSPC time-correlated single photon counting
TD threading dislocation
TLS two-level system
TRPL time-resolved photoluminescence
TTS transit time spread
UV near ultraviolet
VB valence band
VBM valence band maximum
VW Volmer-Weber
WL wetting layer
YL yellow luminescence
ZPL zero-phonon line

Symbols

$g^{(2)}(\tau)$ second-order correlation function
NA numerical aperture
f focal length
λ_cut cut-on wavelength
λ_exc excitation wavelength
λ_SPE SPE peak wavelength
P_exc excitation power
σ_exc excitation power density
Φ_I image diameter
Φ_obj object diameter
f_obj focal length of the objective
Φ_O object diameter
f_foc focal length of the focusing length
$\mathscr{R}$ Airy radius
w_0 beam waist
$w(z)$ beam width
z_R Rayleigh range
Θ_div beam divergence
I_max maximum intensity
ω_diff diffraction-limited Gaussian width
P_meas measured power
η_setup setup efficiency
η_c collection efficiency
α_l setup losses
η_ph photon detection efficiency
n_GaN GaN refractive index
n_air air refractive index
i_m maximum angle of collection
Ω_c light collection solid angle
T transmission coefficient
R reflection coefficient
n_AlN AlN refractive index
θ_c critical angle
θ_d dipole off-axis angle
φ_d dipole in-plane angle
c-axis wurtzite c-axis
m-plane wurtzite m-plane
a-plane wurtzite a-plane
I_min minimum intensity
δ_p degree of linear polarization
Γ_IRF response width of the IRF
Γ_el response width of the electronics
Γ_disp monochromator temporal dispersion
Γ_det response width of the detector
Γ_pulse FWHM of the laser pulse
$G^{(2)}(\tau)$ experimental second-order correlation histogram
$g^{(2)}(0)$ single photon purity
T_FP transmittance of a Fabry-Perot cavity
IIIA group 3A of the periodic table
c-plane wurtzite c-plane
$\mathbf{P}_\mathrm{sp}$ spontaneous polarization
$\mathbf{P}_\mathrm{pz}$ piezoelectric polarization
E_g bandgap
L_QD QD width
h_QD QD height
m^* effective mass
Ψ_e electron wavefunction
Ψ_h hole wavefunction
E_X exciton energy
J_{eh} Coulomb interaction energy
m total angular momentum

δ_0 dark state-bright state splitting
δ_{FSS} fine structure splitting
$\sigma_{\mathrm{GaN/AlN}}$ surface charge density at the GaN/AlN interface
$\mathbf{F}_{\mathrm{bi}}$ built-in electric field
a_{B} effective Bohr radius
γ_1 recombination rate (exciton state or excited state in TLS)
$\mathscr{D}_{\mathrm{X}}$ exciton transition dipole moment
I_{eh} electron-hole vertical envelope function overlap integral
$\tau_{\mathrm{X}}^{\mathrm{rad}}$ radiative exciton decay time
f_{osc} oscillator strength
$\boldsymbol{\mu}$ dipole moment
π excitation rate
N_{EHP} number of EHP
ρ_{SNR} SNR
$E_{\mathrm{XX}}^{\mathrm{b}}$ biexciton binding energy
E_{XX} biexciton energy
$|\mathrm{XX_c}\rangle$ conventional biexciton state
$|\mathrm{XX_h}\rangle$ hybrid biexciton state
$\overline{\mu}$ mean occupation number
$\tilde{n}_i$ scaling factor
I_{TRPL} TRPL intensity
γ^{AM} AM-related recombination rate
γ_i^{d} decay rates in a three-level model
E_{exc} excitation energy
τ_{cap} capture time
τ_{rel} relaxation time
τ_{rise} TRPL rise time
Γ_0 homogeneous broadening
γ_{ac} acoustic phonon broadening constant
Γ_{LO} LO-phonon broadening constant
N_{LO} LO-phonon occupation number
Γ_{th} thermal broadening
Γ_{SD} SD-related broadening
E_{LO} LO-phonon energy
k_{B} Boltzmann constant
$\gamma_{\nwarrow}^{i}$ spin-flip rate (upwards)
$\gamma_{\searrow}^{i}$ spin-flip rate (downwards)
γ_{SF} 0 K spin-flip rate
N_{ph}^{i} spin-flip-related phonon occupation number
$\delta_{\mathrm{B_1}}$ dark-to-B$_1$ splitting
$\delta_{\mathrm{B_2}}$ dark-to-B$_2$ splitting
δ_{XX} hybrid-to-conventional biexciton splitting
$\gamma_1^{\mathrm{B_1}}$ bright state (B$_1$) radiative recay rate
$\gamma_1^{\mathrm{B_2}}$ bright state (B$_2$) radiative decay rate
γ_2^{c} conventional biexciton radiative decay rate
γ_2^{h} hybrid biexciton radiative decay rate
δ_2 dark state splitting
$\mathbf{F}_{\mathrm{ext}}$ external electric field
F_{ext}^{z} vertical component of the external electric field
p_{oc} probability of occupation
$\tau_{\downarrow}$ trapping time
$\tau_{\uparrow}$ release time
$\tilde{c}$ SD-related defect concentration
γ_{in} 'jump in' rate
γ_{out} 'jump out' rate
γ_{SD} SD rate
$\gamma_{\mathrm{i}}^{\mathrm{rad}}$ radiative recombination rate of state i
α_{abs} QD absorption coefficient
σ_{sat} saturation excitation power density
$I_{\mathrm{i}}^{\mathrm{bp}}$ PL intensity of line i integrated over the HBT bandpass
ρ_{bp} biexciton/exciton intensity ratio
τ_{L} long-lived TRPL decay time
$I_{\mathrm{TRPL}}^{\mathrm{tot}}$ integrated TRPL intensity
$I_{\mathrm{TRPL}}^{\mathrm{L}}$ long-live component TRPL intensity
$r_{\mathrm{L/S}}$ intensity ratio $I_{\mathrm{TRPL}}^{\mathrm{L}}/I_{\mathrm{TRPL}}$
τ_{S} short-lived TRPL decay time
$r_{\mathrm{L/S}}^{0}$ intensity ratio $I_{\mathrm{TRPL}}^{\mathrm{L}}/I_{\mathrm{TRPL}}$ for vanishing excitation power
E^{f} defect formation energy
E_{F} Fermi energy
$\epsilon(q/q')$ thermodynamic transition level
e^{-} electron
h^{+} hole
Q configuration coordinate
E_{abs} absorption energy
E_{em} emission energy
d_{FC}^{e} Franck-Condon shift (excited state)

d^{g}_{FC} Franck-Condon shift (ground state)
d_{FC} Franck-Condon shift
E_{ZPL} ZPL energy
S Huang-Rhys factor
w_{ZPL} Debye-Waller factor
I_{ZPL} intensity of the ZPL
I_{PSB} intensity of the PSB
S_{exp} experimental Huang-Rhys factor
c^{eq} equilibrium defect concentration
c_{opt} optically-determined concentration of defects
V_{N} nitrogen vacancy
V_{Ga} gallium vacancy
γ^{e}_{m} de-shelving rate (toward the defect excited state)
γ^{r}_{m} de-shelving rate (toward the defect ground state)
γ_{e} radiative decay rate of the defect excited state
I_{SPE} PL intensity of a defect line
I_{sat} saturation intensity
τ_{AB} transition time from state $|A\rangle$ to state $|B\rangle$
τ_{BA} transition time from state $|B\rangle$ to state $|A\rangle$
γ^{r}_{e} shelving rate

Johann STACHURSKI

PhD at EPFL

@ johann.stachurski@epfl.ch
@ stachurski.johann@gmail.com
in johstachurski

EDUCATION

2024
2019 | **ÉCOLE POLYTECHNIQUE FÉDÉRALE DE LAUSANNE (EPFL)**, Switzerland
PhD in Physics

2019
2017 | **EPFL**, Switzerland
Master in Physics

2017
2015 | **EPFL**, Switzerland
Bachelor in Physics

2015
2012 | **LYCÉE JOFFRE**, France
Scientific Preparatory Classes, PCSI-PC*,
› Admitted to EPFL through ENS Lyon competition—Admitted to Centrale Lyon.

CORE EXPERIENCE

2024
2019 | **ADVANCED SEMICONDUCTORS FOR PHOTONICS & ELECTRONICS LAB | EPFL**, Switzerland
Doctoral Assistant
Spectroscopist : Designed and implemented a micro-photoluminescence setup, developed experimental protocols, and created software for investigating single-photon emitters in solid-state materials.
Teaching Assistant : Guided bachelor students, offered feedback on assignments, led problem-solving sessions, moderated forums, created instructional videos, and supervised master students in the completion of their end-of-study research works and dissertations.

2019
2016 | **PHYSICS SECTION & CQFD ASSOCIATION | EPFL**, Switzerland
Student Assistant
Assisted with Physics courses for 1st and 2nd year EPFL-UNIL students.
Assisted with 2nd year Physics lab sessions, including supervision and report grading.
Provided tutoring in Physics and Mathematics for 1st year EPFL-UNIL students and high school students.

Awards

2023 **Dean's Award for Excellence in Teaching | SB Faculty**, EPFL, Switzerland
Title : *Supervising students with a great deal of pedagogy, precision, and kindness.*

2020 **Teaching Excellence Award | Institute of Physics**, EPFL, Switzerland
Exceptional award granted by the Institute of Physics (IPHYS-EPFL) for pedagogical commitment.

Selected Conferences

Oct. 2022 **Contributed Talk | International Workshop on Nitride Semiconductors**, Berlin
"Single photon emission and recombination dynamics in self-assembled GaN/AlN quantum dots".

Mai 2022 **Contributed Talk | 5th International Workshop on Ultraviolet Materials and Devices**, Jeju
'Single photon emission and carrier dynamics in GaN/AlN quantum dots".

Dec. 2020 **Contributed Talk | 11th International Conference on Quantum Dots** , Munich
"Towards Bright and Pure Single Photon Emitters at 300 K Based on GaN/AlN Quantum Dots on Silicon".

Publications

- J. Stachurski, S. Tamariz, G. Callsen, R. Butté, and N. Grandjean, "Single photon emission and recombination dynamics in self-assembled GaN/AlN quantum dots", Light : Science & Applications **11**, 114 (2022).
- S. Tamariz, G. Callsen, J. Stachurski, K. Shojiki, R. Butté, and N. Grandjean, "Toward Bright and Pure Single Photon Emitters at 300 K Based on GaN Quantum Dots on Silicon", ACS Photonics **7**, 1515-1522 (2020).

Expertise

Characterization	**(Micro)-photoluminescence**, Time-resolved photoluminescence, Interferometry (HBT device)
IT	LabVIEW, Python, LaTeX, Onshape (CAD), Microsoft Office (Word, Excel, PowerPoint)
Languages	French (native), English (fluent), German (proficient)